

# **Encapsulant Discoloration in Photovoltaic Modules in Different Climates of India and its Correlation with Hot Cells and Electrical Degradation**

*Submitted in partial fulfillment of the requirements  
for the degree of*

**Doctor of Philosophy**

by

**Shashwata Chattopadhyay**

**Roll no. 11317R002**

*Supervisors*

**Prof. Chetan Singh Solanki**

**Prof. Anil Kottantharayil**



Department of Energy Science and Engineering

INDIAN INSTITUTE OF TECHNOLOGY

2021



*Dedicated to my family...*



## Approval Sheet

This thesis entitled “Encapsulant Discoloration in Photovoltaic Modules in Different Climates of India and its Correlation with Hot Cells and Electrical Degradation” by Shashwata Chattopadhyay is approved for the degree of Doctor of Philosophy.

  
\_\_\_\_\_

Examiners

  
\_\_\_\_\_  
\_\_\_\_\_

Supervisor (s)

  
\_\_\_\_\_

Chairman

Date: 22/12/2021

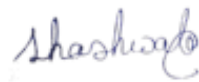
Place: \_\_\_\_\_



## Declaration

I declare that this written submission represents my ideas in my own words and where others' ideas or words have been included, I have adequately cited and referenced the original sources. Some parts of Chapters 4, 5 and 6 have been published in the form of All-India survey reports by the National Center for Photovoltaic Research and Education (NCPRE) at IIT Bombay, and also in various international conferences and journals, as listed at the end of this thesis. Different aspects of the electrical losses and degradation modes data generated in the All-India Surveys of Photovoltaic Module Reliability have been analyzed by myself and Mr. Rajiv Dubey from IIT Bombay and Mr. Birinchi Bora from National Institute of Solar Energy and each have presented their respective analysis in their thesis work.

I hereby declare that I have adhered to all principles of academic honesty and integrity and have not misrepresented or fabricated or falsified any idea/data/fact/source in my submission. I understand that any violation of the above will be cause for disciplinary action by the Institute and can also evoke penal action from the sources which have thus not been properly cited or from whom proper permission has not been taken when needed.



---

**Shashwata Chattopadhyay**

**Roll: 11317R002**

Date: 06-05-2021

Place: **Mumbai**



# Abstract

Complete understanding of degradation mechanisms is important for assessing the reliability of PV modules in the field. This has been the objective of the All-India Surveys of PV Module reliability, carried out in 2013, 2014 and 2016, in various climatic zones of India. The visual degradation of the field-aged modules has been quantified in order to correlate it with the degradation in electrical parameters. Extent of discoloration has been quantified in terms of “Discoloration Index” (*DI*) derived from the visual images using in-house developed software, and has been correlated to the short-circuit current loss. The analysis of survey data has shown that the “Hot” climatic zone (comprising of Hot & Dry, Warm & Humid and Composite) is more severe than the “Non-Hot” climates for encapsulant, metallization and backsheet. Snail tracks have been observed in about 26% of the young modules (less than 5 years old), and is found to be a major contributor to the higher degradation rate observed in many of the young modules. The small/medium sites (capacity less than 100 kW) have been found to suffer from higher percentage of modules with various defects, as compared to the large sites, which raises concern about the module quality.

Encapsulant discoloration is a commonly observed problem that affects more than 10% of the young modules and almost all crystalline silicon modules aged more than 10 years. Localized discoloration in few selective cells has been observed in many of the young modules, the primary cause for which has been found to be higher operating temperature of the cells due to defects (cracks, shunts etc.). The severity of thermal mismatch in the PV module has been quantified in terms of “Thermal Mismatch Index” (*TMI*) and it has been found that there is significant power loss in a PV module if the *TMI* exceeds 0.5 (which is equivalent to an inter-cell temperature difference of 5 °C for standard 18% efficiency 60-cell modules). The primary contributor to the power loss has been found to be fill factor degradation (which is caused both due to the reduced active cell area in the cracked cell and also the encapsulant discoloration on top of the cracked cell).

The discoloration of EVA encapsulant due to UV and temperature has been studied further in the laboratory through accelerated tests in Xenon chamber (total UV intensity around 75 W/m<sup>2</sup>) and a UV-365 chamber (UV intensity around 880 W/m<sup>2</sup> at wavelength of 365 nm). Xenon chamber tests are preferred for service life prediction of PV modules, as the Xenon

spectrum (with suitable filters) is very similar to the outdoor solar spectrum (spectral mismatch is within 0.5% in the UV wavelength region of 300 nm to 400 nm and within 5% for the wavelength region between 400 nm to 800 nm, for the Q-Lab Q-Sun Xe3 chamber with Daylight Q filters). In the Xenon chamber tests, the UV absorber based (UV-cut) EVA has been found to degrade much faster than the UV-transparent (UV-pass) EVA. The activation energy for discoloration of UV-cut EVA has been determined as 0.61 eV which compares well with the value reported in literature, but no value of activation energy could be obtained for the UV-pass EVA (due to very low discoloration). Acceleration factor for the Xenon chamber tests at  $75 \text{ W/m}^2$  UV intensity with sample temperature of  $85 \text{ }^\circ\text{C}$  is estimated to be 27 for Jodhpur (Hot & Dry climate) while it is about 6 times higher for Leh (Cold & Dry climate). Hence, it is estimated that the discoloration in 25-year service life of PV modules installed in Jodhpur can be simulated in about 319 days exposure test in the Xenon chamber, while it would take only 55 days to simulate the discoloration of modules installed in Leh. The UV-pass EVA encapsulant discolors at a slower rate than the UV-cut EVA (about 3.5 times slower discoloration observed at  $64 \text{ }^\circ\text{C}$  in Xenon chamber accelerated tests), so it should be the preferred choice for installations in Hot climates to avoid untimely discoloration and consequent power reduction in the solar panels. However, the backsheets of UV-pass EVA samples have been found to delaminate in the Xenon chamber tests (due to the UV light passing into the laminate below the top encapsulant layer and affecting the EVA-backsheet interface). This delamination problem can be avoided by using UV-pass EVA at the top and UV-cut EVA at the bottom of the solar cells. Hence, it is important to consider the compatibility of the bill of materials (EVA and backsheet) before making any changes to the standard product. Though the prices of both types of EVA are similar, additional care would have to be taken during panel manufacturing to ensure that the top EVA and bottom EVA are not interchanged. Further, the accelerated tests in Xenon chamber have shown that the discoloration of UV-cut EVA increases at an exponential rate with the UV dose at temperatures above  $88 \text{ deg. C}$ . So, in applications where panels are expected to operate at high temperatures, such as in direct roof-mounted applications (where cooling from panel backside is hindered) in Hot climates, it is recommended not to use the UV-cut EVA.

Table 1: Comparison of UV-cut and UV-pass EVA

<b>Sl. No.</b>	<b>Property</b>	<b>UV-cut EVA</b>	<b>UV-pass EVA</b>
1	Transmittance at 350 nm	11 %	88 %
2	UV cut-off wavelength	350 nm	225 nm
3	Discoloration rate at 65 °C in Xenon chamber tests	0.007 /kWh	0.002 /kWh
4	Discoloration rate at 90 °C in UV-365 chamber tests	0.073 /kWh	0.015 /kWh

In summary, our study has shown that discoloration is often observed in the young modules in the Hot climates of India, which can be primarily attributed to the composition of the conventional UV-absorber based EVA encapsulant (UV-cut EVA) and high cell temperatures (Hot spots). The UV-cut EVA degrades at an exponential rate at temperatures exceeding 88 °C, so this EVA is not suitable for direct roof-mounted applications in Hot climates. Newer varieties of the EVA encapsulant which do not have UV absorbers (UV-pass EVA) are more resistant to discoloration as compared to the UV absorber-based EVA (UV-cut EVA), but can lead to other degradation effects due to UV aging of the underlying component of the PV laminate (like delamination of the backsheet). It is hence recommended to use the UV-pass EVA on top of the solar cells and UV-cut EVA at the bottom of the solar cells in the PV module. The Bill of Materials should be properly chosen in order to avoid excessive long term degradation effects in the PV modules installed in the Hot climates.



# Contents

<a href="#"><u>List of Tables</u></a>	ix
<a href="#"><u>List of Figures</u></a>	xiii
<a href="#"><u>Abbreviation Notation and Nomenclature</u></a>	xxi
<b>1. <a href="#"><u>Introduction</u></a></b>	<b>1</b>
<a href="#"><u>1.1</u></a> Background.....	1
<a href="#"><u>1.2</u></a> Solar Photovoltaics .....	3
<a href="#"><u>1.3</u></a> Motivation, Aim & Objectives .....	5
<a href="#"><u>1.4</u></a> Thesis Structure .....	6
<b>2. <a href="#"><u>Literature Review</u></a></b>	<b>9</b>
<a href="#"><u>2.1</u></a> PV Module Degradation Reported in Field Surveys .....	10
<a href="#"><u>2.2</u></a> Discoloration of Encapsulant in PV Modules .....	15
<a href="#"><u>2.2.1</u></a> Polymers used in PV Module Encapsulation .....	15
<a href="#"><u>2.2.2</u></a> Degradation of EVA Encapsulant .....	17
<a href="#"><u>2.2.3</u></a> Quantification of EVA Discoloration .....	20
<a href="#"><u>2.2.4</u></a> Effect of UV Radiation and Temperature on Degradation Rate ...	23
<a href="#"><u>2.2.5</u></a> Accelerated Test Models .....	28
<a href="#"><u>2.3</u></a> Localized Discoloration in PV Modules due to Hot Cells .....	30
<a href="#"><u>2.4</u></a> Research Gaps .....	32
<a href="#"><u>2.5</u></a> Summary.....	33
<b>3. <a href="#"><u>Characterization Techniques</u></a></b>	<b>35</b>
<a href="#"><u>3.1</u></a> Introduction .....	35
<a href="#"><u>3.2</u></a> Electrical Characterization .....	36
<a href="#"><u>3.2.1</u></a> Current-Voltage Measurement (Outdoor) .....	36
<a href="#"><u>3.2.2</u></a> Current-Voltage Measurement (Indoor) .....	38
<a href="#"><u>3.2.3</u></a> Quantum Efficiency (QE) Measurements .....	40
<a href="#"><u>3.3</u></a> Optical Characterization .....	41

<u><a href="#">3.3.1</a></u>	UV-Vis Spectroscopy .....	41
<u><a href="#">3.3.2</a></u>	Fluorescence Spectroscopy .....	43
<u><a href="#">3.3.3</a></u>	Fluorescence Imaging .....	44
<u><a href="#">3.3.4</a></u>	Colorimetry .....	46
<u><a href="#">3.3.5</a></u>	Digital (RGB) Photography .....	47
<u><a href="#">3.4</a></u>	Thermal Characterization .....	48
<u><a href="#">3.4.1</a></u>	Infra-red Thermography .....	48
<u><a href="#">3.5</a></u>	Summary .....	49
<b>4.</b>	<b><u><a href="#">Survey Statistics on Visual Degradation Modes</a></u></b> .....	<b>51</b>
<u><a href="#">4.1</a></u>	Introduction .....	51
<u><a href="#">4.2</a></u>	Field Statistics for Various Visual Degradation Modes .....	55
<u><a href="#">4.2.1</a></u>	Encapsulant Discoloration .....	55
<u><a href="#">4.2.2</a></u>	Front-side Delamination .....	61
<u><a href="#">4.2.3</a></u>	Snail Tracks .....	66
<u><a href="#">4.2.4</a></u>	Discoloration on Metallization .....	70
<u><a href="#">4.2.5</a></u>	Backsheet Degradation .....	75
<u><a href="#">4.3</a></u>	Factors affecting Module Degradation .....	79
<u><a href="#">4.3.1</a></u>	Effect of System Quality .....	79
<u><a href="#">4.3.2</a></u>	Effect of Climatic Zone .....	81
<u><a href="#">4.3.3</a></u>	Effect of System Size .....	83
<u><a href="#">4.4</a></u>	Summary .....	85
<b>5.</b>	<b><u><a href="#">Quantification of Discoloration in PV Modules</a></u></b> .....	<b>87</b>
<u><a href="#">5.1</a></u>	Introduction .....	87
<u><a href="#">5.2</a></u>	Image Processing Technique for Quantifying Discoloration .....	88
<u><a href="#">5.2.1</a></u>	Development of Image Processing Tool .....	88
<u><a href="#">5.2.2</a></u>	Tool Validation based on Quantum Efficiency Measurements .....	97
<u><a href="#">5.3</a></u>	Survey Statistics and Correlations based on Discoloration Index .....	107
<u><a href="#">5.3.1</a></u>	Methodology of Survey Data Analysis .....	107
<u><a href="#">5.3.2</a></u>	Survey Statistics .....	111
<u><a href="#">5.3.3</a></u>	Correlations with Electrical Degradation .....	113

	<a href="#">5.4</a>	Summary .....	120
<b>6.</b>		<b><u>Localized discoloration in PV Modules due to Hot Cells</u></b>	<b>121</b>
	<a href="#">6.1</a>	Introduction .....	121
	<a href="#">6.2</a>	Relation between Cell Temperature and Discoloration .....	123
	<a href="#">6.3</a>	Thermal Model of PV Module with Hot Cell .....	127
	<a href="#">6.4</a>	Thermal Image Analysis Methodology .....	132
	<a href="#">6.5</a>	Effect of Hot Cells on Electrical Degradation .....	136
	<a href="#">6.6</a>	Summary .....	147
<b>7.</b>		<b><u>UV-Thermal Accelerated Tests on UV Absorbing EVA Encapsulant</u></b>	<b>149</b>
	<a href="#">7.1</a>	Introduction .....	149
	<a href="#">7.2</a>	Methodology .....	150
	<a href="#">7.2.1</a>	Sample Preparation .....	150
	<a href="#">7.2.2</a>	Details of Test Setup .....	152
	<a href="#">7.3</a>	Results and Discussion .....	157
	<a href="#">7.3.1</a>	Effect on Fluorescence Spectra .....	161
	<a href="#">7.3.2</a>	Effect on Yellowness Index .....	163
	<a href="#">7.3.3</a>	Effect on Electrical Parameters .....	173
	<a href="#">7.3.4</a>	Acceleration Factor for Different Locations.....	181
	<a href="#">7.4</a>	Summary .....	186
<b>8.</b>		<b><u>Comparative Study of UV-cut and UV-pass EVA Encapsulants</u></b>	<b>189</b>
	<a href="#">8.1</a>	Introduction .....	189
	<a href="#">8.2</a>	Accelerated test in Xenon chamber .....	192
	<a href="#">8.2.1</a>	Methodology .....	192
	<a href="#">8.2.2</a>	Results and Discussion .....	194
	<a href="#">8.3</a>	Accelerated tests in UV-365 Chamber .....	201
	<a href="#">8.3.1</a>	Test Chamber Design .....	201
	<a href="#">8.3.2</a>	Effective Intensity of UV-365 Source .....	202
	<a href="#">8.3.3</a>	Methodology .....	204
	<a href="#">8.3.4</a>	Spatial Non-uniformity of UV Intensity .....	205
	<a href="#">8.3.5</a>	Results & Discussion .....	206

8.4	Summary .....	217
<b>9.</b>	<b><u>Conclusions &amp; Future Work</u></b>	<b>221</b>
9.1	Conclusions .....	221
9.2	Scope of Future Work .....	227
<b>Appendix</b>		
I	<u>Visual Inspection Checklist</u> .....	229
	<u>References</u>	<b>233</b>
	<u>List of Publications</u>	<b>253</b>
	<u>Resume</u>	<b>259</b>
	<u>Acknowledgements</u>	<b>263</b>

## List of Tables

<a href="#">Table 1.1:</a>	Different components of PV module and their purpose	4
<a href="#">Table 2.1:</a>	Degradation rates of maximum power output in different climatic zones for crystalline silicon PV modules.	11
<a href="#">Table 2.2:</a>	The values of the coefficients for calculation of $YI$	21
<a href="#">Table 2.3:</a>	IEC recommendations for outdoor IR thermography of PV modules	31
<a href="#">Table 3.1:</a>	Uniformity measurement in area of interest (3 x 3 cells in 20 x 20 cm area) on Spire solar simulator	35
<a href="#">Table 4.1:</a>	Criteria for climatic zone classification in India	53
<a href="#">Table 4.2:</a>	Overall statistics of visual degradation modes in c-Si modules	54
<a href="#">Table 4.3:</a>	Percentage of modules with encapsulant discoloration in Group X and Group Y, in different age groups	59
<a href="#">Table 4.4:</a>	Percentage of modules with encapsulant discoloration in Group X in different climatic zones	60
<a href="#">Table 4.5:</a>	Percentage of modules with encapsulant discoloration in small and large installations	61
<a href="#">Table 4.6:</a>	Percentage of modules with front-side delamination in Group X and Group Y	64
<a href="#">Table 4.7:</a>	Percentage of modules with front-side delamination in Group X in different climates	65
<a href="#">Table 4.8:</a>	Percentage of modules with front-side delamination in small and large installations	65
<a href="#">Table 4.9:</a>	Percentage of modules with snail tracks in Group X and Group Y	69
<a href="#">Table 4.10:</a>	Percentage of modules with snail tracks in Group X in different climates	69
<a href="#">Table 4.11:</a>	Percentage of modules with snail tracks in small and large installations	70
<a href="#">Table 4.12:</a>	Percentage of modules with metallization discoloration in Group X and Group Y	73
<a href="#">Table 4.13:</a>	Percentage of modules with metallization discoloration in Group X in different climates	74

<a href="#">Table 4.14:</a>	Percentage of modules with metallization discoloration in small and large installations	74
<a href="#">Table 4.15:</a>	Percentage of modules with backsheet degradation in Group X and Group Y	76
<a href="#">Table 4.16:</a>	Percentage of modules with backsheet degradation in Group X in different climates	78
<a href="#">Table 4.17:</a>	Percentage of modules with backsheet degradation in small and large installations	78
<a href="#">Table 5.1:</a>	Discoloration index based on BI	89
<a href="#">Table 5.2:</a>	Discoloration index based on <i>PYI</i>	91
<a href="#">Table 5.3:</a>	Reduction in local short-circuit current density due to discoloration and delamination	104
<a href="#">Table 5.4:</a>	Discoloration severity colour code	112
<a href="#">Table 5.5:</a>	Average severity of discoloration in Group X modules in different climatic zones and age groups	112
<a href="#">Table 5.6:</a>	Average severity of discoloration in Group X and Group Y modules in Hot and Non-Hot zones	112
<a href="#">Table 5.7:</a>	Average extent of discoloration in Group A modules for small and large installations in the Hot and Non-hot climatic zones	113
<a href="#">Table 5.8:</a>	Categorization based on discoloration index	116
<a href="#">Table 6.1:</a>	<i>TMI</i> categories for MPP IR images	136
<a href="#">Table 6.2:</a>	Probability values of Mann Whitney U Test for power degradation in different <i>TMI</i> categories	137
<a href="#">Table 6.3:</a>	Probability values of Mann Whitney U Test for electrical degradation in 0-10 year old modules, comparing the modules with and without hot cells.	138
<a href="#">Table 6.4:</a>	Probability values of Mann-Whitney U Test for power degradation in different <i>TMI</i> categories.	142
<a href="#">Table 6.5:</a>	Probability values of Mann-Whitney U Test for power degradation in different crack and hot cell categories	144
<a href="#">Table 6.6:</a>	Hot cell statistics and average power degradation for various types of cracks	144
<a href="#">Table 6.7:</a>	<i>TMI</i> category for short-circuit IR images	144

<a href="#">Table 6.8:</a>	Probability values of Mann-Whitney U Test for power degradation in different <i>TMI</i> categories in short circuit condition.	145
<a href="#">Table 7.1:</a>	Acceleration factors for Jodhpur and Leh in India	186
<a href="#">Table 8.1:</a>	Accelerated tests for EVA discoloration	192
<a href="#">Table 8.2:</a>	UV Intensity at different points, measured using photodiode	205



## List of Figures

<a href="#">Fig. 1.1:</a>	Cumulative installed capacity of solar photovoltaic systems in the world and corresponding solar panel prices.	2
<a href="#">Fig. 1.2:</a>	Schematic diagram showing various components of crystalline silicon PV module.	4
<a href="#">Fig. 2.1:</a>	Chemical formula of Ethylene Vinyl Acetate (EVA) co-polymer.	16
<a href="#">Fig. 2.2:</a>	Reaction pathways for degradation of EVA.	19
<a href="#">Fig. 2.3:</a>	Color matching functions to reproduce any color based on three primary wavelengths - (a) RGB primaries, and (b) XYZ primaries.	21
<a href="#">Fig. 2.4:</a>	Energy diagram for a chemical reaction, showing the activation energy needed to reach the transition state.	24
<a href="#">Fig. 2.5:</a>	Effect of accelerated tests on contemporary EVA films produced by Hangzhou First EVA (China) – (a) UV exposure, and (b) Damp Heat.	27
<a href="#">Fig. 3.1:</a>	Outdoor current-voltage characterization – (a) Schematic diagram of measurement setup, and (b) portable <i>I-V</i> tracer used for outdoor characterization of PV modules.	37
<a href="#">Fig. 3.2:</a>	Indoor current-voltage characterization - (a) schematic diagram of <i>I-V</i> measurement setup, (b) front view of Spire solar simulator and (b) mini-module being measured on Spire simulator.	40
<a href="#">Fig. 3.3:</a>	Schematic diagram of the QE measurement setup for a cell embedded in a solar cell.	41
<a href="#">Fig. 3.4:</a>	UV-Vis spectrometer with integrating sphere - (a) schematic diagram, and (b) photograph of the Jasco V-650 spectrometer.	42
<a href="#">Fig. 3.5:</a>	Measurement of fluorescence spectra using fiber optics spectrometer – (a) schematic diagram, and (b) photograph of the setup at IIT Bombay.	44
<a href="#">Fig. 3.6:</a>	Fluorescence imaging using 365 nm UV source – (a) schematic diagram, (b) UV source and digital camera on tripods, and (c) fluorescence from a UV exposed sample being captured by a digital camera.	45
<a href="#">Fig. 3.7:</a>	Measurement of yellowness index using colorimeter.	46
<a href="#">Fig. 3.8:</a>	Digital camera used for visual (RGB) photography.	47

<a href="#">Fig. 3.9:</a>	Thermography of solar panels – (a) schematic diagram, and (b) FLIR camera used for IR imaging of PV modules.	49
<a href="#">Fig. 4.1:</a>	Climatic zones of India and sites visited during the surveys in 2014 and 2016.	55
<a href="#">Fig. 4.2:</a>	Examples of encapsulant discoloration observed during the survey.	57
<a href="#">Fig. 4.3:</a>	Percentage of modules affected by encapsulant discoloration in different climatic zones and age groups.	58
<a href="#">Fig. 4.4:</a>	Examples of delamination observed during the survey.	63
<a href="#">Fig. 4.5:</a>	Percentage of modules affected by front-side delamination in different climatic zones and age groups.	64
<a href="#">Fig. 4.6:</a>	Examples of snail tracks observed in the survey.	67
<a href="#">Fig. 4.7:</a>	Statistics of non-framing type snail tracks in different climatic zones and age groups.	68
<a href="#">Fig. 4.8:</a>	Metallization discoloration on interconnect ribbons observed during the survey.	71
<a href="#">Fig. 4.9:</a>	Metallization discoloration statistics in different climatic zones and age groups ('All' inspected modules).	68
<a href="#">Fig. 4.10:</a>	Examples of degradation observed in backsheet.	75
<a href="#">Fig. 4.11:</a>	Percentage of modules with backsheet degradation.	77
<a href="#">Fig. 4.12:</a>	Comparison of the percentage of defective panels in Group X and Group Y sites.	80
<a href="#">Fig. 4.13:</a>	Comparison of the percentage of defective panels in Hot and Non-Hot zones (in Group X sites).	82
<a href="#">Fig. 4.14:</a>	Comparison of the percentage of defective panels in small and large installations.	84
<a href="#">Fig. 5.1:</a>	Discolored PV modules used for discoloration study at Arizona State University.	92
<a href="#">Fig. 5.2:</a>	(a) Photograph of a discolored solar cell, (b) <i>PYI</i> and BI of the discolored cell (along the horizontal center line).	94
<a href="#">Fig. 5.3:</a>	False color map based on <i>PYI</i> .	94
<a href="#">Fig. 5.4:</a>	Examples of circular image sections extracted from solar cell images, cut based on the dimension of the colorimeter probe.	95

<a href="#">Fig. 5.5:</a>	Correlation of the computed <i>PYI</i> with the measured <i>YI</i> at different points of solar cells.	96
<a href="#">Fig. 5.6:</a>	Correlation of the computed <i>BI</i> with the measured <i>YI</i> at different points of solar cells.	96
<a href="#">Fig. 5.7:</a>	(a) Image of cell M1, (b) <i>EQE</i> curves at 13 points along centerline of cell M1, and (c) <i>EQE</i> curves for 300 – 500 nm wavelength range.	98
<a href="#">Fig. 5.8:</a>	Local short-circuit current density (computed from <i>EQE</i> data) at 13 points along centerline of cell M1.	99
<a href="#">Fig. 5.9:</a>	(a) Image of cell M2, and (b) <i>EQE</i> curves at 13 points along the centre-line of cell M2.	100
<a href="#">Fig. 5.10:</a>	External quantum efficiency curves in the 300 – 450 nm wavelength range, for the 13 points on cell M2.	100
<a href="#">Fig. 5.11:</a>	Local short-circuit current density (calculated from <i>EQE</i> data) at 13 points along the centerline of cell M2.	101
<a href="#">Fig. 5.12:</a>	(a) Image of cell M3, and (b) <i>EQE</i> curves at 13 points along the centre-line of cell M3.	102
<a href="#">Fig. 5.13:</a>	Local short-circuit current density (calculated from <i>EQE</i> data) at 13 points along the centerline of cell M3.	103
<a href="#">Fig. 5.14:</a>	External quantum efficiency plot for different points on a discolored and delaminated solar cell of module M3.	104
<a href="#">Fig. 5.15:</a>	External quantum efficiency at different points of the solar cell M1.	105
<a href="#">Fig. 5.16:</a>	External quantum efficiency versus discoloration index for different points on the cell (Number of sample points = 13).	106
<a href="#">Fig. 5.17:</a>	Loss in local short-circuit current density versus discoloration index for cell M1.	106
<a href="#">Fig. 5.18:</a>	(a) Image of a discolored solar panel, (b) perspective corrected image, (c) image of a cell extracted from panel image, and (d) K-Means clustered image	108
<a href="#">Fig. 5.19:</a>	Solar cells with different extent of discoloration, and corresponding values of discoloration index (based on <i>PYI</i> ).	110
<a href="#">Fig. 5.20:</a>	Plot of short-circuit current degradation versus severity of discoloration for (a) Group X modules, and (b) Group Y modules.	118

<a href="#">Fig. 5.21:</a>	Plot of electrical degradation versus extent of discoloration (discoloration category) for Group X modules - (a) $P_{max}$ degradation (%), (b) $V_{oc}$ degradation (%), and (c) $FF$ degradation (%).	119
<a href="#">Fig. 6.1:</a>	Discoloration over all cells in a PV module.	122
<a href="#">Fig. 6.2:</a>	(a) Visual image of a PV module showing localized discoloration of encapsulant (marked with yellow border), (b) IR image of the module taken from back-side, (c) zoomed-in visual image of the affected cells, and (d) IR image of the affected area from backside.	123
<a href="#">Fig. 6.3:</a>	(a) Visual image of a normal temperature solar cell C1 (after perspective correction), (b) thermal map of the cell (perspective corrected), recorded at plane-of-array irradiance of $913 \text{ W/m}^2$ , and (c) variation of the $PYI$ and temperature along the center of the cell (in vertical direction).	125
<a href="#">Fig. 6.4:</a>	(a) Visual image of a solar cell (C2) operating at high temperature (after perspective correction), (b) thermal map of the cell (perspective corrected), recorded at plane-of-array irradiance of $913 \text{ W/m}^2$ , and (c) variation of the $PYI$ and temperature along the center of the cell (in vertical direction).	126
<a href="#">Fig. 6.5:</a>	Variation of discoloration index and temperature along the center of cell C2.	127
<a href="#">Fig. 6.6:</a>	Basic schematic of a PV module showing the laminate structure.	128
<a href="#">Fig. 6.7:</a>	(a) IR image of PV module under MPP condition, (b) IR image of same module under short-circuit, and (c) electroluminescence (EL) image of the module.	134
<a href="#">Fig. 6.8:</a>	(a) IR image of PV modules in a power plant, (b) region of interest extracted from the IR image, and (c) temperature histogram of the module.	135
<a href="#">Fig. 6.9:</a>	Plot of $P_{max}$ degradation (%) versus the $TMI$ category for IR images taken at MPP condition.	137
<a href="#">Fig. 6.10:</a>	Plot of degradation in electrical parameters (%) for modules with Hot cells (HC) and without Hot cells (NHC), for (a) all c-Si sites, and (b) c-Si sites aged less than 10 years having modules with Hot cells.	139
<a href="#">Fig. 6.11:</a>	Histogram of (a) normalized shunt resistance, and (b) normalized series resistance, for the modules with Hot cells.	140
<a href="#">Fig. 6.12:</a>	Plot of $P_{max}$ degradation (%) for modules with and without Hot cells in Hot and Non-Hot climates.	141

<a href="#">Fig. 6.13:</a>	Electrical degradation observed in the modules from Hot zone showing excessive power degradation	142
<a href="#">Fig. 6.14:</a>	$P_{max}$ degradation (%) of PV modules with and without cracks and Hot cells.	143
<a href="#">Fig. 6.15:</a>	Plot of $P_{max}$ degradation (%) versus the <i>TMI</i> category for IR images taken at short-circuit condition.	145
<a href="#">Fig. 6.16:</a>	Plot of electrical degradation (%) versus the <i>TMI</i> category for IR images taken at short-circuit condition – (a) $FF$ degradation, (b) $I_{sc}$ degradation and (c) $V_{oc}$ degradation.	147
<a href="#">Fig. 7.1:</a>	Schematic diagram of the mini-modules made using UV absorbing EVA.	151
<a href="#">Fig. 7.2:</a>	Front view of the mini-modules made using UV absorbing EVA - (a) UVC-1 (b) UVC-2 (c) UVC-3 and (d) UVC-4.	152
<a href="#">Fig. 7.3:</a>	Mini-modules placed inside the Xenon chamber for accelerated testing.	153
<a href="#">Fig. 7.4:</a>	Measurement of the irradiance at the position of the solar cells of sample UVC-3.	154
<a href="#">Fig. 7.5:</a>	UV irradiance on the solar cells of the mini-modules (in $W/m^2$ )	154
<a href="#">Fig. 7.6:</a>	Plot of the temperature (extracted from the IR image) versus the cooling time for the mini-modules – (a) UVC-1 (b) UVC-2, (c) UVC-3, and (d) UVC-4.	156
<a href="#">Fig. 7.7:</a>	Temperature of the solar cells in the mini-modules (based on IR measurements).	157
<a href="#">Fig. 7.8:</a>	Digital images under natural sunlight (left side) and fluorescence images under 365 nm UV excitation (right side) of the mini-modules taken after ca. 300 $kWh/m^2$ Xenon-based UV exposure – (a) UVC-1, (b) UVC-2, (c) UVC-3 and (d) UVC-4.	159
<a href="#">Fig. 7.9:</a>	(a) Different regions in the fluorescence image of the UV-cut samples, and (b) pathways of oxygen ingress into sample UVC-4 – along the interconnect ribbons (marked with blue arrows) and also along the back-side thermocouple.	160
<a href="#">Fig. 7.10:</a>	Fluorescence spectra of UVC-2 cell showing the initial decrease in fluorescence around 430 nm.	161
<a href="#">Fig. 7.11:</a>	Fluorescence spectra of the different samples maintained at different temperatures – (a) as measured (b) after baseline correction.	162

<a href="#">Fig. 7.12:</a>	Correlation of change in integrated fluorescence intensity with change in <i>YI</i> (after 300 kWh/m <sup>2</sup> UV dose).	163
<a href="#">Fig. 7.13:</a>	Change in <i>YI</i> of the samples plotted against the UV dose	164
<a href="#">Fig. 7.14:</a>	Change in <i>YI</i> for selected cells. Solid lines indicate linear fit, while dashed line indicated power law fit.	165
<a href="#">Fig. 7.15:</a>	Change in <i>YI</i> versus UV Dose for samples with temperature less than 88 °C (blue diamond indicate the average change in <i>YI</i> at corresponding UV dose and the regression line is fitted to these average values).	165
<a href="#">Fig. 7.16:</a>	Change in <i>YI</i> at center of the cells of sample UVC-1 plotted against UV dose.	166
<a href="#">Fig. 7.17:</a>	Change in <i>YI</i> at center of the cells of sample UVC-2 plotted against UV dose.	167
<a href="#">Fig. 7.18:</a>	Change in <i>YI</i> at center of the cells of sample UVC-3 plotted against UV dose.	168
<a href="#">Fig. 7.19:</a>	Change in <i>YI</i> at center of the cells of sample UVC-4 plotted against UV dose.	169
<a href="#">Fig. 7.20:</a>	Natural logarithm of change in <i>YI</i> at center of the cells of sample UVC-4 plotted against UV dose.	170
<a href="#">Fig. 7.21:</a>	Arrhenius analysis of the slope of <i>YI</i> change versus UV dose. - (a) considering all cells below 88 °C, (b) considering cells below 88 °C, with linear correlation coefficient for UV dose > 0.64. Slope of the linear regression line indicates the activation energy in eV.	172
<a href="#">Fig. 7.22:</a>	Degradation in electrical parameters in the Xenon chamber tests.	174
<a href="#">Fig. 7.23:</a>	Short-circuit current for all the UV-cut samples – (a) normalized to initial pre-exposure value, and (b) normalized to the current output after initial exposure of 25 kWh/m <sup>2</sup> .	175
<a href="#">Fig. 7.24:</a>	Plot of short-circuit current loss in initial 25 kWh/m <sup>2</sup> UV exposure versus the change in <i>YI</i> .	176
<a href="#">Fig. 7.25:</a>	Plot of short-circuit current loss (post LID) versus change in <i>YI</i> . The initial rapid loss has been discounted.	177
<a href="#">Fig. 7.26:</a>	Selection of the affected area from the fluorescence image. The yellow curve is manually drawn to select the discoloured region.	177
<a href="#">Fig. 7.27:</a>	Plot of short-circuit current loss (post LID) versus effective change in <i>YI</i> (averaged over cell area).	178

<a href="#">Fig. 7.28:</a>	Correlation of short-circuit current and discoloration index (calculated from visual images) for UV-cut samples	179
<a href="#">Fig. 7.29:</a>	Visual images of discolored PV modules surveyed in 2016 All-India survey – (a) 18 years old solar panel from Cold & Sunny climate, and (b) 6 years old solar panel from Warm & Humid climate.	180
<a href="#">Fig. 7.30:</a>	Arrhenius analysis of the slope of $I_{sc}$ loss versus UV dose. Slope of the linear regression line indicates the activation energy in eV.	180
<a href="#">Fig. 7.31:</a>	Comparison of plane-of-array irradiance for Jodhpur and Leh – (a) global total irradiance, and (b) global UV irradiance in 300 – 400 nm wavelength range.	184
<a href="#">Fig. 7.32:</a>	Comparison of temperature for Jodhpur and Leh – (a) ambient temperature, and (b) estimated cell temperature	185
<a href="#">Fig. 8.1:</a>	Transmittance spectra of UV-cut and UV-pass EVA coupons (laminated between quartz glass sheets).	190
<a href="#">Fig. 8.2:</a>	UV Absorbance spectra of UV-cut sample (measured) and Cyasorb UV-531 (from datasheet).	191
<a href="#">Fig. 8.3:</a>	Schematic diagram of UV-pass samples (UVP-1).	193
<a href="#">Fig. 8.4:</a>	IR image of sample UVP-1 showing that the temperature of the cells was highest in the middle section (which had highest insulation thickness).	193
<a href="#">Fig. 8.5:</a>	Box plot showing comparison of the change in $YI$ of UV-cut and UV-pass samples.	194
<a href="#">Fig. 8.6:</a>	Comparison of the change in $YI$ of UV-cut and UV-pass samples at selected temperatures (64 °C and 74 °C).	195
<a href="#">Fig. 8.7:</a>	Fluorescence spectra of UV-cut and UV-pass samples with increase in UV dose, under Xenon exposure - (a) UV-cut (UVC-2), (b) UV-pass (UVP-1).	196
<a href="#">Fig. 8.8:</a>	Fluorescence images of the UV-cut and UV-pass samples (taken after ca. 300 kWh/m <sup>2</sup> Xenon exposure).	197
<a href="#">Fig. 8.9:</a>	Section of the UV-pass sample showing the delamination (visible as white bubbles).	197
<a href="#">Fig. 8.10:</a>	Normalized short-circuit current of UV-cut sample ( <i>left</i> ) and UV-pass sample ( <i>right</i> ) with increase in UV dose under Xenon exposure.	198

<a href="#">Fig. 8.11:</a>	Normalized short-circuit current of UV-cut sample (left) and UV-pass sample (right) versus UV dose under Xenon exposure – Comparison of short-circuit and open-circuit cells at 74 °C sample temperature.	199
<a href="#">Fig. 8.12:</a>	Correlation of short-circuit current loss with the effective <i>YI</i> change (cell area normalized) - (a) UVC-2 sample, and (b) UVP-1 sample.	200
<a href="#">Fig. 8.13:</a>	UV-365 test setup – (a) visual image (b) schematic diagram of main unit.	202
<a href="#">Fig. 8.14:</a>	UV irradiance in AM1.5G spectrum.	203
<a href="#">Fig. 8.15:</a>	Relative efficiency of different UV wavelengths in causing yellowing of EVA, relative to 365 nm wavelength.	203
<a href="#">Fig. 8.16:</a>	Construction of the EVA test coupons – (a) UV-cut coupon (b) UV-pass coupon.	204
<a href="#">Fig. 8.17:</a>	Fluorescence images of paper placed inside the UV-365 chamber – (a) digital image taken from top, (b) gray scale image clearly shows the variation in the UV intensity.	206
<a href="#">Fig. 8.18:</a>	Effect of UV-365 exposure on the coupons – (a) unexposed coupon, (b) exposed UV-pass coupon and (c) exposed UV-cut coupon.	207
<a href="#">Fig. 8.19:</a>	Change in <i>YI</i> of UV-cut and UV-pass samples, in UV-365 chamber tests.	207
<a href="#">Fig. 8.20:</a>	Fluorescence spectra of UV-cut and UV-pass coupons after ca. 700 kWh/m <sup>2</sup> exposure in UV-365 chamber.	208
<a href="#">Fig. 8.21:</a>	(a) Baseline correction of fluorescence spectra, indicating the peak intensity and FWHM, (b) evolution of fluorescence peak intensity in UV-cut and UV-pass coupons with UV exposure, and (c) evolution of FWHM in UV-cut and UV-pass coupons with UV exposure.	210
<a href="#">Fig. 8.22:</a>	Ratio of optical properties after ca. 700 kWh/m <sup>2</sup> UV dose with respect to initial values – (a) reflectance (b) transmittance and (c) absorptance.	213
<a href="#">Fig. 8.23:</a>	Absorptance ratio (at 450 nm wavelength) versus UV dose for UV-cut and UV-pass coupons.	213
<a href="#">Fig. 8.24:</a>	Comparison of discoloration in dry air and nitrogen atmosphere in UV-365 chamber.	215
<a href="#">Fig. 8.25:</a>	Comparison of discoloration in dry air and nitrogen atmosphere in UV-365 chamber, based on logarithm of the change in <i>YI</i>	216

[Fig. 8.26:](#) Difference in  $YI$  of UV-cut coupon between dry air and nitrogen atmosphere, 216  
plotted against UV dose.

## Abbreviation, Notation and Nomenclature

$\alpha$	Temperature coefficient of current, A/K
$A$	Surface area of unit laminate, m <sup>2</sup>
<b>a-Si</b>	Amorphous silicon
<b>ASTM</b>	American Society for Testing and Materials
<b>ASU-PRL</b>	Arizona State University – Photovoltaic Reliability Laboratory
$\beta$	Temperature coefficient for voltage, V/K
<b>BOM</b>	Bill of materials
<b>c-Si</b>	Crystalline silicon
<b>CdTe</b>	Cadmium telluride
<b>CIGS</b>	Copper indium gallium selenide
$D$	UV dose, kWh/m <sup>2</sup>
$DI$	Discoloration index
<b>DYI</b>	Change in yellowness index
$\epsilon$	Emissivity of the module surface
$E_a$	Activation energy, eV
$E_A$	Activation energy, J/mol
<b>EL</b>	Electroluminescence
$EQE$	External quantum efficiency, %
$\eta$	Initial electrical efficiency of the solar cell, %
$FF$	Fill factor
$G$	Plane-of-array irradiance, W/m <sup>2</sup>
<b>GW</b>	Giga Watt
$h$	Convective heat transfer coefficient of laminate, W/m <sup>2</sup> ·K
$I_{sc}$	Short-circuit current, A
<b>IEA</b>	International Energy Agency
<b>IEC</b>	International Electrotechnical Commission
<b>IPCC</b>	Intergovernmental Panel on Climate Change
<b>IR</b>	Infra-red
$I-V$	Current-voltage
$K_B$	Boltzmann constant

<b>LID</b>	Light induced degradation
<b>mono c-Si</b>	Mono crystalline silicon
<b>multi c-Si</b>	Multi crystalline silicon
<b>MW</b>	Mega Watt
<b><i>N</i></b>	Total number of cells in the module
<b>NCPRE</b>	National Center for Photovoltaic Research and Education
<b>NIR</b>	Near infra-red
<b>NISE</b>	National Institute of Solar Energy
<b>NREL</b>	National Renewable Energy Laboratory
<b><i>P<sub>e,module</sub></i></b>	Electrical power output of module, W
<b><i>P<sub>max</sub></i></b>	Maximum power output (at standard test condition), W
<b>PV</b>	Photovoltaic
<b><i>PYI</i></b>	Pseudo yellowness index
<b>QE</b>	Quantum efficiency, %
<b><i>R<sub>s</sub></i></b>	Series resistance, Ohms
<b><i>R<sub>sh</sub></i></b>	Shunt resistance, Ohms
<b><math>\sigma</math></b>	Stefan-Boltzmann constant
<b>STC</b>	Standard test condition
<b><i>T<sub>lam</sub></i></b>	Temperature of the laminate (solar cell), K
<b><i>T<sub>amb</sub></i></b>	Ambient temperature, K
<b><i>T<sub>module</sub></i></b>	Representative (modal) temperature of the module, K
<b><i>T<sub>translated</sub></i></b>	Translated temperature, K
<b><i>T<sub>measured</sub></i></b>	Module temperature (obtained from IR image), K
<b><i>TMI</i></b>	Thermal mismatch index
<b><i>U</i></b>	Overall heat transfer coefficient of laminate, W/m <sup>2</sup> ·K
<b>USA</b>	United States of America
<b>UV</b>	Ultra-violet
<b>Vis</b>	Visible
<b><i>V<sub>oc</sub></i></b>	Open-circuit voltage, V
<b><i>YI</i></b>	Yellowness index

# **Chapter 1**

## **Introduction**

### **1.1 Background**

Mankind's energy demand has been rising rapidly since the beginning of the industrial revolution in the 1760s, and the world's energy demand is projected to cross 2,00,000 TWh by 2040 [1]. The major part of our energy demand has been historically (and is currently) met from fossil fuel sources, which emit harmful greenhouse gases (like carbon dioxide, methane, etc.). These greenhouse gases are responsible for global warming, and meteorological measurements indicate that the earth's surface temperatures have increased by 0.8 °C on average in the last 140 years [2]. The rise in global temperatures has started to impact the weather conditions leading to more frequent extreme weather events like cyclones and heatwaves, melting of the polar ice caps leading to higher sea-water levels and also higher wildlife extinction rates [3]. The Paris Climate Agreement signed by 197 countries in 2015 has set a target to limit global temperature rise above the pre-industrial level to less than 2 °C to avoid catastrophic climate

change [4]. The Intergovernmental Panel on Climate Change (IPCC) has released a special report in 2018 indicating that global net emissions of carbon dioxide would need to fall by 45% from 2010 levels by 2030 and become "net zero" by 2050 in order to prevent the average global temperature rise from exceeding 1.5 °C [5]. Hence, there have been concerted efforts by all major economies to shift towards non-fossil-based energy sources like solar, wind, hydro, nuclear, etc. India has started the National Solar Mission in 2010, with the initial target of 20 GW installed solar capacity by 2022, which has been revised upwards to 100 GW [6], in addition to 75 GW from non-solar based renewable energy sources. Buoyed by the rapid installation of renewable capacity in the country in the last few years, the Indian Government further revised the targets to 500 GW of renewable energy capacity by 2030 [7]. Solar photovoltaic (PV) has shown rapid capacity growth worldwide in the last decade, as shown in Fig. 1.1 [8], due to the rapid fall in the prices of solar panels and the relative ease of deploying solar PV modules in all scales (be it small roof-top systems for households or large megawatt scale power plants in solar farms).

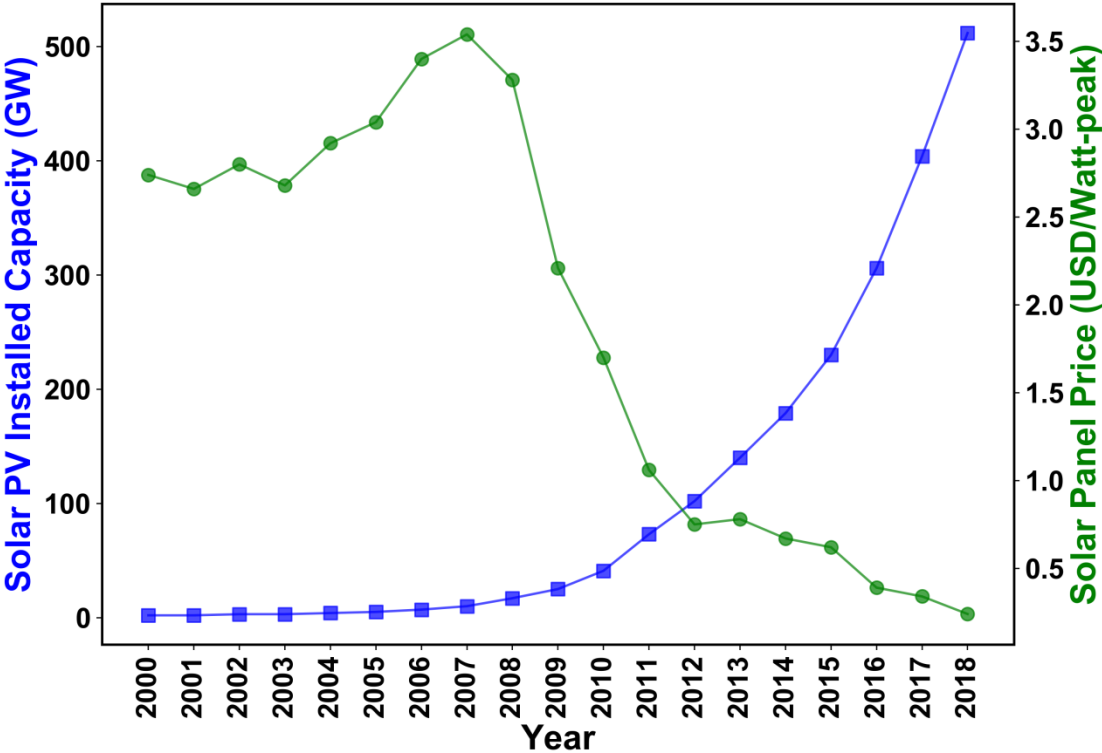


Fig. 1.1: Cumulative installed capacity of solar photovoltaic systems in the world [8] and corresponding solar panel prices (based on [9,10]). The prices have been decreasing as the installed capacity increased over the years.

## 1.2 Solar Photovoltaics

Sun is the ultimate source of energy for all life on earth. Even the fossil-based energy sources are derived from solar energy, since coal and petroleum come from the fossils of the plants that existed on the planet millions of years ago [11]. The total solar energy incident on the earth's surface is estimated to be 3,400,000 EJ per year [12], which is approximately 8500 times of the annual primary energy consumption in 2016 [13]. Thus, there is potential to meet the total energy demand of mankind using solar energy alone (even after considering future growth in energy demand).

There are two major technologies that convert solar energy into electricity – solar photovoltaics and solar thermal. Solar thermal technologies convert the incident solar radiation into thermal energy and then into electricity. On the other hand, solar photovoltaic (PV) technology converts the incident solar radiation directly into electricity by utilizing the photovoltaic effect. Photovoltaic effect refers to the absorption of electromagnetic waves by certain crystalline materials (semiconductors), which ionizes the crystal atoms thereby generating mobile electrons and positively charged ions (holes) in the material. In the crystalline silicon solar cells, a p-n junction is formed by doping the silicon semiconductor with boron (for the p-type region) and phosphorus (for the n-type region), and the charge carriers generated by the absorption of the incident photons, get separated due to the electric field at the p-n junction [14]. In simplified terms, it can be said that the electrons travel through the electrical load in the external circuit and finally combine with the positively charged hole in the solar cell, giving rise to electrical current. The solar cell is encapsulated in a PV module using glass and various polymers. The structure of the photovoltaic module of crystalline silicon (c-Si) technology is shown in Fig. 1.2, and the roles of the various components of the PV module are listed in Table 1.1. All the components are important from reliability point of view, but these components are affected by the environment stressors in different ways. The earliest solar panels manufactured for terrestrial applications carried a modest warranty of 5 years [15], but the warranty period has been revised upwards over the years as the production capacity and module deployment has increased. Solar panel manufacturers presently provide 25-year warranty on the solar panels, with a power warranty of maximum 20% reduction in 25 years.

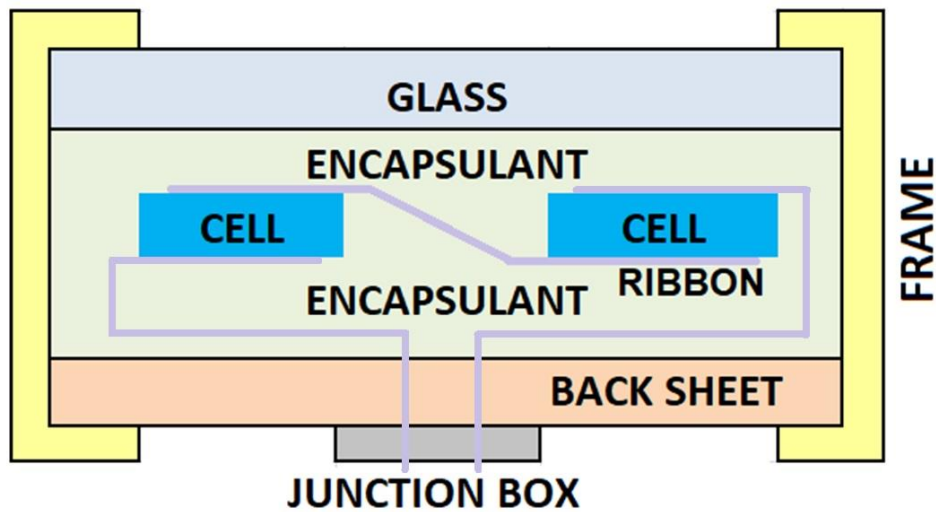


Fig. 1.2: Schematic diagram showing various components of the crystalline silicon PV module. Only two cells are shown for representation purpose (while actual full-size modules have 6 cells in a row, and 12 such rows). Drawing is not to scale.

Table 1.1: Different components of PV module and their purpose [16]

Component	Purpose
Glass	Provides mechanical strength and rigidity to the solar panel and protects the solar cells from direct contact with environmental factors (like rain, dust, etc.) while transmitting the incident light with minimum loss.
Encapsulant	Provides electrical isolation and cushions the solar cells. It provides adhesion between the various components and ensures optical coupling between the glass and solar cell.
Solar Cell	Converts the incident light into electricity
Backsheet	Provides electrical isolation and prevents moisture ingress.
Frame	Provides mechanical rigidity to the module and holds the various components of the laminate together
Bypass Diode	Prevents hot spot generation due to partial shading of solar cells by bypassing the current
Junction Box	Protects the output terminals and bypass diode, from dust and water ingress.
Ribbons	Connects the solar cells to the external circuit

### 1.3 Motivation, Aim & Objectives

There is a worldwide push towards renewable energy technologies, which has resulted in high investments from public and private funds into solar photovoltaic power plants. The long-term reliability of the solar PV modules will decide the overall energy generation (and not the initial installed capacity). Even though most modules sold in the market carry a nameplate indicating that it is certified as per IEC 61215 standard [17], the reality is that only a few modules from the manufacturer's production line are actually tested by the certifying agency (as it is a product design qualification test). Any changes by the manufacturer in the Bill of Materials can impact the performance and reliability of the modules. Sometimes, manufacturers may be forced to make such changes owing to the non-availability of raw materials. Also, the certifying laboratory performs a series of tests as per IEC 61215, which can at best screen modules for infant mortality [18] but cannot guarantee the 25-years field life as claimed in the warranty clause by the module manufacturer. These laboratory tests are generic in nature and do not take into account the climatic zone variations (presently efforts are underway to introduce separate IEC testing protocols for hot climates). Severe competition in the PV market has ensured that the price per watt of installed capacity is reducing continuously, but this may also impact the quality of the raw materials used by the module manufacturers. Hence, it is important to conduct regular field surveys to investigate the performance of the installed PV systems and identify the degradation modes active in the field aged modules in different climatic zones. So, the National Centre for Photovoltaic Research and Education (NCPRE) and the National Center for Solar Energy (NISE) have jointly undertaken field surveys in 2013 [19], 2014 [20] and 2016 [21] on a pan-India scale to evaluate the reliability and performance of the PV modules in different climatic zones of India. In these surveys, various characterization techniques have been applied to measure the performance of the PV modules and evaluate their present state of health, which includes current-voltage ( $I$ - $V$ ) characterization, infrared thermography, electroluminescence imaging, leakage resistance test, visual inspection, etc. The characterization techniques can be broadly classified into two categories – (a) non-contact measurements, and (b) contact-based measurements. Visual inspection and infrared thermography are the non-contact characterization techniques while there are multiple contact-based characterization techniques like current-voltage characterization, electroluminescence imaging, leakage resistance measurement, etc. Each of these techniques indicates some aspect

of the overall health of the solar panel, but a combination of these measurements is necessary to generate a complete picture of the solar panel's health. The non-contact measurements can be taken even when the PV system is in operation, since the connection of the PV modules to the inverter does not need to be interrupted. On the other hand, the contact-based measurements generally require isolation of the PV modules from the inverter, which halts the power generation from the system. Given that the contact-based techniques require disconnection of the PV system wiring (requiring both time and expertise and lead to generation loss), it is not feasible to perform these tests on regular basis in large megawatt scale PV systems. The non-contact measurements do not hamper the operation of the plant and can be performed regularly (say monthly or quarterly) to estimate the health of the power plant. Our work focuses on the visual degradation modes prevalent in different climatic zones in India. Encapsulant discoloration has been commonly observed particularly in the hot climates, and hence we have focused on developing a non-contact characterization technique for the discoloration in PV modules and correlating it with the electrical degradation observed in modules. We have also studied discoloration of different encapsulants in the laboratory through accelerated testing so as to identify the encapsulant best suited for hot climates.

## **1.4 Thesis structure**

The thesis has been divided into nine chapters. Degradation of photovoltaic modules has been studied since the 1980s, and a brief literature review of the relevant degradation modes is presented in Chapter 2.

Chapter 3 provides an overview of the various characterization tools and methodologies used in the field surveys and in the laboratory as part of this thesis.

The statistics of the visual degradation modes observed in the field-aged modules are given in Chapter 4. Snail tracks have been found to be the most frequently observed problem in the young modules (aged less than 5 years), while encapsulant discoloration has been observed in many young modules and in almost all old modules.

The results of indoor studies for the quantification of discoloration are discussed in Chapter 5. Based on indoor and outdoor experiments, discoloration index (*DI*) has been defined, which serves to quantify the extent of discoloration in the PV module based on the analysis of digital images.

In some cases, hot cells have been found to lead to localized discoloration in some of the solar panels. The correlation of the hot cells with discoloration and electrical degradation is presented in Chapter 6.

Since encapsulant discoloration is one of the most common degradation modes in the Hot climates of India, we have performed UV-thermal accelerated tests to study the degradation of EVA encapsulants with and without UV absorbers. The UV-pass EVA has been found to discolor much less than the UV-cut EVA samples, but the UV-pass samples have suffered delamination. The results of the UV accelerated tests are discussed in Chapters 7 and 8.

Finally, the conclusions and scope of future work are outlined in Chapter 9. The implications of the All-India Surveys on PV Module Reliability in Indian climatic conditions have been highlighted, considering the ambitious target for solar PV installations of the Indian government. The conclusions of the indoor accelerated tests have been summarized, and relevant future work has been outlined in this chapter.

This page is intentionally left blank.

## **Chapter 2**

### **Literature Review**

The performance and degradation of PV modules upon exposure to the outdoor environment has been the focus of scientific investigations for many decades [22]. The solar panels are warranted to last for 25 years in the field, with only 20% reduction in the power output. Long term field studies in different climatic conditions are necessary to evaluate the durability of the PV modules and validate the warranty terms, but this is made difficult by the fast evolution of the technology. The relevant literature associated with field and laboratory studies on material degradation in PV modules (with a focus on encapsulants) is summarized in the following sections.

## 2.1 PV Module Degradation reported in Field Surveys

Field data is of great significance in evaluating the durability of the PV modules in different climatic conditions. The manufacturing industry depends on accelerated tests to quickly ascertain the ability of a product to survive certain stress levels. However, the actual validation of the accelerated test results depends on confirmation with field data, since often the accelerated tests can cause degradation and failure modes that are not seen in the field and hence are irrelevant for assessing the product lifetime. Hence, manufacturers depend on the field data for driving improvements in the product design. The test standard recognized worldwide for qualifying the PV module product design is IEC 61215 standard [17]. This standard specifies various tests for checking the tolerance of the module to various environmental factors like temperature, humidity and UV light, which includes UV preconditioning, Temperature Cycling test, Damp Heat test, Humidity Freeze test, to name a few. These tests are performed under extreme conditions for a short span of time to determine the tolerance capability of the solar panel. For example, the Damp Heat test is performed at 85 °C and 85% relative humidity for 1000 hours. If the power loss in the solar panel is less than 5% after going through the test sequences in IEC 61215, then the panel design is considered as qualified. The IEC 61215 test standard is, however, only useful for qualifying the product design for outdoor operation and ensures that the product would not suffer infant mortality (catastrophic failure in the initial years of outdoor exposure). These tests cannot determine the lifetime of the solar panel and, hence, cannot guarantee the durability of the panel for the 25-year lifetime for which the manufacturer usually provides warranty [18]. In the absence of laboratory tests for determining the lifetime of solar panels, tracking the performance degradation in the field assumes greater importance. The degradation in electrical performance of the PV modules installed at the first large scale PV site at Carissa Plains in USA in the 1990s was found to be associated with the degradation of the packaging materials (breakages in the solder joints and the discoloration of the encapsulant) [22], which initiated efforts to improve these materials. However, discoloration in modules is still observed in different parts of the world. The IEA report on “Assessment of Photovoltaic Module Failures in the Field” [23] has indicated that the major defects observed in crystalline silicon modules in the Moderate and Cold/Snow climates in different parts of Europe are moisture ingress (19%), frame damage (17%), snail tracks (12%) and backsheet defects (9%). The authors have noted that the encapsulant and backsheet play a major role in

the reliability of the PV modules, since humidity and acetic acid (generated by EVA encapsulant degradation) tend to accelerate most of the degradation modes observed in PV modules [23]. There have been several studies in solar power plants located in the USA, by Arizona State University Photovoltaics Reliability Laboratory. Sai *et al.* [24] have reported on the defects observed in different PV module technologies, aged 1.5 to 19 years, in four different climatic zones. In the “Hot-Dry” climate, front encapsulant delamination and backsheet burns are the major safety defects, while encapsulant discoloration, delamination and cell chipping/cracks are the major performance defects. Encapsulant discoloration and delamination are also the major defects in the “Hot-Humid” climate. Jordan *et al.* have analyzed more than 11000 degradation rates reported in various studies from around the world [25]. The median degradation rate for crystalline silicon solar panels has been found to be 0.5 – 0.6 %/year, with the mean value around 0.8 – 0.9 %/year (indicating that significant number of panels have degradation rates in excess of 1 %/year). The panels in hot climates have higher degradation rates than the panels installed in cold climate [25]. The performance degradation rates for crystalline silicon modules reported in some of the field studies from different parts of the world is presented in Table 2.1.

Table 2.1: Degradation rates of maximum power output in different climatic regions for crystalline silicon PV modules. The degradation rates reported from India have been highlighted in bold. The climatic zone classification is based on Bansal and Minke [26].

Climate	Location	Age of Panels (Years)	Average Degradation Rate of Power at MPP (%/year)		Reference
			Mono c-Si	Multi c-Si	
Hot and Dry	Tuscon (Arizona, USA)	1	1	1.65	[27]
	Sede Boqer (Israel)	3	0.5	NA	[28]
	Mesa, Arizona (USA)	4	0.4	0.53	[29]
	Mesa, Arizona (USA)	2.4 – 6.7	NA	0.5	[30]
	Tempe, Arizona (USA)	12 – 18	0.57 – 4.96		[31]
	Tempe, Arizona (USA)	6 - 16	1.17		[32]

Climate	Location	Age of Panels (Years)	Average Degradation Rate of Power at MPP (%/year)		Reference
			Mono c-Si	Multi c-Si	
Warm and Humid	La Réunion Island (French island in Indian Ocean)	2	NA	5	[27]
	<b>Gujarat (India)</b>	2	<b>1.93</b>	NA	[33]
	Serpong (Indonesia)	3	1.0	NA	[28]
	Texas (USA)	5	NA	1.07	[32]
Composite	<b>Gurugram (India)</b>	2.3	NA	0.51	[34]
	<b>Gurugram (India)</b>	10	<b>&lt;1 (best group)</b> <b>2.8 (worst group)</b>	NA	[35]
	<b>Gurugram (India)</b>	21	<b>0.4 (maximum)</b>	NA	[36]
	<b>Gurugram (India)</b>	22	<b>1.9 (range: 0.3 – 4.1)</b>	NA	[37]
Cold and Cloudy	Berlin	1	1.25	1.05	[27]
	Perth (Australia)	1.5	2.7	2.9	[29]
	INES, Chambéry (France)	2	NA	4	[27]
	<b>Himachal Pradesh (India)</b>	2.5	<b>0.51</b> <b>(50 % in worst panel)</b>	NA	[38]
	Cologne (Germany)	3	0.5	NA	[28]
	Zugspitze (Germany)	3	2	NA	[28]
	New York (USA)	3 - 19	NA	0.65	[32]
	Hamamatsu (Japan)	10	0.62	NA	[29]
	Lugano (Switzerland)	20	0.53	NA	[29]
	Ispra (Italy)	22	0.67	0.3	[39]
<b>Himachal Pradesh (India)</b>	28	<b>1.4</b>	NA	[40]	
Cold and Sunny	Colorado (USA)	3 - 5	0.15		[32]
	Golden, Colorado (USA)	8	0.75	NA	[29]

Bogdanski *et al.* have studied the impact of different climatic conditions on crystalline silicon panels installed in four different countries [28]. They have observed very low degradation (less than 1%) in Cologne, whereas the degradation was much higher (more than 4% in 3 years in some modules) in the panels installed in the mountains of Zugspitze, Germany. This high degradation has been attributed to cracks in the solar cells due to heavy snow loads and windy weather. Also, higher degradation has been observed in the panels installed in Israel

and Indonesia, which has been partly attributed to higher light induced degradation of the panels installed near the tropics [28]. Va'zquez *et al.* have compared the degradation data reported from different sites in Australia, Japan, Switzerland and USA [29]. They have observed that the degradation rate of cSi panels ranged from 0.3 to 3%/year. Further, the variability in the power output of panels in a system increases over time, thereby reducing the overall system performance due to current mismatch. In their view, the power degradation rate should be less than 0.5 %/year to guarantee the performance of the panels for 25 years, given the increase in the variability of the module power output as the system ages [29]. In Table 2.1, the degradation data for India is mainly from the Composite and the Cold climatic zones. Rajput *et al.* have reported on the various degradation modes observed in 22-year-old solar panels, which have shown power degradation rate between 0.3 to 4%/year [37]. Discoloration on the solar cells, metallization and backsheet chalking and discoloration has been observed in all the panels, while bubbles and hot spots has also been observed in significant percentage of panels. The degradation in the power output has been mainly contributed by loss in fill factor and short circuit current and there has been no degradation in the open circuit voltage [37]. Some of the solar panels installed in street lighting systems in the NISE campus in Gurugram have shown negligible degradation (with respect to name plate ratings) in 21 years of operation [36]. The solar panels with discoloration have shown about 9% degradation in power output, and detailed investigation using lock-in thermography and electroluminescence imaging has shown severe shunts in some cells of the degraded panels. Sharma *et al.* have reported the degradation in different PV technologies after 28 months of outdoor operation. They have found degradation rate of 6.4%/year (a-Si), 0.5%/year (multi c-Si), and 0.36%/year (HIT). Glass soiling and oxidation of silver gridlines and ARC coating in multi c-Si modules has been reported by the authors [34]. Kumar *et al.* have reported a degradation rate of 1.93 %/year for a 2.8-year-old canal top PV system installed in Gujarat, India. This degradation rate is much higher than the warranty limit and the authors have attributed this higher loss to the high humidity in the canal top micro-environment [33]. Sastry *et al.* have reported on the degradation rate of crystalline silicon solar panels installed in NISE test bed around 1998-99. There are 11 manufacturers, who have been grouped into 5 different groups based on performance of the panels. The worst performing group has suffered average 28% power degradation in 10 years (so degradation rate is approx. 2.8 %/year) whereas the degradation rate of the best performing group is within 1%/year [35]. The degradation modes observed in these panels include browning of encapsulant, corrosion of metallic contact, corrosion of the gridlines, delamination on cells, and

corrosion in the output terminals. Chandel *et al.* have done degradation analysis of 28-year field exposed mono c-Si modules which are directly coupled to a water pumping system in Himachal Pradesh. The power degradation rate is found to be 1.4 %/year (which is acceptable since the panels are almost 3 decades old and have surpassed the warranty period). The degradation modes observed in the PV modules include encapsulant discoloration and delamination, backsheet bubbles, oxidation of gridlines and glass breakage [40]. Vikrant *et al.* have studied the performance of a 1 KWp rooftop system, after 2.5 years of installation in Hamirpur, Himachal Pradesh. Out of 10 panels, 7 panels have shown reasonably good performance with average degradation rate of 0.51 %/year, but 3 panels have shown very high degradation close to 50% within 3 years. In one of the three faulty panels, there is severe hot spot in a cell with associated browning of encapsulant and root cause analysis revealed disconnected interconnect ribbon in the cell. In the other two panels, the authors have reported soldering failure in junction box to be the root cause for the low power output. A common degradation mode observed in all the panels at this site is snail tracks [38].

Snail tracks have become a cause for concern in the last 10 years, as there has been almost no report of such defects in the older literature. Snail tracks are greenish/brownish curved lines on the solar cells, usually seen within a few months of installation [41]. It has been reported that the brownish discoloration associated with snail tracks is caused due to silver nano-particles accumulating within the encapsulation film [42]. It is commonly observed that the snail tracks occur along cracks in the cells [43], which indicates that the transport of ions/moisture through the cell crack plays a critical role in snail track formation. Snail tracks thus serve as visual indicator of cracks in the solar cells. There is also a form of snail track that appears along the edges of the solar cells and is referred to as framing [41]. Framing is not associated with cell cracks (instead related to the cell-to-cell gaps), but does indicate the vulnerability of the material combination towards snail track formation. Meyer *et al.* [44] have found that certain combinations of EVA and backsheet give rise to snail tracks, whereas other combinations are not susceptible to snail track formation. Thus, the material combination is one of the critical factors for snail track formation.

Backsheet is a protective layer that isolates the active circuit from outside world, and its degradation can have severe consequences with regard to the safety of operators. Traditionally, the multi-layered backsheet consisted of a polyester film (PET) as the inner layer, laminated

between two layers of polyvinyl fluoride (PVF) [45]. Chalking of backsheet is a common phenomenon in older modules (more than 10 years old), and is caused due to photo-thermal degradation of the backsheet outer layer. Chalking reduces the backsheet thickness by a few microns, which is generally not considered to be hazardous. Bubbles in the backsheet are another form of defect, which increases the temperature of the affected cells (as the heat transfer is impeded) and decreases the power output of these cells. Sometimes, shunts in the solar cells can cause very high temperatures locally, which would often lead to burn marks in the backsheet. A recent survey by a leading manufacturer of backsheets found that cracks, delamination and yellowing are common problems of backsheet in the recent installations, and year-on-year increase in defects is around 47% [46]. Cracks in the backsheet are a critical problem as they would expose the middle layer (usually PET, which is susceptible to hydrolysis) to water ingress, and also compromises (reduces) the insulation resistance (which can create an electrocution hazard).

In order to standardize the documentation of the degradation and failure modes noticed in the field, Packard *et al.* [47] have developed a Visual Inspection Data Collection Checklist. A modified version of this checklist has been used for the All-India Survey of Photovoltaic Module Reliability in 2014 and 2016 (given in Appendix-I).

## **2.2 Discoloration of Encapsulant in PV Modules**

### **2.2.1 Polymers used in PV Module Encapsulation**

The primary functions of encapsulant materials are to provide structural support to the solar cells while maintaining physical isolation between the cells and other electrical circuitry and also maintain good optical coupling between the solar cells and the glass (with at least 90% transmittance at the beginning of module life) [48]. The PV modules manufactured in the 1960s and 1970s mostly used either Polydimethylsiloxane (PDMS) [49] or Poly Vinyl Buteryl (PVB) [50] as the encapsulant. PDMS is highly stable to UV and thermal stress [49] but also significantly costlier than PVB, which was adopted from the automobile safety glass industry. The flat plate solar array project [50] of the US government investigated various polymeric



Buteryl (PVB) are non-cross-linked materials. As opposed to cross-linked encapsulants like EVA (which are chemically bonded to the surfaces of glass and solar cells), the non-cross-linked materials depend on a combination of ionic, hydrogen and Van der Waals forces for adhesion, which is susceptible to de-bonding in case of water ingress into the materials. Hence, there is higher possibility of delamination in such non-cross-linked materials as compared to EVA [49].

### **2.2.2 Degradation of EVA Encapsulant**

Degradation of polymers exposed to outdoor environment usually leads to discoloration of the polymer. The problem of discoloration of EVA encapsulant in PV modules had been extensively studied in the 1990s, after the Carissa Plains' incident. The Carissa Plains power plant constructed in 1984, used 2-axis trackers with V-trough mirrors and had a rated power output of 5.2 MW. The power output from the Carissa Plains power plant degraded at the rate of 10%/year (between the years 1986 to 1989), and the degradation modes included EVA encapsulant degradation and solder bond failure [22]. The use of concentrating mirrors at the Carissa Plains power plant led to severe discoloration of the PV module encapsulant. Czanderna and Pern [48] have reviewed the experimental literature available at that time and came to the conclusion that the Vinyl Acetate (VA) pendant group undergoes de-acetylation upon exposure to UV and high temperature, leading to the formation of acetic acid. The primary degradation products of EVA degradation due to exposure to UV, temperature, and humidity are [48]:

- Aldehyde, Methane and Carbon dioxide (Norrish I reactions)
- Polyenes and Acetic acid (Norrish II reactions)
- Ketones and Aldehydes (Norrish III reactions)

The long-chain conjugated polyenes formed in Norrish II reactions result in the discoloration of the polymer. However, the polyenes can get photo-bleached in the presence of Oxygen, leading to the removal of discoloration. UV absorbers (like Cyasorb UV-531) and stabilizers (like Tinuvin 770) are added to the EVA encapsulant to prevent untimely discoloration, but the ratio and concentration needs to be optimized otherwise the desired UV protection is not obtained [48]. Polymer processing conditions used in lamination/curing steps affect the initial degradation rates from residual chromophores. Curing of the EVA film at

around 145 °C produces UV-excitable chromophores in the EVA, and their concentration is significantly greater in slow cure EVA as compared to fast cure EVA (longer processing time leads to higher chromophore concentration). The slow-curing Lupersol 101 peroxide is the main oxidizing agent that promotes the generation of chromophores, so replacing Lupersol 101 by the fast-curing Lupersol TBEC reduces the formation of the UV-excitable chromophores [53]. Pern *et al.* [54] have also studied the effects of EVA discoloration on the quantum efficiency of solar cells. The authors have reported that there was a 9% reduction in cell efficiency due to light brown EVA while dark brown EVA caused almost 50% reduction in efficiency. Quantum efficiency (QE) measurements show that the QE reduces in the 400-750 nm range with increased yellowing of the EVA, but in the last stages (dark brown EVA), an enhancement in the QE in 750 – 1000 nm range is also observed (which however cannot compensate for the huge loss in the shorter wavelength ranges). Klemchuk *et al.* [55] have indicated that reaction between peroxides and UV absorbers can also lead to chromophore precursor molecules. The chromophores generated during the lamination process are excitable by UV above (wavelength greater than) 360 nm, but the commonly used UV absorber, Cyasorb UV-531, does not provide adequate protection in this wavelength range [55]. Advanced formulations of High Light Transmitting EVA are available nowadays, which do not contain any UV absorbers and are claimed by the manufacturer to have almost no discoloration in accelerated UV tests [56].

In order to understand the degradation mechanisms of encapsulants and develop quality assurance standards and service life prediction models, research and standards organizations like National Renewable Energy Laboratory (NREL), National Institute of Standards and Testing (NIST), etc. have initiated detailed studies in recent years. Researchers from NIST [57] have developed an artificial UV aging chamber, SPHERE (Simulated Photo-degradation via High Energy Radiant Emission), in which EVA samples were tested at 85 °C, 0% RH with maximum UV intensity of 170 W/m<sup>2</sup>.

Pieke *et al.* [58] have compared the degradation in seven types of crystalline silicon-based PV modules subjected to indoor accelerated tests (Thermal aging, UV aging, Damp Heat, and UV/Damp Heat) and also monitored their outdoor degradation in four different climates (arid, tropical, moderate and mountain). Comparison of Raman spectra between the indoor and outdoor tested modules showed that the UV and UV/DH aged modules have similar Raman spectra as the modules aged in arid climate for 3 years. High fluorescence intensity was

observed in the encapsulant above the center of the cells, while the fluorescence intensity at the edges was lower. The fluorescence intensity was higher for modules exposed to arid and tropical climates as compared to moderate climate.

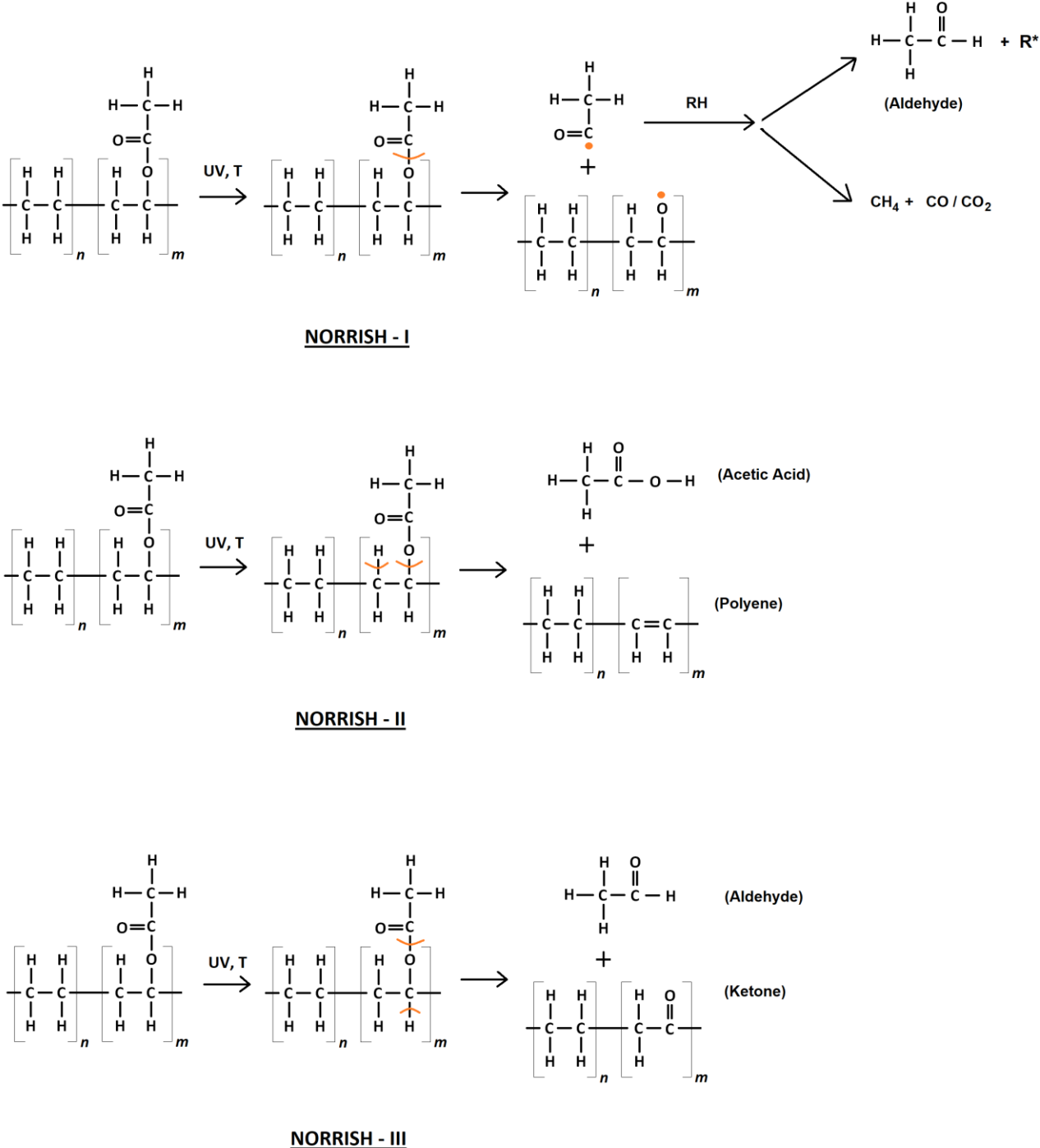


Fig. 2.2: Reaction pathways for degradation of EVA (based on ref. [48]), showing the bond cleavage positions (marked with orange color). All degradation mechanisms are associated with the VA group.

Kempe *et al.* [59] have presented an overview of the scientific issues involved in selection of polymers for PV applications. Their Xenon lamp accelerated test data shows that PDMS (silicone) based encapsulants degrade less than EVA based encapsulants. The reason is that the Si-O bond is much stronger than the C-C bond (bond dissociation energy is 108 kcal/mol versus 83 kcal/mol). At 108 kcal/mol, only UV light of wavelength smaller than 263 nm (which is rarely present in sunlight at sea level) can cause bond breakage. The investigators have pointed out that the cross-linked polymers like EVA and silicone (PDMS) have better adhesion to glass as compared to non-cross-linking type encapsulants (like Ionomers, TPU, TPO, PVB etc.). Thus, silicone emerges as the best choice for PV module encapsulant if the PV module price is not a constraint.

### **2.2.3 Quantification of EVA Discoloration**

The human perception of color is associated with the light reflected (or emitted) from an object in the wavelength range of approximately 400 nm to 700 nm [60]. This perception is made possible by three sets of photo-receptors (called cones) that are sensitive to long, middle and short wavelengths of light. Consequently, our vision is trichromatic, meaning that any color (monochromatic wavelength of light) can be created using different intensities of the three primary colors (wavelengths of light), called tristimulus values. Stiles and Burch [61] derived the color matching functions for the three primary colors - Red (645 nm), Green (526 nm), and Blue (444 nm). The color matching function indicates the amount in which the three primary colors have to be added together to match the monochromatic test color (of a specific wavelength). However, these color matching functions based on real primary colors have negative values in certain wavelength regions (shown in Fig. 2.3a), to get rid of which, the International Commission on Illumination (CIE) adopted a different set of primary colors, referred to as XYZ, which are actually imaginary colors.

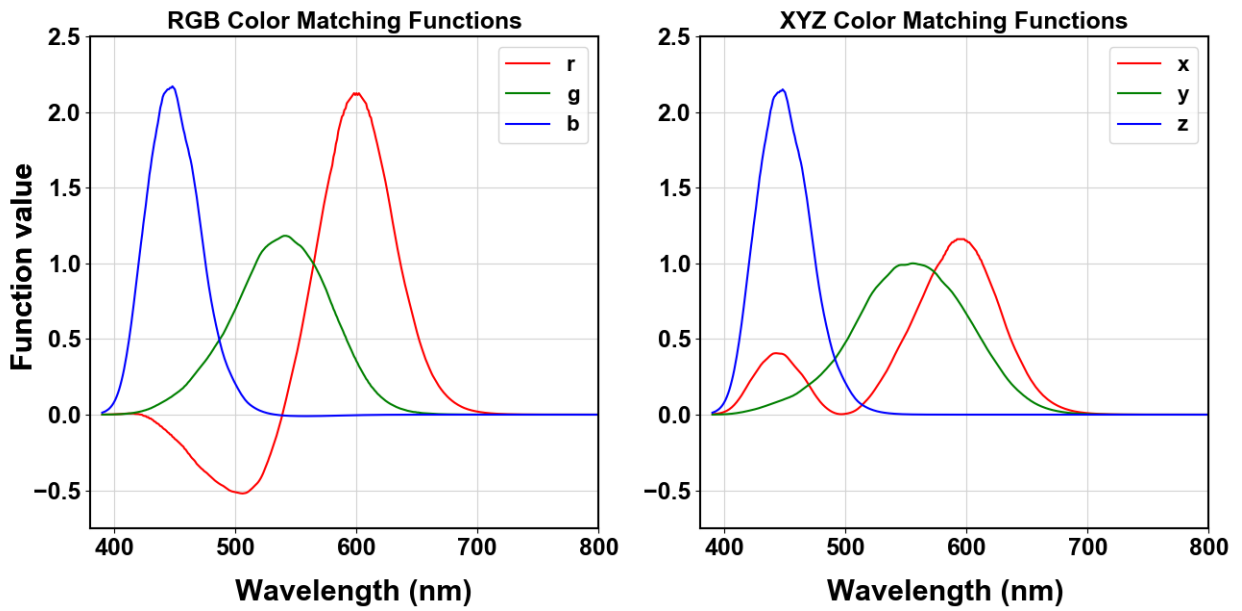


Fig. 2.3: Color matching functions for generating any color based on three primary color wavelengths - (a) RGB primaries, and (b) XYZ primaries (after Xrite [62]).

The degradation of polymers on exposure to UV rays and heat usually leads to a yellowish color. Yellowness index ( $YI$ ) has been defined for the quantification of such changes in color towards yellow. The ASTM standard E313 provides the following equation for the calculation of the  $YI$  from  $X$ ,  $Y$ ,  $Z$  tristimulus values [63].

$$YI = \frac{100 (C_x X - C_z Z)}{Y} \quad \dots (2.1)$$

where,

$YI$  = Yellowness index

$X$ ,  $Y$ ,  $Z$  are the CIE tristimulus values, and coefficients ( $C_x$  and  $C_z$ ) depend on the illuminant and the observer, as per table 2.2.

Table 2.2: The values of the coefficients for calculation of  $YI$  (based on ref. [63]).

Coefficient	Illuminant / Observer (angle)			
	C/2°	D65/2°	C/10°	D65/10°
$C_x$	1.2769	1.2985	1.2971	1.3013
$C_z$	1.0592	1.1335	1.0781	1.1498

The D65 illuminant is widely used in colorimetry measurements. The D65 illuminant is meant to simulate the noon-time light from the northern sky in northern hemisphere, with color temperature of 6500 K [64] and it is comparable to (though not exactly same as) the AM1.5G spectrum [65]. The observer angle of 2° or 10° means that observer has to look through a hole, which provides them an angle of view of 2° or 10° respectively. A simplified understanding of the yellowness index can be as  $\frac{(red\ component - blue\ component)}{green\ component}$ . The *YI* values will be positive if the red component ( $C_X \cdot X$ ) is greater than the blue component ( $C_Z \cdot Z$ ) and it would be negative if the reverse is true. Hence, for the crystalline silicon PV modules having an initial blue colour, the *YI* values will be initially negative, but as the encapsulant gets discolored (yellowish), the *YI* will increase towards positive values. For light discoloration in PV modules, it is thus possible for the *YI* value to be negative.

Gudla *et al.* [66] at Arizona State University have worked on identifying the color change in PV modules through digital image processing and tried to establish a correlation between the change in color and the loss in power output of the modules. They have used a color palette comprising of 30 different colors (ranging from blue to brown) and defined a Browning Index for each pixel of the image as follows:

$$Browning\ Index = \frac{\sum Pixel\ count \cdot Pixel\ Weight}{\sum Pixel\ count} \dots (2.2)$$

where,

Pixel count = number of pixels of the image having a particular color (out of 30 color bins)

Pixel Weight = random number assigned to every color bin to quantify the severity of browning (ranging from 0 to 1000).

Gudla *et al.* [66] obtained poor correlation between the average value of Browning Index and the module  $I_{SC}$  loss (%) in case of modules in dry state, but the correlation improved when the module surface was wet ( $R^2 = 0.928$  on a set of 11 nos. 18-year-old discolored modules). They attributed the poor correlation in the dry state to a whitish layer on top of these old modules.

We have developed a technique to quantify the extent of discoloration from the digital (RGB) images, based on correlation with actual measurements of  $YI$  (based on colorimeter readings). This procedure is discussed in detail in Chapter 5.

## 2.2.4 Effect of UV Radiation and Temperature on Degradation Rate

### a) Effect of UV radiation on chemical reactions - Reciprocity Law

The Reciprocity law, proposed by Bunsen and Roscoe [67] in 1859, states that the effect of light on a photographic film is proportional to the total light energy incident on the film, given by the product of light intensity (controlled by camera aperture) and the exposure time (controlled by shutter speed). Karl Schwarzschild [68] observed deviations in the reciprocity law for photographic films in long-term studies of stellar objects and proposed that light sources with different intensity ( $I$ ) will cause the same amount of darkening of the photographic film provided that the exposure time ( $t$ ) follows the relation:

$$I \cdot t^{0.86} = \text{constant} \quad \dots (2.3)$$

Later observations showed that the exponent of time varies for different photosensitive materials, and the Schwarzschild Law for photochemical reactions is generalized as:

$$I \cdot t^p = \text{constant} \quad \dots (2.4)$$

where,  $p$  is a material-dependent coefficient. Martin *et al.* [69] have critically reviewed the available literature on reciprocity law experiments on different photo-sensitive materials and found that the  $p$ -coefficient for photo-degradation of materials usually ranges between 0.9 to 1 (in 60% reported cases) and 0.5 to 0.7 (in 20% reported cases). The low values of  $p$ -coefficient (lower than 1) indicate that in these materials, the efficiency of the exposure reduces with the exposure time. They have also found reports in literature that same material tends to have different  $p$ -coefficient in different ranges of light intensity ( $\sim 1$  at low radiant flux, while reducing to 0.5 at high radiant flux). If the  $p$ -coefficient is unity, the change in property (degradation) will be directly proportional to the UV dose.

## b) Effect of temperature on chemical reactions – Activation energy

Svante Arrhenius [70] looked at the dependence of the chemical reaction rate on the reactant temperature from eight different published studies (on various materials) and came to the conclusion that the rate constant of the reaction can be expressed as an explicit function of temperature (T):

$$k(T) = A \cdot \exp\left(-\frac{C}{T}\right) \quad \dots (2.5)$$

where A and C are constants for the particular reaction. Further, the constant C can be expressed as  $E_a/R$  where  $E_a$  is the activation energy while R is the Boltzmann constant. The activation energy is related to the minimum energy required by the reactants to cross the energy barrier, as shown in Fig. 2.4.

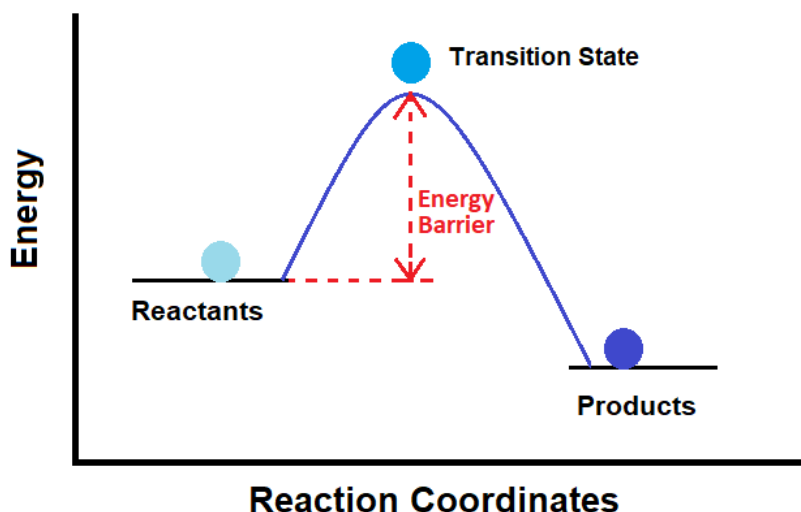


Fig. 2.4: Energy diagram for a chemical reaction, showing the energy needed to reach the transition state (based on ref. [71]). The energy barrier is the minimum energy required by the reactants to form the products.

The exponential part of the Arrhenius equation denotes the fraction of reactant molecules that possess enough kinetic energy to react, as governed by the Maxwell-Boltzmann law [71]. The pre-exponential factor, A, represents the fraction of molecules that would react if either the activation energy was zero (possible in barrier-less reactions), or if the kinetic energy of all molecules exceeded  $E_a$  (possible at very high temperatures). This term is related to the frequency of collisions in the correct orientation to bring about a reaction and hence has temperature dependence as well [71].

The Arrhenius equation is not valid under certain circumstances, like in the presence of multiple parallel reaction mechanisms with different temperature dependencies [70]. Further, the pre-exponential factor,  $A$ , has been found to be a non-linear function of temperature. Also, the activation energy has been found to vary with the temperature, particularly at high temperatures exceeding 1000 K. However, over a limited temperature range, the activation energy is usually found to be constant. Meeker and Escobar [72] have pointed out that the Arrhenius relation for reaction rates is an empirical model without any direct physical basis. Alternatively, the Eyring model for temperature is based on physical theory and is similar to the Arrhenius model but considers the pre-exponential factor to include a temperature term, with an exponent ‘ $m$ ’ ranging from 0 to 1.

$$\text{Reaction Rate} = \gamma \cdot T^m \cdot \exp\left(-\frac{E_a}{K_B \cdot T}\right) \quad \dots (2.6)$$

where,

$\gamma$  = constant for the reaction

$T$  = absolute temperature of reactants, K

$m$  = exponent of temperature

$E_a$  = activation energy, eV

$K_B$  = Boltzmann constant, eV/K

Both the above models for temperature dependence of chemical reactions may not be applicable for complicated reactions involving multiple parallel and series reaction steps unless there is a rate-limiting step, which is effectively controlling the entire reaction rate [72].

### c) Photo-thermal degradation of EVA encapsulant

Xiahong *et al.* [57, 73] have performed accelerated UV aging of EVA polymers in the NIST SPHERE test setup. They have observed that the  $YI$  versus exposure time plot is quasi-linear for wavelengths in the UV range. Loss of UV absorbers and growth of yellowing increased over time for UV exposure at 306 nm, 326 nm and 354 nm, but it stabilized under 452 nm exposure probably due to photo-bleaching. Increase in  $YI$  has been found to correlate well with the loss of UV absorbers. Shorter wavelength UV is more efficient in causing yellowing as compared to longer wavelength (326 nm is 15 times more effective than 354 nm).

Studies by the same research group on EVA film, spin casted on CaF<sub>2</sub> substrate and cured in a vacuum oven at 160 °C, has indicated that there is higher degradation in Oxygen atmosphere than inert atmosphere in Xenon chamber UV accelerated tests. Higher chain scission and loss of ester C=O group has been reported in Oxygen atmosphere for the cured EVA films, thereby indicating that Oxygen can cause damage to the EVA polymer [57]. Oxygen is known to accelerate degradation in other polymers, primarily through formation of unstable peroxide radicals [74, 75].

Beinert *et al.* [76] have exposed EVA foils with different additive compositions to UV radiation (135 W/m<sup>2</sup>) at 60 °C using a UVA lamp. The virgin samples without any stabilizers first liquefied, then hardened and cracked upon prolonged exposure. Probable degradation mode is deacetylation accompanied by ketone and lactone formation as well as chain scission. Samples with stabilizers showed an increase in chromophoric and fluorescent species and loss of UV absorber. The combination of Tinuvin 234 (UV absorber) and Tinuvin 770 (HALS) seems to generate more fluorescent species. UV absorber Cyasorb 531 is found to be more stable than Tinuvin 234. The UV absorbers absorb the incident high-energy photons before they can cause damage to the EVA polymer chain, and dissipate the absorbed energy as heat [77]. On the other hand, the Hindered Amine Slight Stabilizers (HALS) converts reactive peroxide radicals (formed due to polymer degradation) into alcohol and carbonyl compounds, in a cyclic process that regenerates the HALS molecules [77].

Studies by Miller *et al.* [78] have found that the Xenon and UV-340 sources cannot be considered as equal alternatives for purposes of accelerated weathering, due to differences in the spectrum of the light sources. They performed accelerated weathering tests on six different encapsulant materials, with different additive compositions and found that the discoloration is dependent on the additive composition. In particular, EVA without any UV absorber showed negligible discoloration. Also, they have reported an alternative degradation regime at temperature greater than 80 °C, wherein rapid degradation set in after ~ 0.4 GJ/m<sup>2</sup> (~ 110 kWh/m<sup>2</sup>) UV exposure. They have indicated the following possible reasons for the accelerated degradation – (i) the depletion of the additives, (ii) phase transition (melting) of the EVA base resin, (iii) kinetics of different parallel chemical reactions, and (iv) auto-catalysis by the degradation products. Activation energy of the order of 50 kJ/mol (~ 0.52 eV) has been obtained

in their study based on transmittance measurements, while it is around 0.6 eV based on *YI* measurements.

Dolia *et al.* [79] have studied the effect of UV radiation and temperature on UV absorbing and UV transparent EVA materials and reported that the UV-transparent material discolors at much slower rate than the UV-absorbing EVA. They determined the activation energy for discoloration of the UV-absorbing EVA to be 0.62 eV based on change in *YI* after 400 kWh/m<sup>2</sup> exposure, but could not determine activation energy for UV-transparent EVA (since its discoloration was very low). In their study, the activation energy from short-circuit current loss came out to be higher at 0.81 eV, which is logical since the short-circuit current corresponds to the whole cell area and hence includes the effect of both discolored region and photo-bleached (transparent) region.

One of the largest suppliers of EVA in the world, Hangzhou First PV Material Co. Ltd. (China), has indicated in their product datasheet that there is marginal increase in *YI* of the EVA film upon UV exposure (up to 30 kWh/m<sup>2</sup> dose), but in case of Damp Heat test at 85 °C and 85% RH, the EVA films discolor much faster as shown in Fig. 2.5 [80]. Xenon chamber tests conducted at IIT Bombay also show similar results for a standard EVA from a different manufacturer, which is discussed in Chapter 7 of this report.

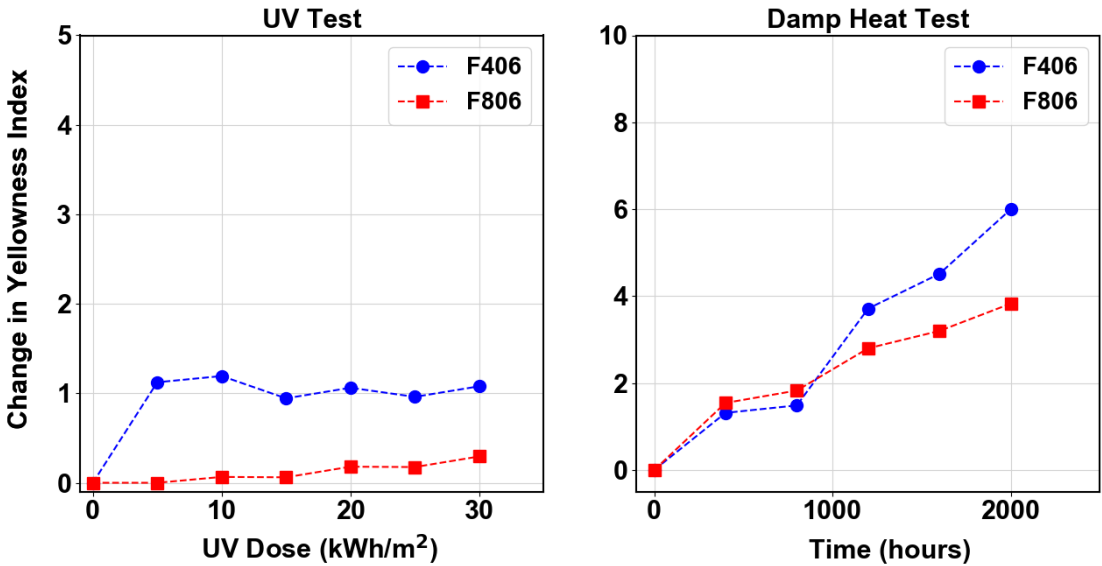


Fig. 2.5: Effect of UV exposure (a) and Damp Heat (b), on contemporary EVA films produced by Hangzhou FIRST EVA (China). The F806 encapsulant has UV absorbing property while F406 is more transparent to UV light (after Hangzhou [80]).

## 2.2.5 Accelerated Test Models

Pern [81] identified that the rate of discoloration from light yellow to brown follow a sigmoidal pattern. Nehme *et al.* [82] have considered literature data to arrive at the following model for EVA discoloration:

$$DYI = A \cdot \exp\left(\frac{-90000}{R \cdot T}\right) \cdot I \cdot \log(t) \quad \dots (2.7)$$

where,

DYI = change in *YI*

A = pre-factor (=  $9.1 \times 10^{-24}$ )

R = universal gas constant (=  $8.314 \text{ J} \cdot \text{mol}^{-1} \cdot \text{K}^{-1}$ )

T = absolute temperature, K

I = irradiance,  $\text{W} \cdot \text{m}^{-2}$

t = time, hours

Mikofski *et al.* [83] have modeled the degradation process of the polymeric encapsulant in PV modules as a two-step reaction. In the first step, the UV absorbers in the EVA are depleted by the UV rays, and in the second step, the EVA polymer is degraded (in a first order reaction).

Meeker and Escobar [72] have done a comprehensive review of accelerated test models. They have indicated that in the case of photo-degradation, the photons absorbed by the material is responsible for the degradation, so the appropriate time scale is the total (cumulative) UV dose. The UV dose depends on the spectrum of the light source, the spectral absorbance by the material, and the relative efficiency of the photons of different wavelengths in causing damage, as indicated in the following equations.

$$D_{Tot}(t) = \int_0^t D_{Inst}(\tau) d\tau \quad \dots (2.8)$$

$$D_{Inst}(\tau) = \int_{\lambda_1}^{\lambda_2} E_0(\lambda, \tau) \cdot \{1 - \exp(-A(\lambda))\} \cdot \phi(\lambda) \cdot d\lambda \quad \dots (2.9)$$

where,

$D_{Tot}(t)$  = total UV dose up to time  $t$

$D_{Inst}(\tau)$  = instantaneous UV dose at time  $\tau$

$\lambda_1$  = lower limit of the wavelength range (considered at 280 nm for UV content in sunlight)

$\lambda_2$  = upper limit of the wavelength range (considered as 400 nm for UV content in sunlight)

$E_0(\lambda, \tau)$  = spectral irradiance of the light source at time  $\tau$

$1 - \exp(-A(\lambda))$  is the spectral absorbance of the material being exposed

$\phi(\lambda)$  = quasi quantum efficiency of the absorbed radiation (considering certain wavelengths are more effective in causing damage than others). It is usually an exponential function of the wavelength. The real-world degradation of the material at time 't' can be modeled as [72]:

$$Damage(t) = f(z) \quad \dots (2.10)$$

$$z = \log\{d(t)\} - g(T, RH) \quad \dots (2.11)$$

$$d(t) = D_{Tot}(t) \cdot \left( \frac{UV \text{ intensity in test}}{UV \text{ intensity in sunlight}} \right)^p \quad \dots (2.12)$$

where,

$Damage(t)$  = Degradation at time 't'

$f(z)$  = linear or exponential function of the scaled time,  $z$  (depending on the order of the reaction kinetics)

$g(T, RH)$  = function of the explanatory variables like temperature and relative humidity

$D_{Tot}(t)$  = UV dose till time 't'.

Michael Koehl [84] has indicated that the time transformation function for accelerated tests on PV modules involving UV dose and temperature can be expressed as:

$$t_{test} = \left( \frac{UVI_o}{UVI_{test}} \right)^n \cdot t_o \cdot \exp \left\{ \frac{-E_A}{R} \cdot \left( \frac{1}{T_{test}} - \frac{1}{T_o} \right) \right\} \quad \dots (2.13)$$

where,

$UVI_o$  = UV intensity in use environment,  $W \cdot m^{-2}$

$UVI_{test}$  = UV intensity in accelerated test,  $W \cdot m^{-2}$

$t_o$  = time in use environment, hours

$E_A$  = activation energy,  $\text{J}\cdot\text{mol}^{-1}$

$R$  = universal gas constant ( $= 8.314 \text{ J}\cdot\text{K}^{-1}\cdot\text{mol}^{-1}$ )

$T_{test}$  = temperature of accelerated test, K

$T_o$  = temperature in use environment, K

$n$  = reciprocity coefficient (will be equal to 1 if reciprocity is valid)

We have considered similar formulation for modeling our experimental data, which is discussed in detail in Chapter 7.

## 2.3 Localized Discoloration in PV modules due to Hot Cells

It has been usually observed that the discoloration of the encapsulant in crystalline silicon modules happens in the center of the solar cells (all cells are usually affected) while the edges of the cells retain their initial colour (as the encapsulant stays transparent at the edges due to photo-oxidative bleaching) [48]. However, there are instances where the discoloration occurs only in a few solar cells with the majority of the cells remaining unaffected. This phenomenon has been found to be associated with high temperature operation of the solar cells, which can be identified through infrared thermography [23].

The PV module operating temperature depends on the solar cell efficiency, resistive losses and many other factors like the incident solar insolation, the ambient temperature, wind speed, mounting configuration and even the thermal resistance of the module packaging materials [85]. The International Electrotechnical Commission (IEC) has indicated the technical requirements for outdoor infrared thermography of PV modules, which are listed in Table 2.3 [86].

Table 2.3: IEC recommendations for outdoor IR thermography of PV modules (after ref. [86])

Parameter	Criteria
IR Camera spectral response	8 micron – 14 micron
Thermal sensitivity of camera	Noise Equivalent Temperature Difference (NETD) $\leq 0.1$ K at 30 °C
Geometric resolution	Maximum 3 cm of the module edge per pixel
Absolute measurement error	$< \pm 2$ K
Adjustable parameters of camera	Emissivity, reflected temperature
Recommended camera resolution	$\geq 320 \times 240$ pixels
Plane-of-array Irradiance	Minimum 600 W/m <sup>2</sup>
Wind speed	Maximum 28 km/h
Cloud cover	Maximum 2 okta
Soiling in panels	No or low (cleaning recommended)

In case of inhomogeneous defects in the modules (like cracks or delamination which affect only a few of the cells and not all), the cells with severe defects often have lower power output and a higher average temperature as compared to the surrounding cells without hot spots [87]. Voder Mayer *et al.* [88] have reported that a single hot cell, running 9 K hotter than the surrounding cells (i.e.  $\Delta T = 9$  K), is associated with a decrease of almost 20% in the maximum power point current output (with a corresponding decrease in power output of 15%). Tatapudi *et al.* [24] have considered modules with inter-cell temperature difference greater than 10 K as performance failures. They have inspected 39,431 crystalline silicon modules in different climatic zones in USA and reported 53 nos. modules with hot spots ( $\Delta T > 10$  K). Buerhop *et al.* [89] have discussed the reliability of IR imaging for identification of defective modules by comparing illuminated IR and dark IR images with electroluminescence (EL) images and *I-V* characteristics of the modules. They have concluded that IR thermography is able to effectively identify all modules with reduced power output. The most frequently detected damages are bypassed substrings ( $\Delta T = 4$  °C  $\pm$  2 °C), fractured cells ( $\Delta T = 2.5$ -45 °C or higher), deficient soldering ( $\Delta T = 12.5$  °C  $\pm$  3.6 °C), and shunted cells ( $\Delta T = 1.2$  °C  $\pm$  0.4 °C). Tsanakas *et al.* [90] have used an IR camera on unmanned aerial vehicle (drone) to capture IR images of PV power plants and shown that the thermal power dissipation of the module can be estimated from the temperatures extracted from IR images [91]. Camus *et al.* [92] have performed aerial IR

thermography at a PV power plant and detected hot cell temperature close to 100 °C, owing to cracks in the solar cell (crack is confirmed using EL imaging). They have found that the viscoelastic properties of the encapsulant near the hot cell degrades, resulting in increased stiffness and brittleness, which can induce further damages in the solar cells. If the encapsulant becomes stiff, it loses its flexibility to expand and contract under the influence of the daily thermal cycling (higher temperature at day time and lower temperature at night). Since the EVA is bonded to the top glass and the solar cells (materials with different thermal expansion coefficients), if the EVA loses flexibility and is unable to expand/contract with the cells, it creates excess stress in the solar cells and the cells may crack due to such stresses. Also, the brittle fracture of the encapsulant creates voids in the laminate wherein moisture and other gases can accumulate and react with the solar cell and the metallization leading to corrosion. We have analyzed Hot cells observed in the All-India surveys and correlated them with electrical degradation, which is presented in Chapter 6.

## 2.4 Research Gaps

The available literature points towards the following gaps in research with respect the long-term degradation of PV modules in Indian context, which we have tried to address in our study:

- The internationally accepted PV module qualification standard IEC 61215 screens the module design primarily for infant mortality and is not intended to estimate the long-term performance or the service lifetime of the panels. International PV community is presently working on development of new standards aimed towards service life prediction of PV modules.
- Most of the experimental data for the international PV qualification standards like IEC 61215 have come from the countries that were early adopters of PV technology (mostly developed western countries), where the climate is much cooler than the hot sub-tropical climate of India. These standards do not take into consideration the difference in the climatic stress levels at different installation sites. Degradation data from different countries are pointing towards higher

degradation in warmer climates which needs further investigation to inform the revision of the qualification standards.

- Degradation data of field-aged modules in India is available from only a few locations like Gurgaon (composite climate) and Himachal Pradesh (Cold & Cloudy climate), but there is scarcity of data from the other climatic zones in India. This available data is mostly from small-scale installations (mostly test-beds in research institutions) and not from actual operating power plants. Further, this degradation data indicates that many of the PV systems are degrading at much higher rate than the warranty limit (in spite of the panels being IEC certified), and raises concern about the lifetime energy output projections. This indicates the need to evaluate the module degradation in hot climate of India, and develop suitable accelerated tests for determining the long-term performance degradation of solar panels under different climatic conditions. Since degradation data from field exposed modules is the primary requirement to validate such accelerated tests conducted in laboratories, it is necessary to collect degradation data for the current PV technology, from different climatic zones of India, and for all types of installations (ground-mounted and roof-top).
- The quantification of the different degradation modes in the field is an important step in the development of the life-time accelerated tests. Presently, there is no means to quantify the degradation modes like discoloration in-situ in the field. Development of a quantification technique for the various degradation modes can help to estimate the loss in power generation due to the various defects without the need for current-voltage measurements on the solar panels (which need sophisticated equipment, and also requires disconnection of the PV string during daytime, leading to loss of energy generation).

## **2.5 Summary**

From the literature survey, it is can be seen that the various components of PV modules undergo different types of degradation which may or may not lead to power loss in the PV modules. Not only the solar cells, but also the packaging materials (like the encapsulant and the

backsheet) play a significant role in the long-term performance and reliability of the solar panels. The internationally accepted PV module design qualification test standard, IEC 61215, is primarily intended to screen modules for infant mortality and does not provide information regarding the long-term durability of the panels. The available literature on the outdoor performance of solar panels in India indicates that many of the IEC certified panels have degraded at excessively high rates, exceeding the warranty limits, which raises concern regarding the long-term performance of the PV modules in hot climate of India. Hence, extensive studies are needed to develop test protocols for determining the long-term performance of the solar panels in sub-tropical hot climates. There is limited field data on the performance degradation of PV modules in the different climates of India, which has motivated us to undertake the All-India surveys of Photovoltaic Module Reliability in 2013, 2014 and 2016. As discussed in detail in Chapter 4, the surveys have shown that cell cracks in the young modules (aged less than 5 years) and discoloration of the encapsulant in the old modules (aged more than 5 years) are very frequently observed in the field-aged modules. There is no effective technique to quantify the extent of discoloration in a solar panel *in-situ* in the field, so we have worked on developing a suitable methodology, which is discussed in Chapter 5. We have further studied the different types of commercially available EVA encapsulants to determine the EVA type better suited to the Hot climate of India, which is discussed in Chapters 7 and 8. Before presenting the results of our study, we discuss the various characterization techniques used in the All-India surveys and also in our indoor tests in Chapter 3.

## **Chapter 3**

### **Characterization Techniques**

#### **3.1 Introduction**

A brief overview of the available literature on the degradation modes prevalent in PV modules in different climatic zones has been presented in the previous chapter. We have surveyed different PV installations in different parts of India and performed various characterization tests in the field. Indoor tests have also been carried out to study the degradation of the encapsulant materials when exposed to UV and temperature. We shall present the characterization techniques in this chapter, before moving on to the test results from the various studies which are presented from Chapter 4 onwards.

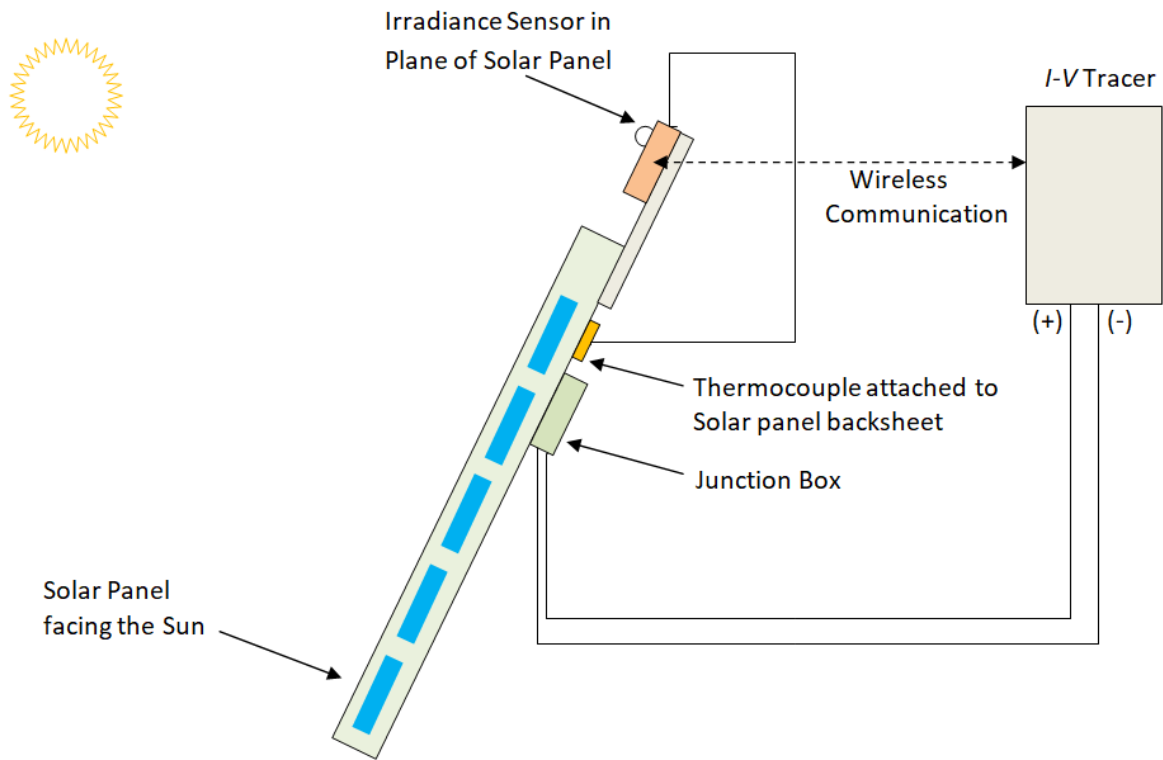
## 3.2 Electrical Characterization

### 3.2.1 Current-Voltage Measurement (Outdoor)

The current-voltage ( $I$ - $V$ ) characteristic is the most important electrical characteristics of the PV module as it is directly related to the module's power generation capability. The  $I$ - $V$  curve indicates the following important parameters of the PV module (at the test temperature and irradiance):

- maximum current generation capability of the module (the short-circuit current),
- maximum voltage generation capability of the module (the open-circuit voltage),
- maximum power generation capability of the module (the maximum power point), and,
- series and shunt resistances and the fill factor of the module.

The  $I$ - $V$  characteristic was measured during the field surveys using a portable  $I$ - $V$  tracer (make: Solmetric, model: PVA 1000S). The accuracy of this instrument is 0.5% ( $\pm 0.04$  A) in current and 0.5% ( $\pm 0.25$  V) in voltage [93]. The Solmetric  $I$ - $V$  tracer comes equipped with a Solsensor unit which has a silicon photodiode for irradiance measurement and also connection ports for thermocouples to measure the PV module temperature. During measurement, the thermocouple is attached to the backsheet at the center of the solar panel, below a solar cell. The irradiance measurement accuracy is 2% (typical). Figure 3.1 (a) shows the schematic diagram for outdoor  $I$ - $V$  measurement, and the Solmetric  $I$ - $V$  tracer along with the Solsensor unit (on the left side of main unit) is shown in Fig. 3.1(b). The Solsensor unit has to be fixed on the plane-of-array (POA) for reading the effective irradiance incident on the solar panels.  $I$ - $V$  measurements taken above  $700 \text{ W/m}^2$  POA irradiance have been considered in our analysis as lower values of irradiance introduce significant uncertainty in the translated characteristics.



(a)



(b)

Fig. 3.1: Outdoor current - voltage characterization – (a) schematic diagram of the measurement setup, and (b) portable *I-V* tracer (Solmetric PVA-1000S) used for outdoor characterization of PV modules.

### 3.2.2 Current-Voltage Measurement (Indoor)

The indoor characterization of the PV modules and mini-modules has been performed on the Spire Solar Simulator (model: SPI-SUN 5600 SLP BLUE), which has a Class A+A+A+ certification from the equipment manufacturer [94]. As per IEC 60904-9 [95], AAA classification means that the spectral match to AM1.5G solar spectrum is within 25% in the different wavelength bands, the spatial non-uniformity is within 2%, and the temporal instability is also within 2%. The manufacturer (Spire Corporation) has defined the A+ classification as within 50% of the tolerance band allowed by IEC standard for Class A. An important feature of this simulator is that it generates light spectrum from 300 nm to 1100 nm, with the 300 nm to 400 nm spectrum being an additional feature which most conventional simulators do not possess. With the introduction of new encapsulant types capable of transmitting UV light to the solar cells, the spectrum between 300 – 400 nm has become essential for proper characterization of PV modules.

In our study, crystalline silicon reference module has been used for the calibration of the simulator (using short-circuit current as the calibration parameter). The calibration module has 5% tolerance in its calibrated current rating as per the solar simulator manufacturer. To ensure the repeatability of the measurements, the simulator has been calibrated using the same reference module, for repeat measurements on the samples (after accelerated tests). The solar simulator accuracy is 0.2% for current and 0.2% for voltage with an *I-V* resolution of 0.003% (as per manufacturer's calibration report). The guaranteed repeatability is 0.15% in current, voltage and power. The classification of the simulator is checked every year to maintain the Class AAA classification in conformance to the IEC standard.

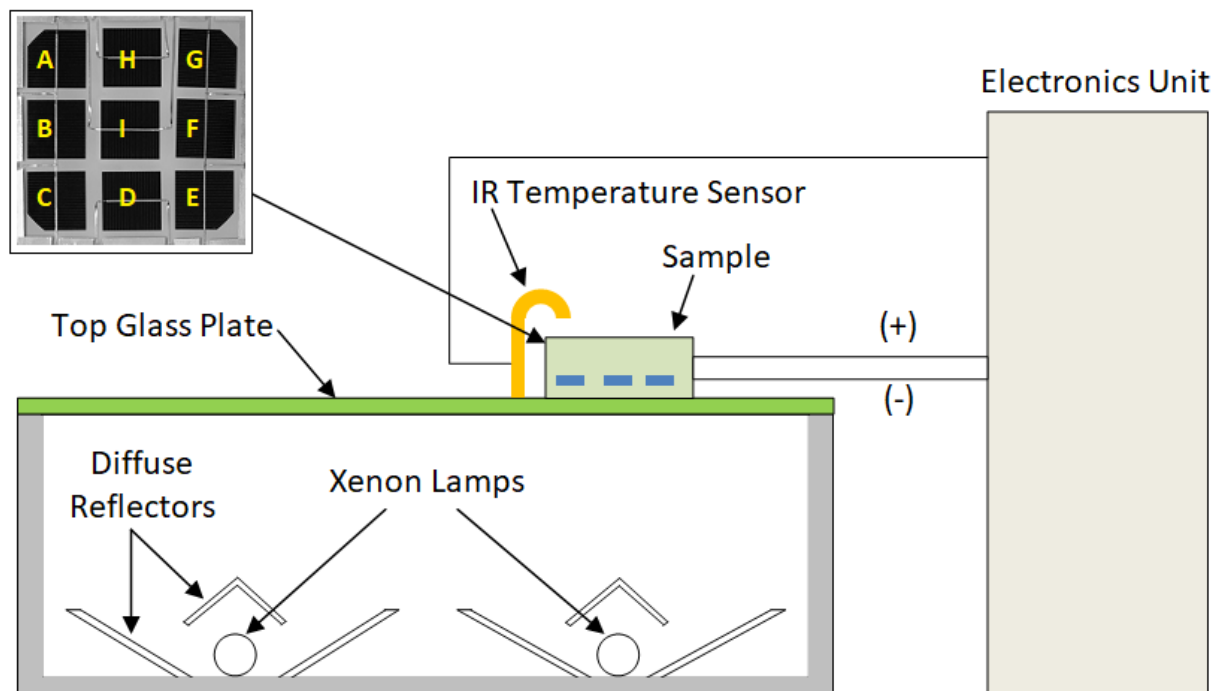
Figure 3.2 (a) shows the schematic diagram for the measurement of *I-V* characteristics on the Spire solar simulator. Photographs of the simulator at IIT Bombay and the position of the mini-module during the *I-V* measurement are also shown in the figure. It has been ensured that the repeated measurements are carried out on the mini-modules at the same position to ensure repeatability. The spatial uniformity of the simulator in this area of interest (for sample size of 20 cm x 20 cm area) has been determined through short-circuit current measurement of a 4 cm x 4 cm silicon solar cell (after calibrating the solar simulator), and the measured currents

are shown in Table 3.1. Based on these readings, the overall uniformity in the area of interest

is  $\frac{\text{Maximum intensity} - \text{Minimum intensity}}{\text{Maximum intensity} + \text{Minimum intensity}} \cdot 100 \% = \mathbf{0.38\%}$ .

Table 3.1: Uniformity measurement in the area of interest (3 x 3 cells in 20 x 20 cm area) on Spire solar simulator.

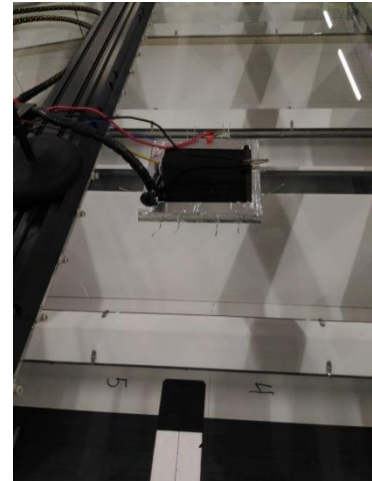
Sl. No.	Position of Cell	Short-circuit Current (A)	Percentage Variation from Average
1	A	0.650	-0.14%
2	B	0.650	-0.14%
3	C	0.649	-0.29%
4	D	0.651	0.02%
5	E	0.650	-0.14%
6	F	0.649	-0.29%
7	G	0.654	0.48%
8	H	0.653	0.32%
9	I	0.652	0.17%



(a)



(b)



(c)

Fig. 3.2: Indoor current-voltage characterization - (a) schematic diagram of  $I$ - $V$  measurement setup, (b) front view of Spire solar simulator and (c) mini-module being measured on the simulator.

### 3.2.3 Quantum Efficiency (QE) Measurements

External quantum efficiency measurements have been performed on individual cells in degraded PV modules for understanding the impact of material degradation (discoloration and delamination) on the electrical performance of cells embedded in PV modules. For this purpose, a module level quantum efficiency instrument (make: PV Measurements, model: C-M-QE) has been used during my internship at Arizona State University. This QE system uses a broadband light source (Xenon arc lamp [96]), the light from which is passed through a chopper and a monochromator, thereby generating a monochromatic (single wavelength) beam pulsating at a specific frequency which is directed towards the device under test. This instrument has the provision of measuring the cell QE from the module terminals for which it uses a white bias light on the surrounding cells, to keep them forward biased and conducting. However, since we studied old discolored modules, we had cut the back-sheet of the modules at some spots to access the solar cell terminals, and we performed direct QE measurement of the solar cell by accessing its cell interconnects. The schematic diagram for the measurement of external quantum efficiency of a cell inside a solar panel is shown in Fig. 3.3.

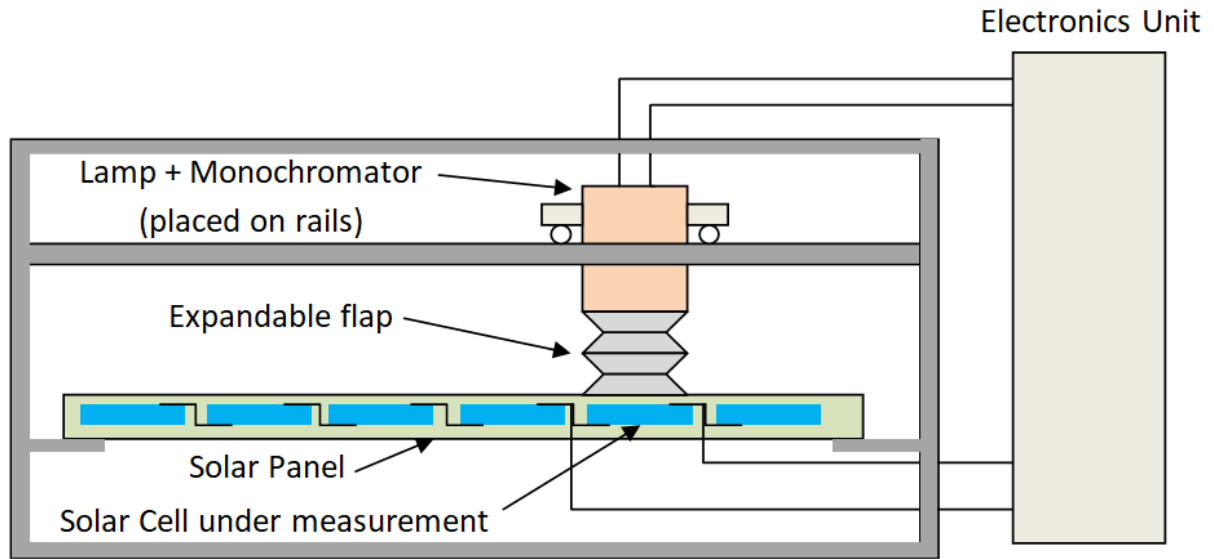
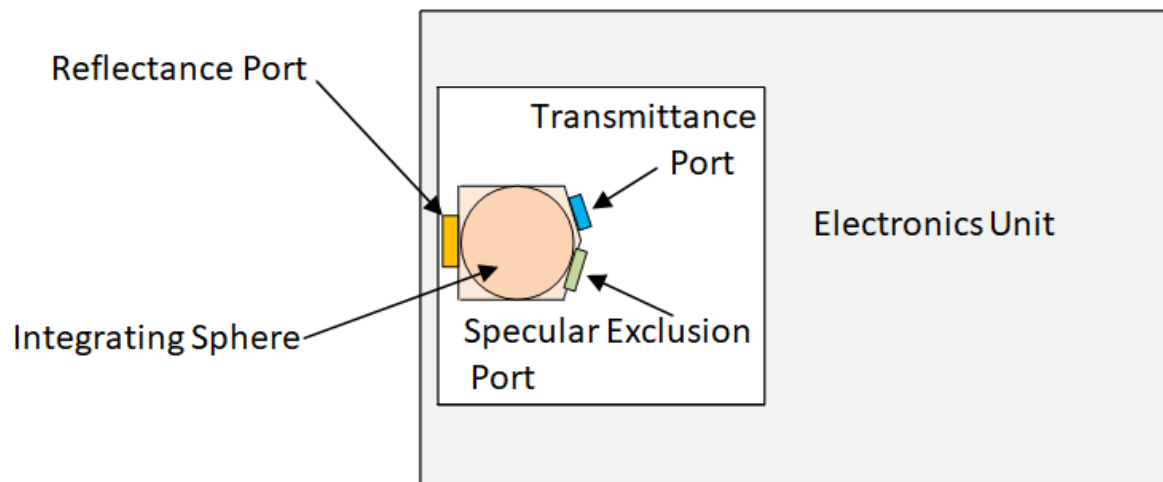


Fig. 3.3: Schematic diagram of QE measurement of a cell embedded in a solar panel. The C-M-QE instrument is located at the Photovoltaic Reliability Laboratory at Arizona State University.

### 3.3 Optical Characterization

#### 3.3.1 UV-Vis Spectroscopy

The UV-Visible spectra in transmittance and reflectance modes can provide important information about the material's optical properties. The transmittance of the top glass and encapsulant layer in the visible region is an important parameter that determines the performance of the PV module. We have used the Jasco V-650 spectrometer [97] (shown in Fig. 3.4) to measure the UV-Vis transmittance (of 2 cm x 2 cm coupons) in the range of 200 nm to 900 nm. This spectrometer is equipped with two different lamps – (i) Deuterium lamp (for use in 190 – 350 nm range) and (ii) Halogen lamp (for use in 330 – 900 nm range). The wavelength accuracy of this instrument is  $\pm 0.2$  nm, and the photometric accuracy is  $\pm 0.3$  % Transmittance. This spectrometer is used with an integrating sphere accessory, and the calibration of the instrument is done using a white reflectance standard coated with Barium Sulphate.



(a)

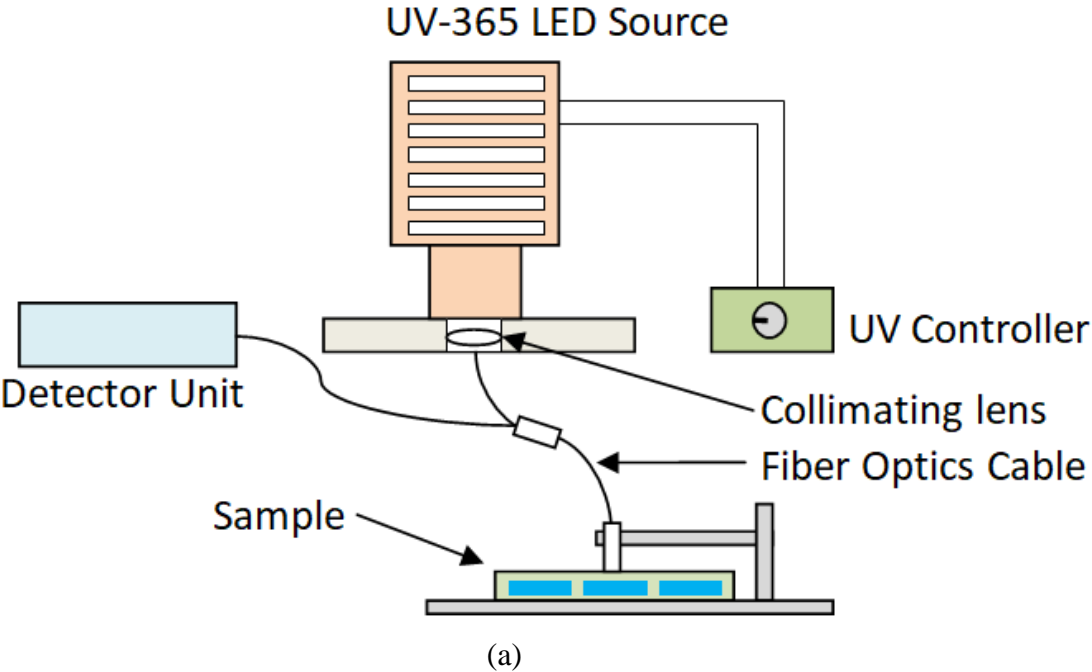


(b)

Fig. 3.4: UV-Vis spectrometer with integrating sphere – (a) schematic diagram, and (b) photograph of the Jasco V-650 spectrometer at IIT Bombay.

### 3.3.2 Fluorescence Spectroscopy

The fluorescence spectra have been measured in accelerated test samples using a 365 nm UV light source (make: Thorlabs, model: SOLIS 365C [98]) and a Silicon detector based fiber-optics spectrometer (make: Research-India, model: RISC [99]). The setup is shown in Fig. 3.5. The UV light source is placed on top of a collimating lens that focuses the UV light on to a fiber optics cable. This UV light is carried to the sample, and the emitted fluorescence light is picked up by a separate set of fiber optics cable (located at the periphery of the probe tip). The captured light is carried over to the detector unit, where a suitable grating is used to split the incoming light into different wavelength regions, and is then directed onto the detector. Before each measurement, the UV light intensity is calibrated by using a white reflectance standard (made of PTFE) at 25000 counts (with integration time of 1 ms). This ensured that the fluorescence intensity could be compared between multiple measurements after different exposure hours. The fluorescence of the actual samples were captured at integration time of 200 ms with boxcar set at 3 and average of 30 samples was taken for each measurement.





(b)

Fig. 3.5: Measurement of fluorescence spectra using fiber optics spectrometer – (a) schematic diagram, and (b) photograph of the setup at IIT Bombay. Thorlabs SOLIS 365C UV light source is combined with fiber optics spectrometer for this measurement.

### 3.3.3 Fluorescence Imaging

Fluorescence imaging has been performed using a 365 nm UV light source (make: Thorlabs, model: SOLIS 365 C [98]) and a DSLR camera (make: Nikon, model: D3200 [100]). The original beam dimension of the UV light source is approx. 4 cm x 4 cm and a diffuser glass plate is used to spread the beam on to the samples (of size 20 cm x 20 cm). The RAW image from the digital camera was extracted in TIFF format. The green channel of the RGB image was extracted since the green sensor is sensitive to the fluorescence emission between 450 to 700 nm, while it will not respond to the blue wavelengths below 400 nm (thereby substantially reducing the interference from the UV light used for excitation of the fluorescence).

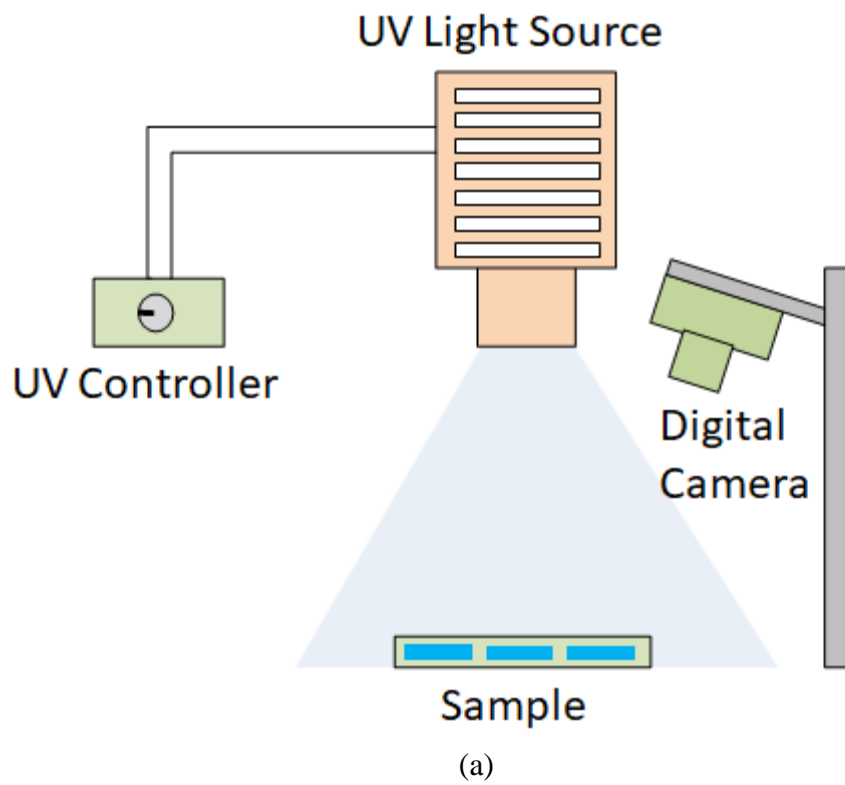


Fig. 3.6: Fluorescence imaging using 365 nm UV source – (a) schematic diagram, (b) UV source and digital camera placed on tripods, and (c) fluorescence from an UV exposed sample being captured by the digital camera. The UV source is Thorlabs SOLIS 365C, and the digital camera is NIKON D5300.

### 3.3.4 Colorimetry

The extent of yellowing of the encapsulant can be determined in terms of the yellowness index. *YI* of the accelerated test samples have been measured using a portable colorimeter (make: Testronix, model: TP110 [101]), shown in Fig. 3.7. This instrument has an observer angle of 10 degree and a D65 light source. Before each measurement, the instrument is calibrated using a white standard and also a dark calibration is done (by pointing the instrument in air, away from any light source). The instrument has to be held manually in direct contact with the sample to take the measurement. Each measurement was repeated 10 times and the average value was taken to improve the accuracy of the reading. Repeated measurements on same sample have shown that the repeatability error in *YI* measurement is within  $\pm 0.25$  units.

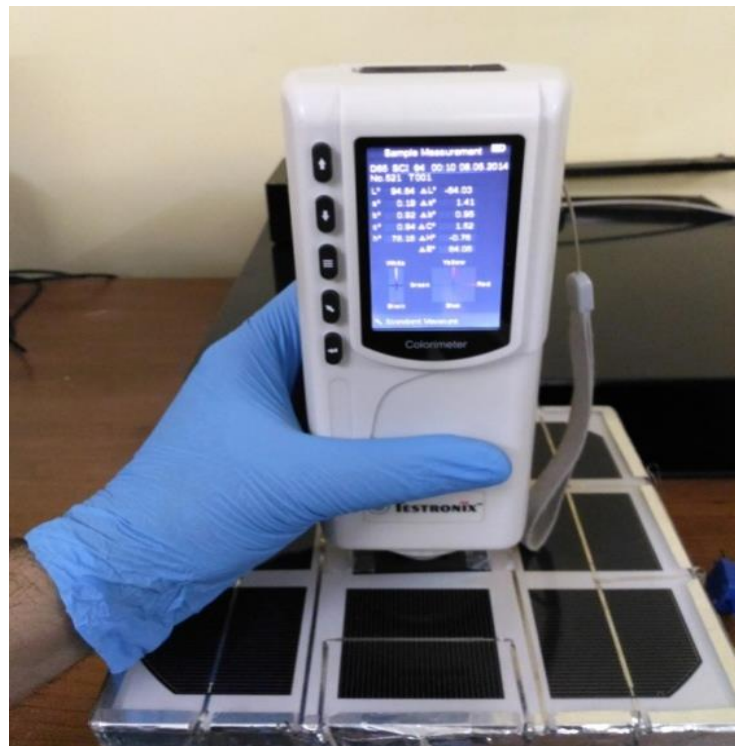


Fig. 3.7: Measurement of *YI* using colorimeter (at IIT Bombay). Testronix TP110 colorimeter is used for this measurement.

### 3.3.5 Digital (RGB) Photography

CMOS detector-based Digital Single Lens Reflex (DSLR) camera (make: Nikon, model: D3200 [100]) has been used in our All-India field surveys for taking visual pictures of the PV modules. Images were taken such that the whole panel comes in the field of view and the module appears as close to rectangular as possible, given the site-specific constraints. Since the objective is to determine the color of the module from the image (through image processing techniques), images taken above  $700 \text{ W/m}^2$  irradiance have been used for processing (as low light conditions can significantly impact the color reproduction in the captured image). The images have been captured in RAW format and these images are later converted to TIFF format for further processing. The camera has been shown in Fig. 3.8.

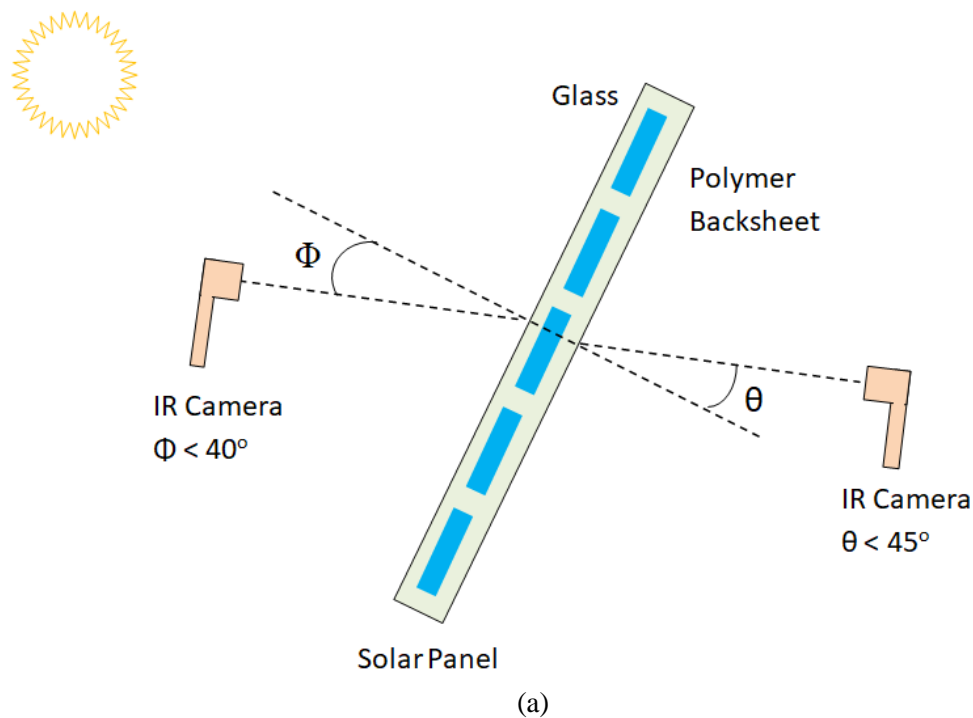


Fig. 3.8: Digital camera (Nikon D5300) used for visual (RGB) photography (at IIT Bombay). This camera is also used for capturing fluorescence images.

## 3.4 Thermal Characterization

### 3.4.1 Infra-red Thermography

Infrared thermography is a contactless temperature measurement technique widely applied in industry for measuring the temperature of the PV modules in the field. FLIR E60 [102] camera, having 320 x 240 pixel resolution, was used for taking the IR images in the field. This instrument uses an un-cooled micro-bolometer for sensing the temperature based on infrared energy emitted by the test device. It has a temperature sensitivity of  $< 0.05$  K, and its temperature accuracy is  $\pm 2$  °C (if correct emissivity of surface is chosen). The IR images of crystalline silicon PV modules have been taken from the backside. All the IR images were taken under high irradiance condition (plane-of-array irradiance  $> 700$  W/m<sup>2</sup>). The emissivity setting of the IR camera was set to 0.95 when taking the images from backside (imaging the backsheet) whereas emissivity was set to 0.85 for the glass side, as per [43]. The angle of IR camera,  $\phi$ , is maintained within the limits of angle of view as indicated in Fig. 3.9(a).





(b)

Fig. 3.9: Thermography of solar panels – (a) schematic diagram (angle of view as per recommendation of Kontges *et al.* [43]), and (b) FLIR camera (model E60) used for IR imaging of PV modules.

### 3.5 Summary

A variety of equipment have been used for electrical, optical, and thermal characterization of the PV modules, as discussed in this chapter. The outdoor measurement tools have been used in the All-India surveys of PV module reliability, the results of which are discussed in Chapter 4, 5 and 6. Results of indoor measurements on accelerated test coupons are discussed in Chapters 7 and 8.

This page is intentionally left blank.

## **Chapter 4**

### **Survey Statistics on Visual Degradation Modes**

#### **4.1 Introduction**

The components of PV modules degrade upon exposure to the outdoor environment. The UV content of the incident solar radiation, the high operating temperatures and the outdoor humidity levels (with intermittent rainfall) affect the PV modules in different ways. In order to develop accelerated test protocols for reliability and service life prediction of PV modules in different climatic conditions, it is important to first understand the degradation modes active in field-aged PV modules. With this objective in mind, a joint team from the National Centre for Photovoltaic Research and Education (NCPRE) and National Institute of Solar Energy (NISE) has conducted surveys of PV systems installed in different parts of the country. The first survey conducted in 2013 [19] looked specifically into degraded modules in some selected locations and was a learning exercise that enabled us to launch more organized surveys on a larger scale

in 2014 [20] and 2016 [21]. Though in the 2013 survey, we primarily used just a current-voltage ( $I$ - $V$ ) tracer for characterization of modules, for the later surveys, both the number of characterization tools and the number of modules surveyed were increased significantly. Different PV technologies surveyed in the All-India surveys include mono-crystalline silicon (mono c-Si), multi-crystalline silicon (multi c-Si), amorphous silicon (a-Si), Cadmium Telluride (CdTe) and Cadmium Indium Gallium Selenide (CIGS). However, the various thin film technologies (a-Si, CIGS, CdTe) are found in only five sites, so the sample size is much lower than that of c-Si modules, and the degradation modes observed in the thin film technologies are very different from the crystalline silicon technologies. Since majority of the PV installations in India utilize the crystalline silicon technology, and since this thesis work focusses on the encapsulant discoloration in crystalline silicon modules, we have discussed the degradation modes observed in the crystalline silicon modules in this chapter. However, the interested reader may refer to the All-India survey reports [20, 21] for details of the thin film module degradation observed in the surveys. Mono c-Si and multi c-Si differ in terms of the crystal structure of the silicon wafer but the influence of the crystal structure on the packaging material degradation is expected to be insignificant, hence these cell types have been grouped together under the “crystalline” silicon category. A total of 983 crystalline silicon (c-Si) modules were inspected in 2014 [20] and 764 in 2016 [21] (with some modules being repeated between the two surveys). However, since the repeat modules had undergone degradation in the intervening period of two years, we have considered the repeat modules as separate samples in our analysis presented in this chapter. Detailed visual inspection was performed on a total of 1699 c-Si modules in the two surveys (in 2014 and 2016). The degradation modes observed in the field-aged modules were recorded with the help of the NREL visual inspection checklist [47], which we have slightly modified and condensed into two pages (provided in Appendix I). For the analysis of the data, the modules have been grouped based on the climatic zone and age group. India has multiple climatic zones, and we have followed the classification criteria proposed by Bansal and Minke [26] (given in Table 4.1). Figure 4.1 shows the sites visited in the different climatic zones, in the All-India surveys of 2014 and 2016. We have, in general, observed that the power degradation rates of the modules is similar for the Hot & Dry, Warm & Humid and the Composite zone [20], so these zones have been clubbed together and referred to as the “Hot” zone. Similarly, the Cold & Cloudy, Cold & Sunny and the Moderate climates have been grouped together as the “Non-Hot” zone.

Table 4.1: Criteria for climatic zone classification in India [26]

Climate	Mean Monthly Temperature (°C)	Mean Relative Humidity (%)
Hot & Dry	> 30	< 55
Warm & Humid	> 30	> 55
Moderate	25 – 30	< 75
Cold & Cloudy	< 25	> 55
Cold & Sunny	< 25	< 55
Composite	This applies when six months or more do not fall within any of above categories	

Analysis of the electrical degradation rates of the surveyed PV modules (performed by Dubey *et al.* [20, 21]) has shown that certain installations have significantly high degradation rate as compared to others. For establishing the correlations of the high degradation rates with the installation size, type and other parameters, it was necessary to segregate the sites into two categories based on the average degradation rate at the site – Group X (sites with average degradation rate < 2%/year) and Group Y (sites with average degradation rate  $\geq$  2%/year) [20]. The “2%/year” figure is used as the segregation criteria as the average degradation rate for all crystalline silicon modules inspected in the 2014 survey was found to be close to this value [20]. It may be noted that some of the modules having excessively high degradation rates have been separated out as “outliers” based on the statistical criteria of 1.5 times of the interquartile range [103], and the remaining modules have been considered when calculating the average degradation rate of the sites. The data will be presented first for “All” inspected modules (which includes Group X, Group Y and also Outliers), and then separately for Group X and Group Y, in order to bring out the differences between these groups. The Group Y modules seem to be affected by various issues arising out of shortfalls in the material quality, production process, and/or handling and installation, and hence may not be good representatives for understanding the climatic zone affects. Hence the Group X modules have been analyzed for determining the influence of climatic zone on module degradation.

Table 4.2 shows the major visual degradation modes observed in our surveys and the percentage of affected modules. It may be noted that certain degradation modes of the active device (semiconductor solar cell) are not visible to the naked eyes (like micro-cracks and potential induced degradation in the solar cells etc.), and these are not included in Table 4.2.

Table 4.2: Overall statistics of visual degradation modes observed in c-Si modules

<b>Component Degraded – Mode of Degradation</b>	<b>Affected modules (%)</b>
Encapsulant – Discoloration	35%
Encapsulant – Front-side bubbles & delamination	18%
Metallization – Snail tracks	19%
Metallization – Discoloration	66%
Backsheet – Degradation	46%
Frame – Corrosion/damage	9%
Glass – Breakage	1%
Glass – Haziness at bottom edge	61%

In the following sub-sections, the various degradation modes observed during the survey are analyzed based on age, climatic zone, and size of installation. The modules have been broadly classified into two age categories – (1) Young (modules installed less than 5 years ago), and (2) Old (modules installed more than 5 years ago), at the time of the survey. Installations have been classified into 2 categories based on installed capacity – (1) Small/Medium (installed capacity < 100 kW), and (2) Large (installed capacity > 100 kW). Overall, 58% of the inspected crystalline silicon modules belonged to the young age group (age < 5 years) and about 14% belonged to large sites (capacity > 100 kW). The percentage of modules belonging to large sites is less because historically solar has been installed as off-grid systems in remote areas, so most of the old sites and even many of the young sites inspected during the surveys have capacity less than 100 kW. The survey statistics shall be discussed in the following sub-sections using tables that will show the percentage of affected modules in different age groups for the various classification of sites. The sample size is indicated in brackets beside the percentage of affected modules in each category.

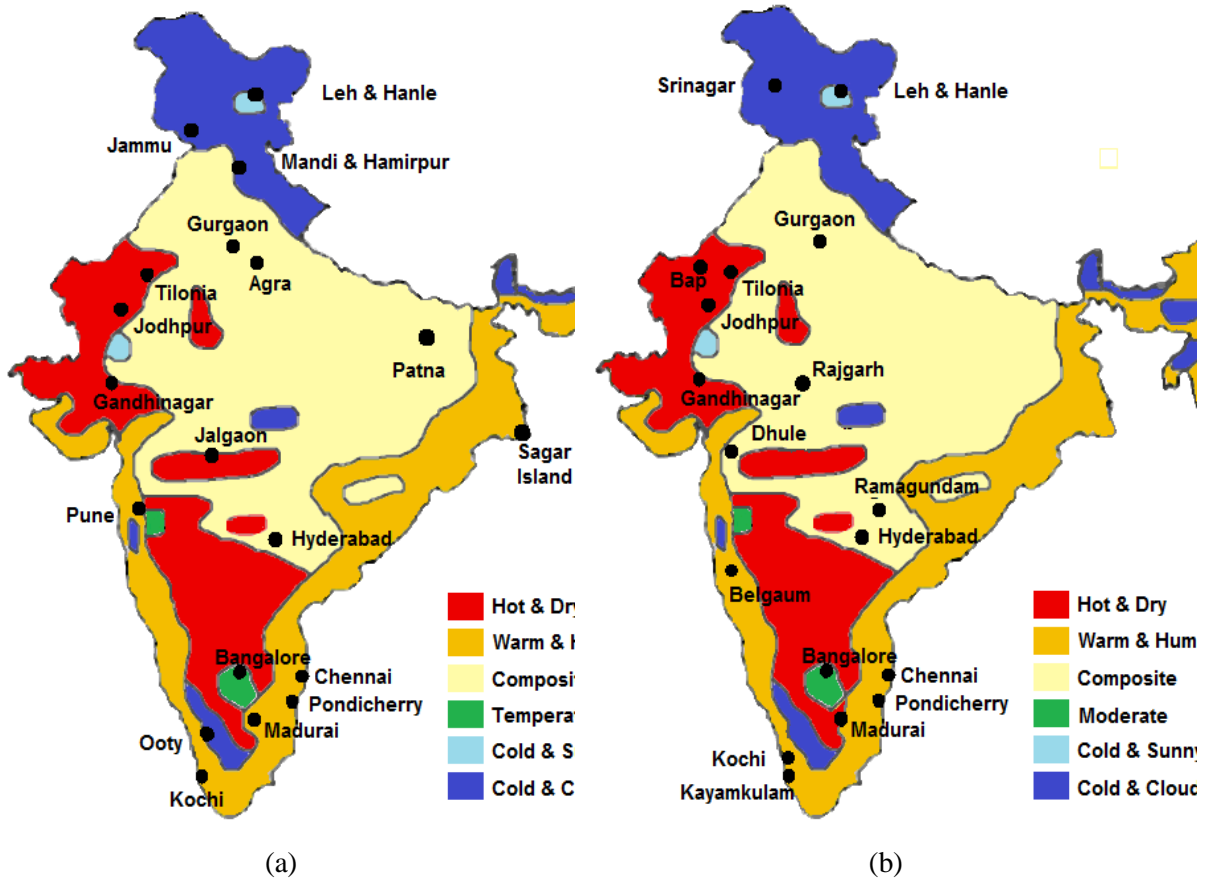


Fig. 4.1: Climatic zones of India and locations visited during the All-India surveys in (a) 2014 [20], and (b) 2016 [21]. Total 51 PV installations were surveyed in 2014 while 37 installations were surveyed in 2016.

## 4.2 All-India Survey Statistics for Various Visual Degradation Modes

### 4.2.1 Encapsulant Discoloration

The encapsulant in a PV module should transmit the incident light (with minimum attenuation) to the underlying solar cells. Discoloration (browning) of encapsulant is one of the most common degradation modes, which causes reduction in short-circuit current ( $I_{sc}$ ) and consequently, power output ( $P_{max}$ ) of field-aged PV modules [18]. The composition of the encapsulant has undergone several changes in the evolution of the PV module construction, in

order to improve its long-term durability. Ethyl Vinyl Acetate (EVA) is the most commonly used encapsulant today due to its favorable properties and low cost, though it is susceptible to photo-thermal degradation and has to be mixed with the proper additives to prevent untimely discoloration [48]. More than a decade ago, Holley and Argo [104] reported that the main culprit for the discoloration of the EVA is an additive used in the EVA formulation (Lupersol 101), and suggested alternatives which will prevent untimely discoloration (like Lupersol TBEC). Figure 4.2 shows some examples of discoloration observed in PV modules during our survey. Modules with discolored EVA usually have clear (not discolored) areas between the cells and also not along the cell edges, due to photo-bleaching action of the oxygen entering through the polymeric backsheet and module edges [48]. Such photo-bleaching is also seen along the cell cracks, as shown in Fig. 4.2(c) - (e). Figure 4.2(f) shows a glass-glass module that has not discolored even after 27 years exposure in the field.

In our field survey, discoloration has been observed even in some of the young modules (aged less than 5 years), as shown in Fig. 4.3. In this figure, the percentage of modules affected in the respective climatic zone and age category is shown. Some EVA formulations used even today have shown discoloration in the field within 5 years of outdoor exposure. *The fact that close to 20% of the young modules inspected in the Hot climates are showing signs of early-stage discoloration is a matter of concern.*

The percentage of affected panels rises rapidly in the Warm & Humid (WH) zone as the panel age increases (as shown in Fig. 4.3), which hints that this zone is very severe for the encapsulant. Double glass crystalline silicon modules were inspected only at two sites (in the same area/locality) in our surveys (total 52 samples in two surveys), and interestingly these modules did not show any significant discoloration even after 27 years of operation. Hence, the percentage of modules affected is low in the “20+ years” category in Fig. 4.3 (represented by the orange bar). This leads us to suspect that the encapsulant used may not be EVA, but some other high-grade alternative (like silicone). Alternatively, it has also been reported that Cerium containing glass used in the older generation panels could prevent UV rays from passing into the module, thereby preventing discoloration of the EVA [48].

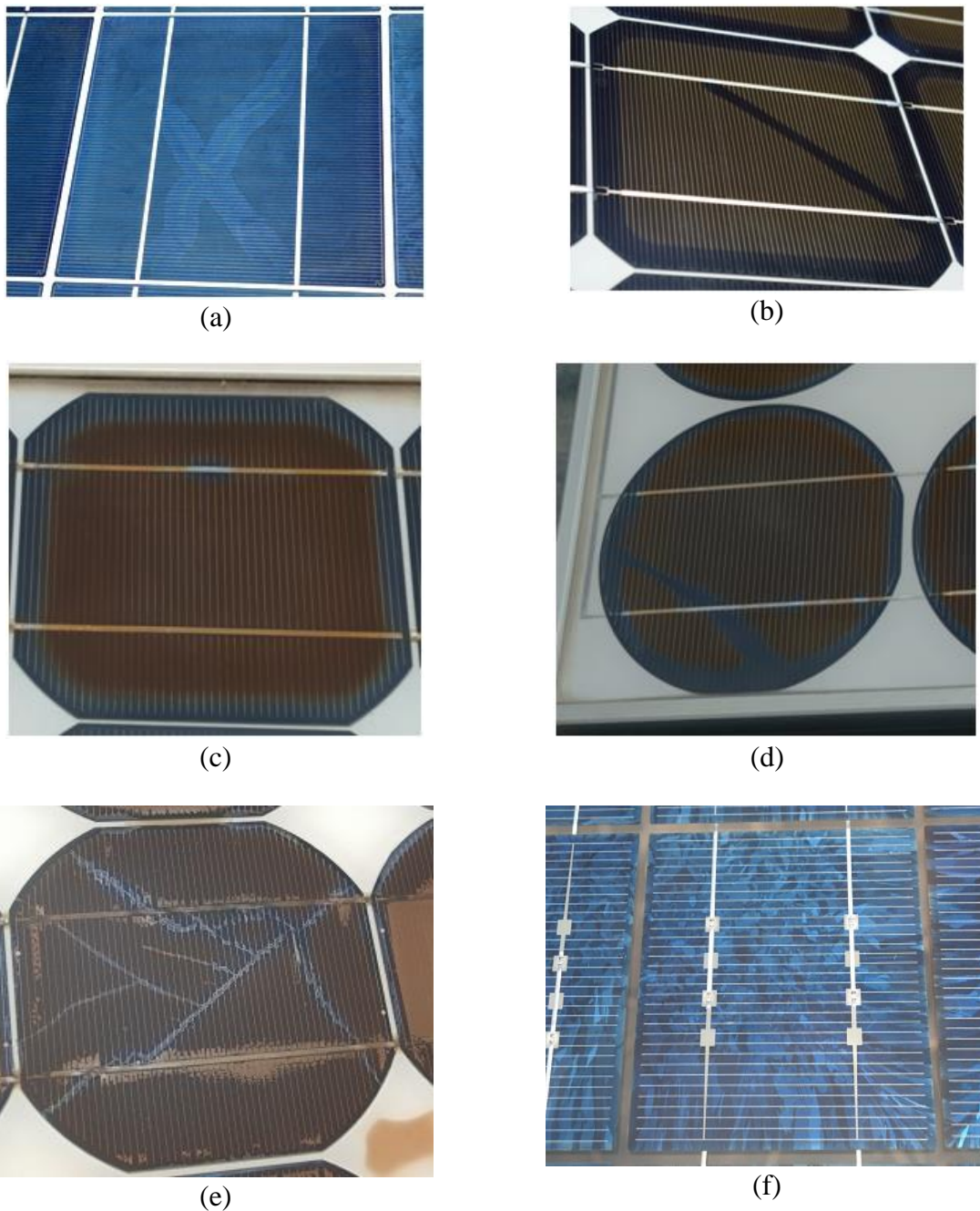


Fig. 4.2: Examples of encapsulant discoloration observed during the surveys – (a) discoloration in a 3 year old module in Hot & Dry zone (with photo-bleaching effect along crack in center of cell), (b) discoloration in a 8 year old module in Warm & Humid zone (with snail track formation along crack), (c) discoloration in a 18 year old module in Warm & Humid zone (with crack induced photo-bleaching near the busbar), (d) discoloration in a 18 year old module in Cold & Sunny climate (with crack induced photo-bleaching), (e) discoloration in a 20 year old module with photo-bleaching and delamination along cracks, and (f) solar cells in a 27 year old glass-glass module in Hot zone showing no signs of discoloration [20, 21].

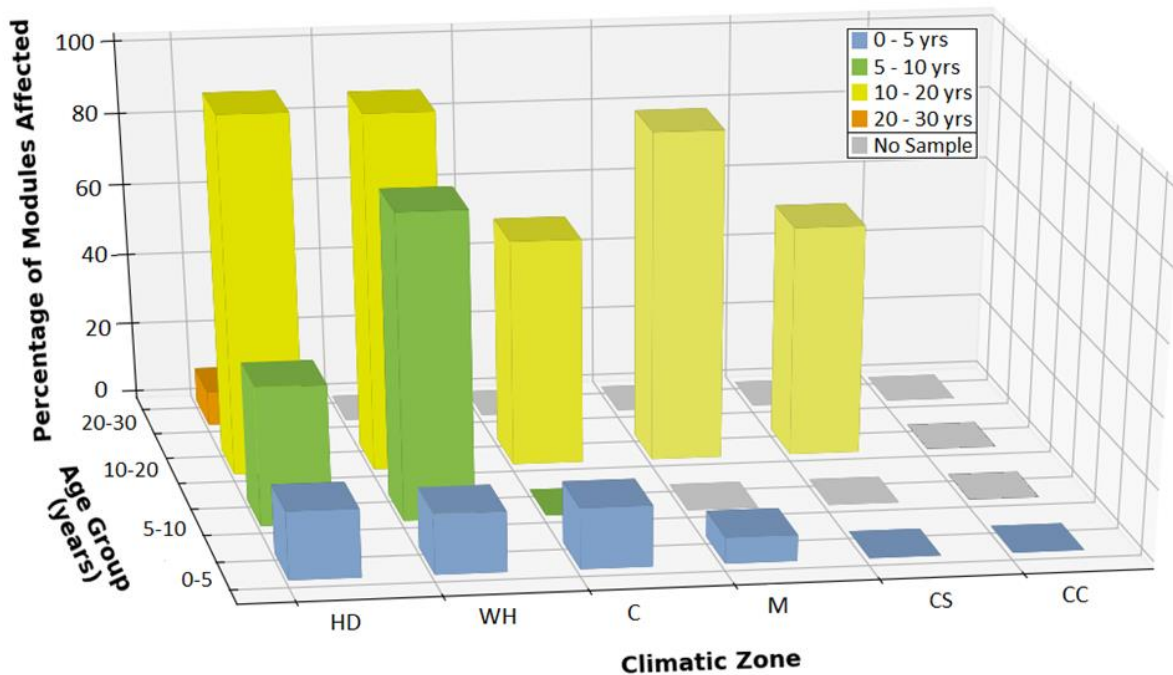


Fig. 4.3: Percentage of modules affected by encapsulant discoloration in different age groups and climatic zones (HD: Hot & Dry, WH: Warm & Humid, C: Composite, M: Moderate, CS: Cold & Sunny, CC: Cold & Cloudy). The data has been colour-coded based on the age of the panels, and groups with no sample data have been marked with grey colour.

As explained before, the modules have been grouped into two groups – Group X and Group Y – based on the average power degradation rate of the site. Group X modules belong to the “good” sites in terms of electrical performance, while the Group Y modules belong to the “not-so-good” sites with average degradation rate above 2%/year. Table 4.3 compares the percentage of modules affected by encapsulant discoloration in Group X with Group Y. The modules are grouped based on their age, and each cell of the table shows the percentage of affected modules in that age group (with the number of modules inspected given in brackets). In order to assess whether the difference in the proportions (percentage of defective panels) in the two groups (X and Y) is statistically significant, two-proportion z-test has been performed and the p-value for the test is mentioned in the table. The p-value indicates the probability of observing the present difference in the defective proportions in the samples even though the actual proportions in the population are equal (i.e. difference is null, which is our null hypothesis), so if the p-value is less than 0.05, we can consider that the difference is statistically significant. The total number of samples is 1750, which is the total crystalline silicon modules inspected in 2014 and 2016 surveys. The data from the survey conducted in 2013 is not

considered as it would give biased information (since in that survey only the visually degraded modules at each site were targeted for inspection).

Table 4.3: Percentage of modules with encapsulant discoloration in Group X and Group Y in different age groups. Number of samples is given in brackets.

%Modules	Age Group					
Group	Young	Old				Overall
	0 - 5 yrs	5 – 10 yrs	10 – 20 yrs	>20 yrs	Total Old	
<b>X</b>	<b>18% (305)</b>	60% (167)	72% (286)	17% (24)*	<b>65% (477)</b>	<b>47% (782)</b>
<b>Y</b>	<b>11% (637)</b>	100% (40)	93% (123)	4% (28)*	<b>82% (191)</b>	<b>27% (828)</b>
p-value**	0.004	<0.0001	<0.0001	0.115*	<0.0001	<0.0001

Note: Total number of samples is 1610 nos. This number is lower than total crystalline silicon modules surveyed (1699) because some modules could not be classified into Groups X or Y due to *I-V* measurement at low irradiance (below 700 W/m<sup>2</sup>).

\* Double glass modules. The p-value for t-test is shown, as number of samples is inadequate for z-test.

\*\* p-value for two-proportion z-test (except for “>20 yrs” category for which t-test result is given).

From Table 4.3, we can see that higher percentage of panels is affected in Group X than Group Y in the overall tally. However, in the old sites (older than 5 years), discoloration has occurred in higher percentage of panels in Group Y than in Group X, which tallies with the fact that the degradation rates are higher in the Group Y panels. In young age group, discoloration is found to be more prevalent in Group X than in Group Y. Considering that the discoloration within 5 years of exposure is usually to a small degree which would not significantly influence the power degradation, this observation in the young age category is plausible. This indicates that discoloration is not the causative factor behind the high degradation rates seen in the young panels in the surveys. The statistics for the discoloration of encapsulant in Hot and Non-Hot climatic zones is presented in Table 4.4 for the Group X sites. Only the Group X category sites have been considered for analyzing the impact of the climate on the degradation of the panels, as it is suspected that the Group Y panels (which show higher than expected degradation rate) are affected by multiple extraneous factors including poor material quality and/or improper manufacturing practices, which can supersede (and hide) the impact of the climate. The difference between the two groups (Hot and Non-Hot) is statistically significant in the overall tally (based on p-values of two-proportion z-test with significance level of 0.05), indicating that

the Hot zone is more severe than the Non-Hot zone. Discoloration is more prevalent in the Hot zone as compared to the Non-Hot zone in the young sites, but this difference levels off in the old sites indicating that most panels tend to discolor in the long term irrespective of the climate.

Table 4.5 shows the comparison between the small/medium sites and the large (>100 kW capacity) sites. The differences between the groups are found to be statistically significant (p-values are less than 0.05) in the different age categories. Highest percentage of modules is affected in the old small/medium installations, but significant percentage of modules are also affected in young and large sites (25% of 181 samples). Majority of the discolored panels for the large and young group come from one single site in Warm & Humid climate, which hints towards use of poor-quality material in that power plant. The fact that discoloration is visible in approximately 12% of the inspected panels in the young age category, points towards poor material quality of these panels.

Table 4.4: Percentage of modules with encapsulant discoloration in Group X in different climatic zones. Number of samples is given in brackets.

%Modules	Age Group					
	Young	Old				Total Old
Group	0 – 5 yrs	5 – 10 yrs	10 – 20 yrs	>20 yrs		
<b>Hot</b>	<b>23% (175)</b>	60% (167)	75% (176)	17% (24)*	<b>64% (367)</b>	<b>51% (542)</b>
<b>Non-Hot</b>	<b>12% (130)</b>	NA	67% (110)	NA	<b>67% (110)</b>	<b>38% (240)</b>
p-value **	0.011	NA	0.115	NA	0.617	0.0008
Note: Total number of samples in Group X is 782 nos. “NA” indicates no samples are available in that category. * Double glass modules. ** p-values for two-proportion z-test						

Table 4.5: Percentage of modules with encapsulant discoloration in Small and Large installations.  
Number of samples is given in brackets.

%Modules	Age Group					
	Young	Old				Overall
Group	0 – 5 yrs	5 – 10 yrs	10 – 20 yrs	>20 yrs	Total Old	
<b>Small/ Medium</b>	<b>9% (837)</b>	78% (144)	79% (419)	10% (52)*	<b>73% (615)</b>	<b>36% (1452)</b>
<b>Large</b>	<b>25% (181)</b>	44% (66)	NA	NA	<b>44% (66)</b>	<b>30% (247)</b>
p-value **	<0.0001	<0.0001	NA	NA	<0.0001	0.068

Note: Total number of samples is 1699 nos.  
“NA” indicates no samples are available in that category.  
\* Double glass modules. \*\* p-value for two-proportion z-test

Based on the above discussion, it is evident that discoloration is more prevalent in the Hot climatic zone than the Non-Hot zone. Many of the young sites installed less than 5 years ago show signs of early-stage discoloration, particularly in the Hot zone, which calls for improvement in the quality of the encapsulant / manufacturing process of the module manufacturers.

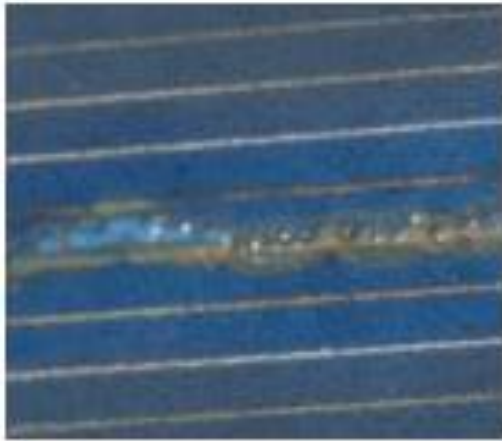
#### 4.2.2 Front-side Delamination

Delamination on the front-side occurs due to loss of adhesion between the encapsulant and glass or between the encapsulant and solar cell. Silane-based additives are generally added to the EVA encapsulant during the EVA manufacturing process to promote its adhesion to glass (through the formation of siloxane bonds at the EVA-glass interface during module manufacturing). However, upon UV exposure in the field, the siloxane bond density reduces which leads to delamination [105]. As a consequence, there is an increase in reflection losses from the affected area, and the current generation of affected cells gets reduced. In our surveys, front-side delamination has mostly been seen in the form of bubbles along cracks/snail tracks (refer Fig. 4.4). Also, at one site in the Hot & Dry climatic zone, all modules showed delamination along the gridlines, as shown in Fig. 4.4(b). Also, severe delamination on top of

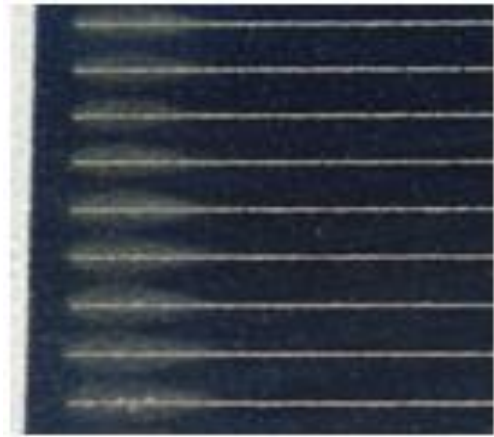
multiple solar cells has been observed at an old installation in Warm & Humid climate (Fig. 4.4f).

Figure 4.5 provides the statistics of front-side delamination (including bubbles) in all surveyed c-Si modules. The double glass modules in Hot zone, which have shown lowest encapsulant discoloration fare poorly in terms of delamination. The probable cause is the glass-glass construction of the modules prevented the escape of the vapors evolved during degradation of the encapsulant, and the trapped vapor led to delamination and bubble formation. At other sites, mostly small bubbles have been observed along snail tracks (which are also associated with cell cracks). Also, delamination along the fingers of the solar cells has been observed in all surveyed modules at a 7-year-old site in Hot & Dry zone, as shown in Fig. 4.4(b). Delamination is rarely found in the young (less than 5 years old) modules, except in the form of bubbles along snail tracks (observed in Composite and Moderate climates), with less than 5% of the solar cell affected by it. Among the older modules, delamination is seen more in the Warm & Humid and the Hot & Dry zone as compared to the colder zones. This points towards the role of temperature in reducing the adhesive property of polymers in the Hot climates leading to preponderance of delamination in these zones.

Table 4.6 compares the delamination statistics for Group X and Group Y, and it can be seen that Group Y modules have a higher incidence of delamination as compared to Group X modules, both in young and old age categories. This difference between Group X and Group Y is in fact created due to the higher incidence of snail tracks in Group Y modules (bubbles have been observed predominately along these snail tracks).



(a)



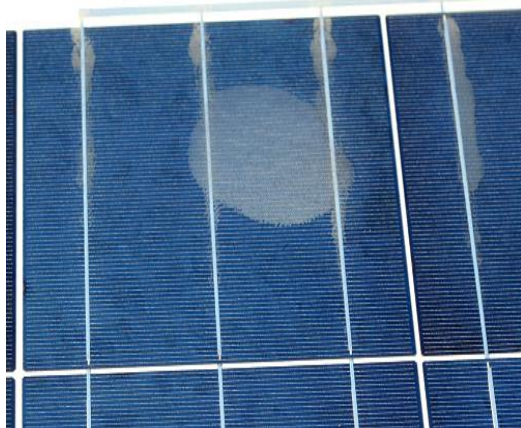
(b)



(c)



(d)



(e)



(f)

Fig. 4.4: Examples of delamination observed during the survey – (a) along snail track, (b) along fingers at cell edge, (c) near the busbar, (d) on top of solar cell in an old glass-glass module, (e) close to the center of a cell in a young module in Non-Hot climate, and (f) in multiple cells in an old module in Hot climate [20, 21].

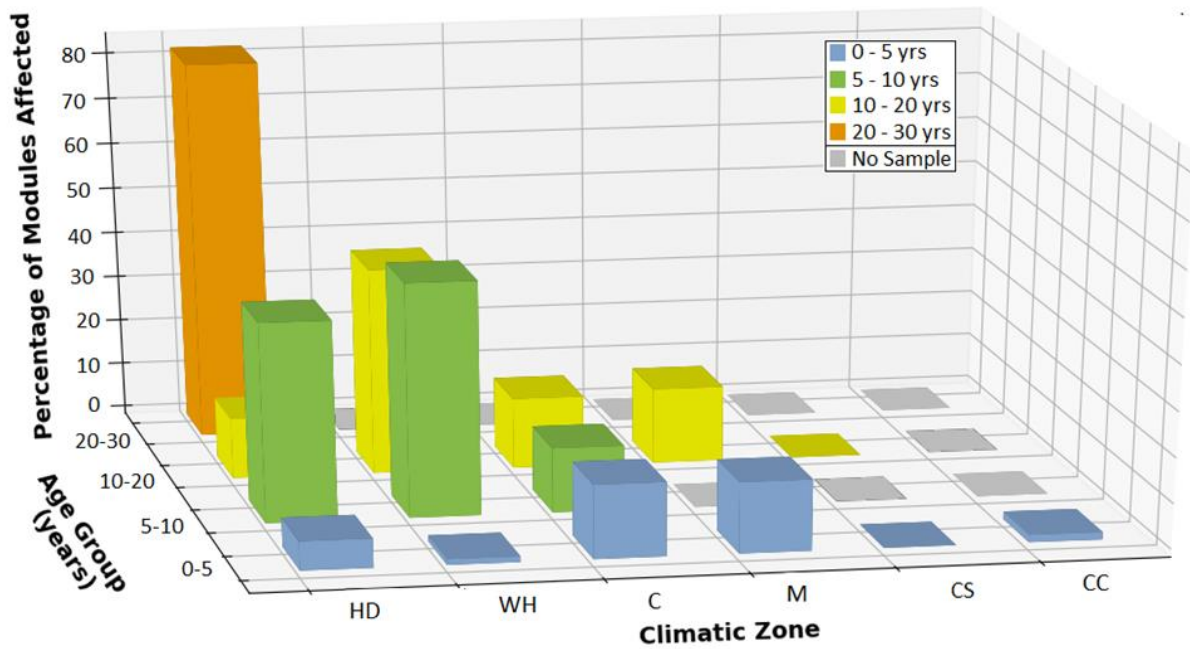


Fig. 4.5: Percentage of modules affected by front-side delamination in different climatic zones and age groups (HD: Hot & Dry, WH: Warm & Humid, C: Composite, M: Moderate, CS: Cold & Sunny, CC: Cold & Cloudy). Delamination is observed more in the Hot zone as compared to the Non-Hot zone, in the old age category.

Table 4.6: Percentage of modules with front-side delamination in Group X and Group Y. Number of samples is given in brackets.

%Modules	Age Group					
	Young	Old				Overall
	0 – 5 yrs	5 – 10 yrs	10 – 20 yrs	>20 yrs	Total Old	
<b>X</b>	<b>6% (305)</b>	38% (167)	18% (286)	88% (24)*	<b>29% (477)</b>	<b>20% (782)</b>
<b>Y</b>	<b>10% (637)</b>	80% (40)	23% (123)	79% (28)*	<b>43% (191)</b>	<b>18% (828)</b>
p-value **	0.041	<0.0001	0.247	0.11*	0.0005	0.31

Note: Total number of samples is 1610, which is lower than 1699 because some modules could not be classified into Groups X or Y due to *I-V* measurement at low irradiance (below 600 W/m<sup>2</sup>).

\* Double glass modules. The p-value of t-test is shown as number of samples is inadequate for z-test.

\*\* p-values for two-proportion z-test (except for “>20 yrs” category, for which t-test result is given).

Table 4.7 shows that the effect of climatic zone on the delamination of panels. Hot zone has a higher percentage of affected modules as compared to the Non-Hot zone, which again emphasizes the severity of the Hot climate. Table 4.8 presents the statistics based on the size of installation. It shows that the large installations in “5-10 year” category have the highest percentage of modules affected by delamination bubbles (though the number of samples is limited). These bubbles are mostly seen along snail tracks, and hint towards the prevalence of snail tracks in these installations (details of which is discussed in next subsection).

Table 4.7: Percentage of modules with front-side delamination in Group X in different climates. Number of samples is given in brackets.

%Modules	Age Groups					
Group	Young	Old				Overall
	0 – 5 yrs	5 – 10 yrs	10 – 20 yrs	>20 yrs	Total Old	
<b>Hot</b>	<b>6% (175)</b>	38% (167)	28% (176)	88% (24)*	<b>37% (367)</b>	<b>27% (542)</b>
<b>Non-Hot</b>	<b>5% (130)</b>	NA	2% (110)	NA	<b>2% (110)</b>	<b>4% (240)</b>
p-value **	0.67	NA	<0.0001	NA	<0.0001	<0.0001

Note: Total number of samples in Group X is 782 nos. “NA” indicates no sample is available.  
\* Double glass modules. \*\* p-values for two-proportion z-test

Table 4.8: Percentage of modules with front-side delamination in small and large installations. Number of samples is given in brackets.

%Modules	Age Groups					
Group	Young	Old				Overall
	0 – 5 yrs	5 – 10 yrs	10 – 20 yrs	>20 yrs	Total Old	
<b>Small/ Medium</b>	<b>7% (837)</b>	49% (144)	19% (419)	83% (52)*	<b>32% (615)</b>	<b>18% (1452)</b>
<b>Large</b>	<b>13% (181)#</b>	65% (66)#	NA	NA	<b>65% (66)*</b>	<b>27% (247)</b>
p-value **	<0.0001	0.043	NA	NA	<0.0001	0.001

Note: Total number of samples is 1699 nos. “NA” indicates no sample is available in that category.  
# Mostly small bubbles along snail tracks in the modules.  
\* Double glass modules. \*\* p-values for two-proportion z-test

The above discussion indicates that the cases of front-side bubbles and delamination are higher in the Hot zone and in Group Y modules. Bubbles have been observed in significant number of modules in large installations, along the snail tracks.

### **4.2.3 Snail Tracks**

Cracks in the solar cells can lead to different effects in the encapsulant. In the old modules having discoloration of encapsulant, cracks in the cells allow oxygen to pass through to the discolored encapsulant at the top of the cells, and this oxygen then bleaches the discoloration (restores the transparency of the encapsulant) in the presence of sunlight [48]. On the other hand, in many of the newer modules, moisture and other gases are able to migrate through the cracks in the cells and cause Snail track formation on top of the cells [41]. Also, the spacing between the cells can serve as a pathway for moisture penetration up to the metallization on top of cells, and in some cases, this leads to framing type snail tracks that occur along the edges of the cells. Examples of the two types of snail tracks are shown in Fig. 4.6 (a) & (b). Figure 4.6 (c) shows the electroluminescence (EL) image of a PV module with cracks spanning multiple solar cells, and the corresponding visual image shows snail tracks at same location. In the survey, we have found good correlation between the cell cracks and non-framing type snail tracks. Both snail tracks (non-framing type) and photo-bleaching effects of the encapsulant serve as visual indications of cracks in the cells. It is important to note that while the electroluminescence (EL) image clearly shows the area affected by the crack (and hence reveal the severity of the crack), snail tracks only delineate the crack's location but do not provide any indication about the severity of the crack. Also, the micro-cracks in the solar cells may not always lead to a visible sign (in terms of snail tracks or photo-bleaching) and Electroluminescence (EL) imaging is the only way to check for such microscopic cracks. In the following analysis, we shall use the term “snail tracks” to refer to the non-framing type snail tracks, which are most often associated with cracks in the solar cells and can have significant impact on the power output of the modules.

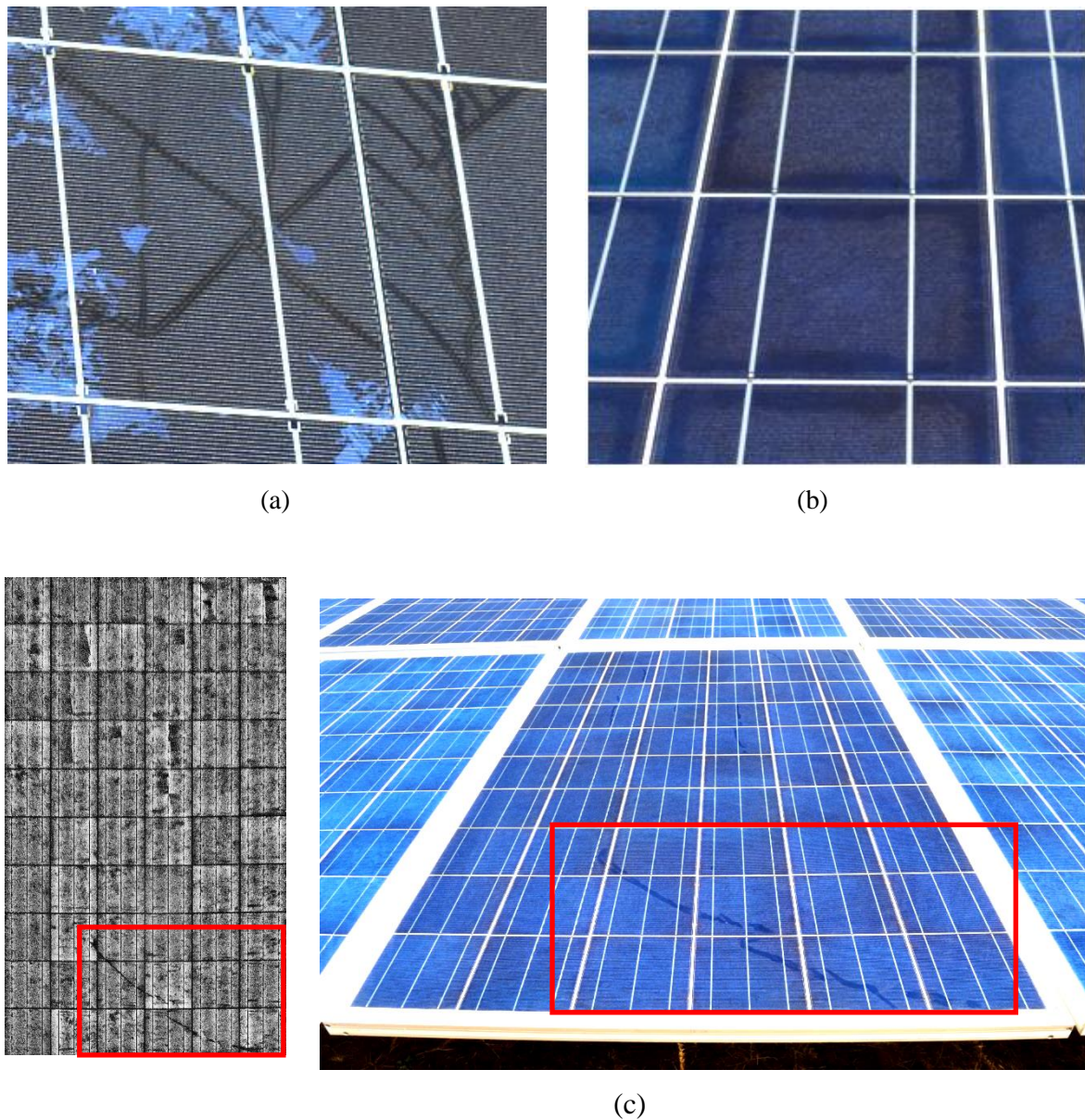


Fig. 4.6: Examples of Snail Tracks observed in the survey – (a) snail track in a young module in Hot & Dry zone, (b) framing type snail track in a young module in Warm & Humid zone, and (c) EL image of a PV module showing crack and the corresponding region in the visual image showing a snail track spanning across multiple solar cells [20, 21].

Figure 4.7 shows the statistics of snail tracks in different climatic zones and age groups. It is evident that snail tracks are mostly observed in the young modules and further, the affected modules are widely dispersed in different climatic zones (Hot & Dry, Composite, Moderate, and Cold & Cloudy).

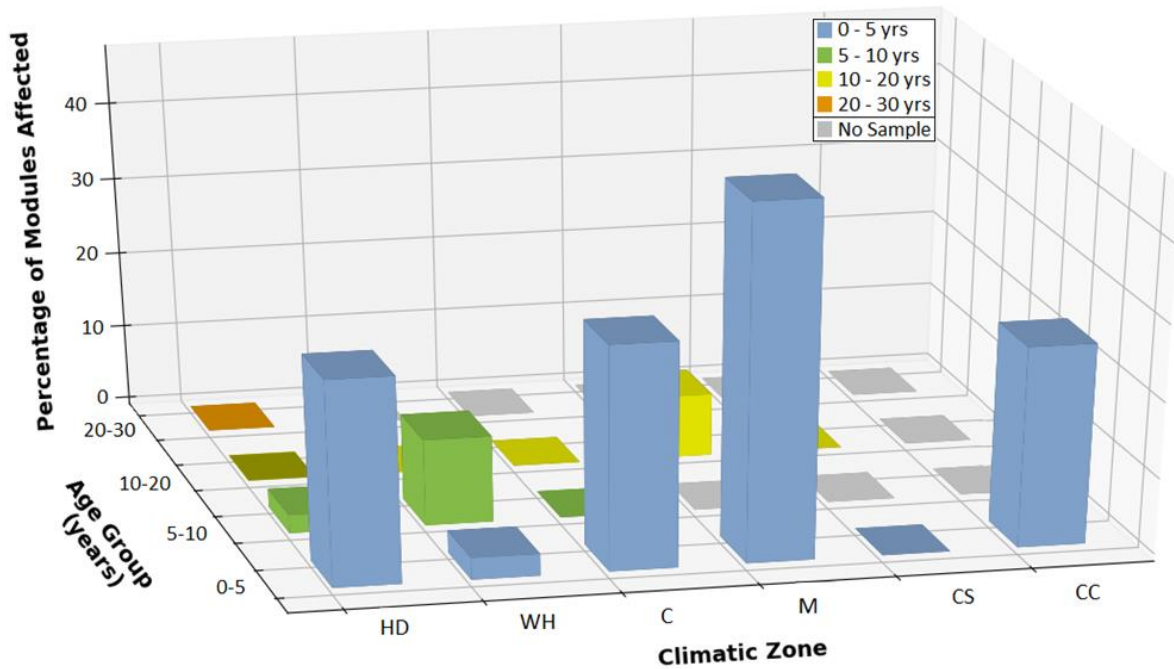


Fig. 4.7: Statistics of non-framing type snail tracks in different climatic zones and age groups (HD: Hot & Dry, WH: Warm & Humid, C: Composite, M: Moderate, CS: Cold & Sunny, CC: Cold & Cloudy).  
Most of the affected panels are in the young age group.

Table 4.9 shows the statistics for the modules affected by snail tracks in Group X and Group Y. The percentage of affected modules is significantly higher in Group Y than in Group X (particularly in the young age category). Snail tracks is thus a distinguishing feature for Group Y and may be one of the factors behind the higher power degradation rate observed in Group Y sites as compared to Group X sites. In fact, detailed analysis of cell cracks based on EL imaging indicates that the cracks are responsible for higher power degradation in Group Y sites (which is discussed in detail in the concurrent thesis of Rajiv Dubey [106]). Table 4.10 provides the statistics based on climatic zone, which indicates that the climate (ambient temperature) is not significantly impacting the snail track formation in the panels.

Table 4.9: Percentage of modules with snail tracks in Group X and Group Y. Number of samples is given in brackets.

%Modules	Age Groups					
Group	Young	Old				Overall
	0 – 5 yrs	5 – 10 yrs	10 – 20 yrs	>20 yrs	Total Old	
<b>X</b>	<b>15% (305)</b>	11% (167)	0.3% (286)	0% (24)*	<b>4% (477)</b>	<b>8% (780)</b>
<b>Y</b>	<b>31% (637)</b>	0% (40)	0% (123)	0% (28)*	<b>0% (191)</b>	<b>24% (828)</b>
p-value**	<0.0001	0.029	0.512	0.512	0.005	<0.0001

Note: Total number of samples is 1610 nos. This number is lower than 1699 because some modules could not be classified into Groups X or Y due to *I-V* measurement at low irradiance (below 600 W/m<sup>2</sup>).  
“NA” indicates no sample is available in that category.  
\* Double glass modules. \*\* p-values for two-proportion z-test

Table 4.10: Percentage of modules with snail tracks in Group X in different climates. Number of samples is given in brackets.

%Modules	Age Groups					
Group	Young	Old				Overall
	0 – 5 yrs	5 – 10 yrs	10 – 20 yrs	>20 yrs	Total Old	
<b>Hot</b>	<b>18% (175)</b>	11% (167)	0% (176)	0% (24)*	<b>5% (367)</b>	<b>9% (540)</b>
<b>Non-Hot</b>	<b>12% (130)</b>	NA	1% (110)	NA	<b>1% (110)</b>	<b>7% (240)</b>
p-value **	0.136	NA	0.206	NA	0.06	0.296

Note: Total number of samples in Group X is 782 nos.  
“NA” indicates no sample is available in that category.  
\* Double glass modules. \*\* p-values for two-proportion z-test

Table 4.11 presents the statistics of snail tracks based on the size of installation. The percentage of affected modules with snail tracks is comparable in small/medium and large installations in the young age category, but in the “5-10 years” category, the prevalence of snail tracks is much higher for the large sites as compared to the small/medium sites. This indicates that either the modules are not properly handled during transportation / installations (which led to excessive cracks in the cells) in these large sites, or the quality of the modules used in these sites is poor.

Table 4.11: Percentage of modules with snail tracks in small and large installations. Large installations are having higher percentage of affected panels in old age category.

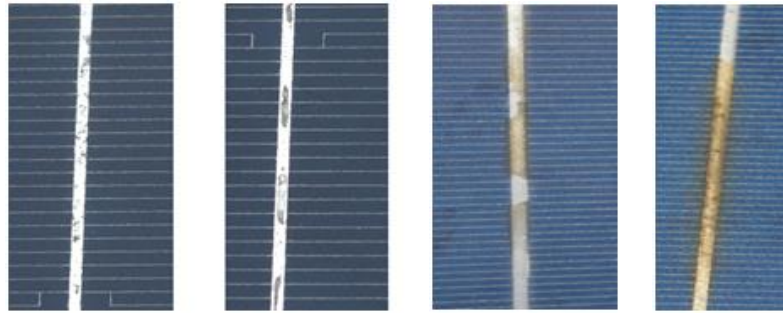
%Modules	Age Groups					
	Young	Old				Total Old
Group	0 – 5 yrs	5 – 10 yrs	10 – 20 yrs	>20 yrs		
Small/ Medium	<b>22% (837)</b>	0% (144)	0.2% (419)	0% (52)*	<b>0.2% (615)</b>	<b>13% (1452)</b>
Large	<b>21% (181)</b>	21% (66)	NA	NA	<b>21% (66)</b>	<b>21% (247)</b>
p-value **	0.77	<0.0001	NA	NA	<0.0001	0.001

Note: Number of samples is given in brackets. Total number of samples is 1699 nos.  
“NA” indicates no sample is available in that category.  
\* Double glass modules. \*\* p-values for two-proportion z-test

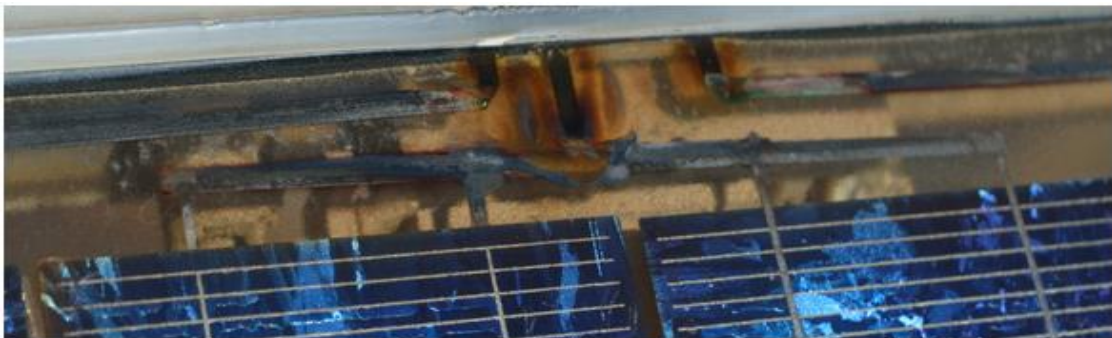
In conclusion, it can be said that snail tracks are seen more in Group Y modules as compared to Group X modules, and is a major distinguishing factor between the two groups. Young modules are affected more than the old modules, which may be partly due to the reduction in wafer thickness (leading to more cracks during transportation and handling) and partly due to improper installation practices (since the present-day power plants are being built in very short time frames).

#### 4.2.4 Discoloration on Metallization

Metallization refers to the gridlines/fingers, busbars and interconnect ribbons that conduct the charge carriers generated in the solar cells to the electric load, through the junction box attached at the backside of the module. The fingers and busbars are usually made of silver, while the interconnect ribbons are usually of copper, coated with tin. The metallization usually has a shiny silvery appearance but may discolor due to corrosion and also, in some cases, due to improper manufacturing processes (like solder flux deposition on top etc.). Further, discoloration of the encapsulant layer on top of the metallization can also give an impression of discoloration of the underlying metallization. Some examples of metallization discoloration observed during the survey are given in Fig. 4.8.



(a)



(b)

Fig. 4.8: Metallization discoloration on interconnect ribbons observed during the surveys – (a) discoloration patterns in cell interconnects observed in young modules, and (b) corrosion in interconnect ribbons observed in old modules [20, 21].

Figure 4.9 shows the statistics for discoloration of metallization observed during the field survey for ‘All’ inspected modules, grouped on the basis of climatic zone and module age. Some discoloration is observed in the young modules (“0-5 years” category), which is mainly due to non-corrosion issues (like deposition of solder flux, non-uniform tin plating, etc., as shown in Fig. 4.8(a)) whereas in the old modules, corrosion seems to be the main factor responsible for metallization discoloration (representative images shown in Fig. 4.8(b)). Thus, there are

manufacturing issues in many of the inspected young modules, which hint towards lapses in quality control.

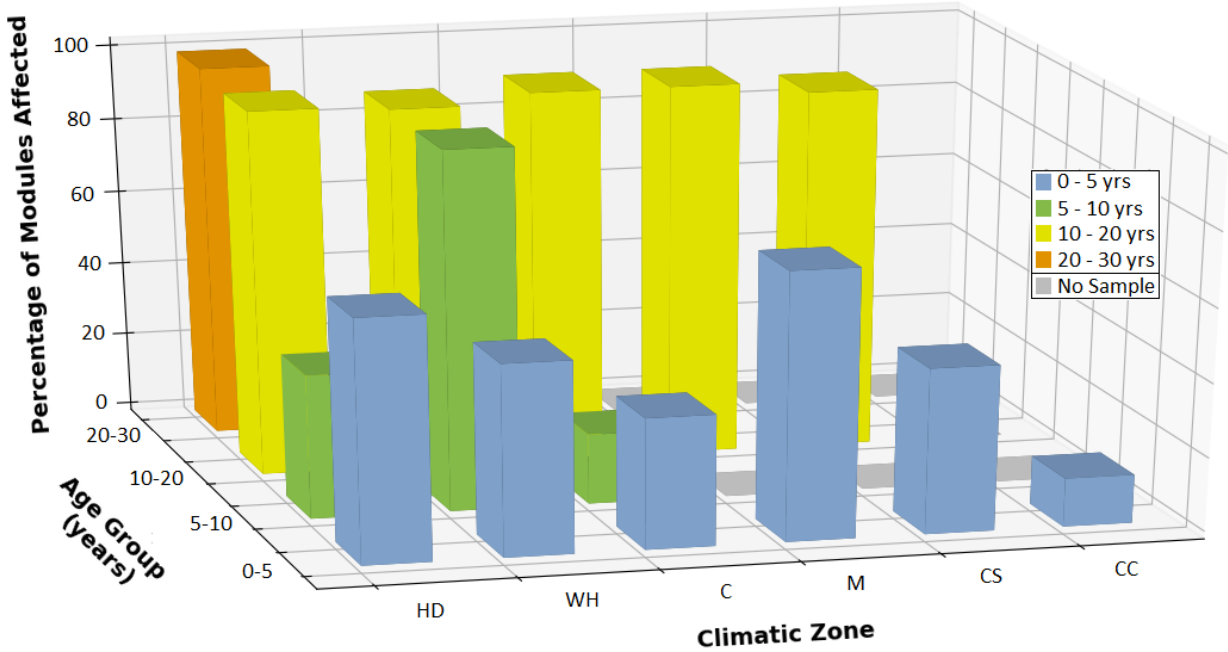


Fig. 4.9: Metallization discoloration statistics in different climatic zones and age groups (HD: Hot & Dry, WH: Warm & Humid, C: Composite, M: Moderate, CS: Cold & Sunny, CC: Cold & Cloudy). Significant discoloration is observed even in the young age group (mostly due to flux deposits and other causes).

The statistics for affected panels in Group X and Group Y have been shown in Table 4.12. The total number of samples is 1605 in this table, which is lower than the total number of modules measured, because some modules could not be classified into Groups X or Y due to *I-V* measurement at low irradiance (below 600 W/m<sup>2</sup>). Also, All-Back-Contact modules have been excluded from this analysis, as the metallization is not visible externally. It is evident from the table that the percentage of affected modules is higher in Group Y as compared to Group X, in modules with age less than 10 years (p-values are less than 0.05 for both “0-5 years” and “5-10 years” age groups, confirming that the differences are statistically significant).

Table 4.12: Percentage of modules with metallization discoloration in Group X and Group Y.  
Number of samples is given in brackets.

%Modules	Age Groups					
Group	Young	Old				Overall
	0 – 5 yrs	5 – 10 yrs	10 – 20 yrs	>20 yrs	Total Old	
<b>X</b>	<b>41% (305)</b>	72% (167)	99% (286)	100% (24)*	<b>89% (477)</b>	<b>70% (782)</b>
<b>Y</b>	<b>56% (632)</b>	100% (40)	98% (123)	100% (28)*	<b>98% (191)</b>	<b>66% (823)</b>
p-value**	<0.0001	0.0001	0.284	0.284	0.0002	0.09

Note: Total number of samples is 1605 nos.  
\* Double glass modules. \*\* p-values for two-proportion z-test.

To investigate the effect of Hot climate on the metallization, the data has been grouped into Hot and Non-Hot climate groups for Group X modules, which is presented in Table 4.13. We can clearly see that the percentage of affected modules in the young age category is higher in “Non-Hot” climate as compared to “Hot” climate. This supports our hypothesis that the metallization discoloration in these modules is not due to corrosion in the field (which would generally be influenced by higher operating temperatures in Hot climates), but rather due to manufacturing related issues.

Table 4.14 shows the percentage of affected modules, grouped on the basis of the system size. It is observed that there is higher percentage of affected panels in the “small/medium” sites as compared to the “large” sites, indicating that the product quality may be compromised in the “small/medium”-sized installations.

Table 4.13: Percentage of modules with metallization discoloration in Group X in different climates.  
Number of samples is given in brackets.

%Modules	Age Groups					
Group	Young	Old				Overall
	0 – 5 yrs	5 – 10 yrs	10 – 20 yrs	>20 yrs	Total Old	
<b>Hot</b>	<b>35% (175)</b>	72% (167)	99% (176)	100% (24)*	<b>87% (367)</b>	<b>70% (542)</b>
<b>Non-Hot</b>	<b>48% (130)</b>	NA	97% (110)	NA	<b>97% (110)</b>	<b>70% (240)</b>
p-value**	0.024	NA	0.151	NA	0.005	0.98

Note: Number of samples is given in brackets. Total number of samples in Group X is 782 nos.  
“NA” indicates no sample is available in that category.  
\* Double glass modules. \*\* p-values for two-proportion z-test

Table 4.14: Percentage of modules with metallization discoloration in small and large installations.  
Number of samples is given in brackets.

%Modules	Age Groups					
Group	Young	Old				Overall
	(0 - 5 yrs age)	5 – 10 yrs	10 – 20 yrs	>20 yrs	Total Old	
<b>Small/ Medium</b>	<b>50% (832)</b>	85% (144)	98% (419)	100% (52)*	<b>95% (615)</b>	<b>69% (1447)</b>
<b>Large</b>	<b>46% (181)</b>	61% (66)	NA	NA	<b>61% (66)</b>	<b>50% (247)</b>
p-value**	0.31	<0.0001	NA	NA	<0.0001	<0.0001

Note: Total number of samples is 1694 nos. (excluding All Back Contact modules which do not have visible metallization).  
“NA” indicates no sample is available in that category.  
\* Double glass modules. \*\* p-values for two-proportion z-test

In conclusion, it can be said that discoloration on metallization has been found to be more prevalent in Group Y modules, and in “Small/Medium” sized installations, which hints towards the poor manufacturing quality of these modules.

## 4.2.5 Backsheet Degradation

The role of the module's backsheet is to prevent ingress of moisture and dust into the module, and provide electrical insulation [43]. The backsheet is commonly made of polymer and can easily get scratched (due to improper handling during transportation and installation), and may degrade upon field exposure leading to loss of adhesion (due to moisture ingress), get burnt due to hot spots in the solar cells, or degrade thermally leading to chalking. Also, in some cases fine crack lines are observed in the outer layer or inner layer of the backsheet. Images of these various defects from the All-India Surveys are shown in Fig. 4.10.

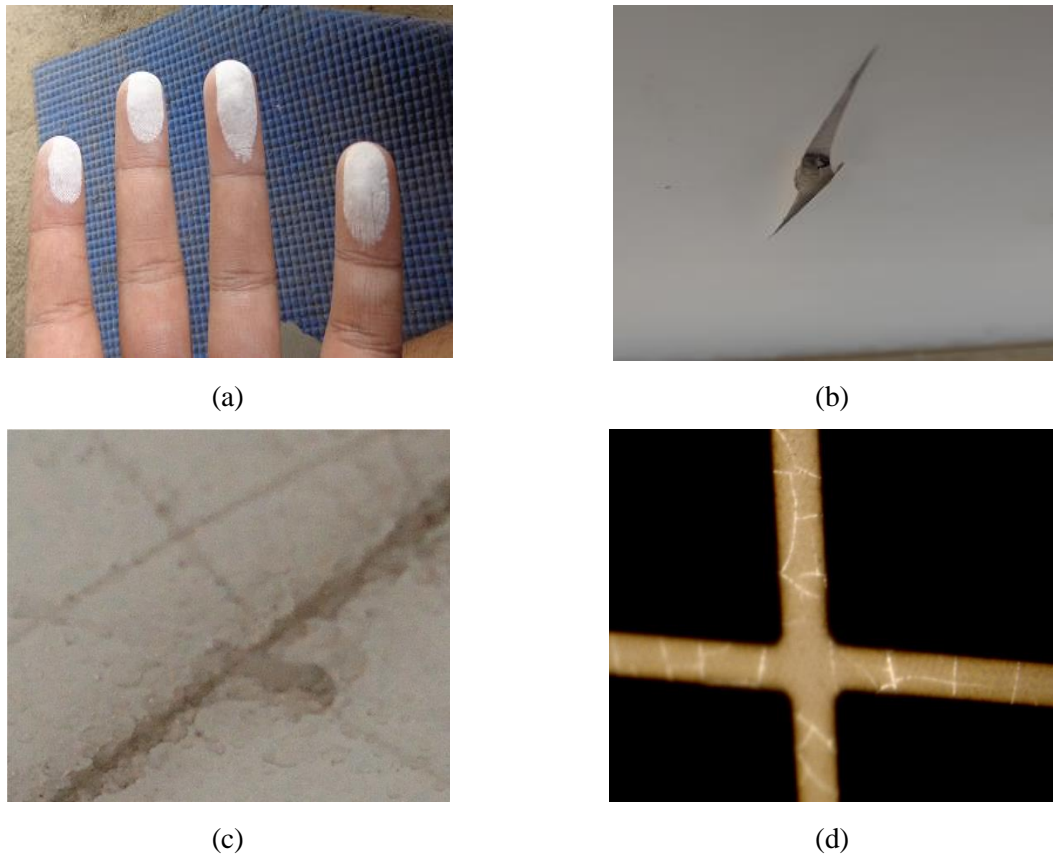


Fig. 4.10: Examples of degradation observed in backsheet – (a) chalking, (b) scratch and delamination, (c) cracks in outer layer of backsheet, (d) cracks in inner layer of the backsheet [20, 21].

The statistics for modules with backsheet damage (like chalking, discoloration, bubbles, delamination, scratches and cracking) is shown in Fig. 4.11(a). Almost all modules aged more than 10 years have shown backsheet degradation (predominantly chalking). However, some

manufacturers consider chalking to be insignificant (since backsheet thickness reduction of a few microns is not expected to adversely affect backsheet performance). So, the statistics for the more critical degradation modes of backsheet – bubbles, delamination and cracks – is shown separately in Fig. 4.11(b). A high percentage of modules in the young age group have shown such defects (the predominant of which are cracks), which indicates the use of poor quality backsheet materials in these modules.

Table 4.15 shows the percentage of modules affected by bubbles, delamination and cracking in backsheet, in Group X and Group Y. Comparison of Group X and Group Y indicates that backsheet defects are prevalent in both categories but, in the old modules, it is significantly higher in Group Y as compared to Group X (but the trend is reverse in case of young modules).

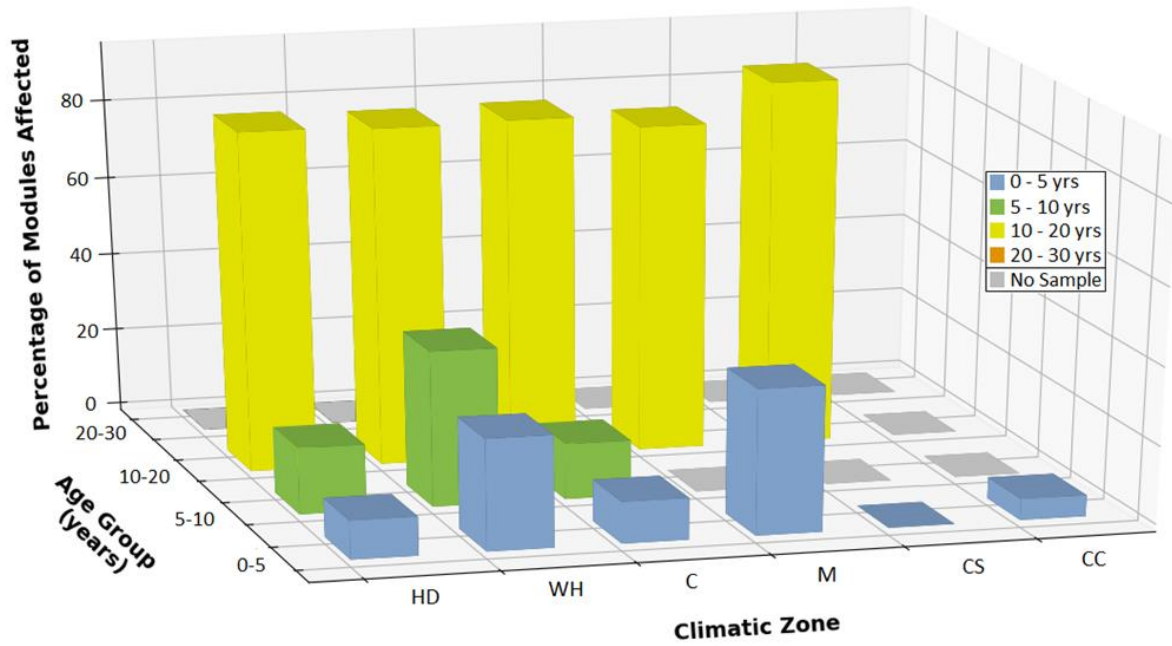
Table 4.15: Percentage of modules with backsheet degradation (bubbles, delamination and cracking) in Group X and Group Y. Number of samples is given in brackets.

%Modules	Age Groups					
	Young	Old				Total Old
Group	0 – 5 yrs	5 – 10 yrs	10 – 20 yrs	>20 yrs		
<b>X</b>	<b>19% (305)</b>	8% (167)	15% (286)	NA	<b>13% (453)</b>	<b>15% (758)</b>
<b>Y</b>	<b>11% (637)</b>	0% (40)	34% (123)	NA	<b>26% (163)</b>	<b>14% (800)</b>
p-value**	0.001	0.068	<0.0001	NA	0.0001	0.61

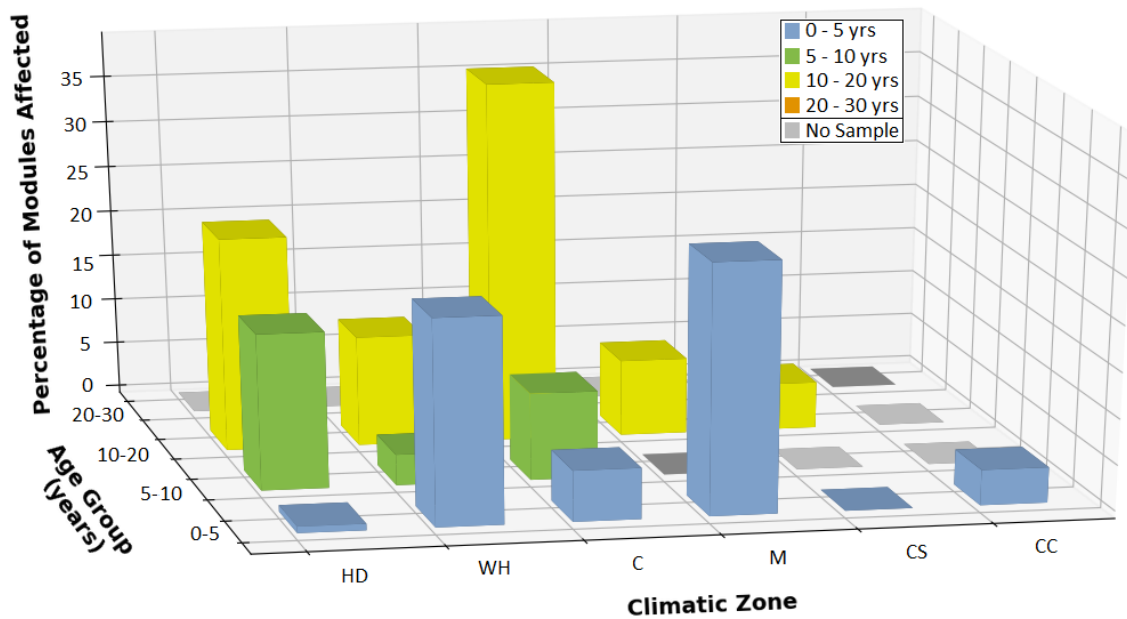
Note: Total number of samples is 1558 nos. This number is lower than 1697 because some modules could not be classified into Groups X or Y due to *I-V* measurement at low irradiance (below 600 W/m<sup>2</sup>) and also modules having glass-glass construction have been excluded.

“NA” indicates no sample is available in that category (as double glass modules are excluded).

\*\* p-values for two-proportion z-test



(a)



(b)

Fig. 4.11: Percentage of modules with backsheets degradation in different climatic zones and age groups – (a) including chalking, discoloration, bubbles, delamination, scratches and cracking, and (b) includes bubbles, delamination and cracking. The presence of defects even in the Young age category is a matter of concern.

The comparison between Hot and Non-Hot climates is given in Table 4.16. It is evident from this table that the percentage of affected modules is comparable in the young age category,

but it is significantly higher for the Hot zone in the old category. This shows that the Hot climate is harsher for the backsheet as compared to the Non-Hot climate, in the long run. Table 4.17 presents the statistics based on the size of installation. The p-values indicate that the differences in the proportions in the different age groups is not significant (as the p-value is greater than 0.05), so it can be concluded that the percentage of affected panels is similar for both small and large sized installations.

Table 4.16: Percentage of modules with backsheet degradation in Group X in different climates. Number of samples is given in brackets.

%Modules	Age Groups					
	Young	Old				Overall
Group	0 – 5 yrs	5 – 10 yrs	10 – 20 yrs	>20 yrs	Total Old	
Hot	18% (175)	8% (167)	22% (176)	NA	15% (343)	16% (518)
Non-Hot	20% (130)	NA	5% (110)	NA	5% (110)	13% (240)
p-value**	0.612	NA	<0.0001	NA	0.004	0.295

Note: Total number of samples in Group X is 758 nos. (excluding modules having glass-glass construction).  
“NA” indicates no sample is available in that category (as double glass modules are excluded).  
\*\* p-values for two-proportion z-test

Table 4.17: Percentage of modules with backsheet degradation in small and large installations. Number of samples is given in brackets.

%Modules	Age Groups					
	Young	Old				Overall
Group	0 – 5 yrs	5 – 10 yrs	10 – 20 yrs	>20 yrs	Total Old	
Small/ Medium	14% (837)	5% (144)	21% (419)	NA	17% (563)	15% (1400)
Large	10% (181)	11% (66)	NA	NA	11% (66)	10% (247)
p-values**	0.146	0.121	NA	NA	0.191	0.028

Note: Total number of samples is 1647 nos. This number is lower than 1697 as modules having glass-glass construction have been excluded from this analysis.  
“NA” indicates no sample is available in that category (double glass modules are excluded).  
\*\* p-values for two-proportion z-test

Based on the above discussion, it can be said that defects in backsheets are more prevalent in Group Y sites in the old age category. More than 10% of the modules in the young sites have backsheet degradation which raises concern regarding the material quality at these sites. Among the old sites, the percentage of affected modules is higher in the Hot zone, which indicates that the Hot zone is more severe.

### **4.3 Factors affecting Module Degradation**

There can be multiple factors responsible for module degradation, including the material quality, manufacturing quality, transportation and installation, the environmental stress levels at the site etc. In this section, we shall discuss the effect of climatic zone, system quality and size of installation on the module degradation modes. These factors have already been partly discussed defect-wise in the previous section, and here the data will be aggregated to generate a better understanding of the influencing factors.

#### **4.3.1 Effect of System Quality**

The overall quality of the system can be judged from the average power degradation rate at the site and accordingly, we have clubbed the installations into 2 groups – Group X (average power degradation less than 2 %/year) and Group Y (average power degradation exceeds 2%/year). The percentage of defective panels has been plotted for Groups X and Y in Fig. 4.12. From the plot, it is clear that among the young installations, snail tracks and metallization discoloration are occurring more frequently in Group Y sites as compared to Group X sites. Among the old installations, the Group Y sites are showing a higher frequency of packaging material defects (encapsulant discoloration, delamination and backsheet defects) as compared to Group X sites. This indicates that Group Y sites are using poor quality materials and/or manufacturing processes, which may be partly the reason for the high degradation rates observed in these sites. Also, the higher prevalence of snail tracks in the Group Y sites is an important contributing factor to the higher degradation rates, since these are generally associated with cell cracks, and this raises serious concerns about the installation quality at these sites.

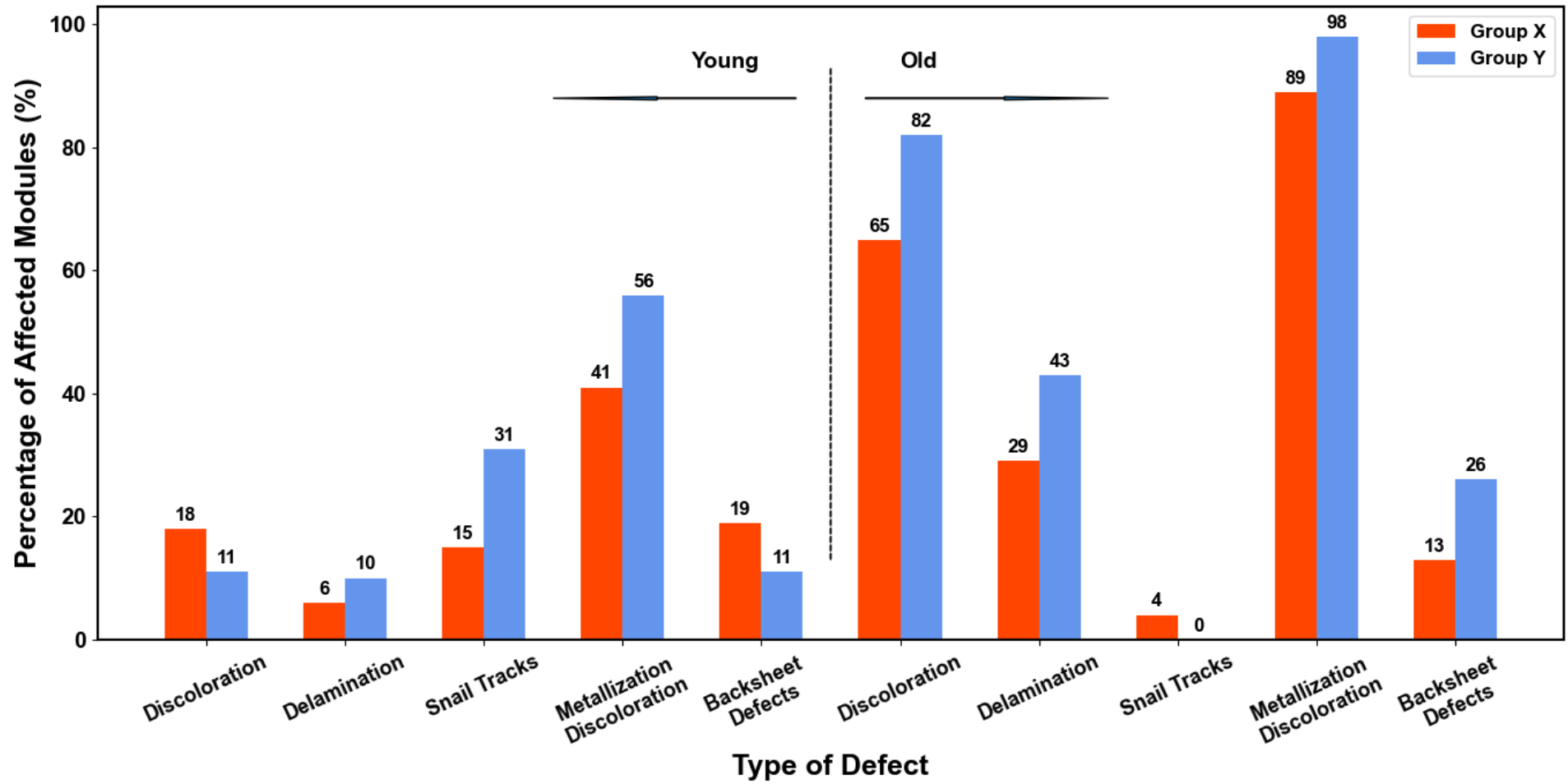


Fig. 4.12: Comparison of the percentage of defective panels in Group X and Group Y sites.

### 4.3.2 Effect of Climatic Zone

Usually, the places on earth that receive high solar irradiance also tend to be hotter. While the higher irradiance increases the power output of the panels, the higher temperatures have the inverse effect on the panel power output. Further, the hotter temperatures also generally increase the degradation rate of the materials, and hence it is important to determine the effect of climatic zone on PV module degradation. The percentage of panels affected by discoloration in Hot and Non-Hot climates is plotted in Fig. 4.13. It is evident that discoloration is more frequently observed in the Hot climate than Non-Hot, particularly for the Young modules, whereas the older modules are more susceptible to delamination in the Hot climate than Non-Hot climate. Also, backsheets degradation is more frequently observed in the Hot climate as compared to the Non-Hot climate. The Hot zone is thus more severe than the Non-Hot zone, and this is also confirmed by the higher average power degradation rates in the Hot zone (1.18 %/year) than in Non-Hot zone (0.39 %/year) [106]. For detailed analysis of electrical degradation rates, interested readers may refer to the concurrent thesis of Rajiv Dubey [106]. It is important to note that even though the Hot climate is more severe than the Non-Hot climate, some panels in the Non-Hot climate have undergone very high degradation within a few years of outdoor exposure. Publications from National Institute of Technology Hamirpur have reported about PV systems having high degradation rates in the Non-Hot climate. Sharma *et al.* have reported the presence of snail tracks on all panels of a 2.5-year-old PV system (comprising of 10 panels). Also, broken interconnect ribbon (with localized discoloration) was found to be the root cause behind hot spot generation and localized discoloration in a panel. Further, sparking in the junction box of two panels lead to burning and melting of the junction box. These three panels (out of total 10 panels) in this young system showed very high power degradation in the range of 30 % - 50 % [38]. A 28-year-old PV system in similar climate showed multitude of defects including encapsulant discoloration and delamination, front grid corrosion, bubbles in backsheets and corrosion in junction box [40]. One panels at this site had glass breakage and hot spots on multiple cells, and showed maximum power degradation close to 80%, though the average power degradation rate at this site was around 1.4 %/year [40]. The Non-Hot climate is mostly found in hilly regions, where it is difficult to transport the panels and hence the chances of damage to panel during transportation to the site is higher than in the plains. Installers in both Hot and Non-Hot climates need to be careful regarding the quality of manufacturing, transportation and also the installation practices followed at site.

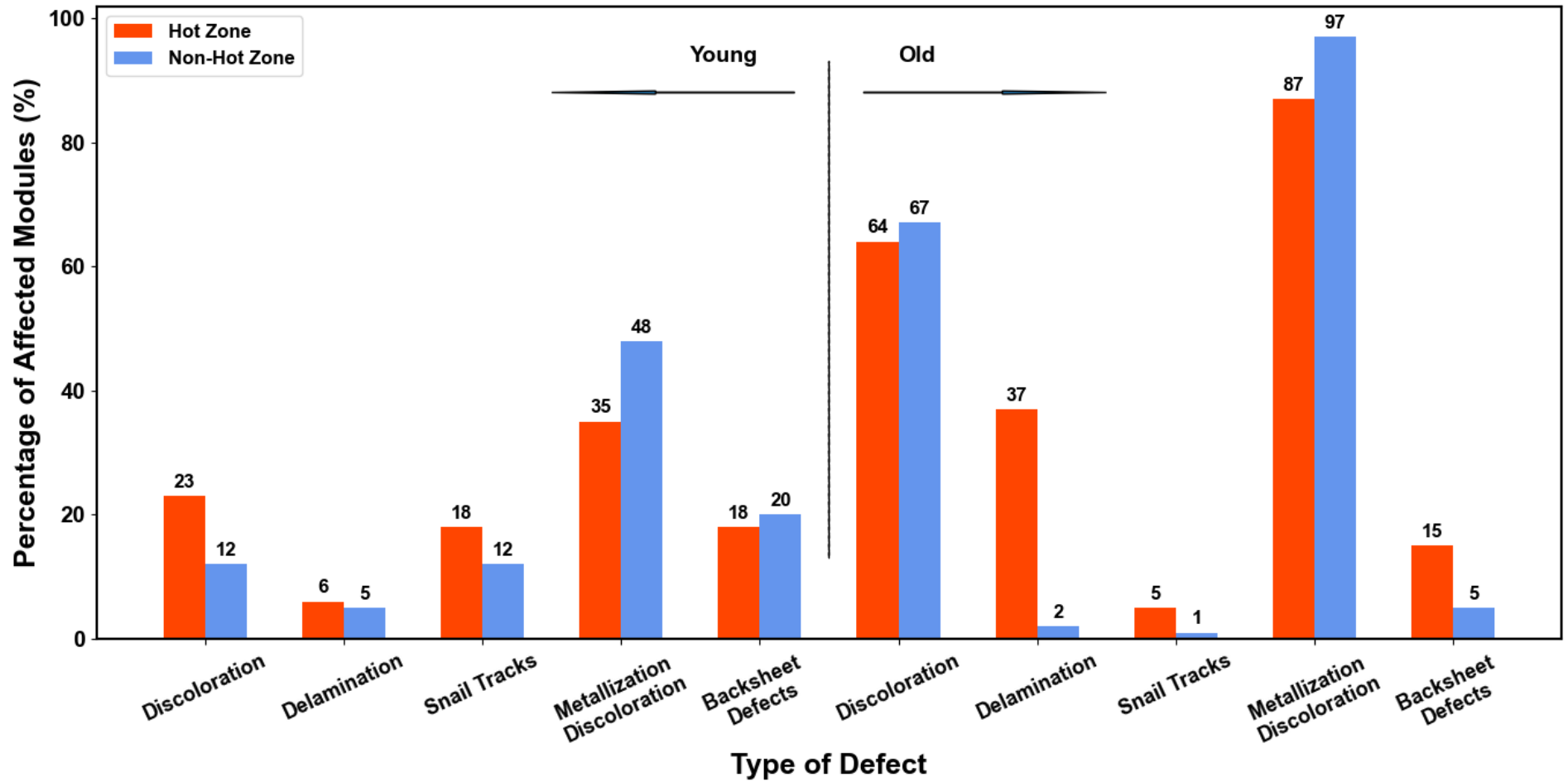


Fig. 4.13: Comparison of the percentage of defective panels in Hot and Non-Hot zones (in Group X sites).

### **4.3.3 Effect of Installation Size**

One of the major advantages of solar PV technology is that the PV system can be scaled as per the available installation area which enables true decentralization of power generation. However, since small system owners have lower budgets, they will be less inclined to perform due diligence on the module quality. In order to assess the impact of the system size on the degradation modes, we have plotted the frequency of defects for the small and large installations, in Fig. 4.14. The data indicates that among the old systems, encapsulant discoloration, metallization discoloration and backsheet defects are observed more frequently in small installations, whereas snail tracks and delamination are more frequently observed in large installations as compared to small installations. Thus, the quality of manufacturing and installation is a cause of concern for both small and large installations.

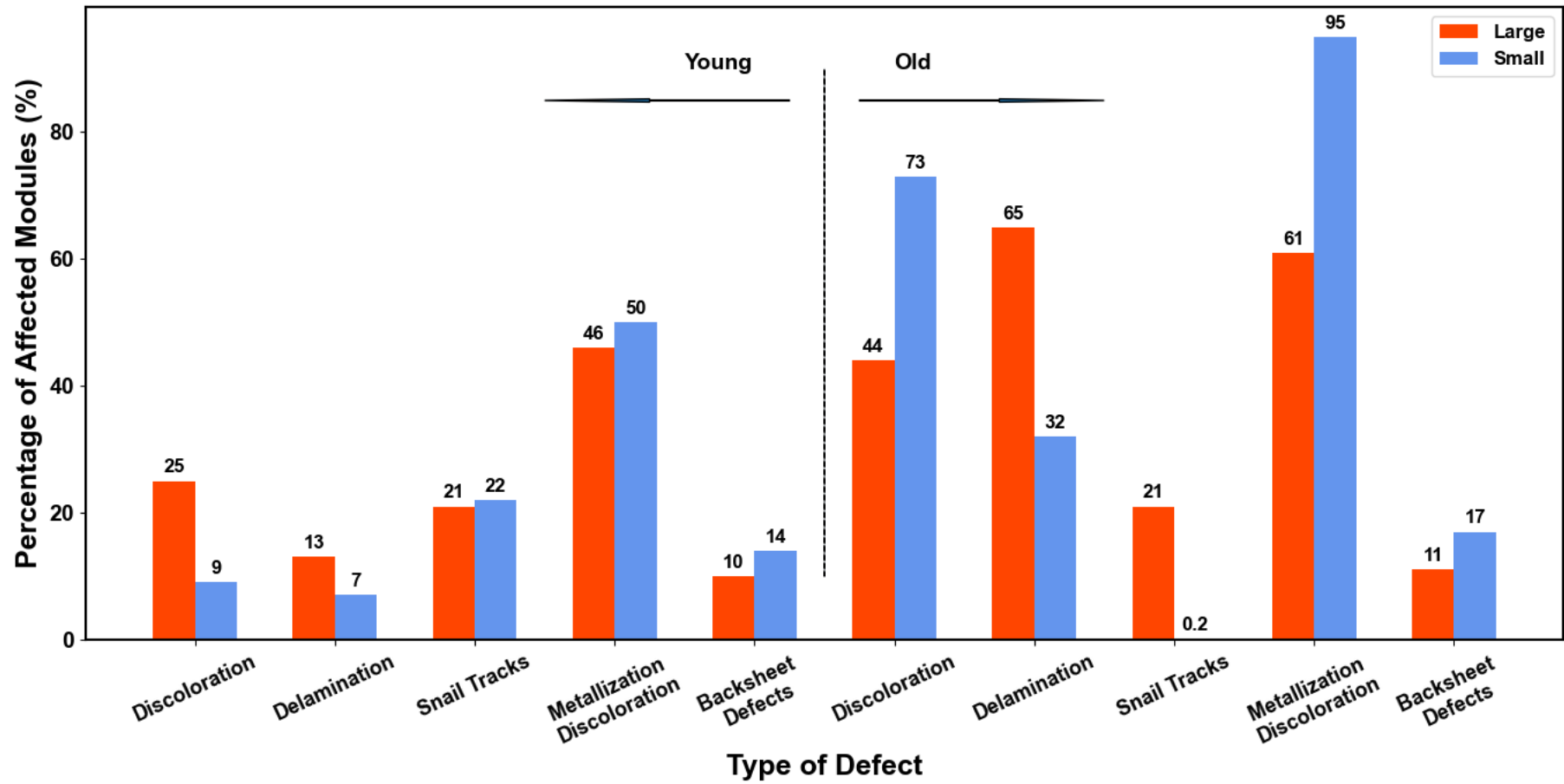


Fig. 4.14: Comparison of the percentage of defective panels in small and large installations.

## 4.4 Summary

The All-India surveys have provided us important insights into the degradation modes prevalent in different climatic zones of India. Degradation of the packaging materials (encapsulant and backsheet) are found to be more prevalent in the Hot climate than the Non-Hot climate. Encapsulant discoloration has been observed more frequently in the Hot climate in case of young modules (aged less than 5 years), while delamination has been observed more frequently in the old modules installed in Hot climate. Though the average degradation observed in Non-Hot climate is lower than the Hot climate in general, there exists specific cases of high degradation in the young modules installed in both Hot and Non-Hot climates. This indicates the limitations of the PV module qualification standards and the need to develop suitable accelerated tests for estimating the service life of PV modules in different climatic conditions. Encapsulant discoloration and backsheet degradation has been observed in more than 10% of the young modules while snail tracks have been observed in 26% of the young modules. This raises concerns about the 25-year warranty claimed by most module manufacturers. Snail tracks are found in significantly higher number of modules in Group Y sites as compared to Group X and hence can be considered as a major contributor to the higher degradation rate observed in Group Y sites. Further, the defects of packaging materials (encapsulant and backsheet) are observed more frequently in Group Y modules than Group X modules in the old age category. Encapsulant and metallization discoloration are found to be more prevalent in the small/medium sites as compared to the large sites, which indicates that the quality of modules used for small installations is not as good as for the large installations. This is a matter of concern as 40% of the 100 GW target of National Solar Mission is allocated to small rooftop installations.

Discoloration of the encapsulant is one of the most common degradation modes observed in the surveys, and it is known to directly impact the power generation capacity of the PV module. Close to 20% decrease in the short-circuit current was observed in some of the dark discolored modules in the All-India surveys. Hence, it was felt necessary to develop a fast characterization technique which can be applied in-situ in the field to determine the extent of current reduction based on visual images of the PV module. This methodology is discussed in detail in Chapter 5.

This page is intentionally left blank.

## **Chapter 5**

### **Quantification of Discoloration in PV Modules**

#### **5.1 Introduction**

It is desirable to quantify the amount of visual degradation seen in the PV modules installed in power plants, and estimate the power loss on the basis of such quantification. However, there are no reliable methods to measure the extent of discoloration in the PV modules in-situ at the installation site, since most color measuring equipment like portable colorimeter or spectrophotometer only measure a small area. As more and more megawatt-scale PV power plants are being installed, it is necessary to characterize the degradation of PV modules in-situ through non-contact techniques. Hence, it was felt necessary to develop a fast non-contact characterization technique for determining the discoloration on panels. Digital photography is an excellent candidate for such purposes as it can capture the color variation in the whole PV module in a single image within a fraction of a second. The photovoltaics industry has already

adopted aerial thermography, and the addition of a visual camera to the UAV (drone) is a small addition that can enable quick estimation of the discoloration and other visual defects in the PV modules. So, the correlation between the color captured by digital photography and the extent of actual discoloration in PV modules has been studied in detail in this chapter.

In this chapter, the process of quantifying the discoloration from digital images has been presented first, followed by its validation using indoor tests. Discoloration index (*DI*) has been formulated as a quantification of the extent of discoloration, and correlated to the degradation of various electrical parameters based on All-India survey data.

## **5.2 Image Processing Technique for Quantifying Discoloration**

### **5.2.1 Development of Image Processing Tool**

Digital cameras capture color images by using red, green, and blue filters in front of their sensors [107]. The popular JPEG image format also stores images in three separate channels (red, green and blue), and it is possible to read the pixel-by-pixel colour information from the image file as intensities of red, green, and blue colour. The crystalline silicon solar cells are predominantly dark blue in colour during manufacturing (the actual shade of blue colour depends on the thickness of the anti-reflective coating deposited on the silicon solar cell). As the PV module ages in the field, the discoloration of the encapsulant leads to gradual yellowing, but usually, the edges of the solar cells still remain blue in colour (in modules with breathable back-sheets) as the degraded encapsulant undergoes photo-bleaching upon exposure to oxygen diffusing from the edges of the cells [6]. Hence, comparing the color of the encapsulant over the cell, at the centre and the edge, can serve as a useful tool to quantify the discoloration in the module. Table 5.1 shows a set of colors starting from blue, and progressively going to full brown. The RGB information of these colors is also given, along with the percentage blue content in the color (which can be called the Blueness Index as defined below).

$$\text{Blueness Index (BI)} = \frac{B}{R+G+B} * 100 \quad \dots (5.1)$$

where, R, G and B are the intensities (grayscale values) of the red, green and blue channels respectively, in the digital image. Since our goal is to determine the extent of discoloration, we define a discoloration index based on the blue content of the colour as follows:

$$Discoloration\ Index\ (DI_{BI}) = 1 - \frac{BI_{present}}{BI_{initial}} \quad \dots (5.2)$$

where,

$BI_{present}$  = present value of blueness index

$BI_{initial}$  = Initial value of blueness index

It is evident from Table 5.1 that the blueness index decreases as the browning increase, with corresponding increase in the discoloration index.

Table 5.1: Discoloration index based on blueness index. Blueness index decreases as browning increases.

											
R,G,B	79, 129, 188	86, 122, 170	93, 117, 153	101, 112, 134	107, 105, 116	115, 100, 97	123, 95, 81	129, 90, 61	137, 84, 44	144, 77, 24	151, 72, 6
BI	57.5	51.5	45.6	39.5	33.9	28.4	22.6	17.4	12.9	7.9	2.6
$DI_{BI}$	0	0.11	0.21	0.31	0.41	0.51	0.61	0.70	0.77	0.86	0.95

Alternatively, the discoloration can be quantified in terms of change in the *YI*, which is widely used to quantify the yellowing of textiles, paints and plastics [108]. It is possible to calculate a *YI* from RGB values of the digital image, under certain assumptions. One of the important assumptions is regarding the illuminant (light source), and the ASTM formula for computing the *YI* (using a colour measuring instrument, known as colorimeter) assumes the illuminant to be D65. The CIE standard D65 illuminant is meant to simulate the noon-time light from the northern sky, with color temperature of 6500 K [64] and it is comparable to (though not exactly same as) the AM1.5G spectrum [65]. Since assumptions are involved, and it is not a direct measurement using a standard instrument (having a standard D65 illuminant), we refer to this index calculated from the visual image as the *Pseudo Yellowness Index (PYI)*.

There are many color spaces and models for representing a color, like HSV, CIE LAB, XYZ etc. A colour space is a three-dimensional coordinate system, in which a colour is represented as a point, characterized by its projections on the three axes. While the RGB tristimulus values can be negative in case of certain colours, CIE committee developed the XYZ colour space such that it would always take positive values [91, 92] . Another advantage of the XYZ colour model is that standard equations are available for determining the yellowness index of a colour, which indicates the amount of yellow in the given colour. The XYZ tristimulus values can be calculated from the RGB values using the following equations [109, 110].

$$[r, g, b] = \left[ \frac{R}{255}, \frac{G}{255}, \frac{B}{255} \right] \quad \dots (5.3)$$

$$\begin{aligned} r_1 &= \left( \frac{r+0.055}{1.055} \right)^{2.4} \cdot 100 \quad \text{if } r > 0.04045 \\ &= r/0.1292 \quad \text{if } r < 0.04045 \end{aligned} \quad \dots (5.4)$$

$$\begin{aligned} g_1 &= \left( \frac{g+0.055}{1.055} \right)^{2.4} \cdot 100 \quad \text{if } g > 0.04045 \\ &= g/0.1292 \quad \text{if } g < 0.04045 \end{aligned} \quad \dots (5.5)$$

$$\begin{aligned} b_1 &= \left( \frac{b+0.055}{1.055} \right)^{2.4} \cdot 100 \quad \text{if } b > 0.04045 \\ &= b/0.1292 \quad \text{if } b < 0.04045 \end{aligned} \quad \dots (5.6)$$

$$\begin{bmatrix} X \\ Y \\ Z \end{bmatrix} = \begin{bmatrix} r_1 \\ g_1 \\ b_1 \end{bmatrix} \cdot \begin{bmatrix} 0.412453 & 0.357580 & 0.180423 \\ 0.212671 & 0.715160 & 0.072169 \\ 0.019334 & 0.119193 & 0.950227 \end{bmatrix} \quad \dots (5.7)$$

The *PYI* is calculated from the CIE XYZ values using a modified version of the ASTM E313-15 formula for *YI* [63], as given below in Eq. 5.8 (the modification being addition of a pre-factor ‘A’ and an offset ‘B’). The pre-factor (A= 0.25) is added to the ASTM equation based on our observation that the yellowness index obtained from digital image analysis (using the ASTM formula) is about 4 times of the value measured using the colorimeter instrument. The offset (B = 9.467) is added to the equation to ensure that zero of *PYI* matches with the zero of *YI* (i.e. fitted line passes through the origin).

$$PYI = A \cdot \left( \frac{1.3013 X - 1.1498 Z}{Y} \right) \cdot 100 - B \quad \dots (5.8)$$

A discoloration index can again be calculated based on the change in the *YI* of the colour:

$$DI_{PYI} = \frac{PYI_{\text{present}} - PYI_{\text{initial}}}{PYI_{\text{range}}} \quad \dots (5.9)$$

where,

$PYI_{\text{present}}$  = present value of pseudo yellowness index

$PYI_{\text{initial}}$  = initial value of pseudo yellowness index

$PYI_{\text{range}}$  = difference in *PYI* between the worst possible browning and the initial (blue) colour.

$PYI_{\text{range}}$  is the normalizing factor which ensures that the discoloration index lies between 0 and 1 (with the worst possible browning denoted by 1). Table 5.2 gives the *PYI* and the discoloration index ( $DI_{PYI}$ ) values for the same set of colors as in Table 5.1. It may be noted that for *PYI* values less than -15, the colour is perceived by our eyes as blue and significant browning is visible in images with *PYI* values greater than zero.

Table 5.2: Discoloration index based on *PYI*. The *PYI* and *DI* values increase with the extent of browning.

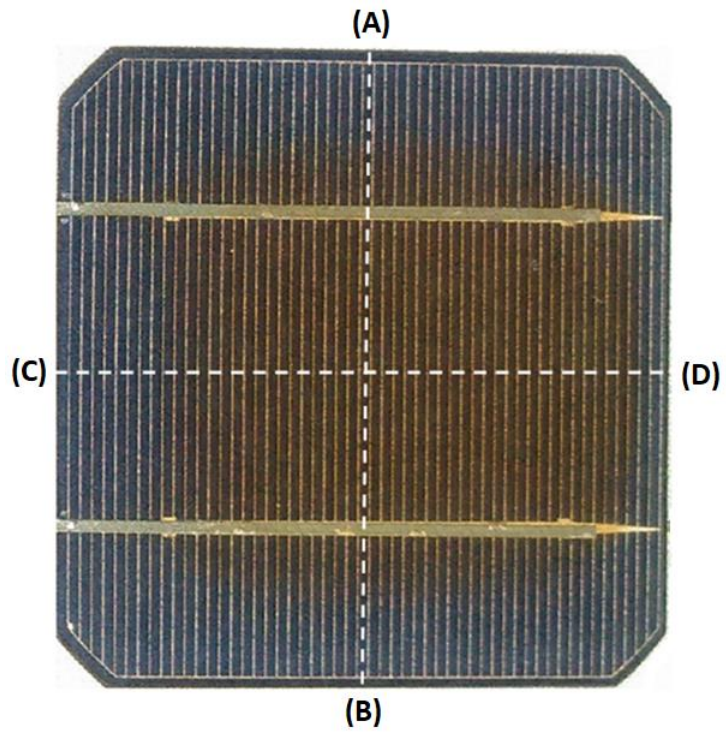
											
R,G,B	79, 129, 188	86, 122, 170	93, 117, 153	101, 112, 134	107, 105, 116	115, 100, 97	123, 95, 81	129, 90, 61	137, 84, 44	144, 77, 24	151, 72, 6
<i>PYI</i>	-66.5	-52.5	-38.8	-23.8	-11.1	0.3	10.2	17.0	22.5	27.3	30.3
$DI_{PYI}$	0	0.15	0.29	0.44	0.57	0.69	0.79	0.86	0.92	0.97	1

Three PV modules are chosen for this study, such that there is a progressive increase in the extent of discoloration (shown in Fig. 5.1). These modules had been exposed to the outdoor environment for more than 10 years. A 12 megapixel digital camera (Sony Cybershot) has been used for taking digital photographs of these PV modules. Software has been developed in Python to compute the BI and the *PYI* for a digital image (in TIFF or JPG format), pixel by pixel, and store as a 2-dimensional matrix. These values are shown for points along the centre-line for a discolored solar cell in Fig. 5.2 (b) and 5.2 (c). Comparing Fig. 5.2 (a), (b) and (c), it can be

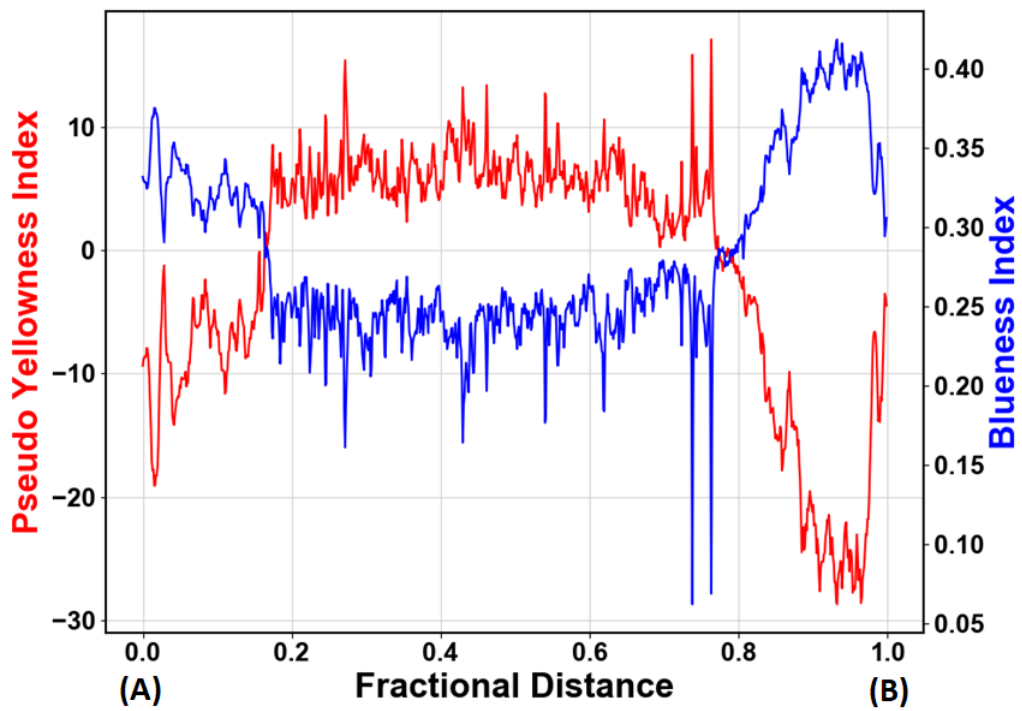
observed that the *PYI* values are negative for the blue region of the solar cell, and it progresses towards positive values as the colour changes to yellow and brown (at the centre of the cell). Also, the *PYI* values follow the opposite trend as the BI, which is expected. Zigzag behavior is observed in Fig. 5.2(c) because the *PYI* (and BI) values are higher on top of the metallization than on the silicon cell area (since the metallization is silvery in colour as opposed to blue colour of the silicon cell). Fig. 5.3 shows the false-color image based on the *YI* values, which closely mimics (matches) the discoloration pattern in the actual visual image of the solar cell. This solar cell is located above the nameplate in the PV module, which seems to be the cause for the asymmetrical discoloration.



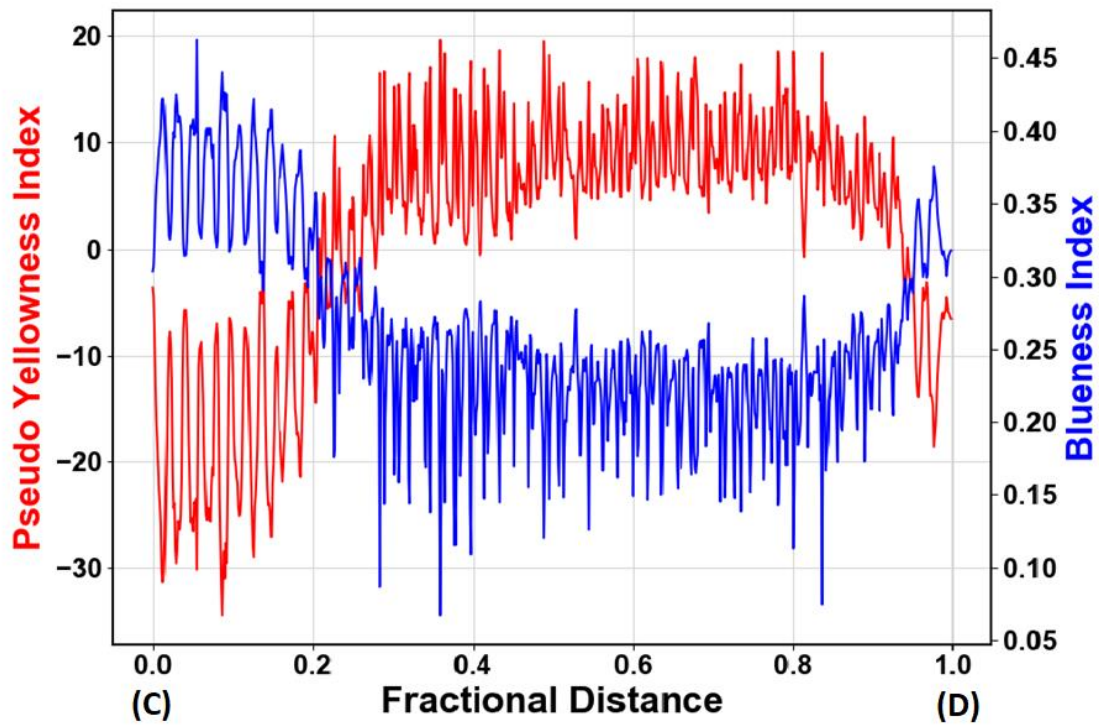
Fig. 5.1: Discolored PV modules used for discoloration study during internship at Arizona State University – Photovoltaic Reliability Laboratory.



(a)



(b)



(c)

Fig. 5.2: (a) Photograph of a discolored solar cell (b) *PYI* and *BI* of the discolored cell, for pixels along the vertical centre line (between points A and B marked in Fig. 5.2 (a)), and (c) *PYI* and *BI* of the discolored cell, for pixels along the horizontal centre line (between points C and D marked in Fig. 5.2

(a)).

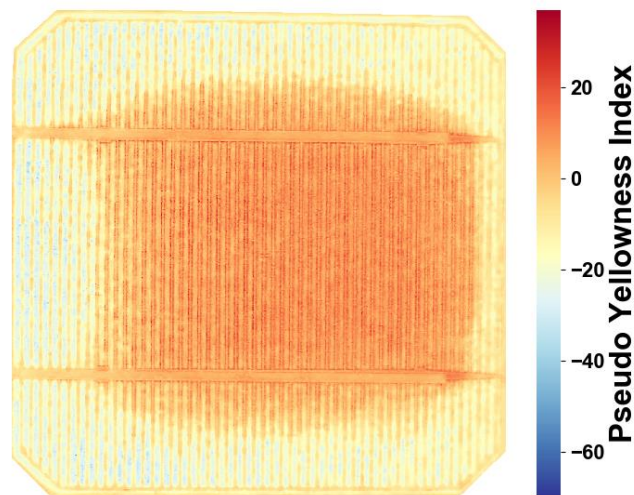


Fig. 5.3: False color map based on the *PYI*. It closely replicates the colour variation in the original digital image.

The pseudo yellowness index is compared with the actual yellowness index measured by a colorimeter (make: Xrite, model: Ci64) to establish a correlation. The *PYI* values are computed from digital images of the three selected modules (shown in Fig. 5.1). The images were taken between 12 noon to 1 PM at Arizona State University Photovoltaics Reliability Laboratory on a cloudless sunny day. Circular image sections were extracted from the solar cell images (as per the dimension of the colorimeter probe), some examples of which are shown in Fig. 5.4. The average *PYI* values for these individual sections are determined using Python based software (the values are indicated in Fig. 5.4). Fig. 5.5 shows the comparison of the *PYI* (computed from digital image) with the *YI* (measured with colorimeter), and it can be seen that there is a positive correlation (with correlation coefficient of 0.96). However, the correlation is better at higher degree of browning (refer to 1<sup>st</sup> quadrant of the figure) but not so good if there is no discoloration (refer to 3<sup>rd</sup> quadrant of the figure). This is not unexpected since the *YI* is a measure of the extent of yellow in the reflected light (and is not optimized for measuring blue color). The blueness index is also computed for these points. The correlation between the blueness index and the measured *YI* is also found to be almost linear, as shown in Fig. 5.6, but the scatter in the plot is much higher than in the case of the *PYI*. Hence, instead of the BI, we have used the *PYI* for further analysis.

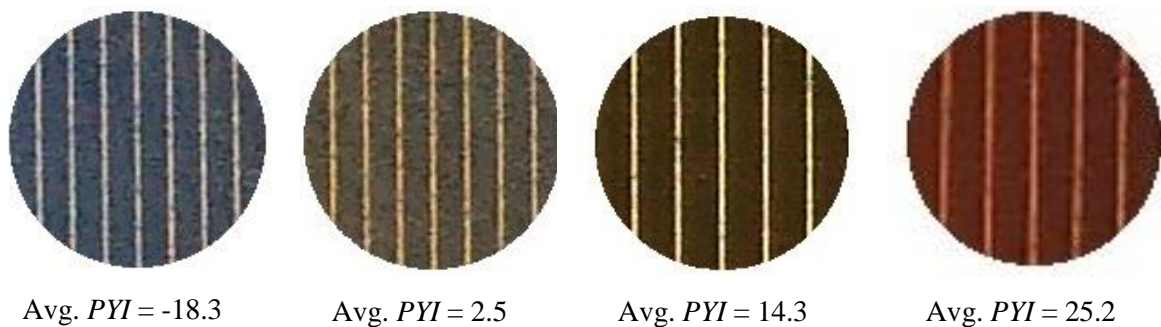


Fig. 5.4: Examples of circular image sections extracted from the solar cell images, cut based on the dimension of the colorimeter probe. Average *PYI* values (computed from these images) are indicated below the figures. The section without discoloration (leftmost) has negative *PYI* while the discolored regions have positive *PYI*.

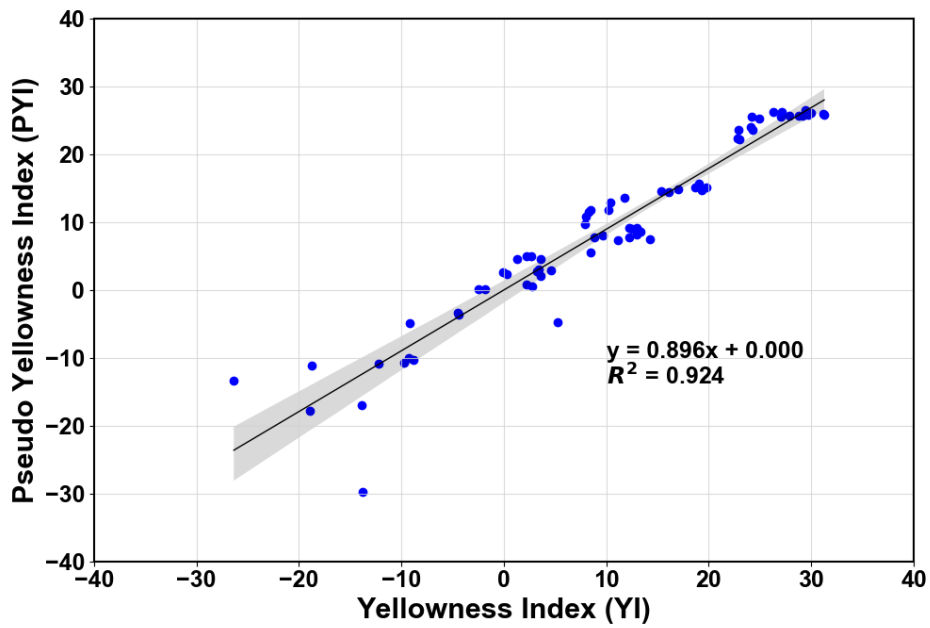


Fig. 5.5: Correlation of the computed *PYI* with the measured *YI* at different points of solar cells from the three selected modules. (Number of sample points = 70). The grey band indicates the 95% confidence interval of the slope.

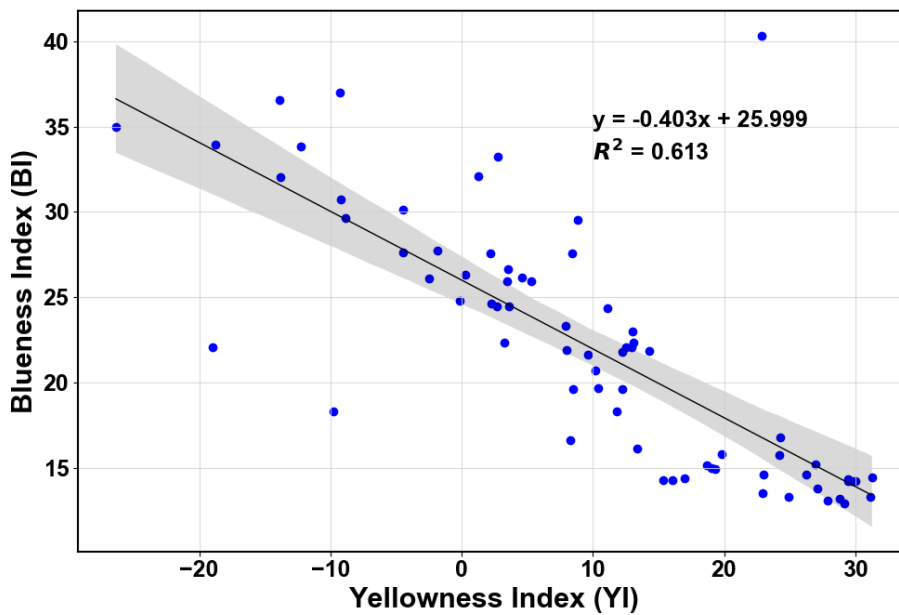


Fig. 5.6: Correlation of the computed blueness index with the measured *YI* at different points of solar cells from the three selected modules. (Number of sample points = 70). The grey band indicates the 95% confidence interval of the slope.

## 5.2.2. Tool Validation based on Quantum Efficiency Measurements

In order to understand the impact of the discoloration severity on the current generation in the solar cells, the external quantum efficiency (*EQE*) was measured at different points along the centerline of some of the discolored cells (belonging to the three selected modules shown in Fig. 5.1). The *EQE* at different points was measured using Module QE machine at Arizona State University Photovoltaics Reliability Laboratory (make: PV Measurements, model: QEX12M). The analysis of the data is presented in the following sub-sections.

External quantum efficiency measurements were performed on the solar cells embedded in the modules, by cutting through the backsheet and accessing the cell interconnect ribbons. The *EQE* measurements were performed at 13 different spots along the centre-line of the solar cells. The solar cells have been designated as M1 (belonging to Module 1, which has least discoloration of the three samples), M2 (belonging to module 2, which has medium discoloration), and M3 (belonging to module 3, which has highest discoloration of the three modules).

Some important features of the *EQE* plots are discussed below. In *EQE* curve of cell M1 (refer Fig. 5.7), which has lowest discoloration compared to other 2 cells discussed here, we can observe that the high wavelength range (above 800 nm) is unaffected by the browning of the encapsulant. The decrease in *EQE* due to discoloration is significant only in 400 to 600 nm wavelength range. The *EQE* decreases towards the center of the cell, which is evident in the local short-circuit current density (computed from the *EQE* curves) plotted in Fig. 5.8. The sharp drop in short circuit current density at the center point is due to the presence of additional metallization at the center of the cell.

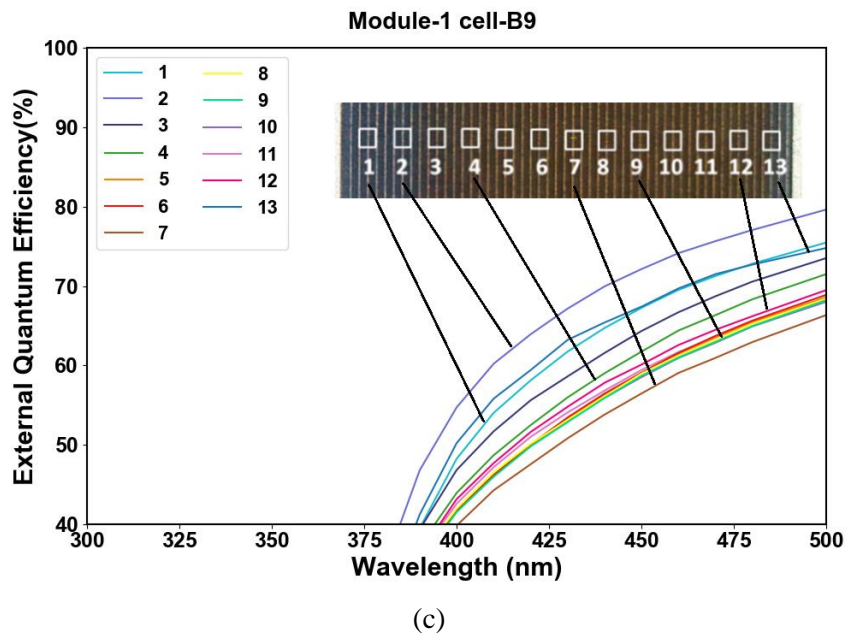
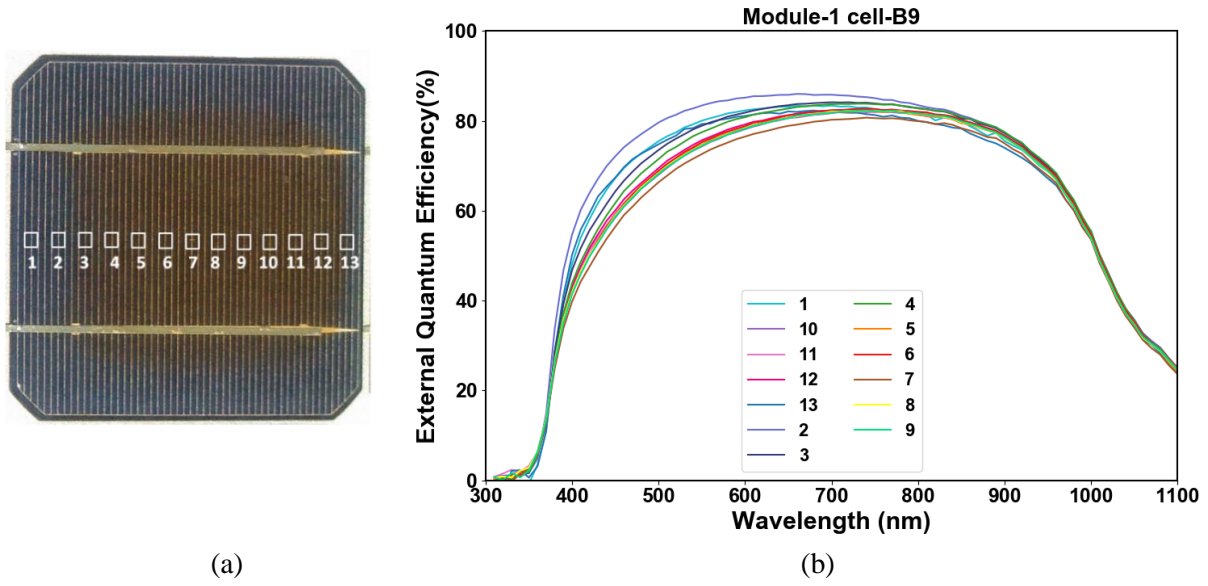


Fig. 5.7: (a) Image of cell M1, (b) *EQE* curves at 13 points along centerline of cell M1, and (c) *EQE* curves for 300 – 500 nm wavelength range. The *EQE* between 400 - 700 nm is lower for points having discolored EVA.

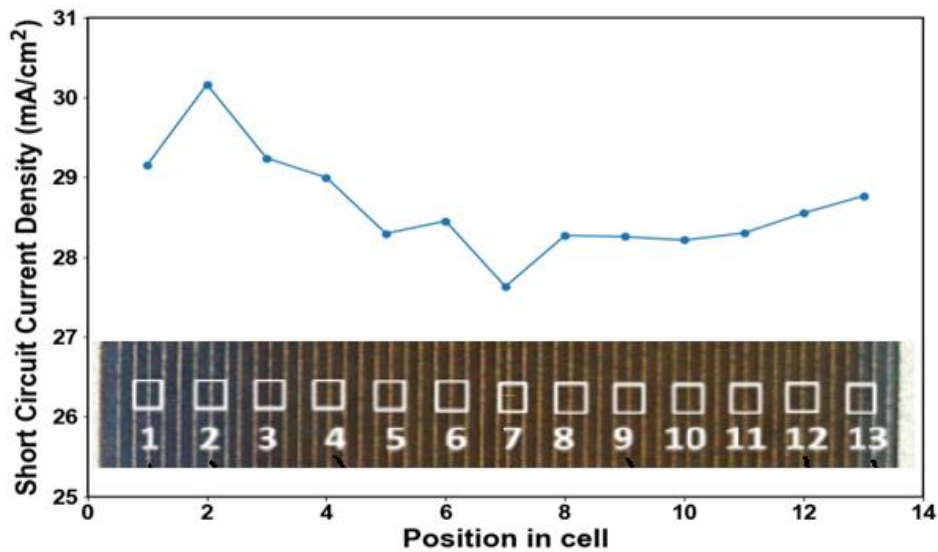


Fig. 5.8: Local short circuit current density (computed from *EQE* data) at 13 points along the centerline of cell M1. The short-circuit current density is about 4% lower in the discolored region than the un-discolored edge.

In *EQE* curve of cell M2 (refer Fig. 5.9 and 5.10), it can be seen that in the UVA range (300 – 400 nm), the spectral response at points 1, 12 & 13 (which lie in the blue photo-bleached region) is low as compared to the discolored areas. This hints at the presence of UV absorbing materials (UV stabilizers) in the photo-bleached region (which prevent the UV light from reaching the solar cell). On the other hand, in the discolored region towards the center of the solar cell, the response in the UVA range is higher, indicating that the UV stabilizers have been de-activated/ depleted. This feature is also present in cell M3 (though the browning is present at the edges also, which has depleted some of the UV stabilizers leading to slight increase in the UV response, but not to the extent seen in the discolored central areas). The local short-circuit current density ( $J_{sc}$ ) for different points of cell M2 is shown in Fig. 5.11. The sharp dip in  $J_{sc}$  in the center of the cell may be (at least partly) due to excess metallization at the center (evident in the visual image). Overall, there is close to 5% reduction in the  $J_{sc}$  due to the discoloration.

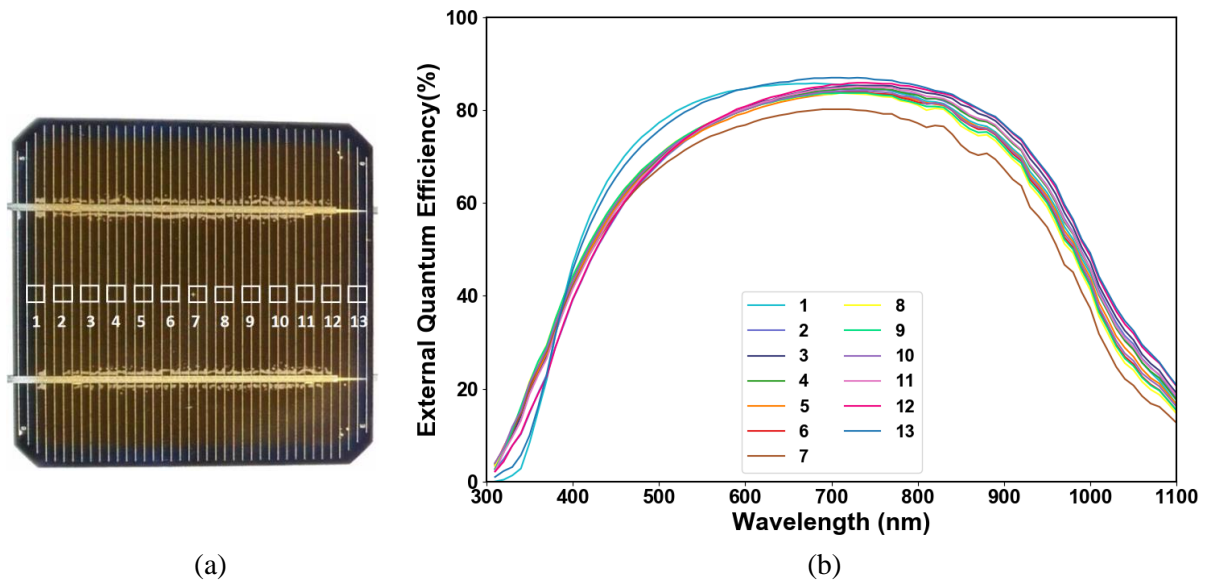


Fig. 5.9: (a) Image of cell M2, and (b) *EQE* curves at 13 points along the centerline of cell M2.

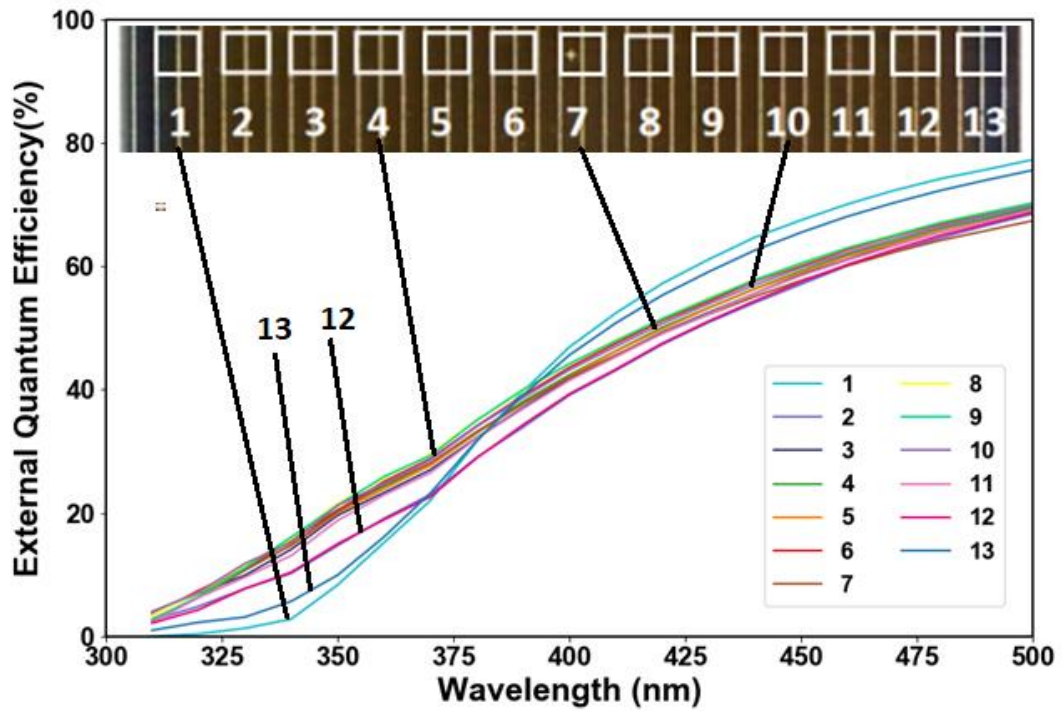


Fig. 5.10: External quantum efficiency curves in the 300 – 450 nm wavelength range, for the 13 points on cell M2. The discolored region (point 4) has higher *EQE* than the un-discolored edges (point 1 & 13) in the UV region (300-400 nm), since the UV-absorbers in the EVA has been depleted in the discolored region.

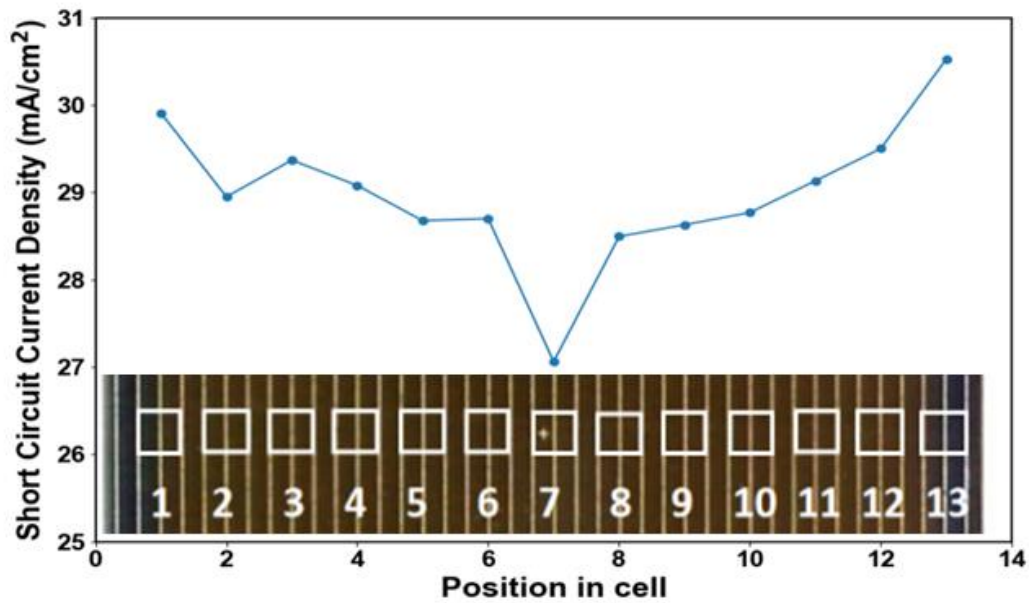
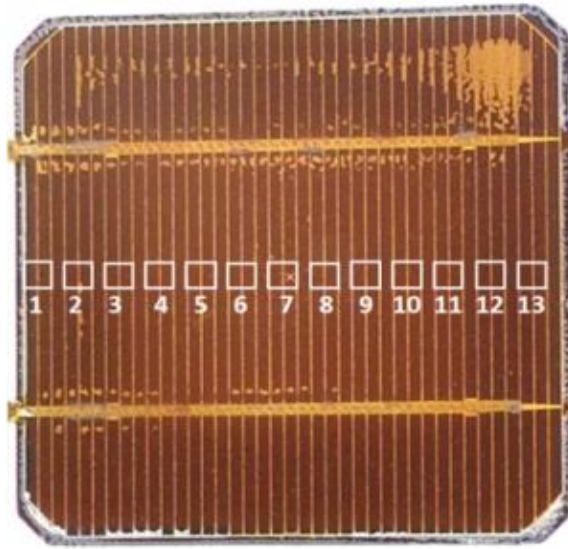
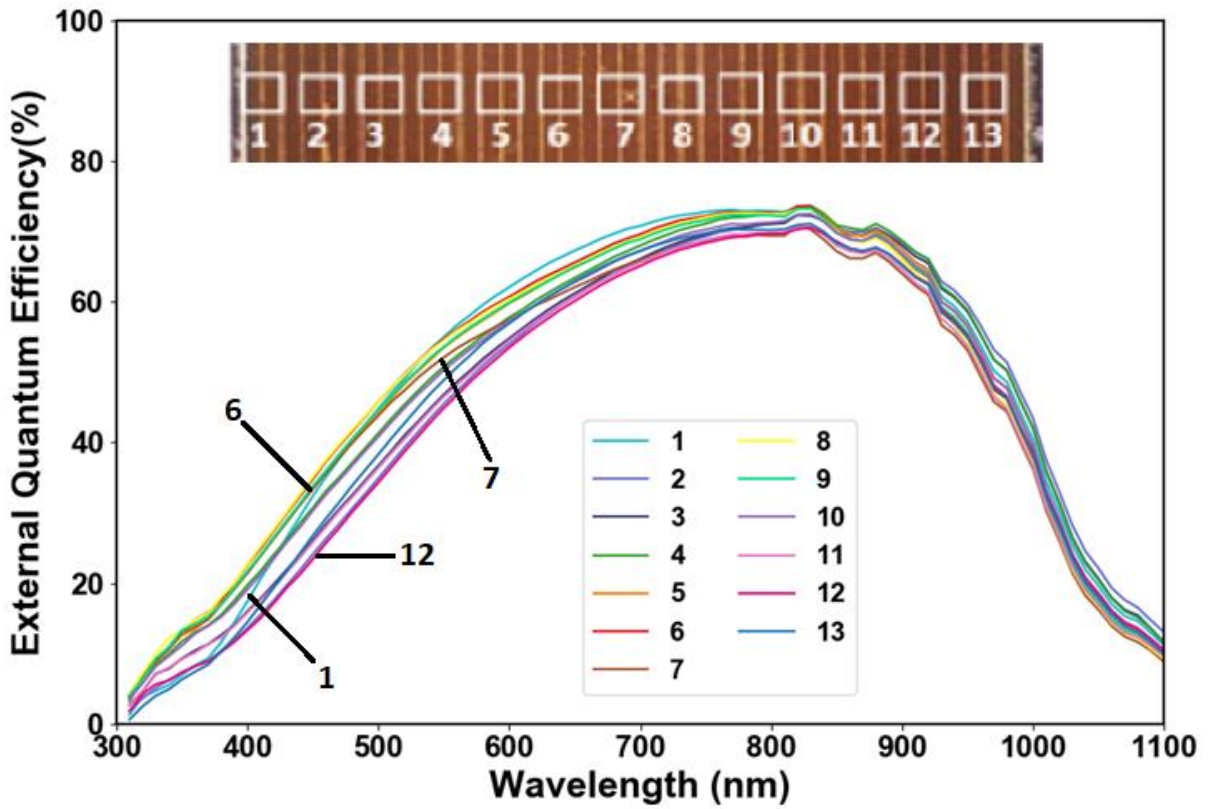


Fig. 5.11: Local short circuit current density (calculated from *EQE* data) at 13 points along the centerline of cell M2. The dip in the center is because of the excess metallization at the center. There is about 7% drop in the current density due to discoloration.

The short-circuit current density (calculated from the *EQE* curves, based on AM1.5G spectrum) for cells M1 and M2 decreases from the edges towards the center of the cell, which is in tune with the extent of discoloration. However, in case of cell M3 (refer Fig. 5.12 and Fig. 5.13), the quantum efficiency is higher in the central region as compared to the region close to the cell edge. This, in fact, is also the discoloration pattern observed in this solar cell (with a dark brown ring around a lighter brown region of the solar cell). Such a discoloration pattern is sometimes seen in field surveys, and this *EQE* measurement proves that the lesser discoloration at the center is not a visual artifact.



(a)



(b)

Fig. 5.12: (a) Image of cell M3, and (b) *EQE* curves at 13 points along the centerline of cell M3. In this cell, the discoloration at the center of the cell (point 7) is lower than at points closer to the edges (point 12) as evident from the lower *EQE* at point 12 as compared to point 7.

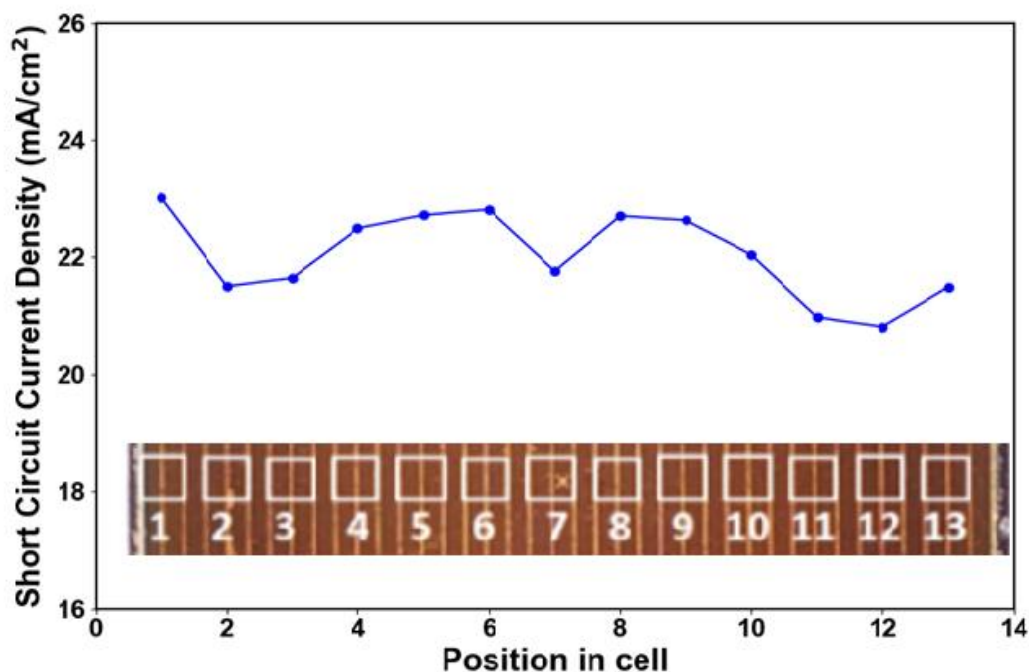


Fig. 5.13: Local short circuit current density (calculated from *EQE* data) at 13 points along the centerline of cell M3. The sharp dip at the center is due to excess metallization (please refer to the visual image). The discoloration is higher close to edge (point 2) than near the center of the cell (point 6).

In some of the cells of the three panels considered for the *EQE* measurements, delamination was observed in addition to discoloration. *EQE* measurements at different areas of a discolored and delaminated solar cell (refer Fig. 5.14) shows that the reduction in *EQE* due to delamination is much more uniform across the wavelengths, as compared to that due to encapsulant browning (which reduces the blue response from the solar cell much more severely than the red response). The distortion in the *EQE* is because of the higher absorption of the blue light by the chromophores generated in discolored EVA encapsulant (please refer to Fig. 8.22 for absorption plot of discolored EVA). Table 5.3 shows the local short circuit current density (computed from the *EQE* data) for cell areas with discoloration and delamination. The loss in short circuit current density with respect to the blue edge (free from discoloration and delamination) is also given in this table. The percentage loss in  $J_{sc}$  due to delamination is comparable to that of brown discoloration (about 25% loss), but a section with dark brown discoloration showed even higher loss (ca. 34%). Since delamination is found to be highly non-uniformly distributed in the solar panels and seldom occurs on all cells of the PV modules, it is not expected to impact the module's short-circuit current but only the fill factor (due to cell-to-cell mismatch).

Table 5.3: Reduction in short-circuit current density due to discoloration and delamination.

Characteristics	$J_{sc}$ calculated from QE (mA/cm <sup>2</sup> )	% Loss in $J_{sc}$
Area without discoloration or delamination (blue edge)	26.7	Reference Value
Area with delamination (blue delam)	19.8	25.6
Area with discoloration (brown centre)	20.4	23.7
Area with discoloration (brown edge)	17.5	34.3
Area having both discoloration and delamination (brown delam)	13.2	50.7

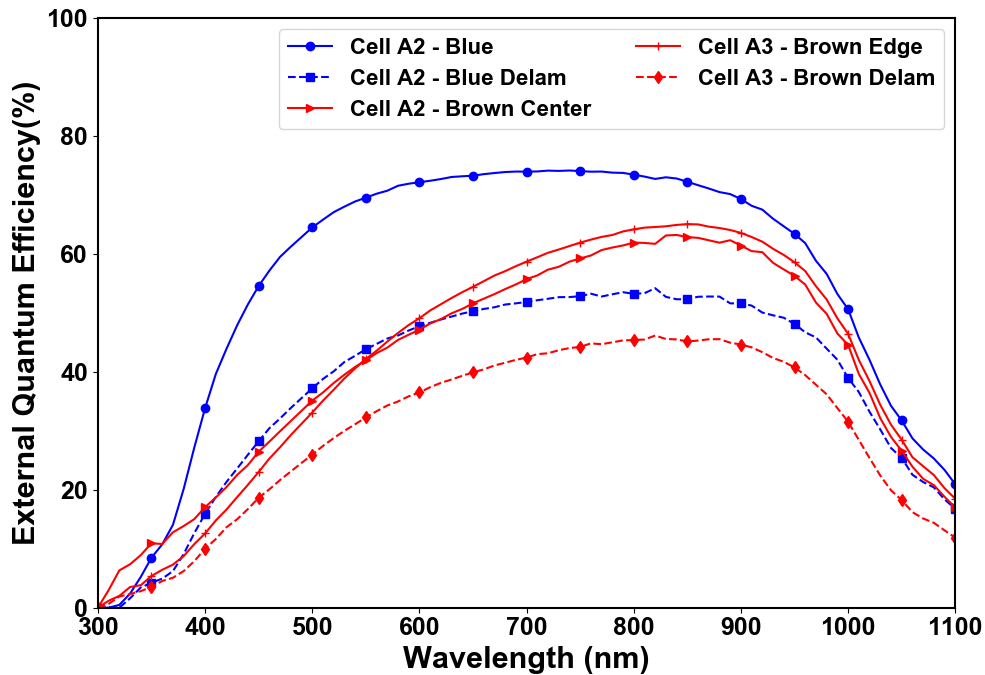


Fig. 5.14: External quantum efficiency plot for different points on a discolored and delaminated solar cell of module M3.

Based on the  $PYI$  values computed for different points on the solar cells, it is possible to calculate the  $DI$  using Eq. 5.9. For this calculation, the value of the denominator is considered equal to maximum possible  $PYI$  minus initial  $PYI$ . The initial  $PYI$  value ( $PYI_{initial}$ ) is assumed equal to the present  $PYI$  value at the edges of the cell (where photo-bleaching action has nullified the discoloration effect). The maximum possible  $PYI$  value seen in any solar cell in

this study is ca. 30, so it is considered as the upper limit in this calculation to determine the maximum *PYI* range. The *EQE* curves for different points of cell M1 has been shown in Fig. 5.15, which indicates that spectral response for wavelengths between 400 – 700 nm are affected due to discoloration. The *EQE* at 500 nm and 600 nm wavelengths have been plotted against the *DI* in Fig. 5.16, which shows a linear correlation.

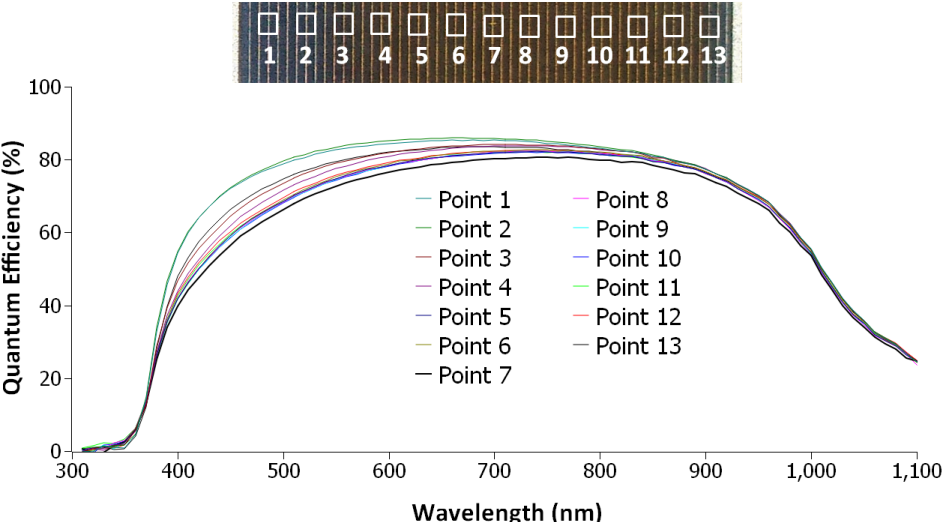


Fig. 5.15: External quantum efficiency at different points along the centerline of the solar cell M1 (locations indicated at top of figure).

The localized short-circuit current density loss (computed from the *EQE* data) is plotted against the *DI* in Fig. 5.17 and shows good correlation. This indicates that it is possible to estimate the loss in short-circuit current density (current generation) based on the discoloration index.



In this section, the relation between quantum efficiency and discoloration has been presented based on measurements on discolored panels. Discoloration reduces the blue response of the cell much more than the response to red light, whereas delamination is found to reduce both the blue and red response almost equally. A linear relation is observed between  $DI$  and the loss in short circuit current density. In the next section, the correlations of  $DI$  and electrical degradation of field-aged modules (inspected in All-India surveys) is discussed.

## **5.3 Survey Statistics and Correlations for Discoloration Severity**

### **5.3.1 Methodology for Survey Data Analysis**

During the field surveys, the digital images of the PV modules have been taken using a digital camera (make: Nikon, model: D3200), under natural sunlight (at irradiance greater than  $700 \text{ W/m}^2$ ) on clear sunny day. The procedure followed for computation of the discoloration index of a PV module is as follows.

1. The digital photo of the module of interest is captured such that the whole module fits in the frame, and at an angle as close to  $90^\circ$  (with reference to the plane of the module) as possible (refer Fig. 5.18a). Images captured at slanting angles (less than  $45^\circ$ ) are not considered for analysis.
2. The raw image (NEF format in Nikon camera) is converted into TIFF format (a lossless image format) to enable manipulation of the image.
3. The region of interest is extracted from the visual image, and perspective transformation is performed to restore the rectangular shape of the PV module (refer Fig. 5.18b).
4. Image of a cell is extracted from the module's image (from the center of the module) in order to determine the threshold value of  $PYI$ . The threshold value is the  $PYI$  value above which the cell section (pixel) is considered discolored, and hence all pixels below this threshold shall be considered as "not discolored" (refer Fig. 5.18c).

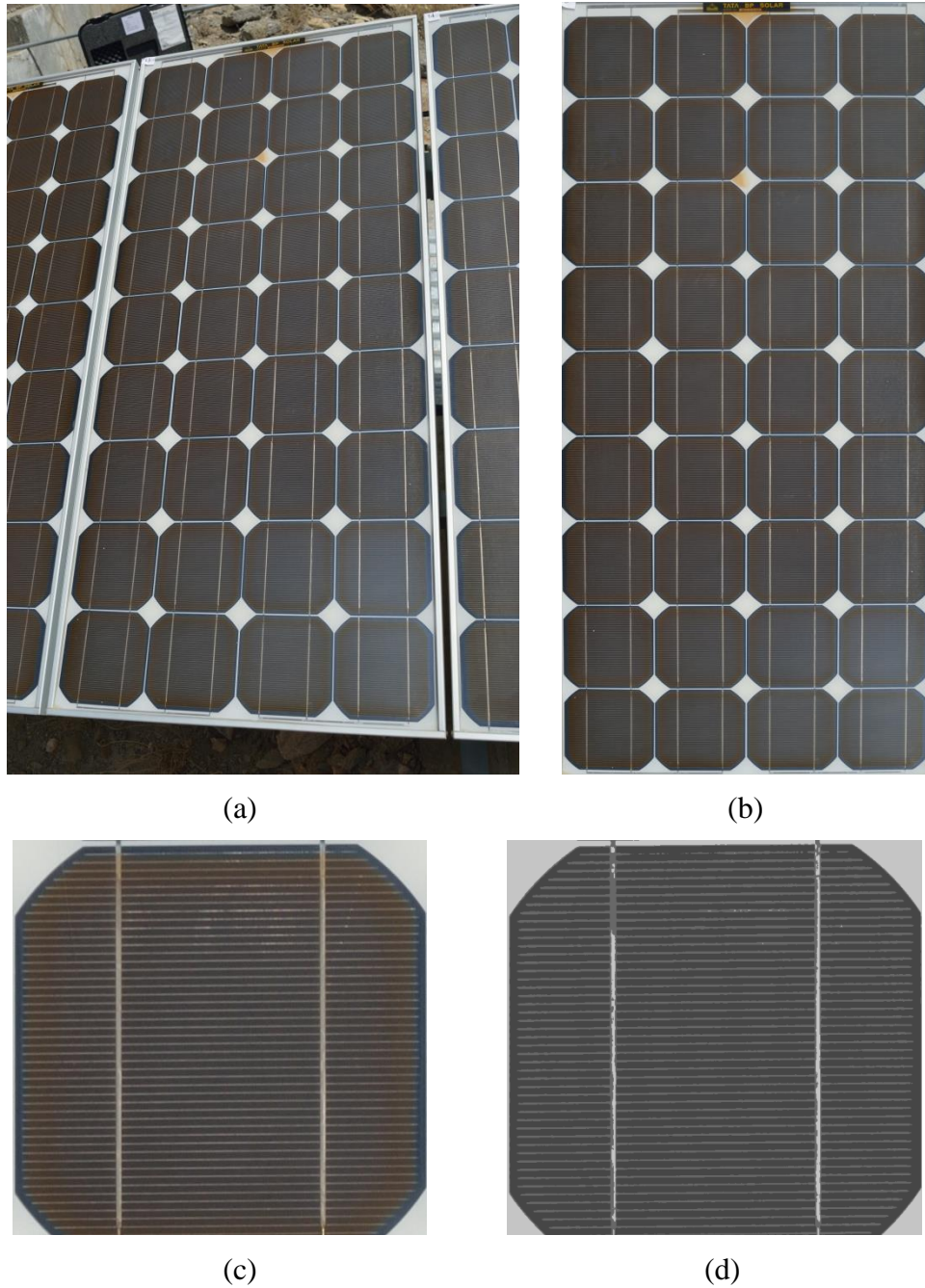


Fig. 5.18: (a) Image of a discolored solar panel, (b) perspective corrected image, (c) image of a cell extracted from panel image, and (d) K-means clustered image of the cell (K=3).

5. K-Means clustering technique [111] is used to segregate the cell's image into three different zones – (i) silicon area, (ii) metallization area, and (iii) backsheets area. So, K=3 is used for clustering (refer Fig. 5.18d).

6. The  $PYI$  of all pixels in the silicon area of the cell's image is computed using equations 5.3 through 5.7 [110] and then eqn. 5.10, based on 10° Observer, D65 Illuminant, and ASTM E313 standard specifications [63].

$$PYI = A \cdot 100 \cdot \left( \frac{1.3013 \cdot X - 1.1498 \cdot Z}{Y} \right) - B \quad \text{if } Y \neq 0$$

$$= 0 \quad \text{if } Y = 0 \quad \dots (5.10)$$

where,  $A = 0.25$  and  $B = 9.3793$  are correlation parameters selected based on measurements on discolored modules (discussed in section 5.2).

7. The median value of the  $PYI$  along the edges of the cell (within 5% area from the edge) is considered as the threshold value for blue (un-discolored) region of the cell ( $PYI_{threshold}$ ).

8. Steps 5 to 7 are repeated on the module's image and then the  $DI$  is calculated as follows.

$$PYI_{avg} = \frac{1}{n} \cdot \sum_{i=1}^n PYI_i \quad \text{if total numbers of pixels in the image } (n) > 0 \quad \dots (5.11)$$

$$PYI_{blue} = \frac{1}{m} \cdot \sum_{i=1}^m PYI_i \quad \text{if } PYI \text{ at pixel 'i' } (PYI_i) \leq PYI_{threshold} \quad \dots (5.12)$$

$$DI = \frac{PYI_{avg} - PYI_{blue}}{30 - PYI_{blue}} \quad \dots (5.13)$$

Where,  $n$  = total number of pixels

$m$  = total number of pixels with  $PYI \leq PYI_{threshold}$  (i.e., total number of "blue" pixels)

Some examples of the  $DI$  for some sample cell images are shown in Fig. 5.19, which proves that this technique is able to differentiate between various levels of discoloration in solar cells.

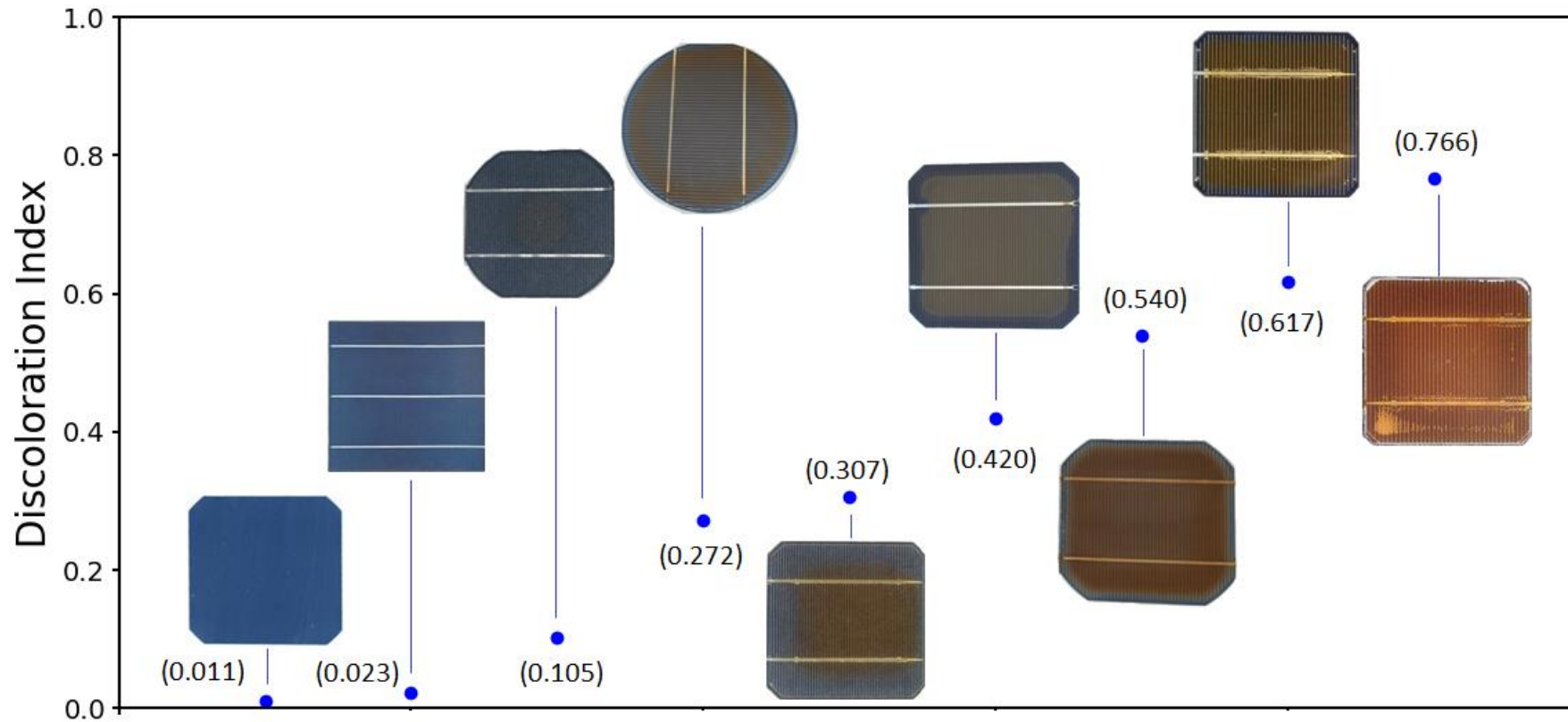


Fig. 5.19: Solar cells with different extent of discoloration, and corresponding values of  $DI$  (based on  $PYI$  computed from digital image).  $DI$  is increasing with the extent of discoloration in the cells.

### 5.3.2 Survey Statistics

Discoloration index has been computed for the crystalline silicon modules inspected in the All-India Survey in 2016, based on the methodology discussed in section 5.3.1. As discussed in Chapter 4, the surveyed modules have been grouped into two categories based on the average power degradation rate at the site – Group X (average degradation rate less than 2%/year) and Group Y (average degradation rate greater than 2%/year). To understand the influence of climatic zone on the discoloration severity, we have analyzed the Group X panels, since the Group Y panels are suspected to have been impacted by extraneous factors like manufacturing and material quality related issues which caused high degradation rates. The average discoloration severity for Group X modules in different age groups and climatic zones is given in Table 5.5. The software cannot be used for c-Si modules having very distinct grain boundaries (where multiple shades of blue are present on the solar cells), and hence the total number of samples for Table 5.5 is restricted to 225 (out of the total 467 crystalline silicon modules inspected in 2016 survey). The average *DI* has been colour coded (for ease of interpretation) based on the severity, with green indicating lowest severity and red the highest severity (as given in Table 5.4). The average severity of discoloration in the young modules seems to be higher in the hot climates (Hot & Dry, Warm & Humid and Composite) as compared to the Moderate zone. Also, for modules in “5-10 years” category, the average severity is highest in Hot & Dry zone followed by Warm & Humid and Composite zones. The highest average discoloration is seen in modules aged more than 10 years, is almost similar in both Warm & Humid (WH) and Cold & Sunny (CS) climatic zones. It may be noted here that the modules from the CS climate are actually installed at a higher altitude (in Ladakh), where the annual temperatures are lower but the incident UV radiation is much higher (which can lead to higher discoloration). Similar high discoloration has also been reported in a separate study of 28-year-old crystalline silicon panels installed in Cold & Cloudy climate in Himachal Pradesh, with a consequent short-circuit current reduction in the range of 20% - 30% [40]. Table 5.6 shows that Group X modules have comparatively higher discoloration severity than group Y modules (particularly in Hot zone), which implies that discoloration of the encapsulant is not a significant contributing factor to the high degradation rates observed in Group Y modules. As an example, a site in Hot zone has shown brown discoloration within 10 years of installation,

but the average power degradation rate is close to 1%/year (so the site falls in Group X category).

Table 5.4: Discoloration severity colour-coding.

Discoloration Index	0 – 0.05	0.05 – 0.1	0.1 – 0.25	0.25 – 0.5	>0.5
Category Colour Code	Nil	Low	Medium	High	Very High

Table 5.5: Average severity of discoloration in Group X modules in different climatic zones and age groups (based on 2016 survey data). Severity is higher in the hotter climates for all age groups.

Climatic Zone	Age Group			
	0 - 5 yrs old	5 - 10 yrs old	10 - 20 yrs old	20+ yrs old
Hot & Dry	NA (0)	0.145 (40)	NA (0)	NA (0)
Warm & Humid	0.061 (47)	0.088 (37)	0.364 (4)	NA (0)
Composite	0.038 (27)	0.040 (4)	NA (0)	NA (0)
Moderate	0.023 (20)	NA (0)	NA (0)	NA (0)
Cold & Sunny	NA (0)	NA (0)	0.345 (46)	NA (0)
Cold & Cloudy	NA (0)	NA (0)	NA (0)	NA (0)

NOTE: The severity values are computed through image processing software and modules with multi crystalline silicon cells having high contrast between grains are excluded.

Table 5.6: Average severity of discoloration in Group X and Group Y modules in Hot and Non-Hot zones (based on 2016 survey data).

Climatic Zone	Group	Age Group			
		0 - 5 yrs old	5 - 10 yrs old	10 - 20 yrs old	20+ yrs old
Hot Zone	X	0.053 (74)	0.114 (81)	0.364 (4)	NA (0)
	Y	0.032 (184)	NA (0)	0.131 (30)	NA (0)
Non-Hot Zone	X	0.035 (65)	NA (0)	0.345 (46)	NA (0)
	Y	0.051 (50)	NA (0)	NA (0)	NA (0)

Table 5.7 shows the average *DI* for modules in Group A (group of all inspected modules), categorized based on the size of installation. In the young age category, large installations show average severity almost similar to small installations. In modules aged “5-10 years”, higher

severity is observed in large installations as compared to small installations. This indicates that the material quality is being compromised even in some of the large power plants which is not unexpected given the rapid fall in the solar panel price over the past decade.

Table 5.7: Average extent of discoloration in Group A modules for small and large installations in the Hot and Non-hot climatic zones (based on 2016 survey data).

Size of Installation	Age Group			
	0-5 Years	5-10 Years	10-20 Years	20+ Years
Small/ Medium	0.039 (313)	0.071 (42)	0.257 (88)	NA (0)
Large	0.034 (83)	0.157 (40)	NA (0)	NA (0)

Based on the above discussion, it is clear that Hot climatic zone is more severe than the Non-Hot zone. The severity of the climatic zones appears to be in the following order: Hot & Dry > Warm & Humid > Composite > Moderate. Some of the young sites (age less than 5 years) are showing initial signs of discoloration, particularly in the Hot zone, which calls for improvement in the quality of the encapsulant used by these module manufacturers.

### 5.3.3 Correlations with Electrical Degradation

The electrical performance of the PV modules inspected during the All-India surveys, was measured using a portable *I-V* tracer under field conditions (irradiance and module temperature different from the standard test conditions). So, it is necessary to convert the measured *I-V* curves to STC conditions, in order to compare the performance with the initial (Nameplate) data. The equations used for this translation to STC condition are discussed briefly in the next sub-section, followed by the correlation of the encapsulant discoloration with the electrical degradation.

### a) Determination of Electrical Performance

The power output from a PV module depends on various electrical parameters like short-circuit current ( $I_{sc}$ ), open-circuit voltage ( $V_{oc}$ ), and fill factor ( $FF$ ). These electrical parameters are reported in the PV module nameplate under standard test conditions (STC) of 1000 W/m<sup>2</sup> and 25 °C module temperature. The degradation in these parameters serves as an indication of the nature and magnitude of defects generated within the module. Knowledge of this degradation can be helpful for determining remedial steps to boost the power plant power generation and also for the improvement of the PV module design for better durability of future products. Since the electrical measurements are done in the field under different set of irradiance and temperatures (different from STC), it is necessary to translate these measurements to the STC conditions (in order to compare with the initial/ nameplate data). The following equations are used for these translations [20]:

$$I_2 = I_1 + I_{SC} * \left( \frac{G_2}{G_1} - 1 \right) + a * (T_2 - T_1) \quad \dots (5.14)$$

$$V_2 = V_1 + \beta * (T_2 - T_1) \quad \dots (5.15)$$

where,

$I_2$  = Translated current, A

$I_1$  = Measured current, A

$I_{SC}$  = Measured short-circuit current, A

$G_2$  = Translated plane-of-array irradiance (= 1000 W/m<sup>2</sup>)

$G_1$  = Measured plane-of-array irradiance, W/m<sup>2</sup>

$T_1$  = Measured temperature of PV module, K

$T_2$  = Translated temperature of PV module (= 298 K)

$a$  = Temperature coefficient of current, A/K

$\beta$  = Temperature coefficient for voltage, V/K

$V_2$  = Translated voltage, V

$V_1$  = Measured voltage, V

The above equations are derived from the IEC translation procedure 1 [112], by setting the curve correction factor (K) and the series resistance (Rs) equal to zero.

During the survey, we have taken *I-V* of the modules using Solmetric *I-V* tracer (model: PVA-1000S). All *I-Vs* were taken at irradiance greater than 700 W/m<sup>2</sup> and then translated to Standard Test Condition. The error due to this translation has been estimated to be within ±5%, with an additional uncertainty in the degradation calculations of 2.5% (maximum) due to the tolerance in nameplate values [20, 21]. For the calculation of the electrical degradation, in the absence of the initial *I-V* data, the nominal ratings, obtained by averaging the nameplate values with maximum and minimum tolerance, have been considered (as explained in detail in [21]). The error in power degradation due to this name plate uncertainty is within 2.5%. Degradation is calculated as per the following equation [21]:

$$\text{Degradation of } Y \text{ (\%)} = \frac{(Y_{Nom} - Y_P) \cdot 100}{Y_{Nom}} \quad \dots (5.16)$$

where, *Y* can be power, short-circuit current, open-circuit voltage or fill factor.

$$Y_{Nom} = \text{Nominal rating} = Y_{NP} \cdot \left(1 + \frac{Tol^- + Tol^+}{2 \cdot 100}\right) \quad \dots (5.17)$$

$Y_{NP}$  = Name Plate rating

$Tol^-$  = Negative tolerance, % \*

$Tol^+$  = Positive tolerance, % \*

$Y_P$  = Present value of *Y* (translated to STC)

\*Nameplate tolerance values are used for the power output, while one-third of the tolerance values are used for short-circuit current, open-circuit voltage, and fill factor.

Detailed analysis of the degradation rates of inspected PV modules in different climatic conditions is part of the concurrent work of Rajiv Dubey [106].

## **b) Correlation of Discoloration Index with Electrical Degradation**

The primary effect of encapsulant discoloration is the reduction in the transmission of light to the underlying solar cells, which causes a reduction in the short-circuit current and the

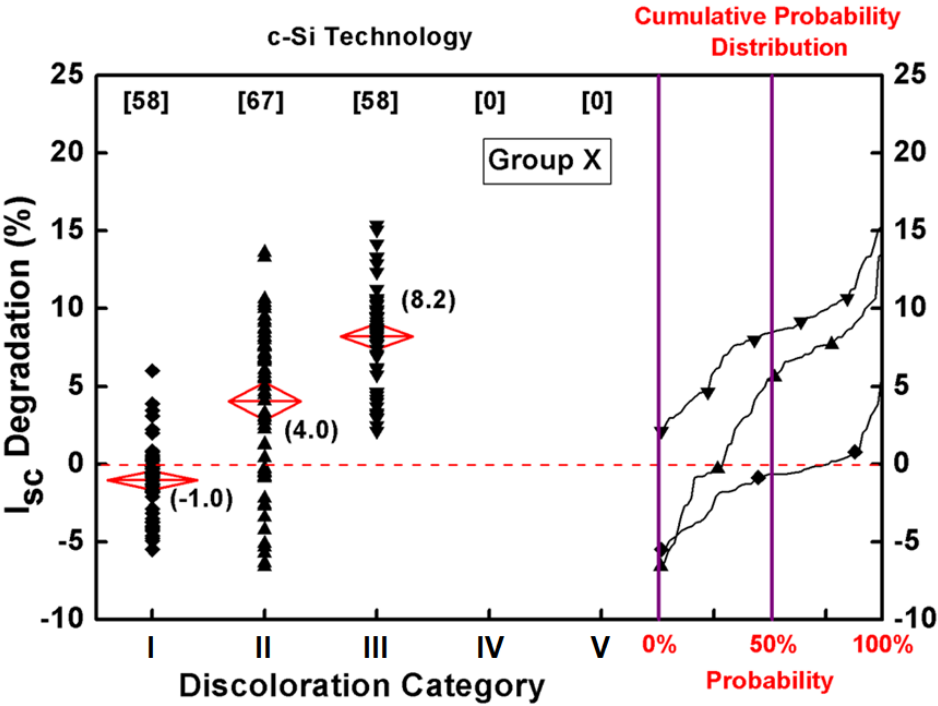
power output. In order to check the effect of discoloration on these electrical parameters, the PV modules have been segregated into five categories based on *DI*, as per Table 5.8.

Table 5.8: Categorization based on discoloration index

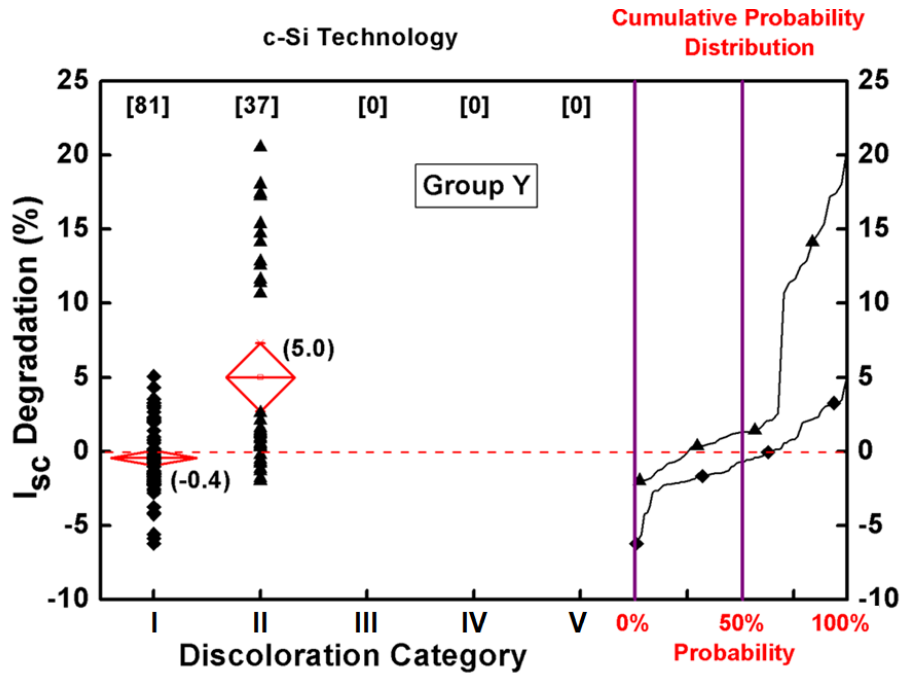
<b>Discoloration Index</b>	0 – 0.05	0.05 – 0.25	0.25 – 0.5	0.5 – 0.75	0.75 – 1
<b>Discoloration Category</b>	I	II	III	IV	V

Figure 5.20 shows the effect of encapsulant discoloration on short-circuit current degradation, for modules from both Group X and Group Y sites (based on 2016 survey data). The modules with snail tracks and other visible signs of cracks have been removed from the dataset for this comparison, since the cracks may influence the short circuit current loss. In these plots, the average degradation values are indicated using the red horizontal lines (and the top and bottom edges of the red diamond indicate the 95% confidence interval of the average value). The cumulative probability distribution is also shown on the right side of the scatter plot, from which the median degradation value can be easily determined. It may be noted that there are no Group X modules in discoloration categories IV and V, and no Group Y modules in discoloration categories III to V. From this plot, we can see that the average  $I_{sc}$  degradation follows an increasing trend with the discoloration category. The difference between the different categories has been found to be statistically significant in Student’s t-test (probability of null hypothesis being true is less than 0.05). In many cases, mostly in the young modules, the  $I_{sc}$  degradation has been found to be negative (which may be due to the uncertainty in the nameplate data and also the uncertainty introduced by STC translation procedures). It is interesting to note that the worst browning in the modules in Group X has caused close to 15% drop in  $I_{sc}$  (in 18 years of field exposure, which indicates a linear degradation rate of ca. 0.83 %/year). Similarly, a separate study of a 28-year-old PV system showed that the discolored panels had average  $I_{sc}$  reduction of 27.7% (indicating a linear degradation rate of ca. 1 %/year) [40]. For Group X modules, the average degradation values follow an almost linear trend. Considering category II as “light discoloration”, and category III as “dark discoloration”, it can be seen that the average  $I_{sc}$  degradation for dark discoloration is approximately twice that of the value for light discoloration. The maximum  $I_{sc}$  degradation in Group Y is higher than Group X (comparing discoloration category II).

Figure 5.21 shows the plot of total electrical degradation (%) against the discoloration categories. Increasing trends are seen for  $V_{oc}$  and  $P_{max}$  degradation, with increase in discoloration category. The differences between the different groups are found to be statistically significant (p-values of two-sample t-test are less than 0.05). In case of  $FF$  degradation, some of the young modules with negligible discoloration (category I) show high  $FF$  degradation, but there is no definite trend with increase in discoloration. It should also be noted that the modules have also suffered other modes of degradation (particularly corrosion of metallization in the old modules, which reduces the fill factor and hence the power output). The worst discolored modules have suffered about 24% degradation in power (after discounting 2% for light induced degradation) in 18 years of field exposure, so the average  $P_{max}$  Degradation Rate for these old modules is 1.2 %/year.

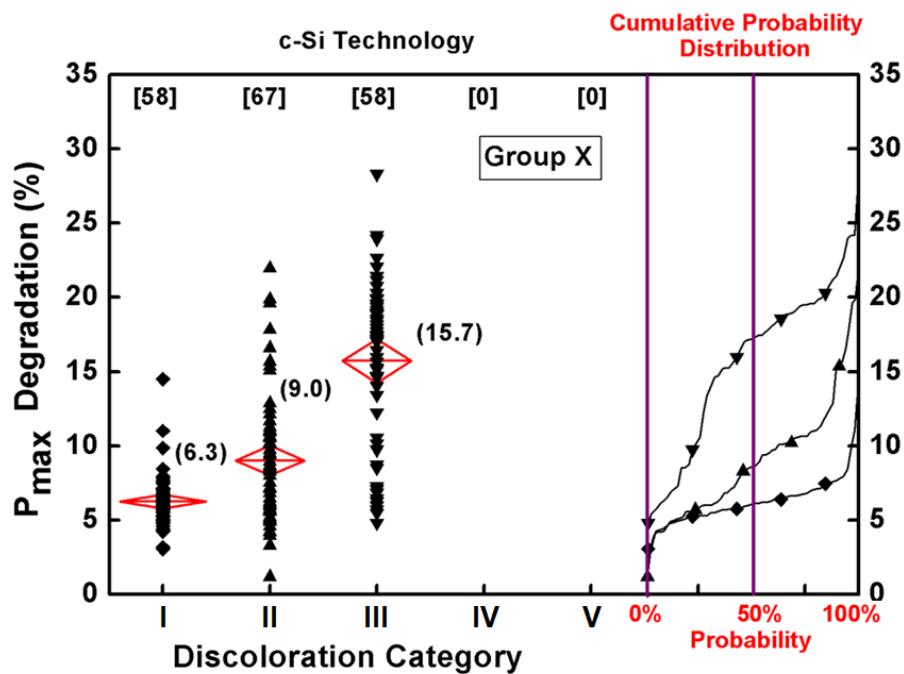


(a)



(b)

Fig. 5.20: Plot of short-circuit current degradation versus severity of discoloration for (a) Group X modules, and (b) Group Y modules. The red diamond indicates the 95% confidence interval for the average degradation (average value indicated in brackets). Total number of samples is indicated at the top of each group in square brackets. These graphs are based on the 2016 survey data.



(a)

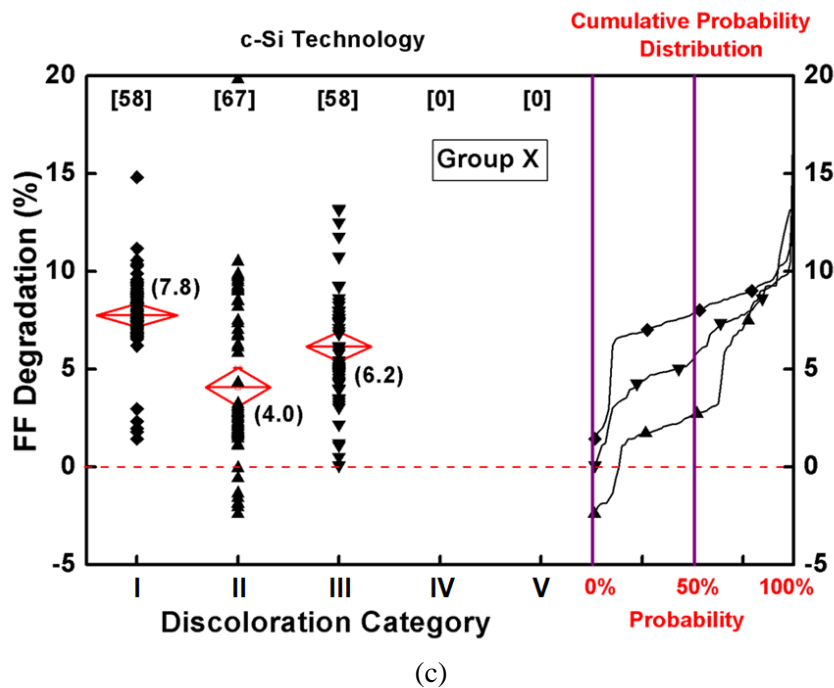
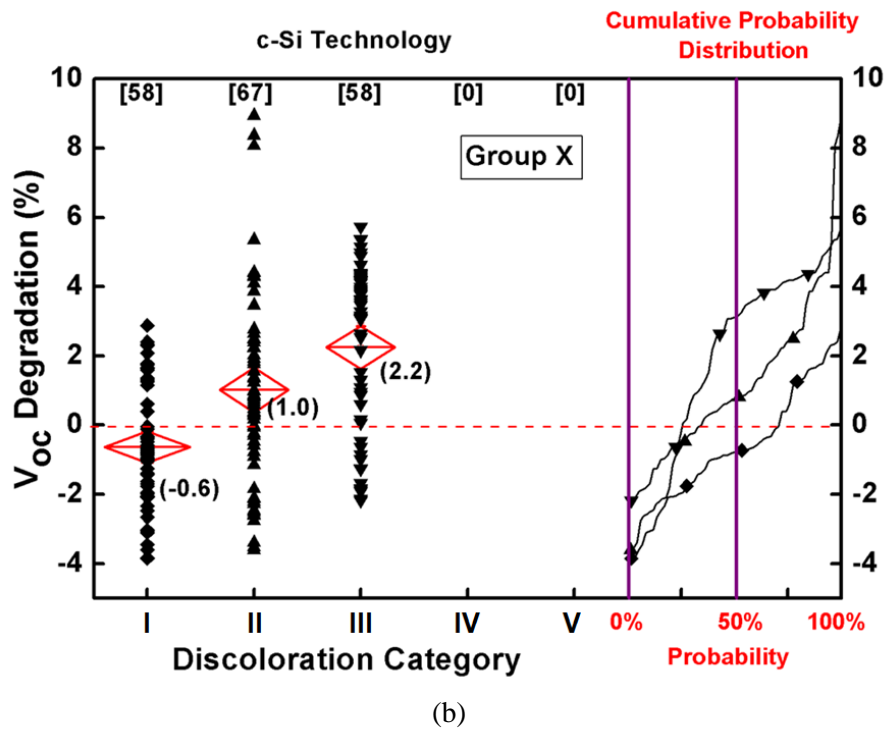


Fig. 5.21: Plot of electrical degradation versus extent of discoloration (discoloration category) for Group X modules - (a)  $P_{max}$  degradation (%), (b)  $V_{oc}$  degradation (%), and (c)  $FF$  degradation (%). The red diamond indicates the 95% confidence interval for the average degradation (average value indicated in brackets). Total number of samples is indicated at the top of each group in square brackets. These graphs are based on 2016 survey data.

## 5.4 Summary

The effect of discoloration has been studied on solar cells through quantum efficiency and yellowness index measurements. A methodology has been developed to quantify the severity of discoloration in a PV module, based on the digital image of the module. The digital image is taken in natural sunlight at irradiance greater than  $700 \text{ W/m}^2$ , and a pseudo yellowness index is calculated for every pixel on the silicon cell area (excluding the metallization and backsheet areas). Discoloration index is calculated based on the difference of the average *PYI* value of the whole cell from the average *PYI* of the un-discolored portion of the cell (5% area along the edge of the cell is considered for this calculation). The discoloration in the PV modules surveyed in the 2016 All-India PV survey has been quantified using this technique and correlated to the average electrical degradation ( $I_{sc}$ ,  $V_{oc}$  and  $P_{max}$ ) based on discoloration categories. It is important to note that in certain cases, the discoloration is only observed in a few localized cells, and in such cases, the effects on the electrical degradation can be very different. The causes for such localized defects and their effects on electrical degradation are presented in Chapter 6.

## **Chapter 6**

### **Localized Discoloration in PV Modules due to Hot Cells**

#### **6.1 Introduction**

Discoloration of the encapsulant in field-aged PV modules is usually observed in all cells of the affected modules, as shown in Fig. 6.1. However, in some cases, discoloration has been observed in the field surveys localized to a few cells of the module while the rest of the cells are unaffected. Further investigation using Infrared thermography has revealed higher cell temperatures in these solar cells, which causes faster degradation (discoloration) of the encapsulant on top of the cells. This chapter deals with the analysis of such thermal mismatch observed in the PV modules in our field surveys. IR imaging of the modules had been performed only under short-circuit condition in the 2014 survey, but in the 2016 survey, the scope was broadened to include both the short-circuited and Maximum Power Point (MPP) IR imaging. It has been generally observed that the cell temperatures are higher when the module is put under

short-circuit condition as compared to the MPP condition. The information conveyed by the two IR images may be quite different, as in MPP condition the module is delivering its maximum power to the load (all cells are in forward bias) whereas in short-circuited module, the power generated by the relatively better cells (operating in forward bias) is dissipated in the other cells having relatively poor current-voltage ( $I$ - $V$ ) characteristics (thereby operating in reverse bias). Fig. 6.2 shows the visual image and the IR image of a PV module having such localized discoloration over a few cells. Fig. 6.2 (c) shows a zoomed view of the visual image, clearly showing that there are cracks in the solar cell (highlighted with yellow dashed lines), and the discoloration has occurred more in one side of the crack as compared to the other side (sections “A”, “C” and “E” are more discolored than sections “B”, “D” and “F” as the sections “A”, “C” and “E” are still connected to the busbar and are conducting current). The part of the cracked solar cell connected to the rest of the cells appears to heat up (since it has to conduct the full current generated by the intact cells, in spite of having a smaller active area after the crack). The influence of such hot cells on the overall performance of the PV module is analyzed in the following sections. Localized discoloration in the cells serves as a visual indication of thermal mismatch (hot spots) in the cells. In this chapter, the relation between discoloration and cell temperature is discussed first, followed by the thermal model for solar panel having hot spots and its application to determine the correlation of hot cells with the electrical degradation. It should be noted that parts of this chapter have already been published in international conferences and journals [113].

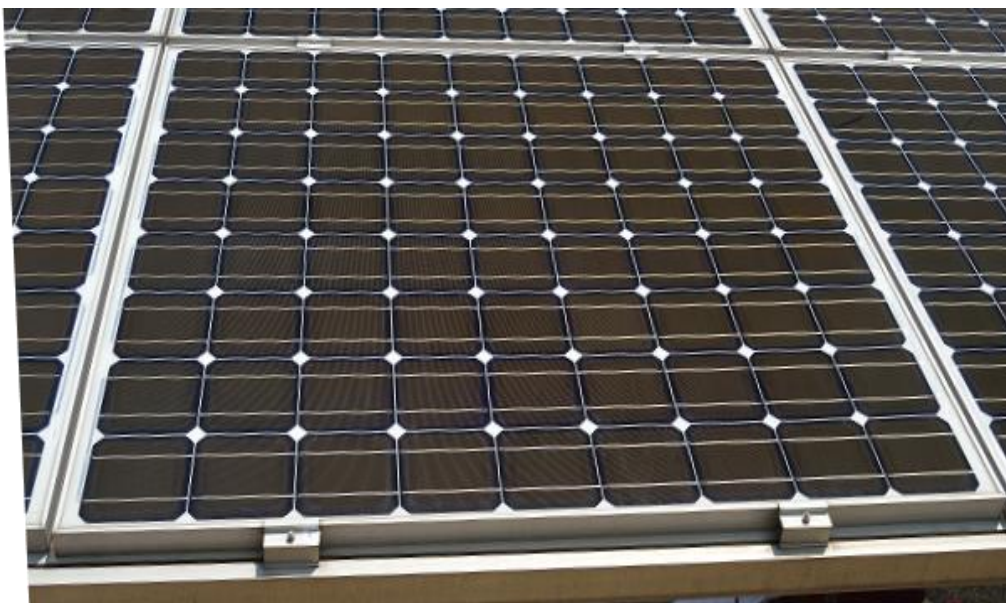


Fig. 6.1: Discoloration over all cells in a PV module.

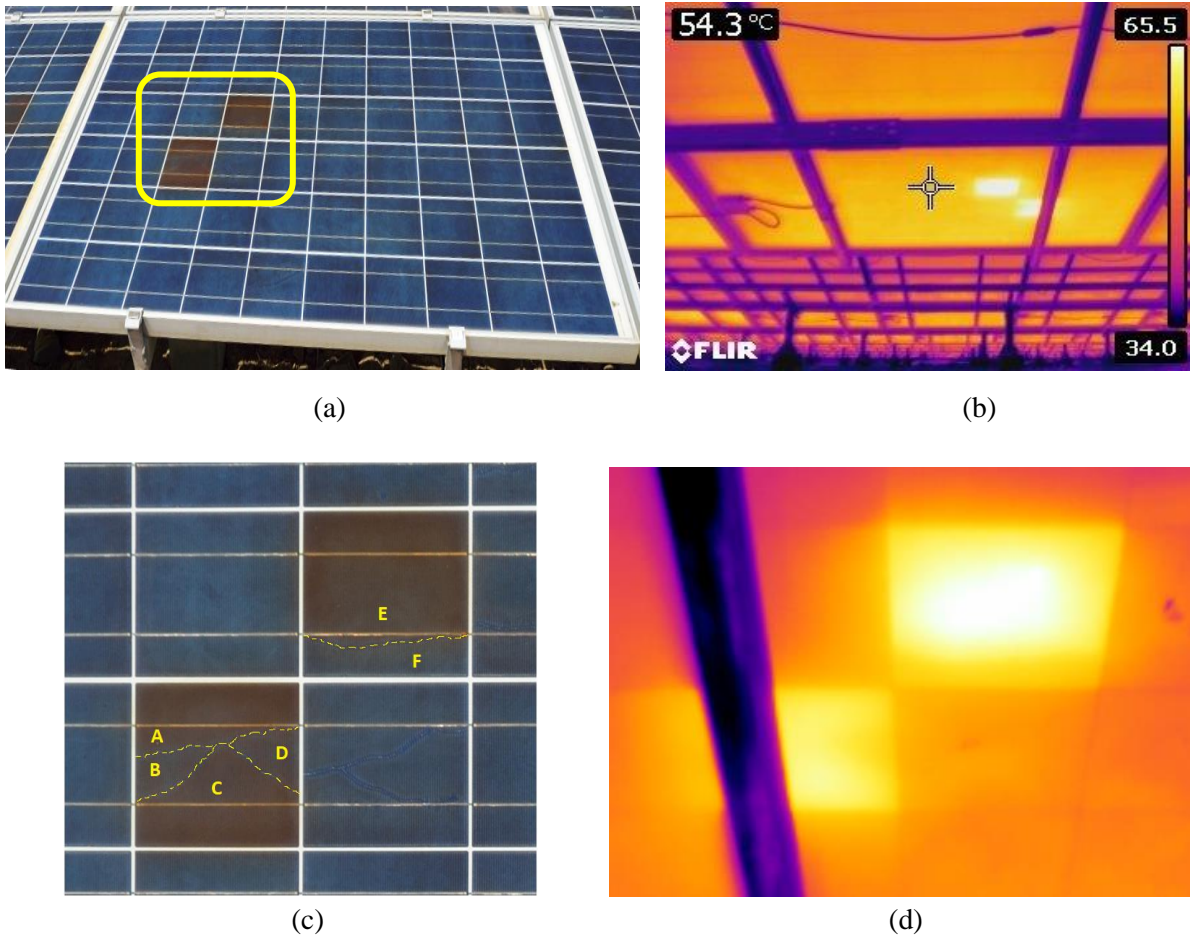


Fig. 6.2: (a) Visual image of a PV module showing localized discoloration of the encapsulant, (b) IR image of the module taken from back-side, (c) zoomed-in visual image of the affected cells (crack lines marked with yellow border), and (d) IR image of the affected area from backside (image is flipped sideways for easy comparison).

## 6.2 Relation between Cell Temperature and Discoloration

The correlation between the encapsulant discoloration and the temperature of the cell is investigated in this section. The solar panel shown in Fig. 6.2 has two cracked cells with hot spots, but there are also some cells with cracks and no hot spots. Hence, this panel provides us a good opportunity to study the impact of cell temperature and cracks on encapsulant discoloration. Figure 6.3 (a) shows one of the cells that does not have any cracks or hot spots, henceforth referred to as cell C1. The temperature of the cell varied from 55 to 56 °C (measured at POA irradiance of 914 W/m<sup>2</sup>), as shown in Fig. 6.3(b). Figure 6.16(c) shows the variation in

the discoloration, measured in terms of the *PYI* (shown in blue, with scale along the left y-axis) and the temperature (shown in red, with scale along the right y-axis) along the center of the cell (indicated with dashed line in figures 6.3(a) & 6.3(b)). It can be seen that the *PYI* values over the silicon cell areas are mostly less than -40 (indicating bluish colour). However, the *PYI* values shoot upwards on top of the silver metallization (and busbars) because the metallization is silvery white in colour.

Figure 6.4(a) shows the visual image of a solar cell operating at high temperature (henceforth referred to as C2) from the same solar panel shown in Fig. 6.2. It is evident that the discoloration is above the crack line (present below the lower busbar). Figure 6.4(b) shows the thermal map of the solar cell (based on IR thermography, after perspective correction) where it is evident that the cell's upper portion above the crack is much warmer (ca. 70 °C) than the lower part of the cell (ca. 60 °C). The thermal boundary in the lower section of the cell corresponds to the crack in the cell. Figure 6.4(c) shows the variation in the *PYI* and the temperature along the center of the cell (marked by horizontal dashed line). The corresponding *DI* is plotted in Fig. 6.5. In the left side of the cell, the discoloration and the temperature both increase simultaneously. The discoloration in the left side of the cell is lower than the right side due to the lower temperatures and also the photo-bleaching effect of oxygen diffusing through the crack. In the right half of the cell, there is a mismatch between temperature and discoloration, since the discoloration is highest close to the right edge of the cell though the temperature is highest at the center of the cell. The ingress of oxygen along the crack and its diffusion to the right side, is suspected to be the cause for this mismatch. The right-side edge of the cell also shows high discoloration, in spite of having oxygen supply from the inter-cell spacing, owing to the higher temperature of the cell (about 8 °C higher than the normal operating cells). Thus, the photo-bleaching action of oxygen is unable to fully neutralize the discoloration in case of high cell temperatures.

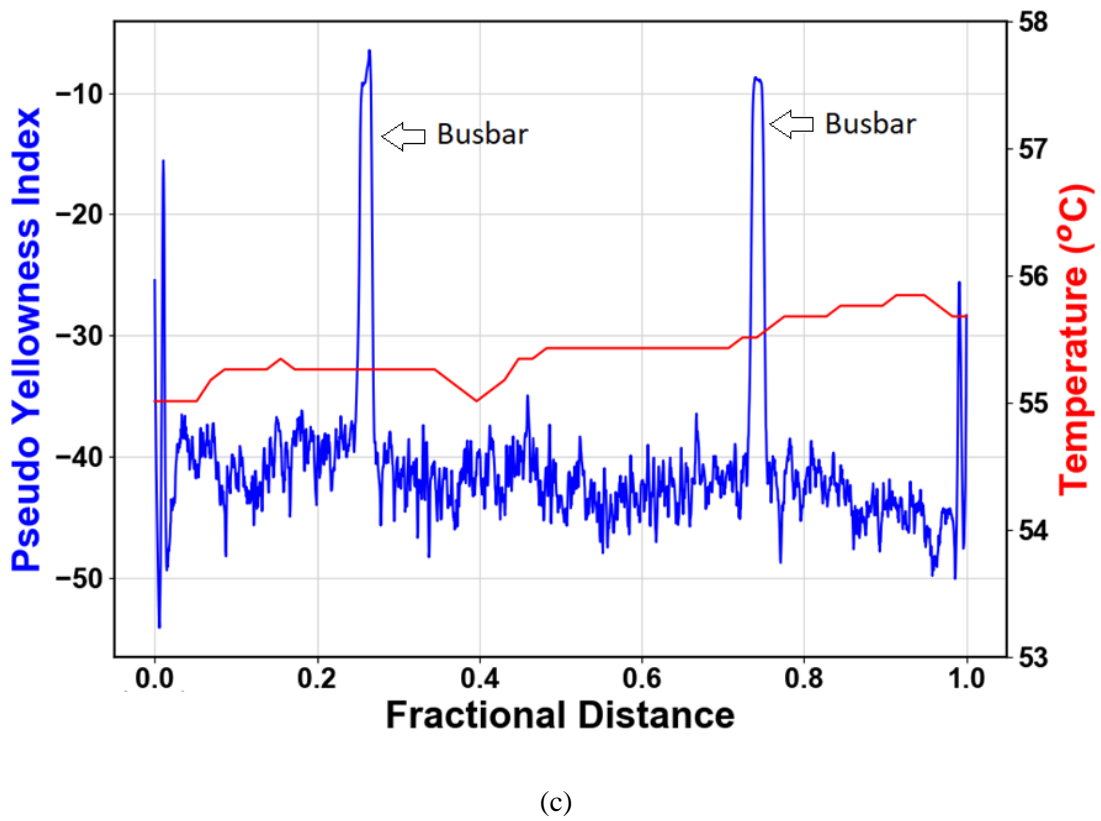
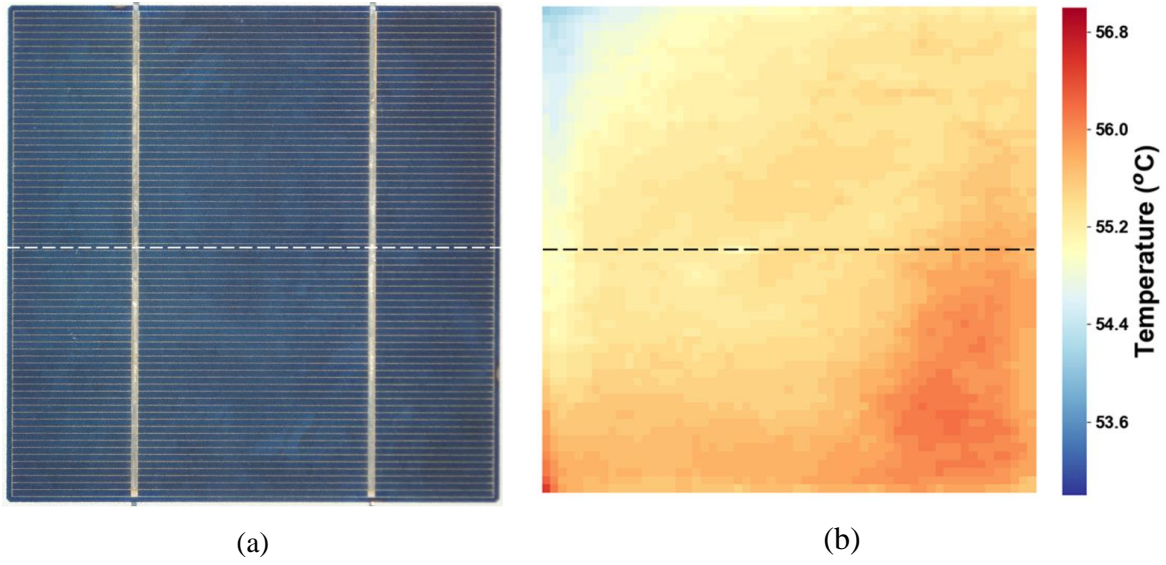
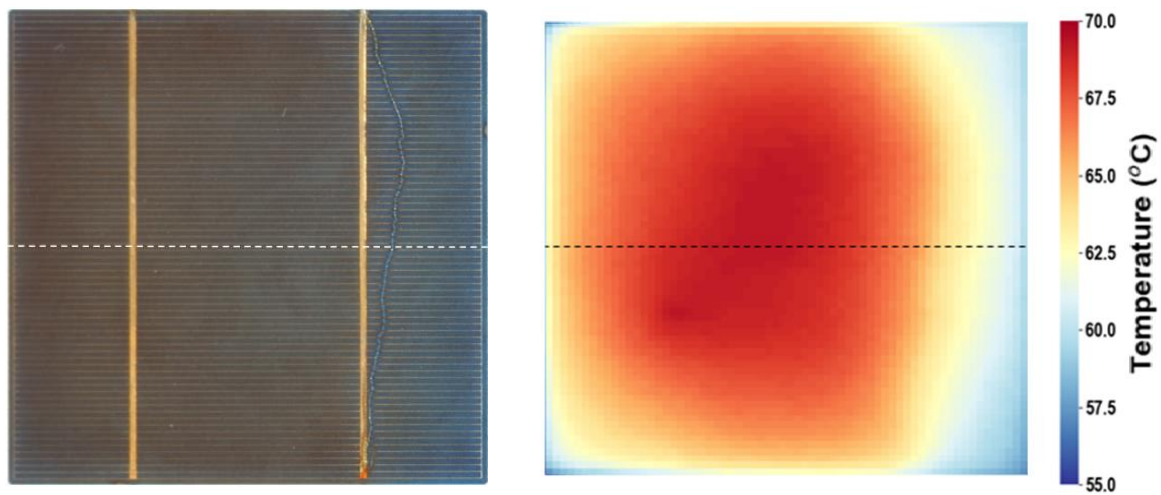
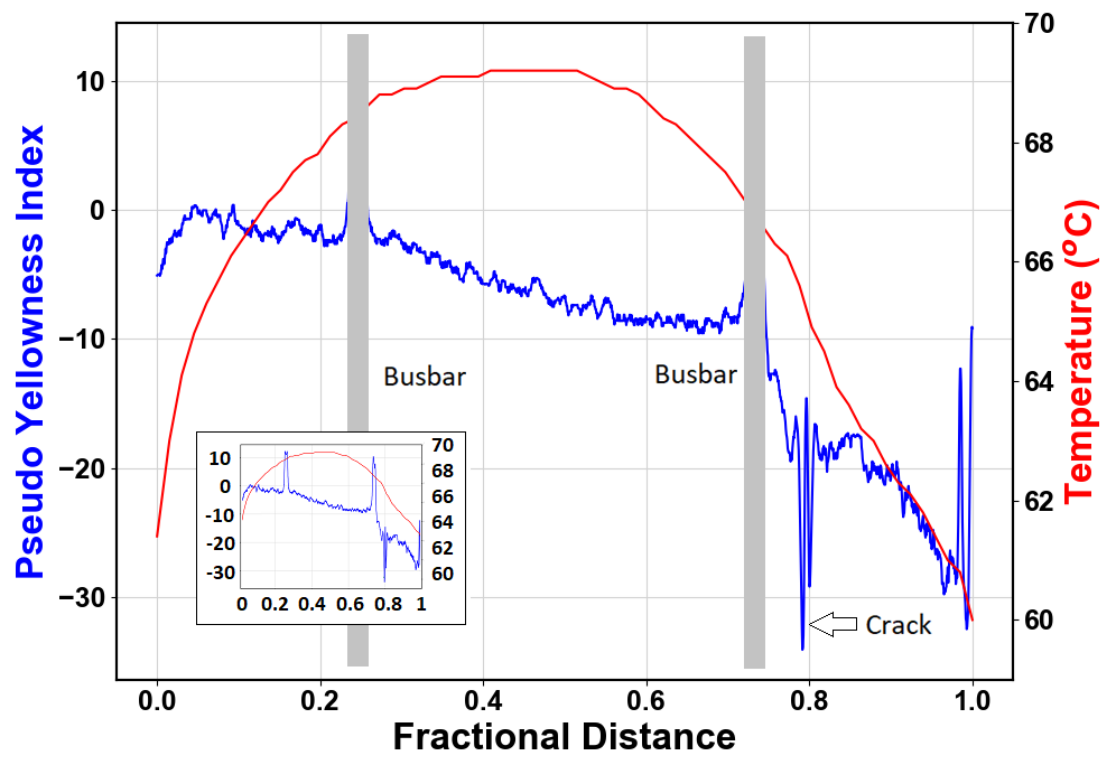


Fig. 6.3: (a) Visual image of a normal temperature solar cell, C1 (after perspective correction), (b) thermal map of the cell (perspective corrected), recorded at Plane-of-array irradiance of  $913 \text{ W/m}^2$ , and (c) variation of the *PYI* and temperature along the centre of the cell (in vertical direction).



(a)

(b)



(c)

Fig. 6.4: (a) Visual image of solar cell C2, operating at high temperature (after perspective correction), (b) thermal map of the cell (perspective corrected), recorded at plane-of-array irradiance of 913 W/m<sup>2</sup>, and (c) variation of the *PYI* and temperature along the centre of the cell (all data points shown in inset, and busbar location is indicated with grey strips in main figure).

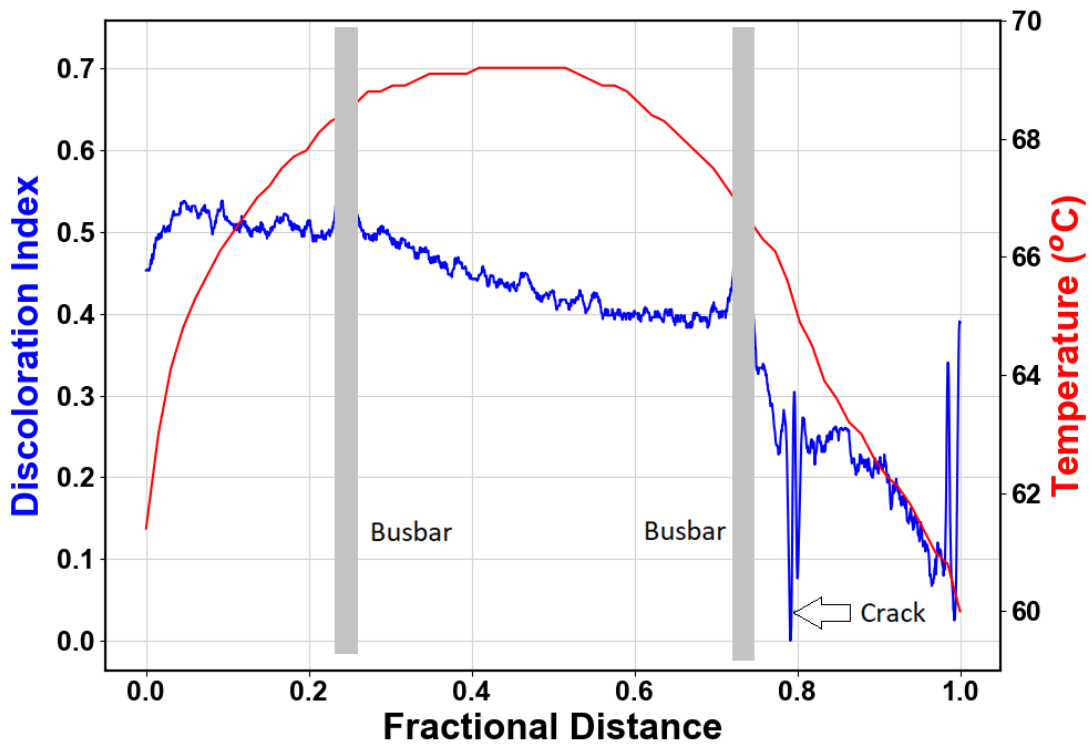


Fig. 6.5: Variation of the discoloration index and temperature along the center of the cell C2.

Thus, it is clear that the discoloration in the hot cell is higher than that of the surrounding cells operating at “normal” temperature. The discoloration in different regions of the hot cell depends on the temperature and the oxygen concentration. The discoloration of the encapsulant cannot be completely bleached by oxygen, in case of high cell temperatures.

### 6.3 Thermal Model of PV Module with Hot Cells

In this section, the effect of solar cell degradation on its operating temperature and power degradation shall be analyzed based on a simplified thermal model of the PV module. The electrical power generation can be correlated with the input light energy and the thermal power dissipation of a module based on the overall energy balance of the PV module under steady state condition, as given below:

$$P_{solar\ input} = P_{electrical} + P_{thermal} + P_{others} \quad \dots (6.1)$$

where,

$P_{solar\ input}$  = Input power from the sun, W

$P_{electrical}$  = Electrical power delivered to load, W

$P_{thermal}$  = Thermal heat loss to surroundings, W

$P_{others}$  = Other losses (including light reflection and transmission losses which can be assumed to be proportional to the incident radiation), W.

The solar spectrum consists of ultra-violet, visible and infra-red light. About 4% of the incident light is reflected off by the top glass, and about 93% is transmitted to the underlying EVA layer [114]. The EVA layer, being very thin, absorbs about 2.5% of the incident light [114]. The silicon solar cell, lying beneath the EVA layer, absorbs the high energy photon flux (wavelength below 1100 nm), converting it into heat and electricity (based on its efficiency). The low energy photons (wavelength greater than 1100 nm) mostly pass unhindered through the semiconductor but are absorbed by the aluminum layer at the backside of the Al-BSF based silicon solar cells, through free carrier absorption [115]. Hence, the solar cell (silicon plus the aluminum backside layer) is the main source of heat generation in the laminate, and this heat is transferred, by conduction and radiation, to the glass and the backsheet (through the encapsulant). The top glass and the backsheet dissipate the heat to the surroundings through convection and radiation. For the sake of simplicity, we shall consider the glass, encapsulant, solar cell and backsheet to be at equal temperature, and treat this laminate as a single unit (marked using dotted lines in Fig. 6.6). So, a 60-cell module is considered to be made up of 60 such laminate units, with heat transfer from each laminate only to the surrounding air but no significant heat transfer between the adjoining laminate units (which enables some cells to stay hotter than their surrounding cells as generally been observed in the IR images in our surveys).

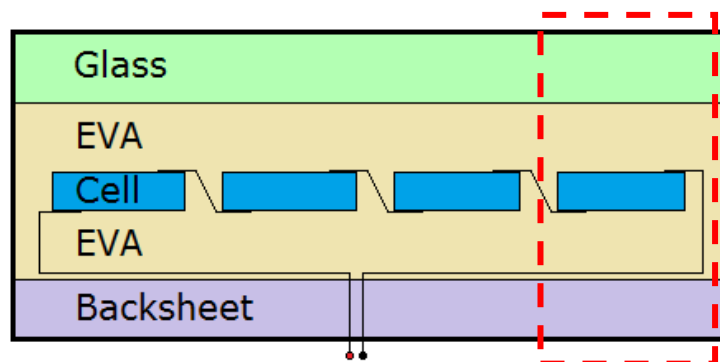


Fig. 6.6: Basic schematic of a PV module showing the laminate structure. The red dotted lines indicate a single unit of the laminate which is discussed in the thermal model in this section.

The heat energy loss from this laminate can be expressed in terms of convection and radiation losses (neglecting any conduction losses through the support structure), as follows:

$$P_{thermal} = h \cdot A \cdot (T_{lam} - T_{amb}) + \sigma \cdot \epsilon \cdot A \cdot (T_{lam}^4 - T_{amb}^4) \quad \dots (6.2)$$

where,

$h$  = Convective heat transfer coefficient of laminate,  $W/m^2 \cdot K$

$A$  = Surface area of unit laminate,  $m^2$

$T_{lam}$  = Temperature of the laminate (solar cell),  $K$

$T_{amb}$  = Ambient temperature,  $K$

$\sigma$  = Stefan Boltzman constant,  $W \cdot m^2 \cdot K^{-4}$

$\epsilon$  = Emissivity of the module surface

When the solar cells degrade (due to cracks, shunts etc.), there is change in electrical output and heat generation, in spite of a constant input solar radiation, so Eqn. (6.1) can be rewritten for individual solar cell laminate as (assuming other losses,  $P_{others}$  to remain constant):

$$\Delta P_{electrical} + \Delta P_{thermal} = 0 \quad \dots (6.3)$$

Thus, decrease in electrical power output of the solar cell will lead to a corresponding increase in thermal heat loss ( $P_{thermal}$ ) and correspondingly, the cell temperature, averaged over the cell area, ( $T_{lam}$ ) would increase. Let this increase in  $T_{lam}$  be denoted by  $\Delta T_{lam}$ . Our usual observation in the field surveys is that  $\Delta T_{lam}$  is about 1 K to 10 K whereas  $T_{lam}$  is around 340 K, so  $\Delta T_{lam} \ll T_{lam}$ . From Eqn. (6.2), one can derive the following relation (for  $\Delta T_{lam} \ll T_{lam}$  in Kelvin):

$$\Delta P_{thermal} = U \cdot A \cdot \Delta T_{lam} \quad \dots (6.4)$$

where,

$$U = h + 4\sigma \cdot \epsilon \cdot T_{lam}^3$$

The total power loss in the PV module is summation of the power loss from the constituent solar cells under operating condition, so it can be said, from Eqn. (6.3) and (6.4), that the change in module electrical power output is,

$$\begin{aligned}\Delta P_{e,module} &= \sum_{N \text{ cells}} -U \cdot A \cdot \Delta T_{lam} \\ &= -U \cdot A \cdot \sum_{N \text{ cells}} \Delta T_{lam}\end{aligned}\quad \dots (6.5)$$

where,

$\Delta T_{lam}$  is the increase in the cell temperature due to degradation (efficiency loss) in the solar cell,

$$\Delta T_{lam} = T_{lam,present} - T_{lam,initial} \quad \dots (6.6)$$

Equations (6.4) and (6.5) have also been mentioned in the work of Tsanakas *et al.* [72, 73] where they have defined the  $\Delta T_{lam}$  by comparing the IR images of the defective module with that of a non-defective reference PV module. However, we propose that it is possible to use the same PV module as the reference to determine the  $\Delta T_{lam}$  under a specific set of condition, which is discussed below.

During solar cell production, differences in wafer quality and manufacturing tolerances lead to variations in the solar cell efficiency. It is reasonable to assume that the cell current and efficiency are matched within small tolerance range during module production, and hence the cells in a module have similar (though not exactly same) electrical characteristics. These cells shall be referred to as “standard cells”. The cell temperatures in such well-matched standard modules can be assumed to be initially uniform after the module production (within a small tolerance of a few degrees Kelvin). However, as some of the cells in the module degrade (due to cracks, shunts etc. generated during transportation and/or field operation), their electrical output reduces and operating temperature increases. The rest of the cells that have not degraded can be assumed to have the same operating temperature after field-operation as the initial (post-production) temperature. This assumption is valid if the operating point of these good cells (on the cell  $I$ - $V$  curve) is not affected by the generation of the defects in the defective cells. As there are small variations in the operating temperature of these standard cells (due to the wafer quality and manufacturing tolerances), for the sake of simplicity we have considered the most frequently observed temperature in the module (modal value of the module’s temperature

histogram) as their representative temperature, which shall be referred to as  $T_{module}$ . Based on above assumptions it can be said that the change in temperature of individual laminate is,

$$\Delta T_{lam} = T_{lam,present} - T_{lam,initial} = T_{lam,present} - T_{module} \quad \dots (6.7)$$

Using equations 6.5 and 6.7, the change in the module's power output is,

$$\Delta P_{e,module} = -U \cdot A \cdot \sum_{N \text{ cells}} (T_{lam,present} - T_{module}) \quad \dots (6.8)$$

Hence, the percentage loss in module power output would be,

$$\begin{aligned} \% \text{ Module Power Loss} &= \frac{-\Delta P_{e,module}}{\text{Initial Power Output}} \times 100 \\ &= \frac{-\Delta P_{e,module}}{1000 \cdot N \cdot \eta \cdot A} \times 100 \\ &= \frac{U}{10 \cdot N \cdot \eta} \sum_{N \text{ cells}} (T_{lam,present} - T_{module}) \quad \dots (6.9) \end{aligned}$$

The above equation shows that the percentage power loss of the module is inversely proportional to the number of cells and initial efficiency and varies directly with the sum of the cell temperature differences. It may be noted that the above equation is derived for modules with defect in cells (like shunts or cracks) and not for defects in the packaging material (like front-side delamination) that can change the transmittance of light and hence the overall expression in Eqn. 6.3. Generally, the cell cracks would not affect the cell's reflectance significantly, as the width of the crack is in micrometers. However, if the cell crack is very wide (say few millimeters, which is a very rare), then the reflectance will be affected and above equations are not valid in that case. Also, the above equations are valid when there are only a few hot cells in the module (which is most often the case observed during our field surveys), and not applicable for modules having majority of hot cells (which may happen in extreme cases of potential induced degradation).

In the All-India Surveys of Photovoltaic Module Reliability, IR images have been taken from the backside of the modules, and in most of the images the module of interest has trapezoidal shape (as evident from Fig. 6.2(b)). Also, some sections of the module were not visible in the IR image due to the support structures. Hence, instead of summation of the

temperatures of each and every pixel of the IR image (as would be required by Eqn. 6.9), we have followed the idea of Moreton *et al.* [87] to define a differential temperature in the module, *Module  $\Delta T$*  based on the highest temperature in the module and the representative module temperature. This *Module  $\Delta T$*  thus represents the temperature rise of the worst hot spot in the module. Based on the *Module  $\Delta T$*  and taking into consideration Eqn. 6.9, a “Thermal Mismatch Index” (*TMI*) has been defined which is explained in detail in the next section.

## 6.4 Thermal Image Analysis Methodology

During the survey, the IR images of crystalline silicon PV modules were taken from the backside, both at maximum power point (MPP) condition (string/array maintained at MPP by string/central inverter) and also under module-level short-circuit condition. For the short-circuited IR image, each module was kept short-circuited for about 5 minutes before taking the image. All the IR images were taken under high irradiance (plane-of-array irradiance greater than  $700 \text{ W/m}^2$ ), using a FLIR E60 radiometric IR camera. The emissivity setting of the IR camera was set to the emissivity of backsheets (0.95) when taking the images from backside, as per [43]. Both MPP and short-circuit IR images were captured at most of the sites in the 2016 survey, except for a few sites where due to time constraints, only MPP or short-circuit IR images could be taken (but not both).

Figure 6.7 shows the IR images of a PV module under MPP and short-circuit conditions, and also the electroluminescence (EL) image of the same module, showing cracked areas in solar cells (dark areas in the EL image). The IR images were taken in daylight, whereas the EL image was taken at night, using a modified CMOS camera, with the module forward biased to carry short-circuit current, which is detailed in [116]. The cell highlighted in blue box in Fig. 6.7(c), has almost 25% of the cell area separated by crack and it shows up as a hot cell in IR images at both MPP condition and short-circuit condition. Many of the cells are hotter in the short-circuit IR image as compared to the MPP image, which is expected considering that the cells with poor *I-V* characteristics go into reverse bias under short-circuit condition of the PV module, resulting in heating of those cells. A second cell is also showing grayish area in EL image (marked with green box), but it created only a minor temperature rise in the MPP IR image, indicating that this

cell is not so severely affected as the other one. As evident from Fig. 6.7, the IR images captured from the back of the module include not only the area of interest (PV module), but also many other features, including parts of the surrounding modules, the supporting structure and wiring. Hence, it is necessary to extract the temperature information of the module of interest from this composite IR image for further analysis. First, the temperature matrix is extracted from the thermal image (using FLIR Tools software). Then, a separate software (developed in-house in Python) is used to select the region of interest from the IR image (plotted using the extracted temperature matrix), and this software saves the histogram of the extracted region [117]. Fig. 6.8 shows the IR image of a PV module in (a), the extracted data in (b), and the temperature histogram in (c). The maximum and modal temperatures are also indicated in this histogram.

Since the IR images were taken at multiple sites under different ambient conditions during the survey, the irradiance and ambient temperature are not the same for all the IR images. It is hence necessary to translate the measured temperature to a reference ambient condition so that comparisons can be made between the data collected during the survey. Based on the work of Moreton *et al.* [87] and Oh *et al.* [118], the IR temperatures were translated to the reference condition of 1000 W/m<sup>2</sup> and 40 °C (i.e., 313.15 K), using the relation [117, 119]:

$$T_{translated} = 313.15 + (T_{measured} - T_{amb}) \cdot \frac{1000}{G} \quad \dots (6.10)$$

Moreton *et al.* [87] have suggested that the hot spots in PV modules can be characterized by the rise in temperature of the hot cells (defective cells) compared to the surrounding cells. The modal temperature of the module (which is the most frequently occurring temperature in the module) is considered as the representative temperature of the “surrounding cells” in the module, as discussed earlier in section 6.3. The temperature mismatch in the module (*Module ΔT*) is calculated by subtracting the translated value of the modal temperature (modal value from temperature histogram) from the translated value of maximum cell temperature in the module [117, 119]:

$$Module \Delta T = T_{maximum} - T_{modal} \quad \dots (6.11)$$

From Eqn. 6.8 and 6.9, it is clear that the electrical power loss (in Watts) is directly related to the cell temperature rise, but the percentage power degradation (relative to the initial power

output) is also dependent on the initial efficiency ( $\eta$ ) and the number of cells ( $N$ ). Hence, these terms have been combined with the *module*  $\Delta T$  to define a “Thermal Mismatch Index” (*TMI*) as given below:

$$TMI = \frac{\text{Module } \Delta T}{\eta \cdot N} \quad \dots (6.12)$$

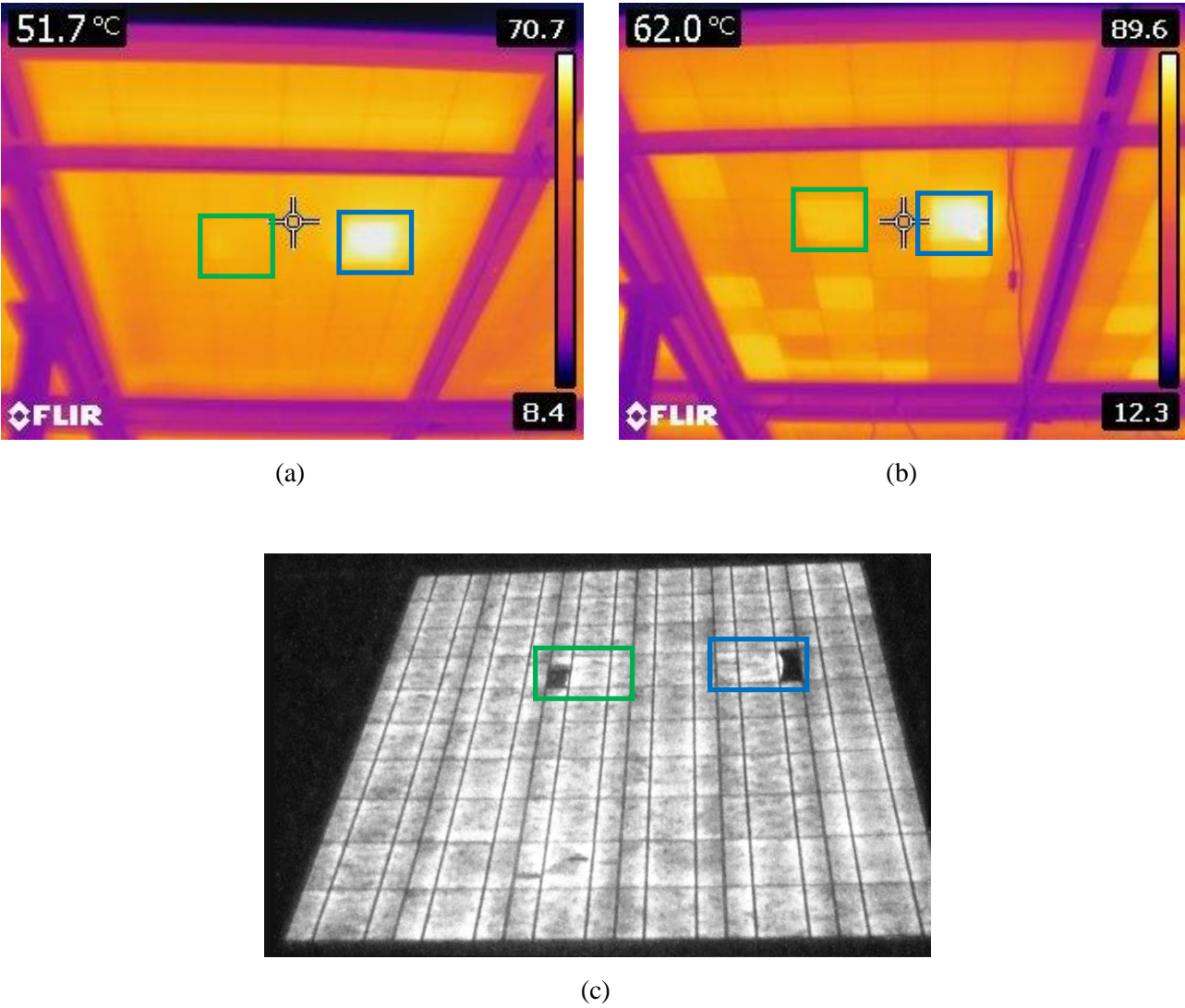


Fig. 6.7: (a) IR image of PV module under MPP condition, (b) IR image of same module under short-circuit condition, and (c) electroluminescence (EL) image of the module showing cracks in cells (the EL image has been flipped sideways to show the correspondence to the IR images which are taken from\_backside). The hot cell is marked in the images by a blue border, and the cracked cell without hot spot is highlighted by green border.

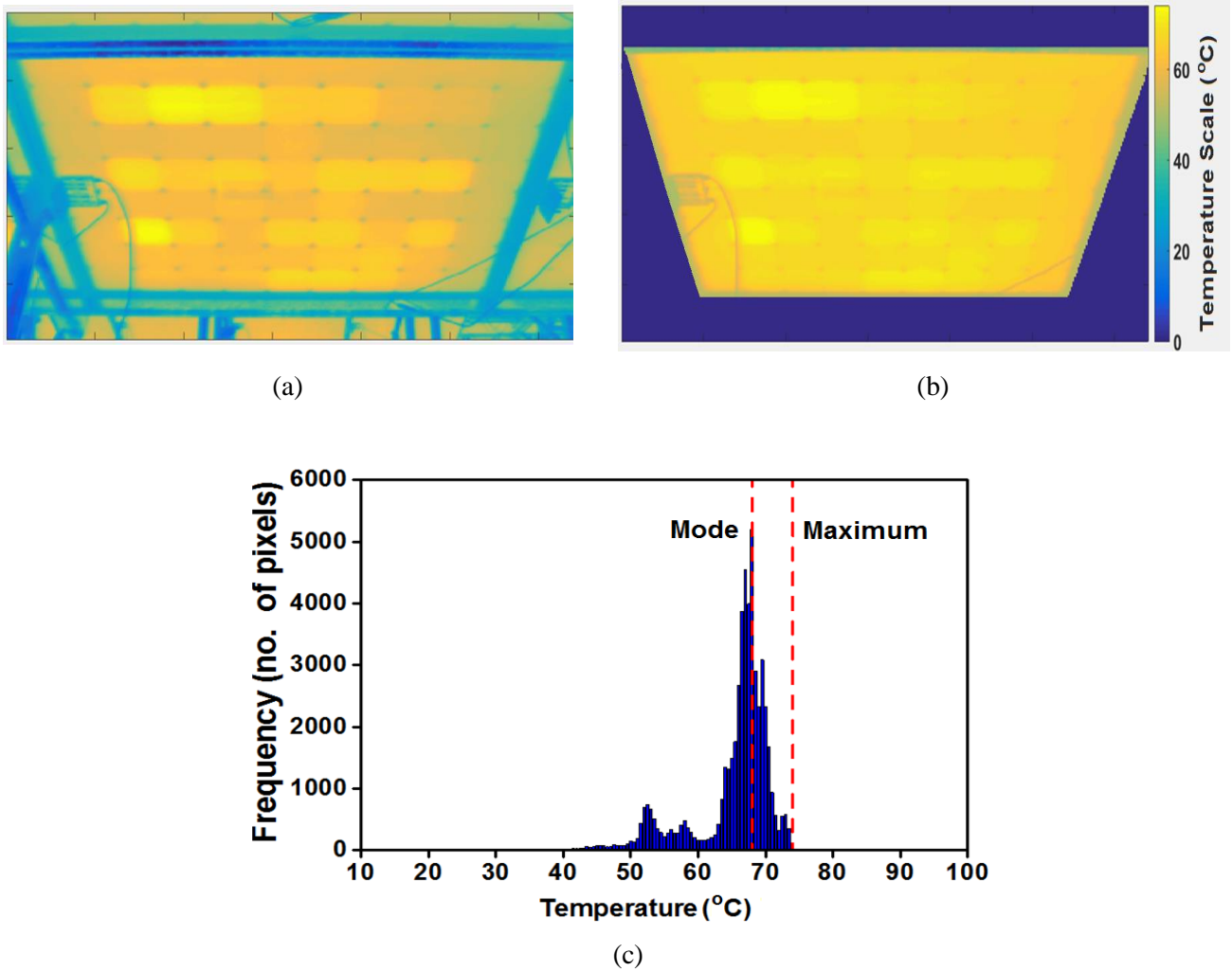


Fig. 6.8: (a) IR image of PV modules in a power plant, (b) region of interest extracted from the IR image, and (c) temperature histogram of the module, showing distinct sections of the module support and ambient (the low temperature humps), and the module backsheet (the high temperature hump).

The plane-of-array irradiance was  $870 \text{ W/m}^2$  and the ambient temperature was  $42.6 \text{ }^\circ\text{C}$  [117] .

The value of the denominator in Eqn. 6.12 ranges between 9 to 15 in case of present-day modules (16% to 20% efficiency, 60 or 72 cells), but the values will be lower for lower wattage modules (usually seen in older installations). This indicates that the same *Module*  $\Delta T$  has a higher *TMI* value in a lower wattage module than a higher wattage module. This index serves as a factor of merit for determining the impact of the cell-to-cell temperature mismatch in a module on the module's power degradation (i.e., power output relative to its initial performance). It considers the maximum temperature variation observed in the module and normalizes this value using the initial (nameplate) efficiency and the number of cells in the module, to arrive at a temperature index which is independent of the module size and cell efficiency. Thereby it enables us to compare between modules of different initial power ratings, but same materials of construction.

## 6.5 Effect of Hot Cells on Electrical Degradation

In this section, the effect of thermal mismatch at MPP condition ( $TMI_{MPP}$ ) on the power degradation of crystalline silicon photovoltaic modules is discussed first. The modules have been grouped into 4 categories based on the  $TMI$  value, as shown in Table 6.1. Table 6.1 also gives the approximate *Module*  $\Delta T$  values for these categories for standard modules (60 cell, 17% efficiency modules). The  $TMI$  values are proportional to the *Module*  $\Delta T$  for modules of the same size and efficiency, but it will be higher for the lower wattage panels (indicating the same temperature difference has a higher impact on power output in a lower wattage panel). Figure 6.9 shows the power degradation (%) for modules of different  $TMI$  categories. The number of samples in each category is indicated in square brackets at the top of the plot. The average degradation values are also indicated in the figure, using first brackets, beside the red diamond symbols. The extreme end of the diamonds indicates the 95% confidence interval for the average value (assuming normal distribution). It is evident from the figure that there is a rise in the average power degradation percentage, with increase in the  $TMI$  category, which supports Eqn. 6.9. The cumulative probability distribution (CPD) has also been shown on the right side in Fig. 6.9, from which one can get the median (50% probability) and other quartile values of the distribution.

Table 6.1:  $TMI$  categories for MPP IR images

<i>TMI</i> values	0 – 0.25	0.25 – 0.5	0.5 – 1	>1
<i>Module</i> $\Delta T^*$ (K)	0 – 2.55	2.55 – 5.1	5.1 – 10.2	>10.2
Category	I	II	III	IV
*for standard modules (60 cells, 17% efficiency)				

From Fig. 6.9, it can be seen that the modules in  $TMI$  category III and IV (i.e., with  $TMI_{MPP} > 0.5$ ) show higher degradation than categories I and II. The CPD plots also indicate that the distribution of data points is different for  $TMI$  categories III and IV compared to categories I and II, thereby indicating significant difference between the two groups. To confirm that there is a statistical difference between the groups, Mann-Whitney U test (a non-parametric statistical test) has been performed. The probability values (p-values) for these tests are given in Table 6.2, which shows that the differences between the groups are significant (as p-value <

0.05), except between the groups III and IV. Hence, groups III and IV have been clubbed together and  $TMI_{MPP} > 0.5$  is considered as the criterion for Hot Cells (which corresponds to translated  $Module \Delta T > 5$  K for 60-cell 17% efficiency solar panels). About 13% of the 457 crystalline silicon photovoltaic modules for which IR images are available under MPP condition (in the 2016 survey), showed Hot Cells as per the above criteria.

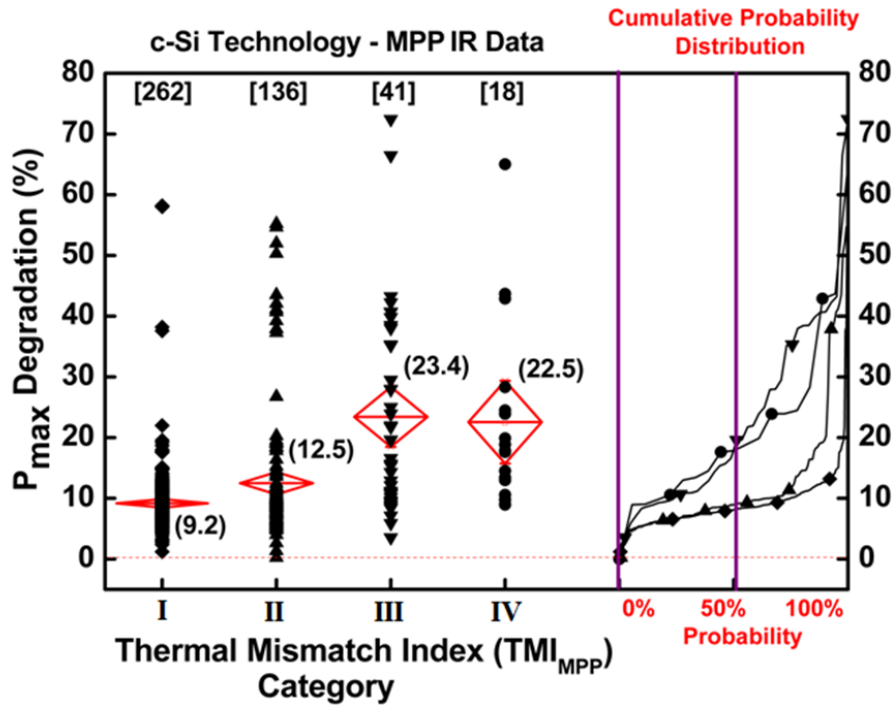


Fig. 6.9: Plot of  $P_{max}$  degradation (%) versus the  $TMI$  category for IR images taken at MPP condition. The red diamonds indicate the 95% confidence interval for the mean value (mentioned inside the round brackets). The number of samples is indicated at the top of the figure in square brackets.

Table 6.2: Probability values of Mann Whitney U Test for Power degradation in different  $TMI$  categories.

Probability	Category ( $TMI$ Value)		
Category ( $TMI$ Value)	II (0.25-0.5)	III (0.5-1)	IV (>1)
I (0 - 0.25)	0.0053	<0.0001	<0.0001
II (0.25 - 0.5)	NA	<0.0001	<0.0001
III (0.5 - 1)	NA	NA	0.8498

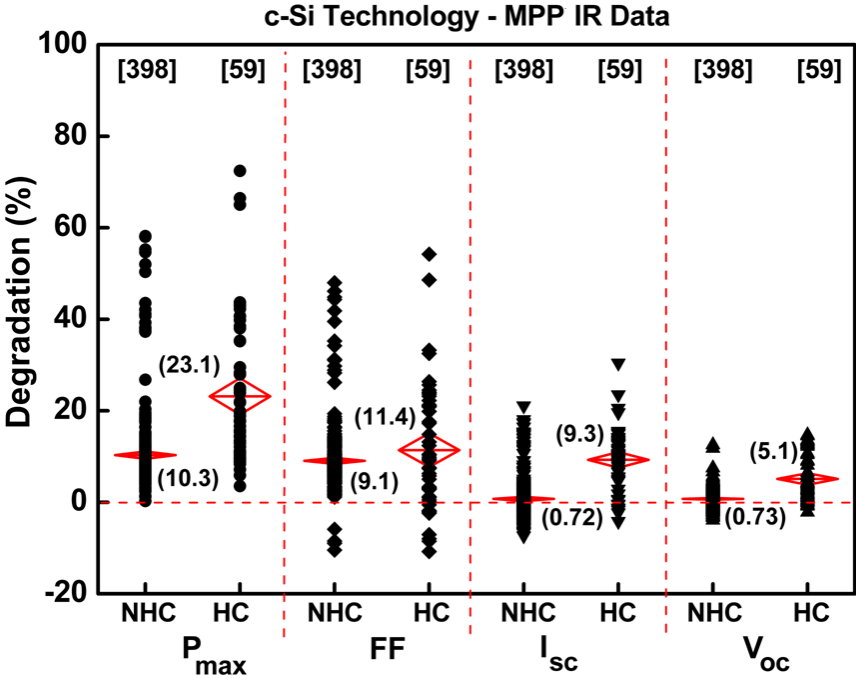
Note: NA means Not Applicable.

Figure 6.10 shows the degradation in the electrical parameters for the modules with and without Hot Cells (henceforth, referred to as “HC” and “NHC” respectively). In Fig. 6.10 (a),

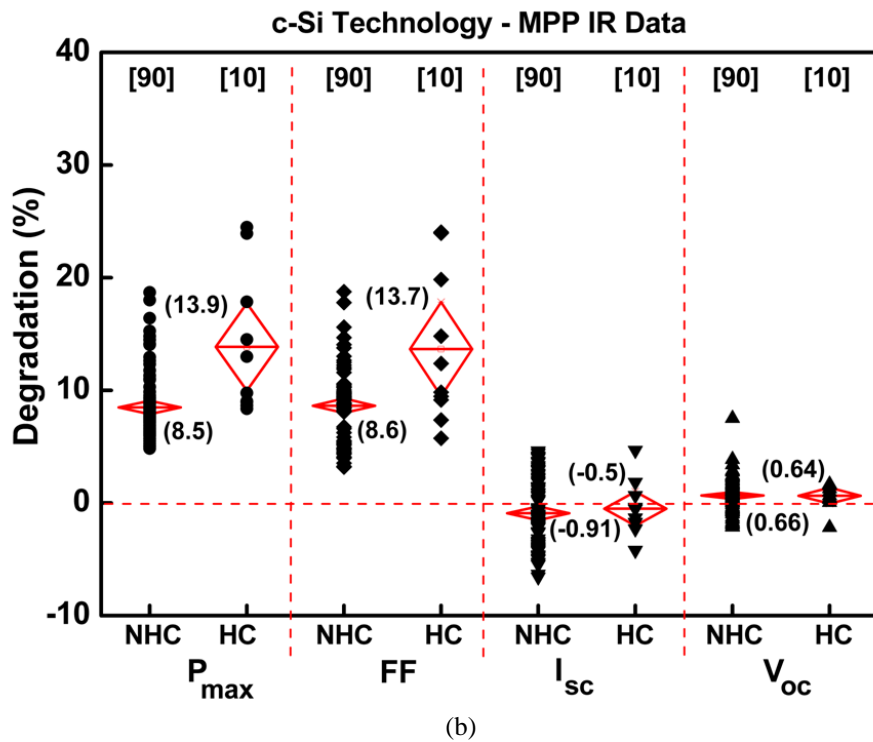
all crystalline silicon sites have been included, and it shows that the modules with Hot Cells are affected by degradation in fill factor ( $FF$ ), short-circuit current ( $I_{sc}$ ) and also open-circuit voltage ( $V_{oc}$ ) to some extent. However, when considering modules from relatively younger sites (aged less than 10 years) having modules with Hot Cells but no discoloration or delamination, fill factor degradation emerges as the main contributor for the higher degradation in the power output of these modules (refer Fig. 6.11(b)). The p-values for the Mann-Whitney U Test (given in Table 6.3) confirm that the difference between the average values of “NHC” and “HC” groups is statistically significant for power loss and fill factor, but not for short-circuit current and open circuit voltage.

Table 6.3: Probability values of Mann-Whitney U Test for electrical degradation in 0-10 year old modules, comparing the modules with and without Hot Cells.

	Parameter			
	$P_{max}$	$FF$	$I_{sc}$	$V_{oc}$
P-value	0.018	0.038	0.883	0.898

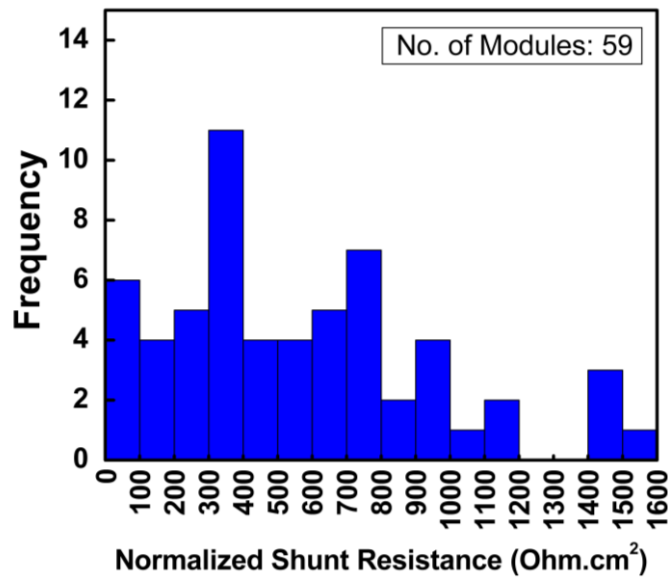


(a)

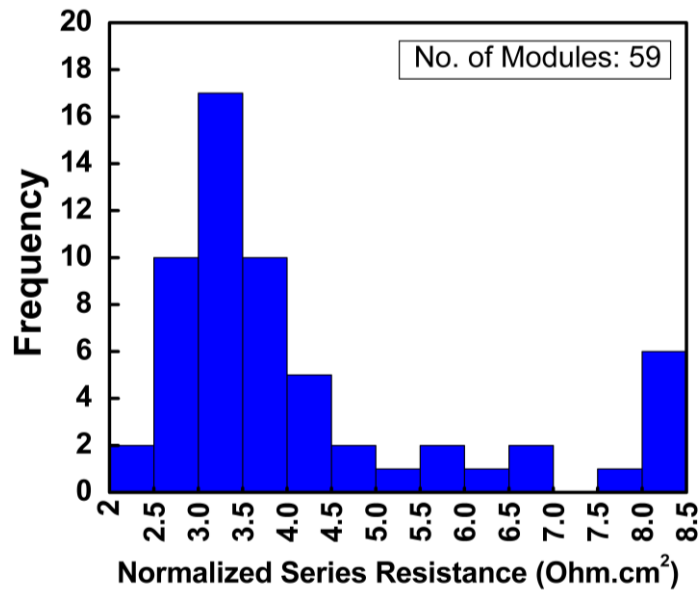


(b)  
 Fig. 6.10: Plot of degradation in electrical parameters (%) for modules with Hot Cells (HC) and without Hot Cells (NHC), for (a) all c-Si sites, and (b) c-Si sites aged less than 10 years having modules with Hot Cells. The red diamonds indicate the 95% confidence interval for the mean value (mentioned inside the round brackets). The number of samples is indicated at the top of the figure in square brackets.

The fill factor degradation observed in the modules may be caused by excessively high series resistance or low shunt resistance. When comparing the series and shunt resistances between modules of different ratings, it is necessary to normalize these resistance values. The normalized (per cell equivalent) series and shunt resistance values for the modules have been calculated by dividing the module shunt or series resistance by the number of cells and then multiplying it with the cell area. Figure 6.11 shows the normalized series and shunt resistances of the modules with Hot Cells. 51% of the modules with Hot Cells have normalized shunt resistance (per cell equivalent value) less than  $500 \text{ Ohm}\cdot\text{cm}^2$ , whereas the standard production cells have a value close to  $1000 \text{ Ohm}\cdot\text{cm}^2$ . Also, about 34% of the modules have normalized series resistance (per cell equivalent value) greater than  $4 \text{ Ohm}\cdot\text{cm}^2$ , while standard production cells have values below  $3 \text{ Ohm}\cdot\text{cm}^2$ . Further, the fill factor ( $FF$ ) degradation can also be caused due to the cell-to-cell current mismatch owing to the cracks in the cells. Due to this current mismatch, the cracked cells go into reverse bias to support the current from the surrounding cells, leading to loss in module operating voltage (which shows up as  $FF$  degradation) and causes higher operating temperature of the affected cell.



(a)



(b)

Fig. 6.11: Histogram of (a) normalized shunt resistance, and (b) normalized series resistance, for the modules with Hot Cells.

Figure 6.12 shows the percentage power degradation of modules with and without Hot Cells in Hot and Non-Hot climates. The modules with Hot Cells show higher degradation than the modules without Hot Cell, in both Hot and Non-Hot climates (corresponding p-values for Mann-Whitney U test are less than 0.05 as shown in Table 6.4). The modules with Hot Cells in the Hot climate have the highest average power degradation. The maximum power degradation is much higher in the Hot zone (72%) than in Non-Hot zone (28%). The modules in the Hot zone that have excessive (more than 28%) power degradation belong to three different sites and

their electrical degradation is shown in Fig. 6.13. The defects observed in these modules are as follows:

(a) 10-year-old modules of manufacturer A have discoloration and cracks in solar cells (47% of cells on average have visible cracks).  $I_{sc}$  loss is the dominant factor in these modules, though the  $V_{oc}$  and  $FF$  degradation are also very high (please refer Fig. 6.13).

(b) 17-year-old modules of manufacturer B have severe shunts (normalized shunt resistance is 136  $\text{Ohm}\cdot\text{cm}^2$  per cell on average whereas standard production cells have around 1000  $\text{Ohm}\cdot\text{cm}^2$  shunt resistance) and discoloration.  $FF$  loss is the dominant factor in these modules (please refer Fig. 6.13).

(c) Glass-glass modules of manufacturer C from a 27-year-old installation which have significant delamination.  $FF$  loss is the dominant factor in these modules (please refer Fig. 6.13).

Such excessive levels of cracks, delamination and shunting have not been observed in the modules in the Non-Hot zone, in our field surveys. Thus, the Hot zone is definitely more severe for the PV modules than the Non-Hot zone.

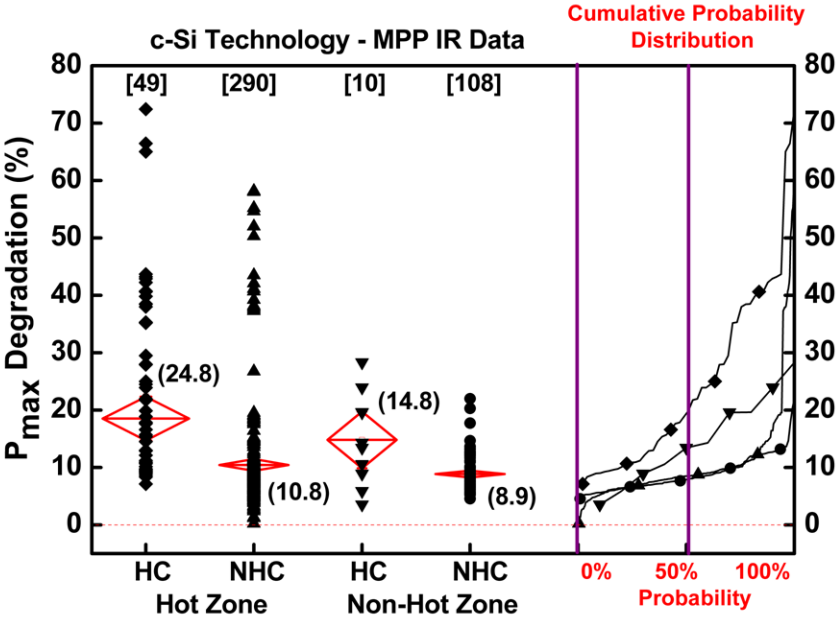


Fig. 6.12: Plot of  $P_{max}$  degradation (%) for modules with and without Hot Cells (HC and NHC) in Hot and Non-Hot zones. The red diamonds indicate the 95% confidence interval for the mean value (mentioned inside the round brackets). The number of samples is indicated at the top of the figure in square brackets.

Table 6.4: Probability values of Mann-Whitney U Test for Power degradation in different *TMI* categories.

Probability	Category		
Category	Hot Zone - NHC	Non-Hot Zone - HC	Non-Hot Zone - NHC
Hot Zone - HC	< 0.0001	0.08	< 0.0001
Hot Zone - NHC	NA	0.034	0.36
Non-Hot Zone - HC	NA	NA	0.013

Note: NA means Not Applicable,

HC refers to modules with Hot Cell, NHC refers to modules without Hot Cell

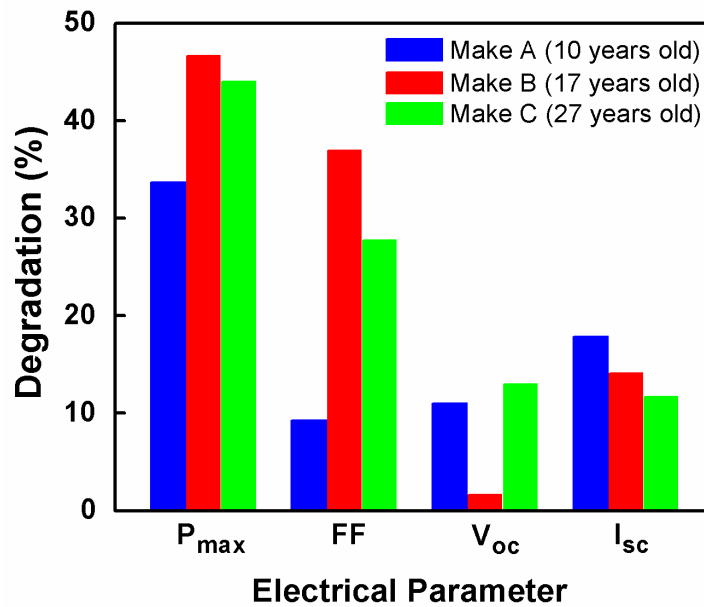


Fig. 6.13: Electrical degradation observed in the modules from Hot Zone showing excessive power degradation.

Hot cells have been found to have cracks in many PV modules. In Fig. 6.14, the PV modules have been grouped into 3 categories depending on whether there are cracks and Hot cells. The cracks have been identified through EL inspection at site, details of which are part of a separate thesis [106]. It may be noted that EL imaging was performed on a selected set of modules and so the number of available samples is small. Hot Cells have been found to predominantly occur in modules with cell cracks. The modules having “Cracks with Hot Cells” have higher degradation of power as compared to modules having “Cracks without Hot Cells”. Modules without cracks show the lowest average power degradation. The differences between the three categories are statistically significant (p-values less than 0.05 as shown in Table 6.5).

This hints that the worst cracks (associated with high power degradation) tend to create Hot Cells in the modules, while the benign cracks do not affect the temperature to that extent. The cracks observed in the EL images sometimes have grey and black areas associated with them, which is indicative of the severity of the crack. The modules can accordingly be classified into three categories– (I) modules having no cracks, (II) modules having cracks associated with grey areas, and (III) modules having cracks associated with dark black areas in EL images [119]. The average power degradation (%) for these categories of modules is shown in Table 6.6, along with the percentage of modules with Hot Cells in these categories. It is clear that cracks associated with black areas are more severe than cracks with grey areas, both in terms of average power degradation and probability for Hot Cell formation. It may be noted that the area affected by the crack and the crack resistance play important role in determining the impact of the crack on the cell’s electrical characteristics [120] which in turn determine the energy loss as heat, so not all cracks lead to Hot Cells. A detailed analysis of cracks in cells and their impact on electrical performance of PV modules is beyond the scope of this work, and the interested reader may refer to concurrent work by Dubey *et al.* [106, 121].

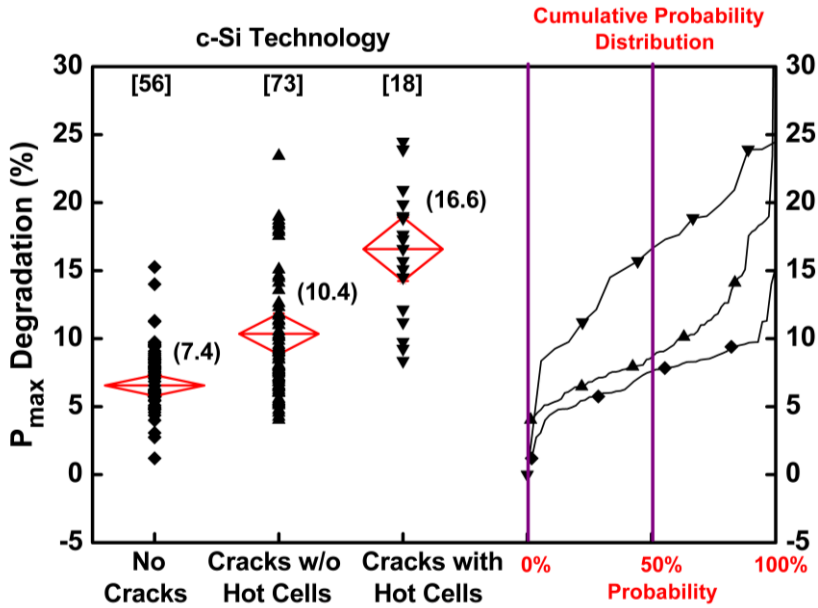


Fig. 6.14:  $P_{max}$  degradation (%) of PV modules with and without cracks and Hot Cells. Cracks have been detected through EL imaging. The red diamonds indicate the 95% confidence interval for the mean value (mentioned inside the round brackets). The number of samples is given at the top of the figure in square brackets.

Table 6.5: Probability values of Mann-Whitney U Test for Power degradation in different crack and Hot Cell categories.

Probability	Category	
Category	Cracks without Hot Cells	Cracks with Hot Cells
No Cracks	0.001	< 0.0001
Cracks without Hot Cells	NA	< 0.0001

Table 6.6: Hot cell statistics and average power degradation for various types of cracks.

Parameter	Module Category		
	I	II	III
Average power degradation (%)	6.56	9.39	13.11
% Modules with Hot Cells	0	17.9	22
No. of samples	65	39	50
I: modules having no cracks II: modules having cracks associated with grey areas III: modules having cracks associated with dark black areas in EL images			

In addition to MPP condition, IR images were also captured under short-circuit condition at some of the power plant sites. The temperature mismatch in a PV module is much higher in short-circuit condition as the better performing cells drive the relatively worse cells into reverse bias and create hot cells with high temperatures. *TMI* has been calculated from the short-circuit images (referred to as  $TMI_{SC}$ ). The modules have been categorized using the short-circuit *TMI* values ( $TMI_{SC}$ ) into four (4) bins as shown in Table 6.7. It may be noted that the *TMI* ranges for the various categories are much higher for short-circuit IR images as compared to the MPP IR images, as the temperature differences between the cells become higher under short-circuit condition.

Table 6.7: *TMI* category for short-circuit IR images.

<i>TMI</i> values	0 – 1	1 – 2	2 – 3	$\geq 3$
Category	I	II	III	IV

Fig. 6.15 shows the variation of the percentage power degradation versus the short-circuit  $TMI$  category, where the increase in power degradation with the  $TMI_{SC}$  is clearly visible. The differences between the various categories are statistically significant ( $p$ -value  $< 0.05$ ) except for categories I and II, as shown in Table 6.8. Similar plots for fill factor, open-circuit voltage and short-circuit current are presented in Fig. 6.16. These plots again confirm that the fill factor degradation is the primary factor associated with the thermal mismatch in the modules. The contributions of open-circuit voltage and short-circuit current degradation in the power loss are much lower than that of fill factor.

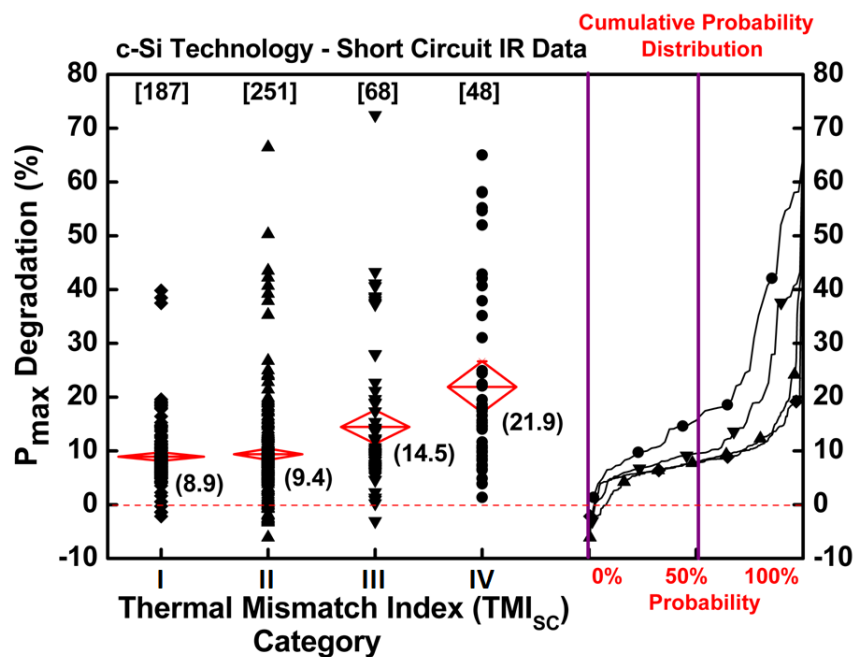
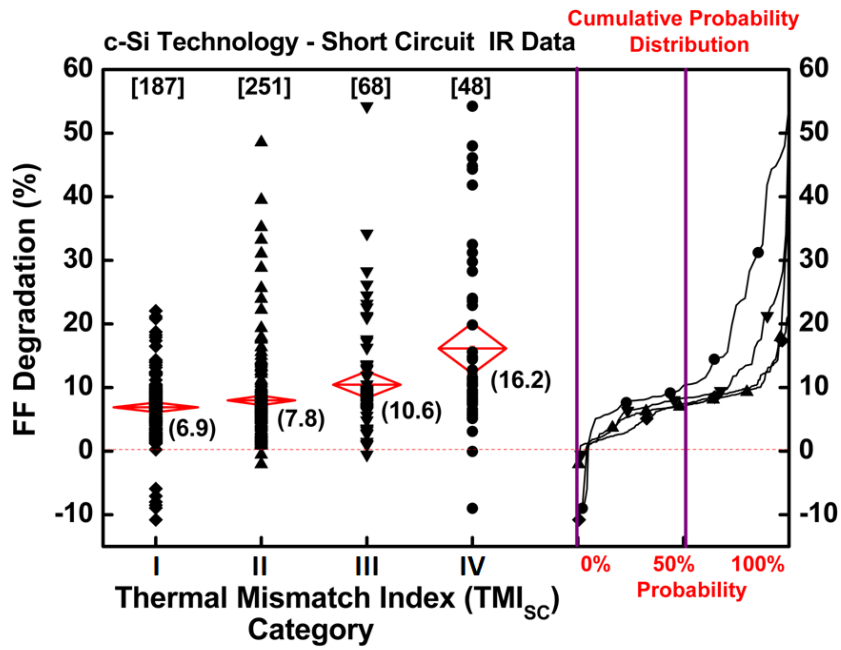


Fig. 6.15: Plot of  $P_{max}$  degradation (%) versus the  $TMI$  category for IR images taken at short-circuit condition. The red diamonds indicate the 95% confidence interval for the mean value (mentioned inside the round brackets). The number of samples is given at the top of the figure in square brackets.

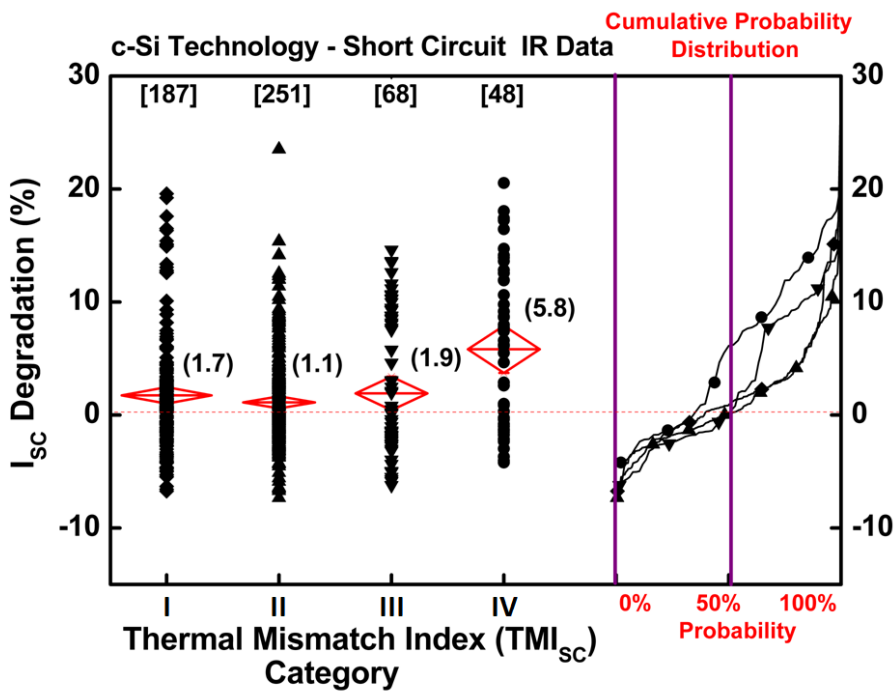
Table 6.8: Probability values of Mann-Whitney U Test for Power degradation in different  $TMI$  categories in short circuit condition.

Probability	Category		
Category ( $TMI$ Value)	II	III	IV
I	0.89	0.001	$< 0.0001$
II	NA	0.002	$< 0.0001$
III	NA	NA	0.001

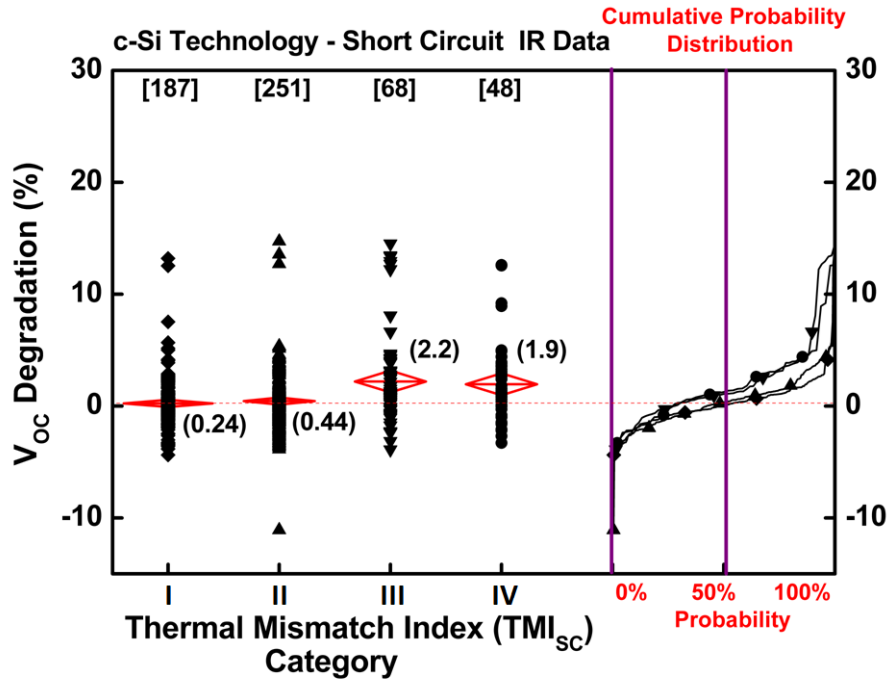
Note: NA means Not Applicable.  
I:  $0 \leq TMI_{SC} < 1$ , II:  $1 \leq TMI_{SC} < 2$ , III:  $2 \leq TMI_{SC} < 3$ , IV:  $3 \leq TMI_{SC}$



(a)



(b)



(c)

Fig. 6.16: Plot of electrical degradation (%) versus the  $TMI$  category for IR images taken at short-circuit condition – (a)  $FF$  degradation, (b)  $I_{sc}$  degradation and (c)  $V_{oc}$  degradation. The red diamonds indicate the 95% confidence interval for the mean value (mentioned inside the round brackets). The number of samples is given at the top of the figure in square brackets.

## 6.6 Summary

Localized discoloration of EVA encapsulant on solar cells is caused due to hot spots on these cells, which can be detected through Infrared thermography under operating conditions. The discoloration pattern is influenced by the cell operating temperature and the extent of oxygen ingress into the cell through cell cracks. While oxygen is widely reported to have photo-bleaching effect on discoloration, the All-India Survey data indicates that oxygen cannot fully bleach the discoloration products in the cells operating at high temperatures, which leads to discoloration even at the cell edges in hot cells.

IR images have been taken under both MPP and short-circuit condition during the All-India surveys. The maximum cell temperature under short-circuit condition is much higher as compared to that measured under MPP condition, which is expected. The thermal mismatch in the modules has been quantified in terms of the “Thermal Mismatch Index” ( $TMI$ ), which is

calculated based on the difference between the highest cell temperature and the representative module temperature (modal value of temperature histogram), normalized by the number of cells and initial module efficiency. *TMI* greater than 0.5 (under MPP condition) has been considered as the criteria for defining Hot Cells (this corresponds to Module  $\Delta T$  of about 5 K for standard 17% efficiency 60 cell modules). Analysis of the IR thermography images shows that average power degradation (%) is higher for modules with Hot Cells, and the effect is accelerated in the Hot climate. Modules with both “Cracks and Hot Cells” have higher degradation than modules with “Cracks but no Hot Cells”. This indicates that the worst cracks tend to create Hot Cells in the modules, while the benign cracks (which have lesser impact on power output) do not affect the cell temperature to that extent. Modules without cracks and Hot Cells show the lowest average power degradation. The major contributing factor to the higher power degradation of modules with Hot Cells is fill factor degradation. Thus, the electrical degradation due to localized Hot spot discoloration (having major contribution from FF degradation) is different from the case of uniform discoloration in panels (where the electrical degradation is primarily due to short circuit current reduction). In the modules with hot spots, the localized discoloration is generated due to high temperatures owing to an underlying defect in the solar cell (usually cell cracks) and tends to further increase the mismatch between the cells, as the discoloration reduces the light incident on the cell, leading to further decrease in module’s fill factor.

So far, the statistics for discoloration and other visual defects have been presented and the correlation of discoloration and hot cells (which cause localized browning) with electrical degradation has been investigated. It is also necessary to understand the impact of the environmental stressors – UV and temperature on the discoloration rate. Hence, accelerated tests have been performed on different EVA materials, which are presented in the forthcoming chapters.

## **Chapter 7**

# **UV-Thermal Accelerated Tests on UV Absorbing EVA Encapsulant**

### **7.1 Introduction**

Discoloration of encapsulant has been found to be one of the most prevalent degradation modes in the All-India Surveys, affecting 33% of the inspected modules. Given the pressure on the manufacturers to reduce the prices of solar panels, there is a possibility that some manufacturers compromise on the quality of the materials. In our All-India surveys, higher degradation of the PV modules is seen in the Hot climates as compared to Non-Hot climates, so it is important to understand the effect of hot climates on the degradation rate of the EVA encapsulants. The majority of the PV module manufacturers use EVA encapsulant having UV absorbers. Hence, the impact of UV and temperature on UV absorbing EVA has been studied

over a wide temperature range (55 °C to 95 °C). These accelerated tests have been performed in the Xenon chamber (make: Q-Labs, model: Q-Sun Xe3), in which the spectrum from Xenon lamps has been modified to suit the outdoor solar spectrum using a special glass filter (supplied by the chamber manufacturer). Also, the UV-absorbing EVA has been compared to a UV-transparent EVA in two separate chambers – (a) Xenon chamber and (b) UV-365 test chamber, the results of which are presented in Chapter 8.

In this chapter, the sample preparation and the test setup are presented first, followed by the results of the accelerated tests on the UV-absorbing EVA laminates. The activation energy for discoloration of the UV-absorbing EVA has been determined, and the implications of using such EVA in Hot climates have been discussed.

## **7.2 Methodology**

### **7.2.1 Sample Preparation**

A commercially available fast cure Ethyl Vinyl Acetate (EVA) sheet, having UV blocking additives and other stabilizers, was procured from a reputed manufacturer and laminated into multiple 9-cell mini-modules using solar glass, crystalline silicon solar cells and fluoropolymer based backsheets. The lamination was done in a laboratory-scale laminator at 150 °C for 15 minutes. Each cell inside the mini-modules was connected with interconnect ribbons for electrical measurements. After the lamination, 3 mini-modules (UVC-2 to 4 in Fig. 7.1) were covered with Aluminum layer at the backside to minimize the ingress of Oxygen. Further, 2 of these mini-modules (UVC-3 and UVC-4) were covered with insulation layers to maintain these samples at higher temperatures during the Xenon aging tests (as shown schematically in Fig. 7.1). These samples were laminated at Arizona State University as part of a joint project to investigate the effects of UV aging on different EVA materials from different manufacturers (one each from China and India), initiated under the SERIUS- MAGEEP fellowship for internship at Arizona State University Photovoltaics Reliability Laboratory (ASU-PRL).

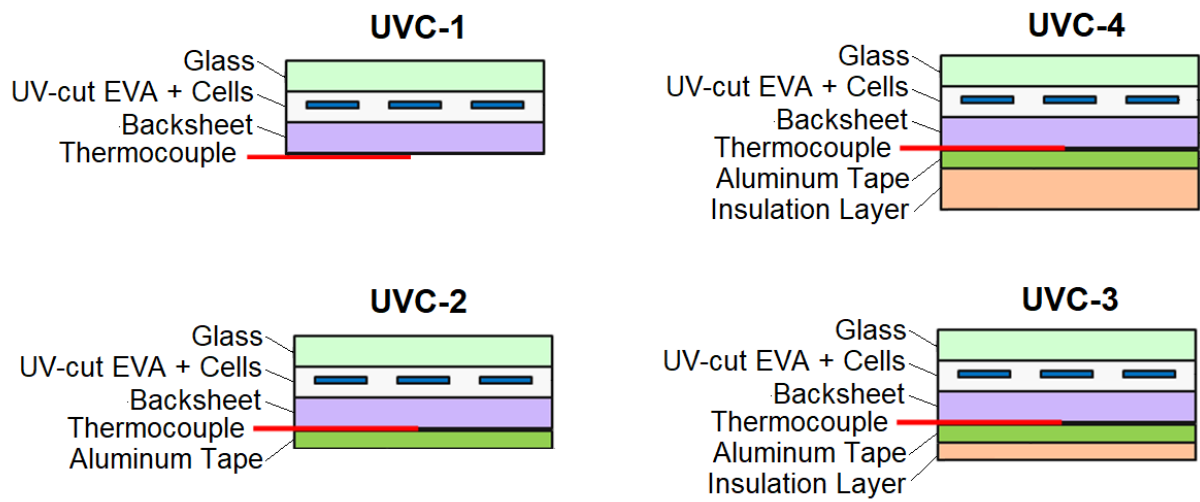
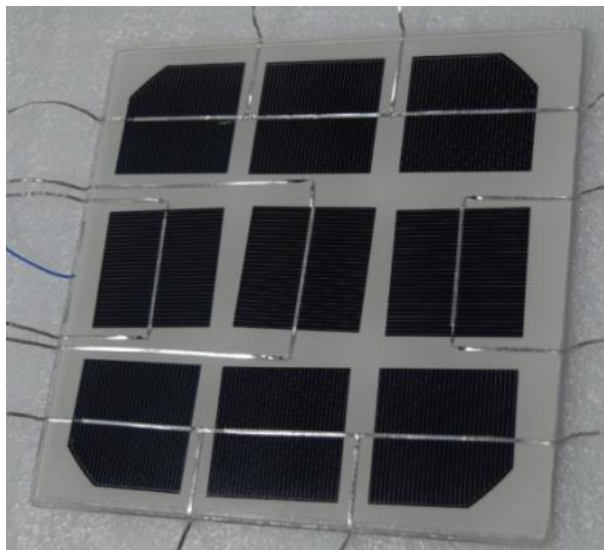


Fig. 7.1: Schematic diagram of the mini-modules made using UV absorbing (UV-cut) EVA.



(a)



(b)

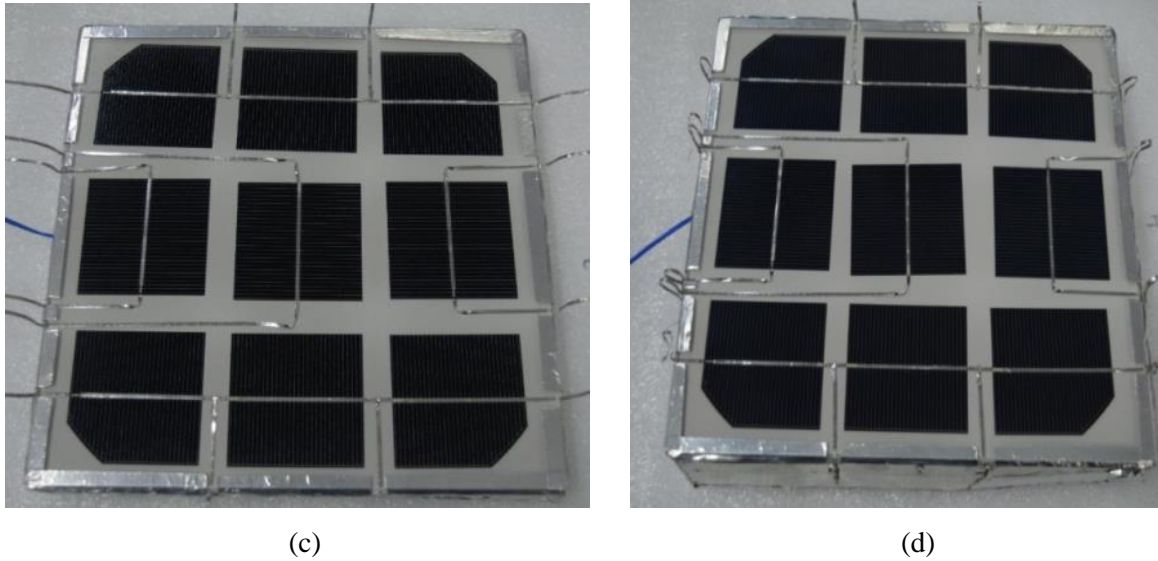


Fig 7.2: Front view of the mini-modules made using UV absorbing (UV-cut) EVA - (a) UVC-1 (b) UVC-2 (c) UVC-3 and (d) UVC-4. Each laminate is comprised of 9 cells with individual electrical connections. The blue wire is the connection to a thermocouple attached to the backsheet of the laminate.

## 7.2.2 Details of Test Setup

The mini-modules were placed on both sides of the Black Panel temperature sensor inside the Xenon chamber as shown in Fig. 7.3. An additional mini-module laminated using UV transmitting EVA film was also placed inside the chamber (which will be discussed in Chapter 8). The thermocouple from each mini-module was connected to a data logger (make: Campbell Scientific, model: CR1000). The central cell in each mini-module have been maintained under short-circuit condition in order to compare it with the other open-circuited cells. The accelerated test has been carried out in the Xenon chamber, operated with the following set points:

- Total UV intensity: 75 W/m<sup>2</sup>
- Black Panel temperature: 60 °C
- Chamber air temperature: 40 °C
- Chamber Humidity: 20% RH

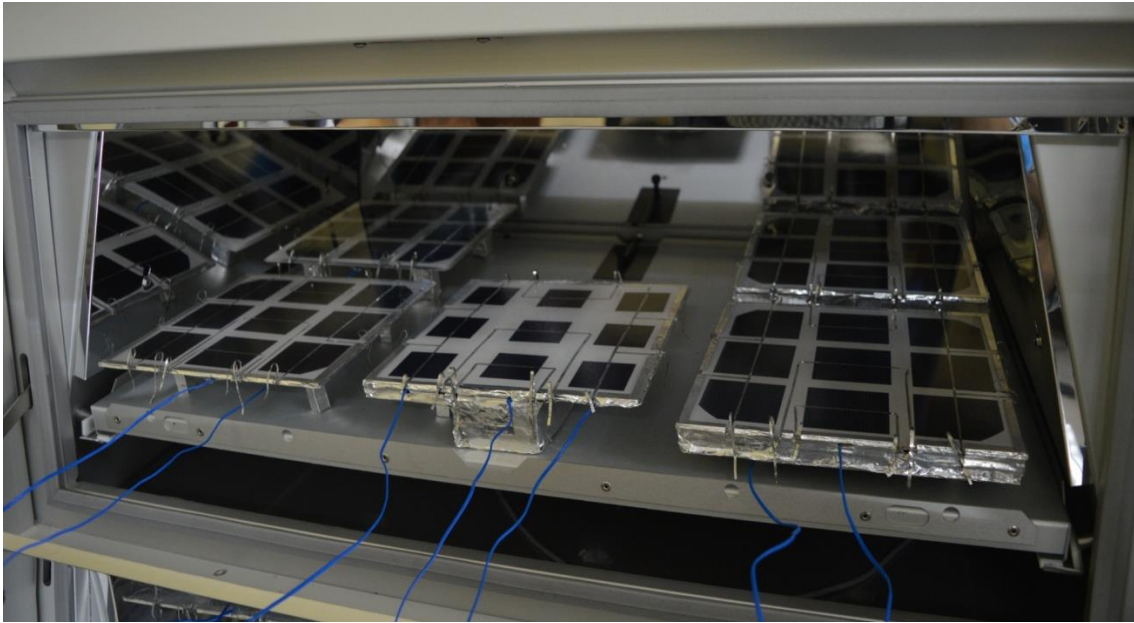


Fig. 7.3: Mini-modules placed inside the Xenon chamber for accelerated testing.

Xenon lamps have a spectrum which closely matches the solar spectrum outside the earth's atmosphere. However, to take care of the UV filtering effects of the atmosphere, the Xenon chamber is fitted with additional filters (Daylight Q) which ensures that the light spectrum closely matches the outdoor solar spectrum (with less than 0.5% spectral mismatch in the UV wavelength band between 300 to 400 nm, and within 5% mismatch in the wavelength bands between 400 to 800 nm) [122].

The Xenon chamber was calibrated to operate at  $75 \text{ W/m}^2$  total UV intensity (which is the maximum rating for this chamber) on the plane of the sample holder. However, since the samples had additional insulation at the back, which raised their height by ca. 5 cm, the effective UV irradiance on top of each solar cell varied depending on the position inside the chamber. A calibrated radiometer (make: Q-Labs, model: CR20) was used to measure the irradiance at the center of each solar cell (in the presence of the other mini-modules) as shown in Fig. 7.4. The distribution of the UV irradiance on the samples is shown in Fig. 7.5.

In addition to the thermocouples connected to the middle of the mini-modules on the backside, infrared (IR) thermography has been used to detect the temperature of the individual solar cells in the mini-modules. For this purpose, the sample was taken out of the chamber, and its IR image was taken using a handheld IR camera at an interval of ca. 10 seconds. From the

cooling curves of the module, the initial temperature of the cells was estimated (by extrapolating backwards to time zero), as shown in Fig. 7.6. The IR images at the beginning and end of the measurement cycle are also shown in Fig. 7.6. Fig. 7.7 shows the temperature of the solar cells in the various mini-modules, as estimated by the above procedure.



Fig. 7.4: Measurement of the irradiance at the position of the solar cells of sample UVC-3.

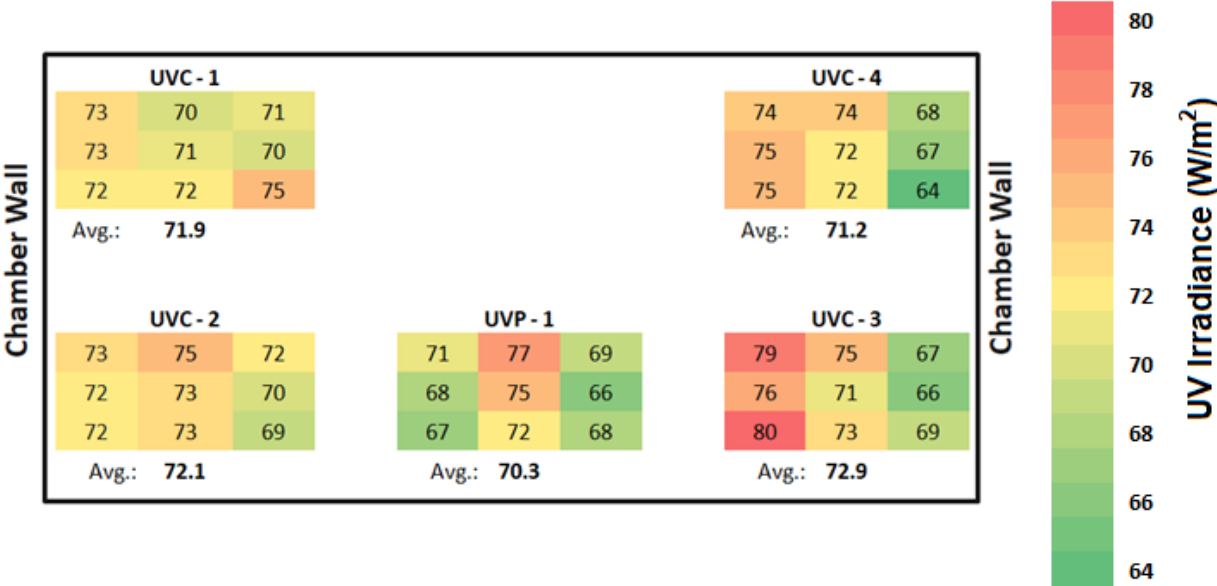
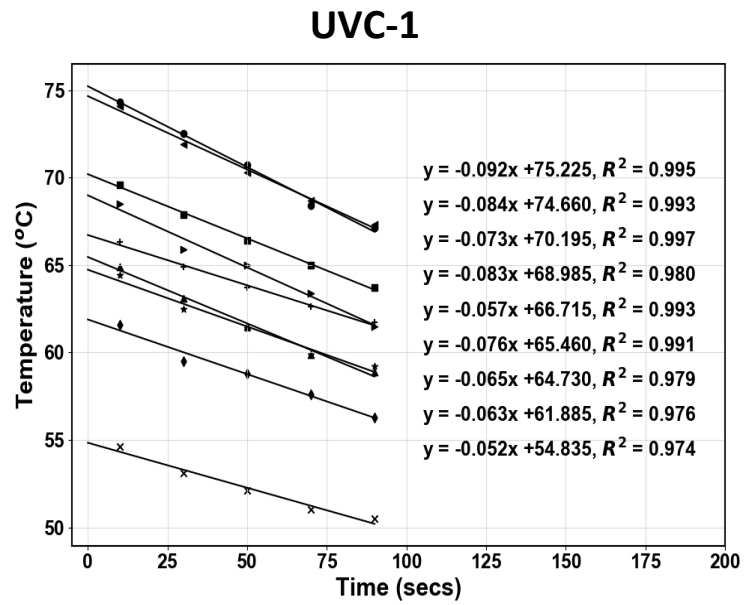
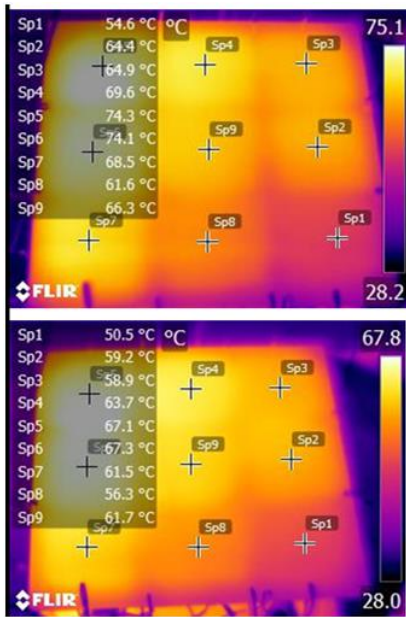
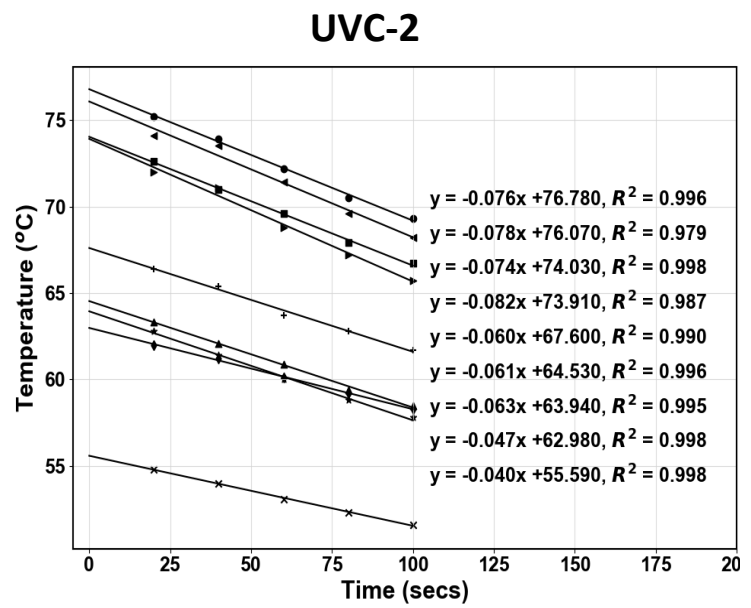
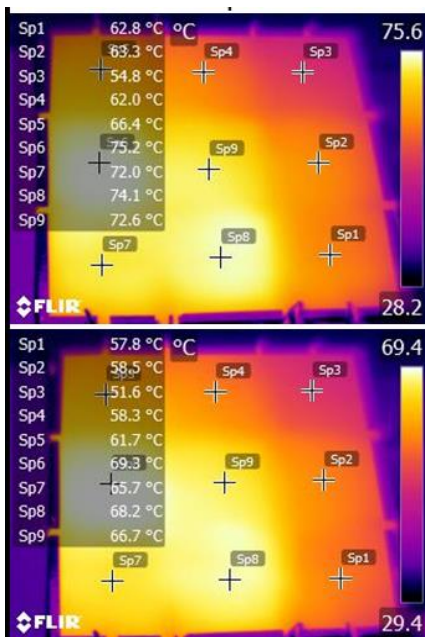


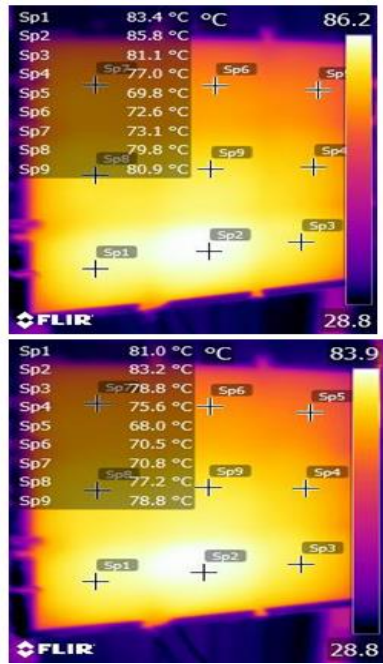
Fig. 7.5: UV irradiance on the solar cells of the mini-modules (in  $W/m^2$ ). The cells have been colour-coded based on the cell temperature, with green representing low irradiance (ca.  $64 W/m^2$ ), while red indicates high irradiance (ca.  $80 W/m^2$ ). The average intensity for the whole sample (9 cells) is indicated below each sample.



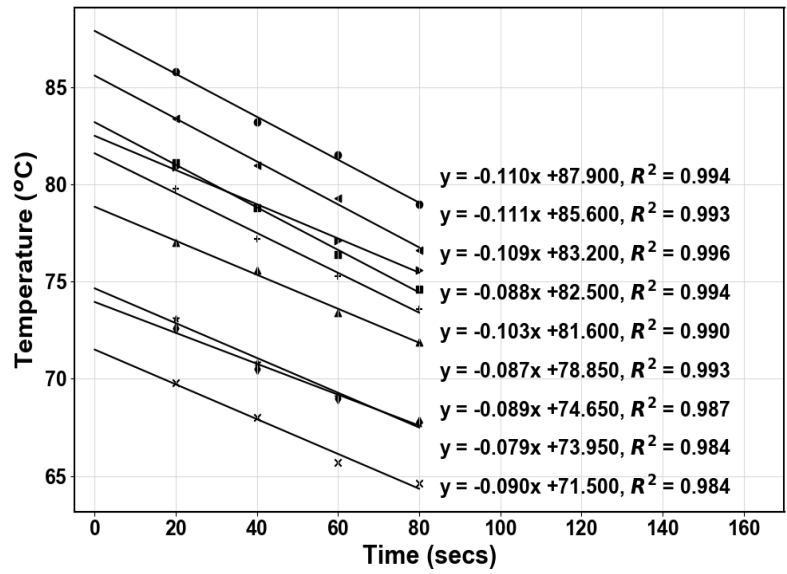
(a)



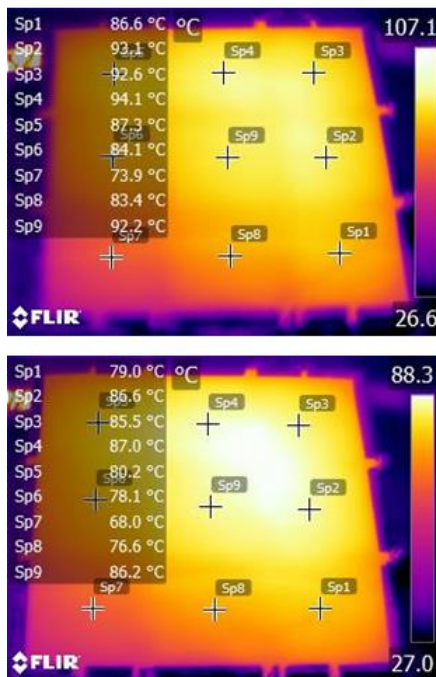
(b)



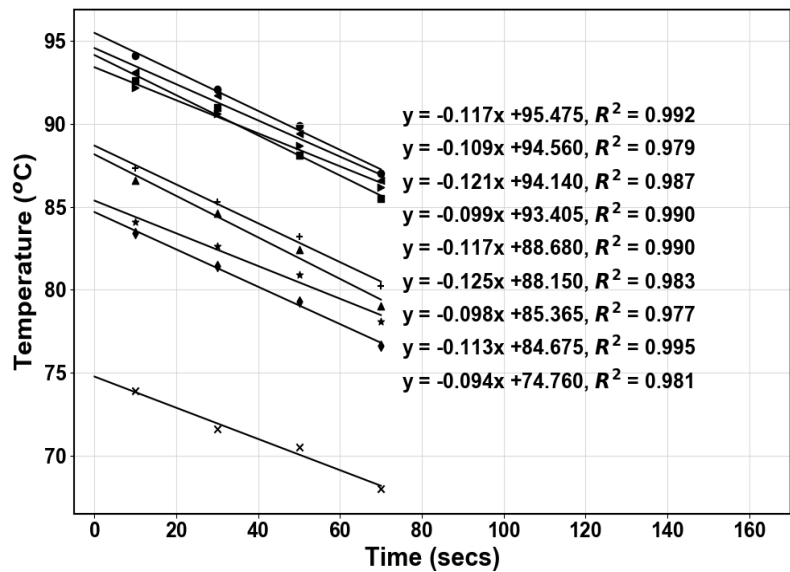
### UVC-3



(c)



### UVC-4



(d)

Fig. 7.6: Plot of the temperature (extracted from the IR image) versus the cooling time for the mini-modules – (a) UVC-1 (b) UVC-2, (c) UVC-3, and (d) UVC-4. Representative IR images are shown on the left side. IR image on top is taken after sample is taken out of the Xenon chamber and the bottom IR image is the last IR image taken for the sample.

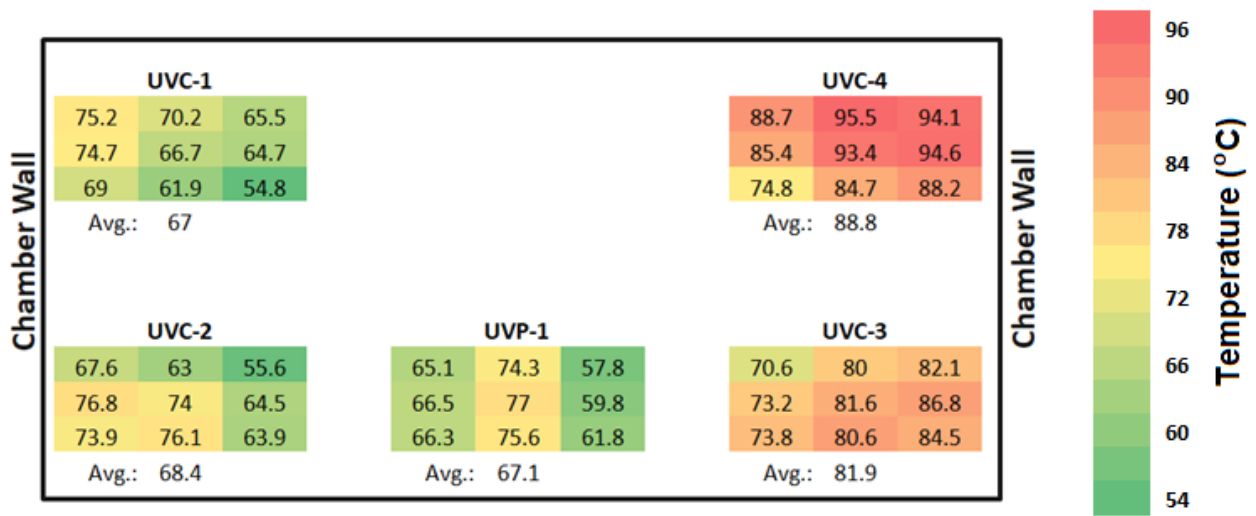


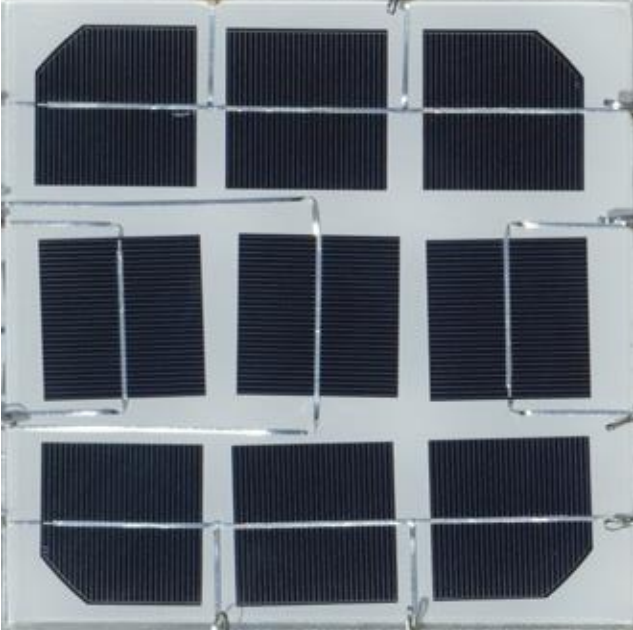
Fig. 7.7: Temperature of the solar cells in the mini-modules (based on IR measurements).

### 7.3 Results and Discussion

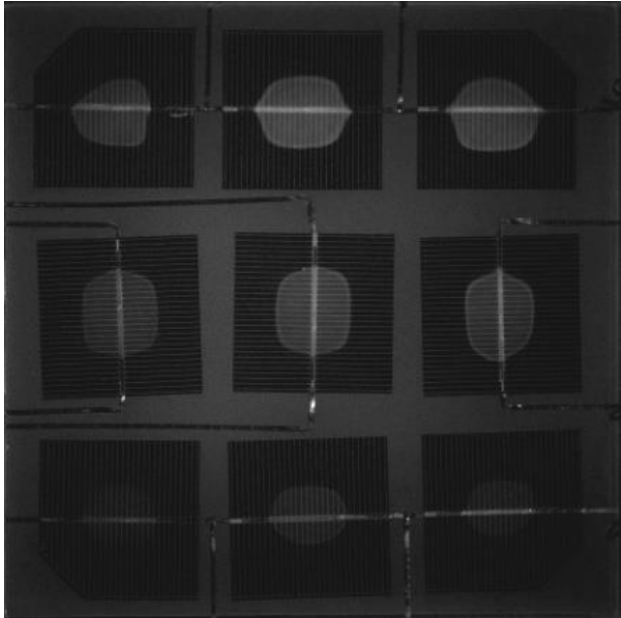
Four mini-modules with UV absorbing EVA were studied in the Xenon chamber. Out of the four samples, sample #1 (UVC-1) did not have any aluminum backing layer. Hence it had maximum photo-bleaching effect due to ingress of oxygen. This is evident from the fluorescence image of the sample shown in the right side of Fig. 7.8(a), wherein the fluorescence is concentrated only at the central portion of the cells, with no fluorescence at the cell edges (due to photo-bleaching). However, no discoloration is visible in the sample (as evident from the image on the left side). Discoloration is visible to the naked eye only in samples UVC-3 and UVC-4, but the fluorescence images clearly show fluorescence at the center of the cells of all four samples. Thus, fluorescence imaging serves as an early indicator of discoloration. There was some amount of oxygen ingress in the aluminum-taped samples as well (samples UVC-2 to UVC-4), along the cuts in the aluminum tape at the edges where interconnect ribbons and the thermocouples had been brought out (as shown in Fig. 7.9). Sample 4 (UVC-4) had an aluminum layer and also maximum insulation thickness, which ensured that most of its cells operated at the highest temperatures. So, the sample UVC-4 showed the maximum yellowing effect (and highest levels of fluorescence). Figure 7.9 explains the different regions in the fluorescence images, and also shows the entry points for oxygen ingress into the laminates. The effect of UV

aging on the yellowness index, fluorescence intensity, and short-circuit current has been discussed in the following subsections.

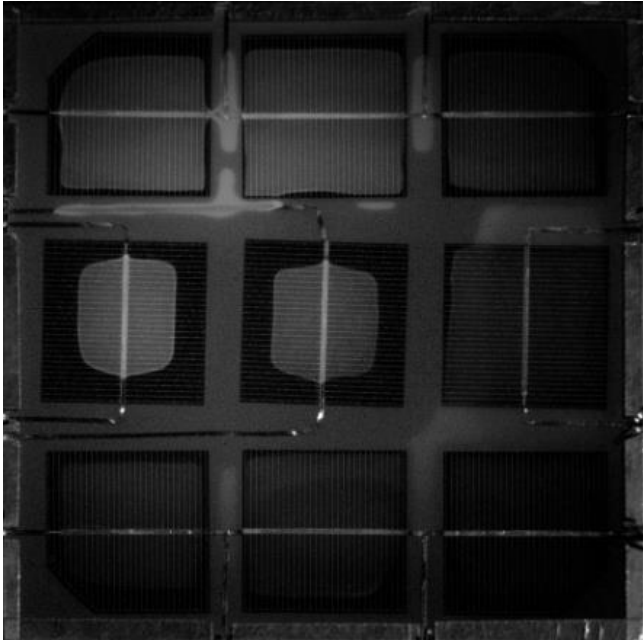
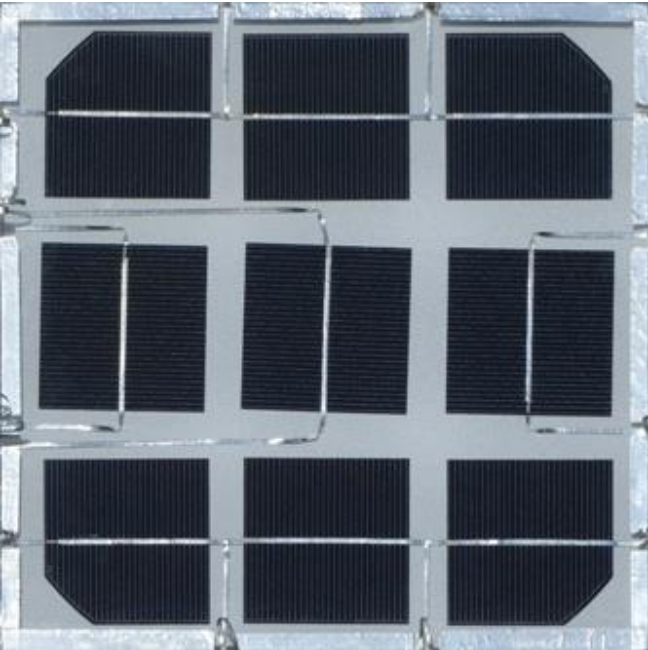
**Visual image under natural sunlight**



**Fluorescence image under 365 nm UV light**



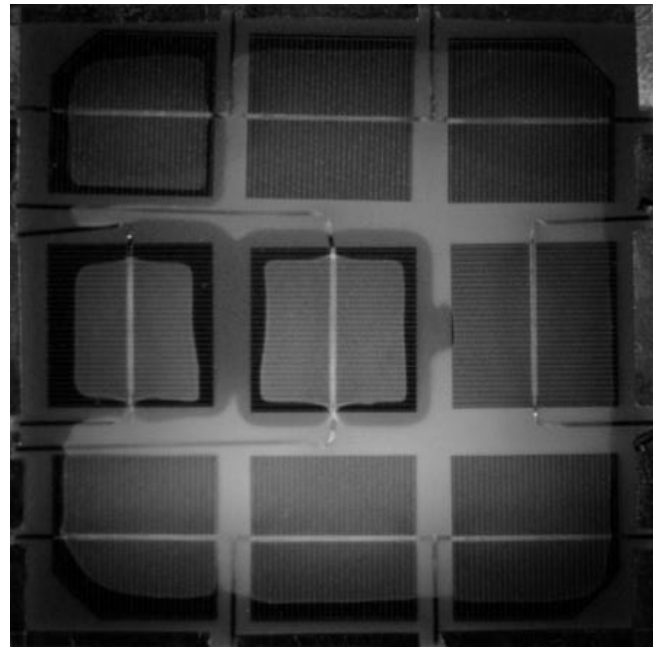
(a)



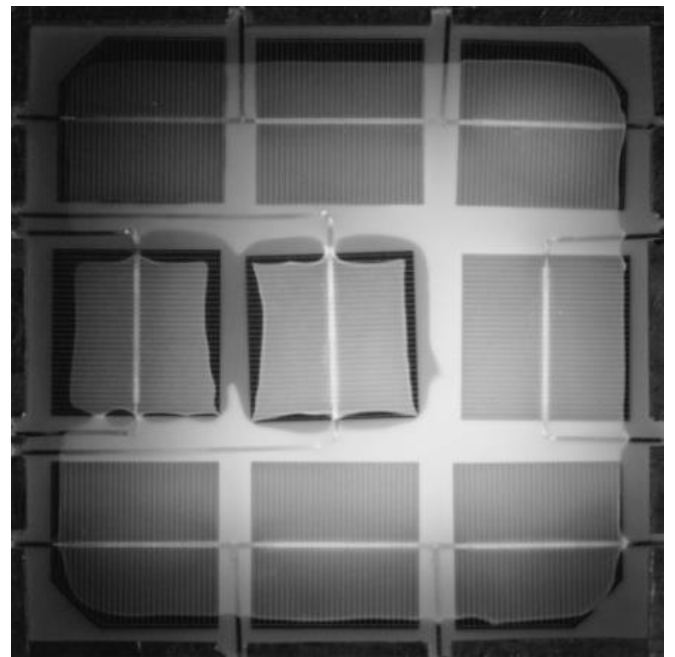
(b)

**Visual image under natural sunlight**

**Fluorescence image under 365 nm UV light**

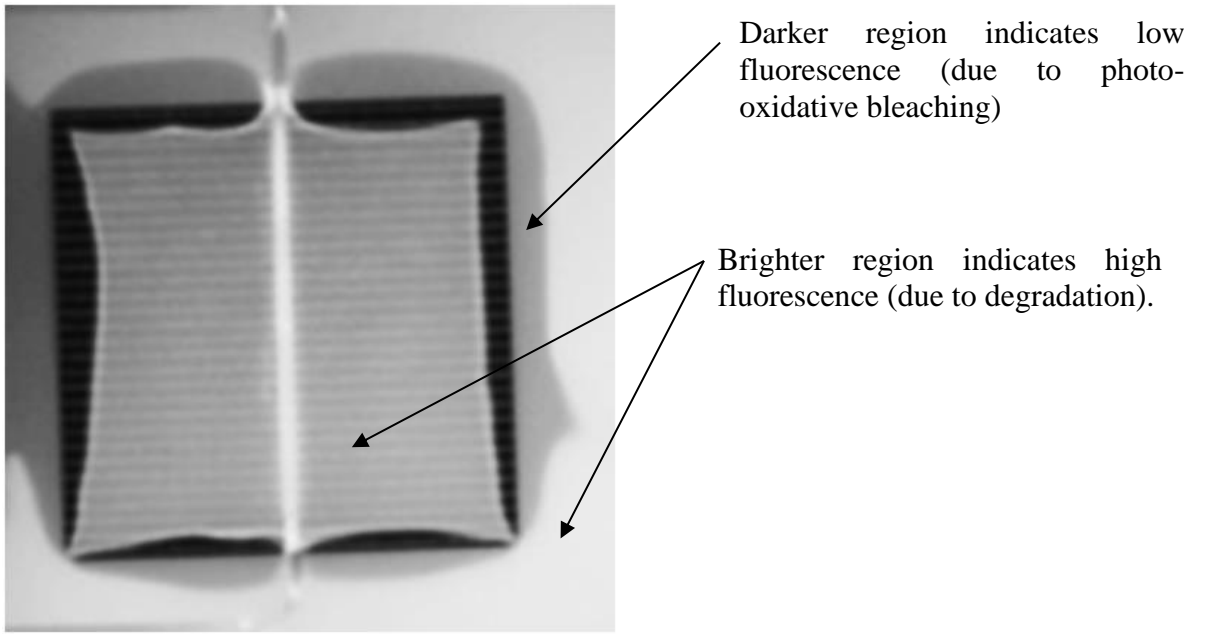


(c)

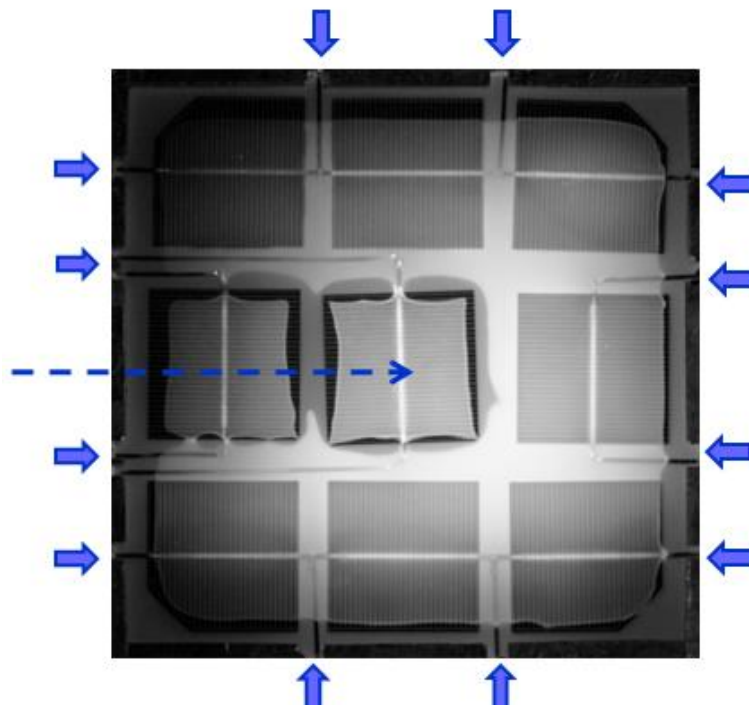


(d)

Fig.7.8: Digital images under natural sunlight (left side) and fluorescence images (right side) under 365 nm UV excitation (right side) of the mini-modules taken after ca. 300 kWh/m<sup>2</sup> Xenon-based UV exposure – (a) UVC-1, (b) UVC-2, (c) UVC-3, and (d) UVC-4.



(a)



(b)

Fig. 7.9: (a) Different regions in the fluorescence image of the UV-cut samples, and (b) pathways of oxygen ingress into sample UVC-4 – along the interconnect ribbons (marked with solid blue arrows) and also along the backside thermocouple (marked with dashed blue line).

### 7.3.1 Effect on Fluorescence Spectra

The discoloration in the EVA encapsulant is due to the generation of fluorophores (molecules that absorb UV light and emit in the visible wavelength range) [53]. The fluorescence spectra from such fluorophores have been measured under 365 nm UV excitation, as shown in Fig. 7.10. The samples initially show a decrease in the fluorescence intensity at around 480 nm, followed by an increase in the fluorescence intensity (with peak close to 570 nm). This fluorescence in the blue wavelength may be attributed to curing-generated fluorophores, which disintegrate upon UV exposure. Such extinction of fluorescence has also been reported in field-aged PV modules by Morlier *et al.* [123]. Fig. 7.11 shows the fluorescence spectra measured at the center of the cells exposed to UV at different temperatures, and also resultant spectra after baseline correction. The spectra peaks around 580 nm, and the fluorescence intensity is higher for samples exposed to radiation at higher temperatures. The integrated UV fluorescence intensity (from the baseline-corrected spectra) has been found to scale with change in  $YI$ , despite the scatter in the data, as shown in Fig. 7.12.

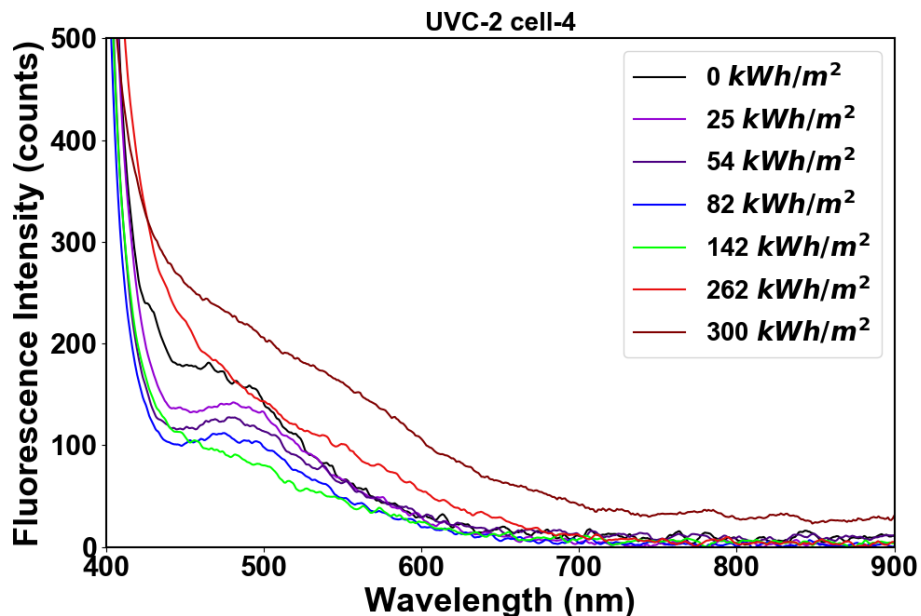
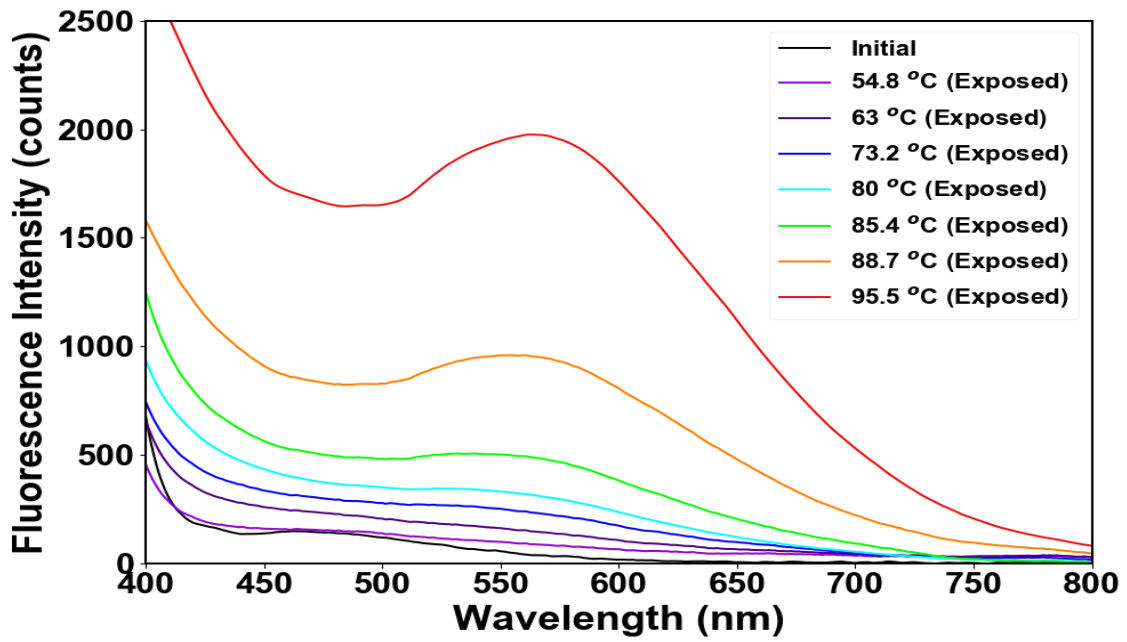
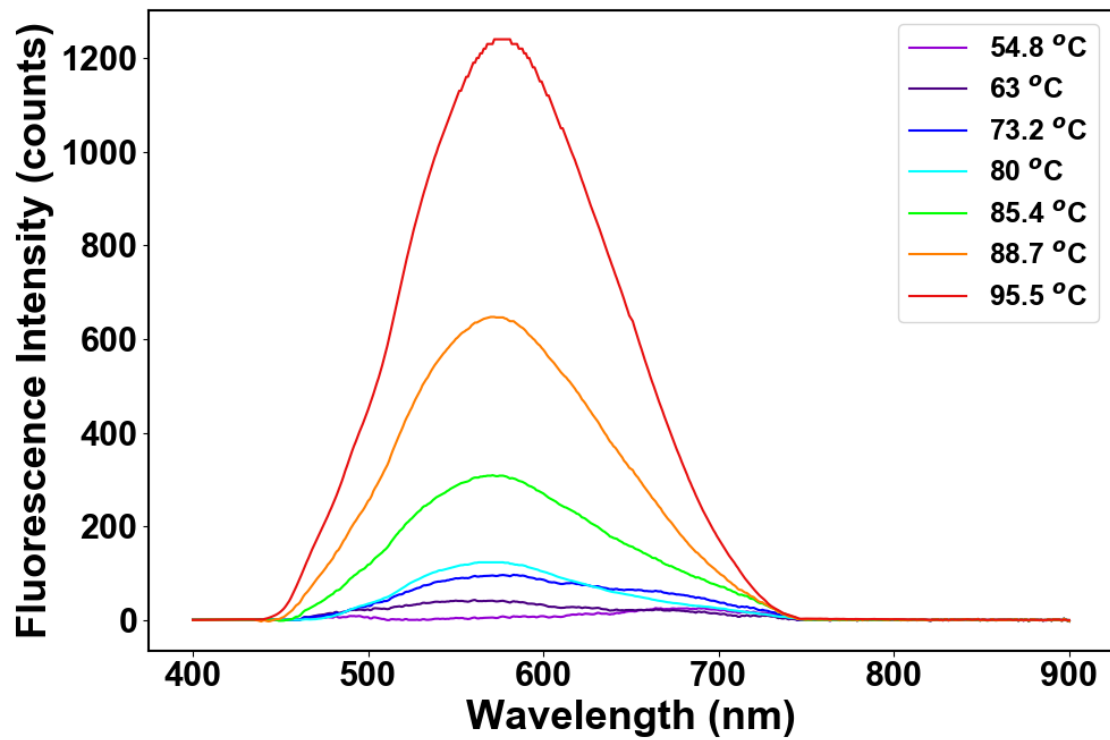


Fig.7.10: Fluorescence spectra of UVC-2 cell showing the initial decrease in fluorescence around 430 nm.



(a)



(b)

Fig.7.11: Fluorescence spectra of the UV-cut coupons maintained at different temperatures – (a) as measured (b) after baseline correction.

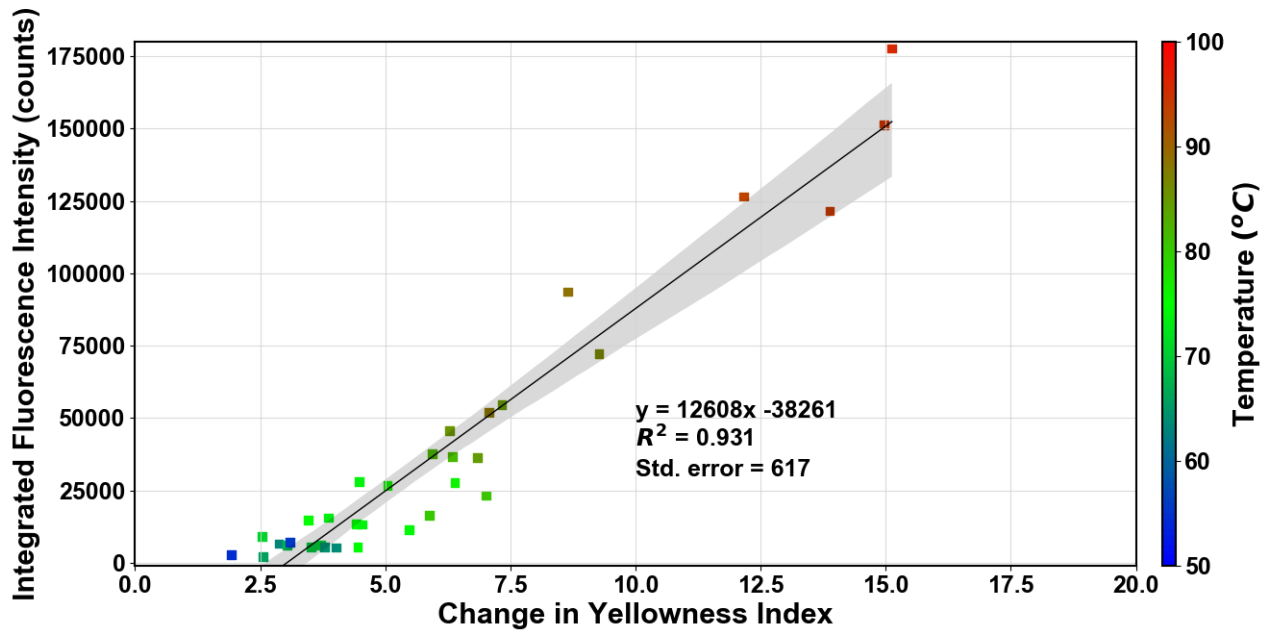


Fig. 7.12: Correlation of change in integrated fluorescence intensity with change in *YI* (after 300 kWh/m<sup>2</sup> UV dose).

### 7.3.2 Effect on Yellowness Index (*YI*)

The effect of UV exposure on the *YI* (increase above the initial pre-exposure value) is plotted for the mini-modules in Fig. 7.13. The data points are color-coded based on the temperature of the solar cell (temperature at center of cell, estimated through IR thermography). It is evident from this figure that the samples with lower temperatures (say around 55 – 60 °C, marked in blue colour) have shown very little increase in *YI* while the samples at higher temperatures have suffered significant discoloration. In particular, *YI* of the samples at temperatures > 85 °C has increased more rapidly than for samples at temperatures between 70 – 85 °C, after UV dose of 200 kWh/m<sup>2</sup>. There is a gap in the data points near UV dose of 200 kWh/m<sup>2</sup>, where the Xenon chamber was not halted for measurements due to the maintenance of the module solar simulator.

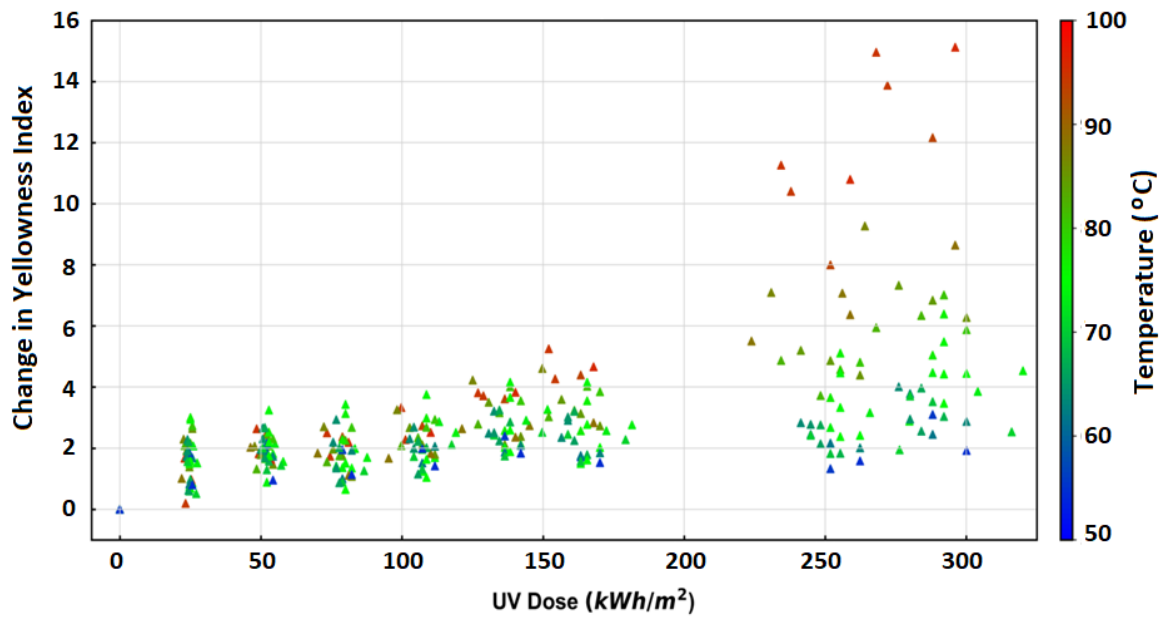


Fig.7.13: Change in *YI* of the samples plotted against the UV dose.

Figure 7.14 shows the change in *YI* for some selected cells (covering the full temperature range). It can be seen that there is an initial rapid increase in the *YI* within the first 25 kWh/m<sup>2</sup> UV exposure (a jump of 1 to 2 units), after which the rate of yellowing slows down, but continues at almost linear rate (except for the high sample temperature of 94 °C). Figure 7.15 shows the *YI* data for all cells with temperature less than 88 °C. The blue diamonds indicate the average of “change in *YI*” for every dose at which measurement was made. The linear regression line presents a good fit to these average values, with a  $R^2$  of 0.9. Hence, the discoloration can be considered as linearly proportional to the UV dose, for temperatures below 88 °C. Figures 7.15 to 7.18 show the *YI* versus UV dose plots for each cell of the four laminates. The slope of the yellowing rate increases with increase in the sample temperature. In these figures, the linear fit is considered for the points after the initial rise in *YI* (and not directly from the initial zero value, since non-linear behavior is observed around the initial value). For very high-temperature cells (above 88 °C), the yellowing rate seems to follow power law relation with UV dose (which is evident from the plot of natural logarithm of change in *YI* versus UV dose for sample UVC-4, shown in Fig. 7.19, in cells - 1,2,3,5,6,9).

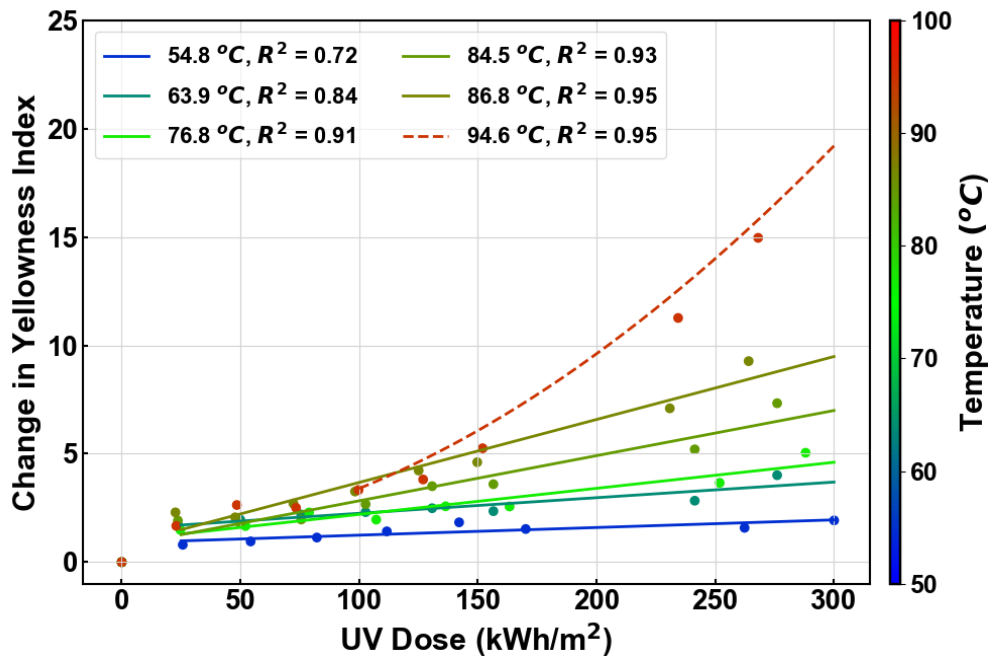


Fig.7.14: Change in *YI* for selected cells. Solid lines indicate linear fit, while dashed line indicates non-linear fit.

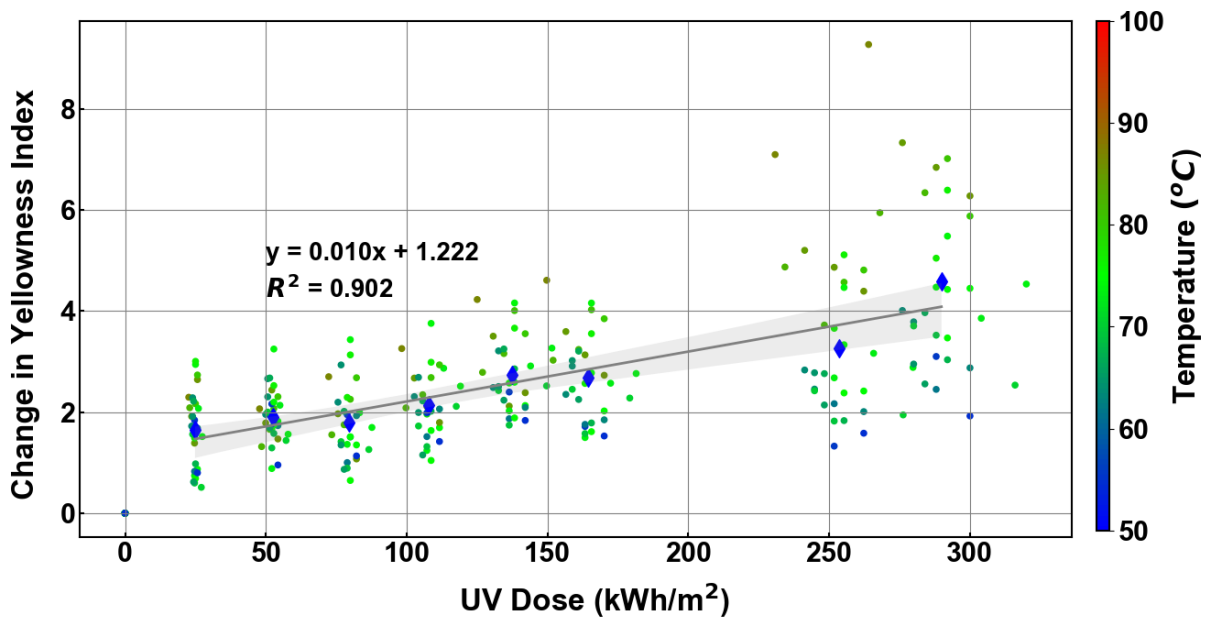


Fig.7.15: Change in *YI* versus UV dose for samples with temperature less than 88 °C (blue diamond indicate the average change in *YI* at corresponding UV dose and the regression line is fitted to these average values).

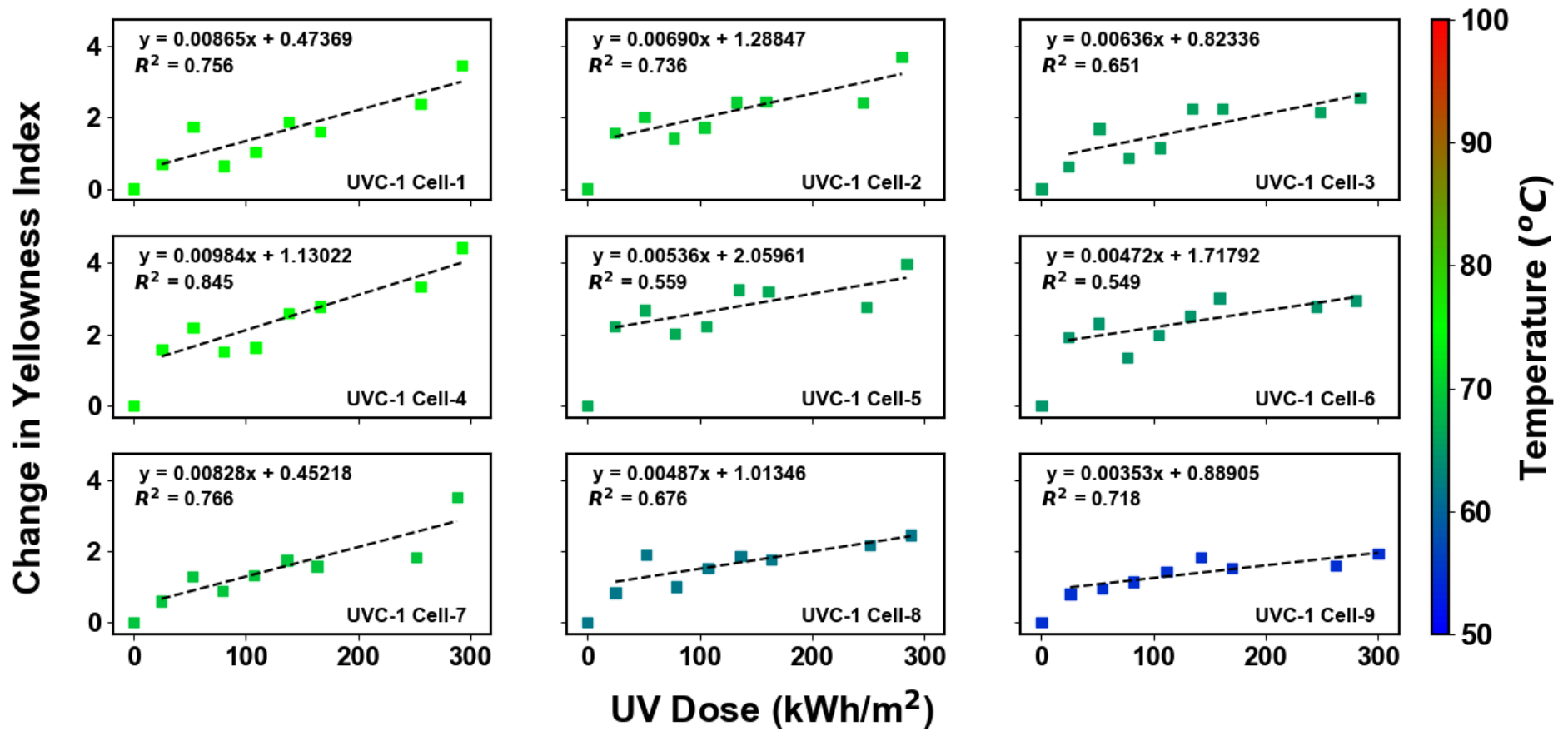


Fig.7.16: Change in *YI* at the center of each cell of sample UVC-1 plotted against UV dose. The straight trend line is fitted to the data points after the initial UV dose of 25 kWh/m<sup>2</sup>. The data points are colour-coded based on the sample temperature.

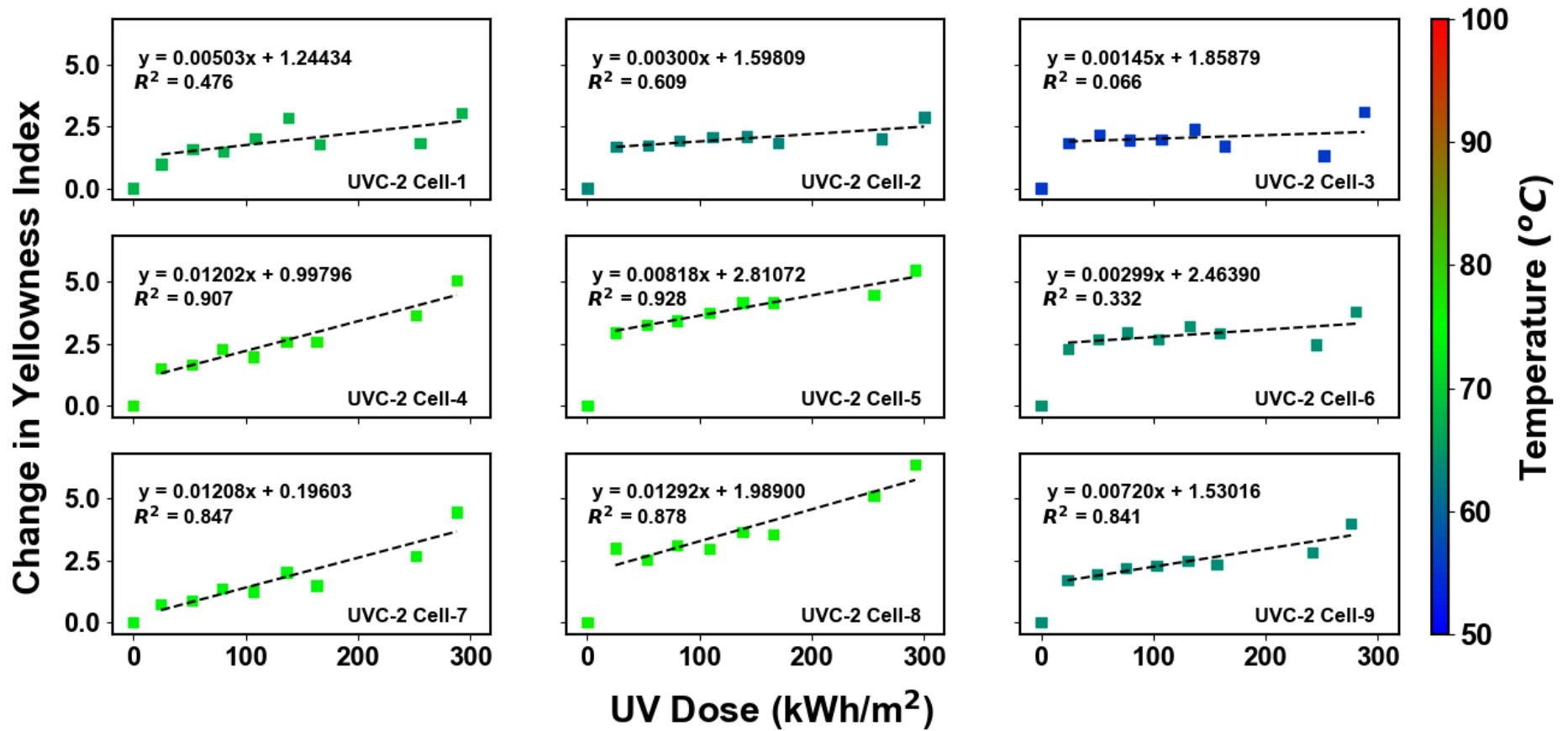


Fig.7.17: Change in YI at the center of each cell of sample UVC-2 plotted against UV dose. The straight trend line is fitted to the data points after initial UV dose of 25 kWh/m². The data points are colour-coded based on the sample temperature.

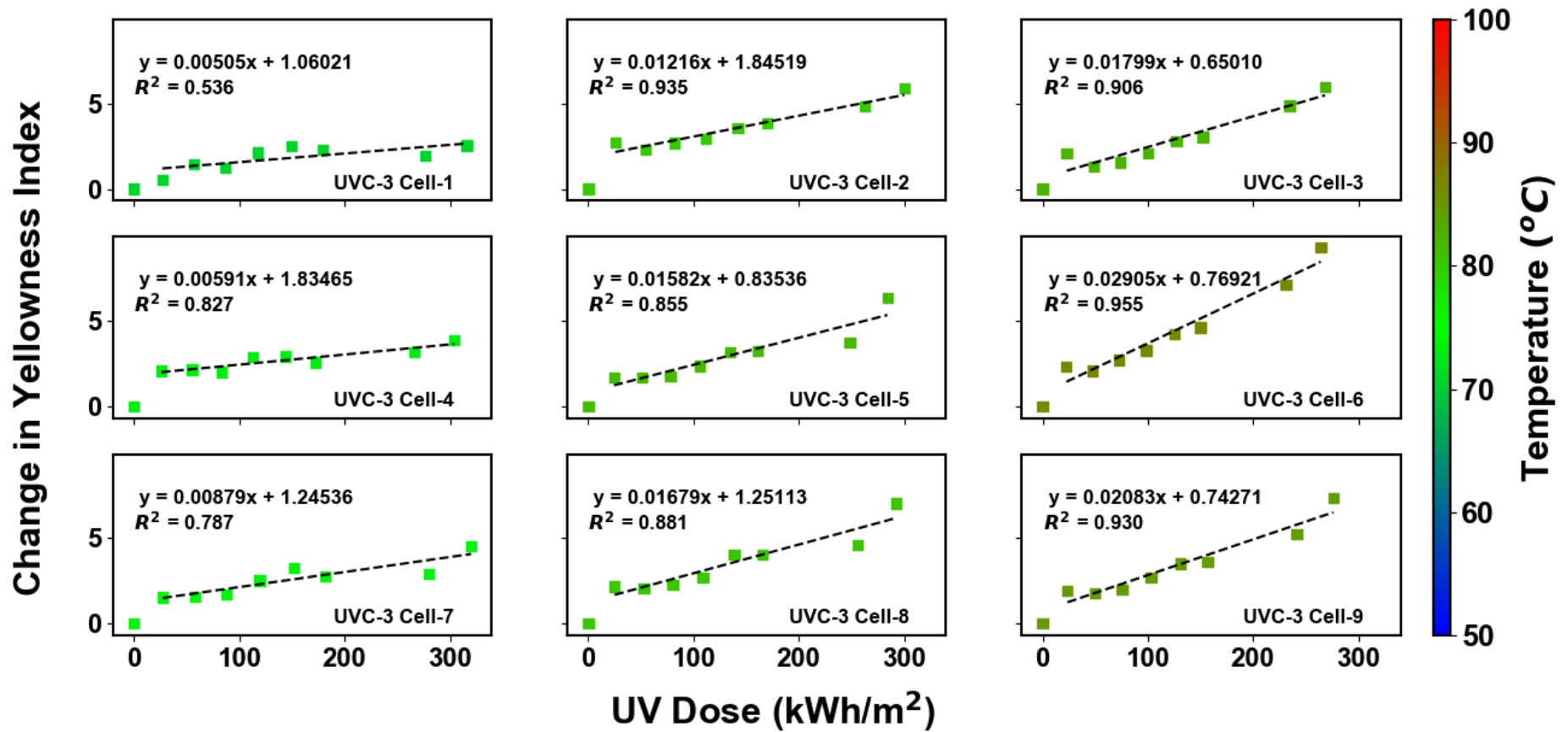


Fig.7.18: Change in *YI* at the center of each cell of sample UVC-3 plotted against UV dose. The straight trend line is fitted to the data points after initial UV dose of 25 kWh/m<sup>2</sup>. The data points are colour-coded based on the sample temperature.

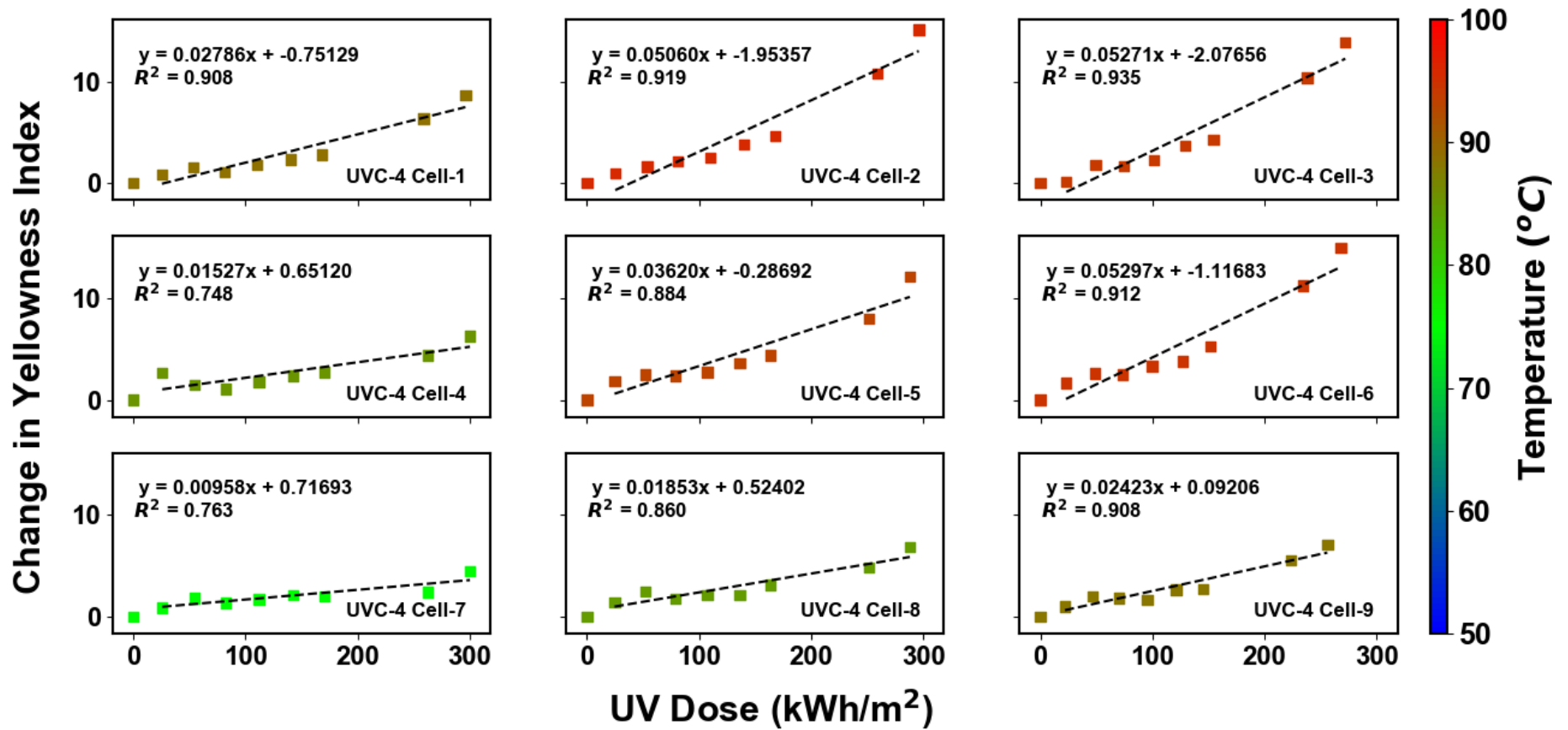


Fig.7.19: Change in *YI* at the center of each cell of sample UVC-4 plotted against UV dose. The straight trend line is fitted to the data points after initial UV dose of 25 kWh/m<sup>2</sup>. The data points are colour-coded based on the sample temperature.

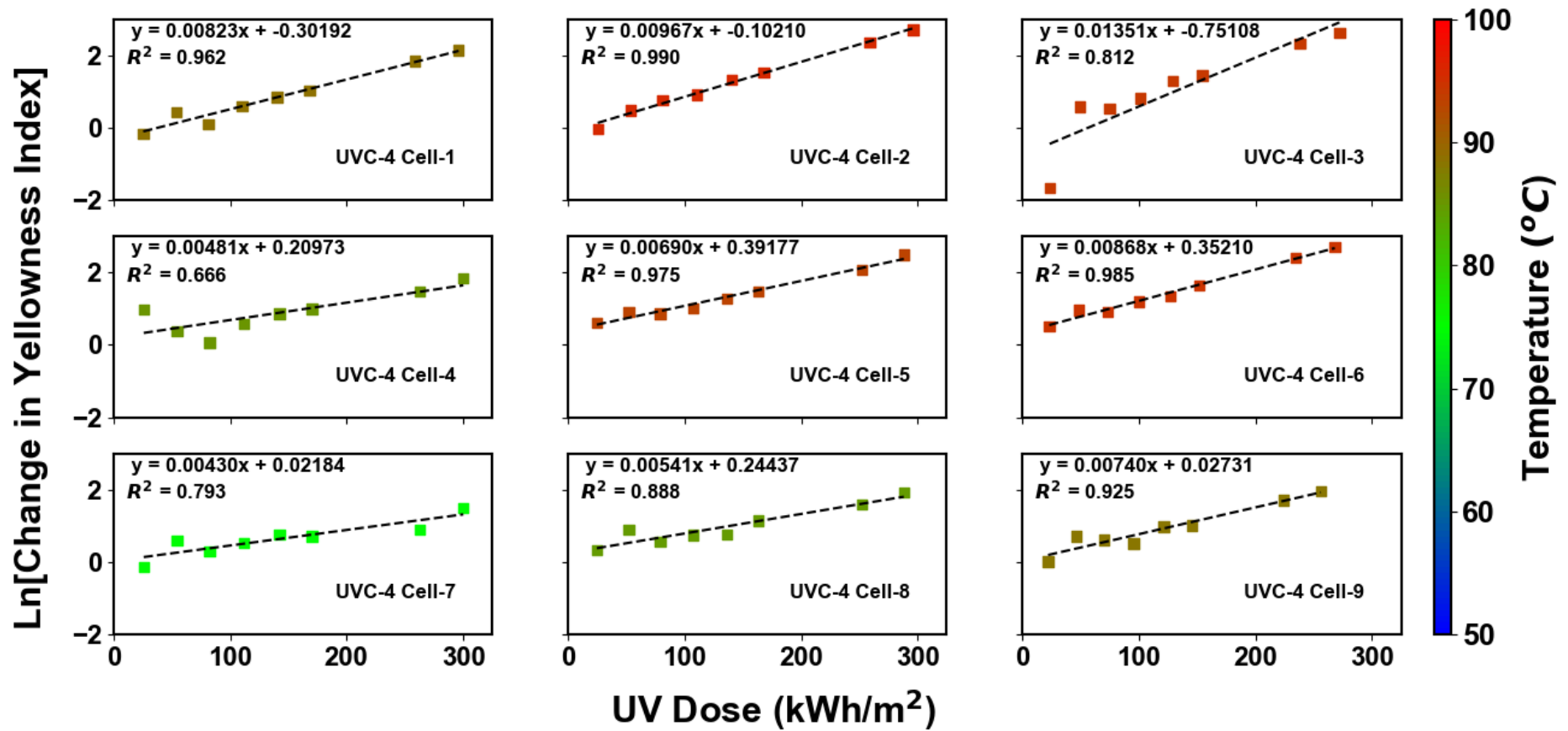
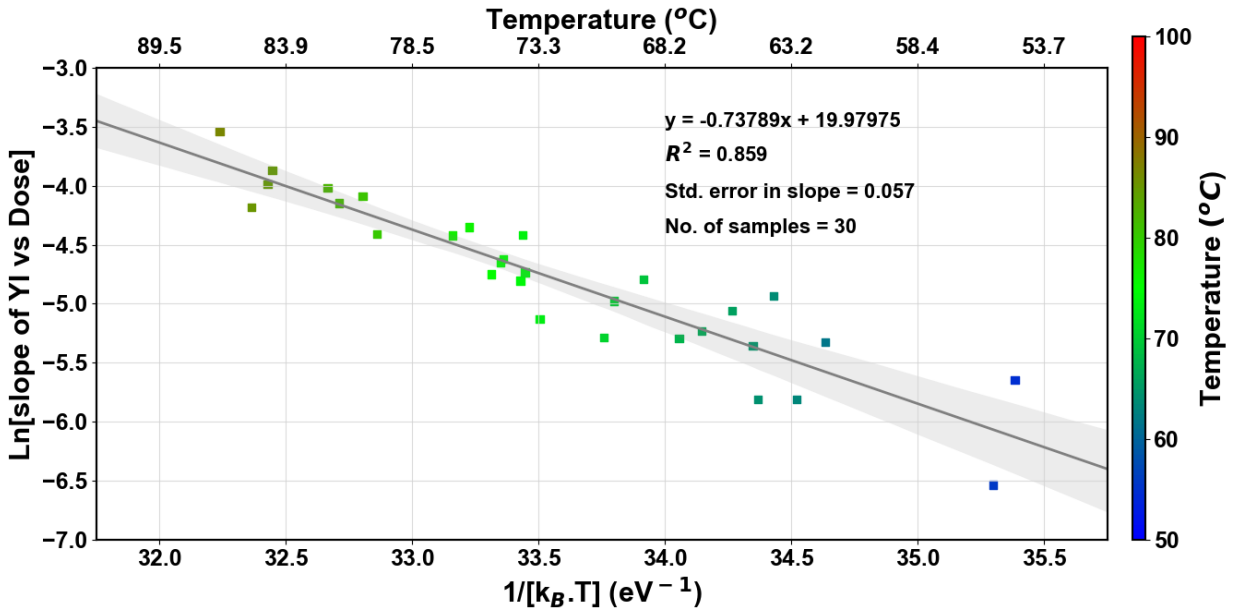
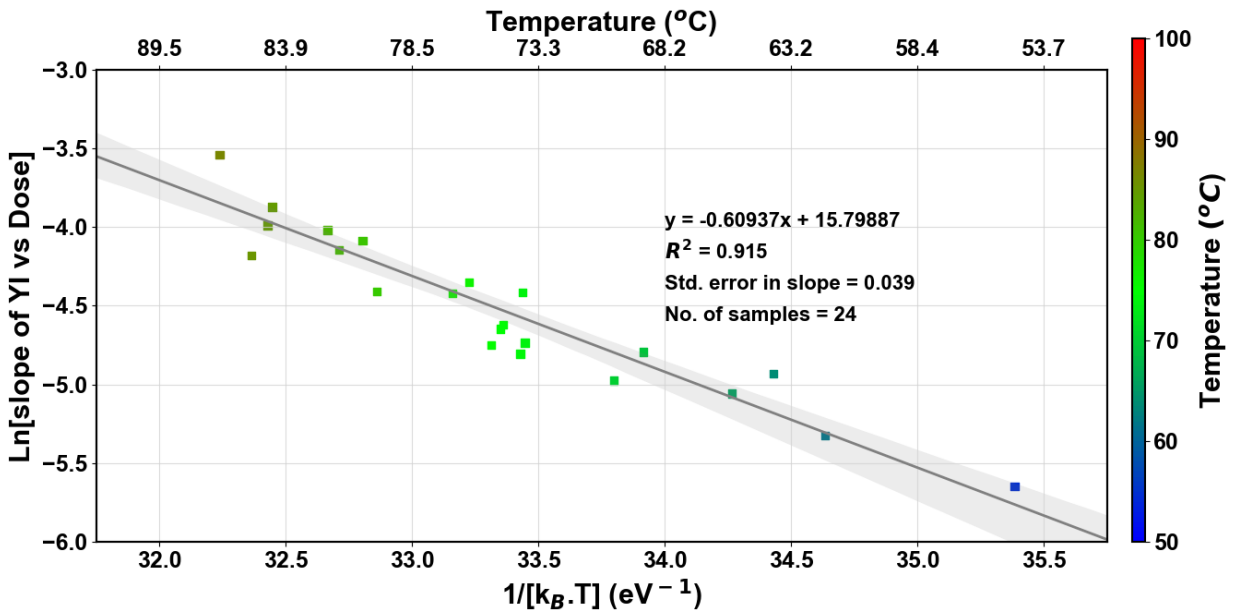


Fig.7.20: Natural logarithm of change in  $YI$  at the center of each cell of sample UVC-4 plotted against UV dose. The straight trend line is fitted to the data points after initial UV dose of 25 kWh/m<sup>2</sup>. The data points are colour-coded based on the sample temperature.

According to the transition state theory, activation energy is the minimum energy needed by the reactant molecules to react and form the product molecules [124]. As per the empirical Arrhenius law, the activation energy can be calculated from the slope of the plot of logarithm of the dependent variable (here change in  $YI$ ) versus the inverse of temperature [124]. However, instead of depending on the single degradation value at the end of the experiment, it is better to consider the slope of the degradation path, as done by Miller *et al.* [125]. Accordingly, the slopes of the linear fit lines (shown in Figures 7.16 to 7.19) have been considered for further analysis (excluding the high temperature cells showing exponential trends), and the natural logarithm of these slopes has been plotted in Fig. 7.21. Some of the samples (6 out of 30) showed erratic yellowing leading to a correlation coefficient below 0.8 ( $R^2$  of the linear fit below 0.64). Such samples have been separated out, and the remaining samples with linear fit  $R^2 > 0.64$  have been considered as “good fits” and plotted in Fig. 7.21(b). The x-axis of Fig. 7.21 is the inverse of the product of Boltzmann constant and the absolute temperature of sample ( $1/(K_B \cdot T)$ ), so the slope of the linear regression line in Fig. 7.21 directly gives the value of Activation energy in electron-volts (eV). From Fig. 7.21(b), the activation energy is found to be 0.609 eV, with a standard error of 0.039 eV (the coefficient of determination  $R^2$  is 0.91). This means that the 95% confidence interval for the activation energy is  $0.61 \pm 0.08$  eV (i.e., 0.53 to 0.69 eV). The value of 0.61 eV is within the range of Activation energy reported by Miller *et al.* [125] (0.52 to 0.70 eV) for their fast-cure EVA sample containing Cyasorb UV-531 (same UV absorber as in our case, as explained in Chapter 8).



(a)



(b)

Fig. 7.21: Arrhenius analysis of the slope of  $YI$  change versus UV dose. - (a) considering all cells below 88 °C, (b) considering cells below 88 °C, with linear correlation coefficient for UV dose > 0.64. Slope of the linear regression line indicates the activation energy in eV. The grey area around the trend-line indicates the 95% confidence interval for the slope. The data points have been colour-coded based on the cell temperature.

In the above discussion, it has been shown that the discoloration rate is proportional to the UV dose and has Arrhenius type temperature dependence (with activation energy of 0.61

eV). Hence the following model for discoloration of the UV-cut encapsulant has been adopted, which has also been suggested by Koehl [84] :

$$\Delta YI = A \cdot D \cdot \exp\left(\frac{-E_a}{k_B \cdot T}\right) \quad \dots (7.1)$$

where,

$A$  = pre-factor

$D$  = UV dose (integrated value between 280 – 400 nm), kWh·m<sup>-2</sup>

$E_a$  = activation energy, eV

$k_B$  = Boltzmann constant (= 0.0000861733 eV/K)

$T$  = absolute temperature, K

This model has been further analyzed to determine the acceleration factor in section 7.3.4.

### 7.3.3 Effect on Electrical Parameters

The electrical current-voltage characteristics have been measured on the Spire solar simulator, at sample temperature between 24 to 26 °C. The total degradation in the  $I$ - $V$  parameters has been shown in Fig. 7.22. It is evident that the degradation in power output is primarily due to short-circuit current loss. Majority of the cells showed degradation in the power output, but there are a few cells (5 out of total 36) that showed improvement in Power output (due to increase in Fill Factor, most probably due to contact resistance variation between the measurements). Since the yellowing of the encapsulant reduces the light transmitted to the underlying solar cells, it decreases the short-circuit current ( $I_{sc}$ ) of the cell (which is the predominant factor observed here). Hence, the  $I_{sc}$  degradation due to the accelerated tests is analyzed in detail in the forthcoming sections.

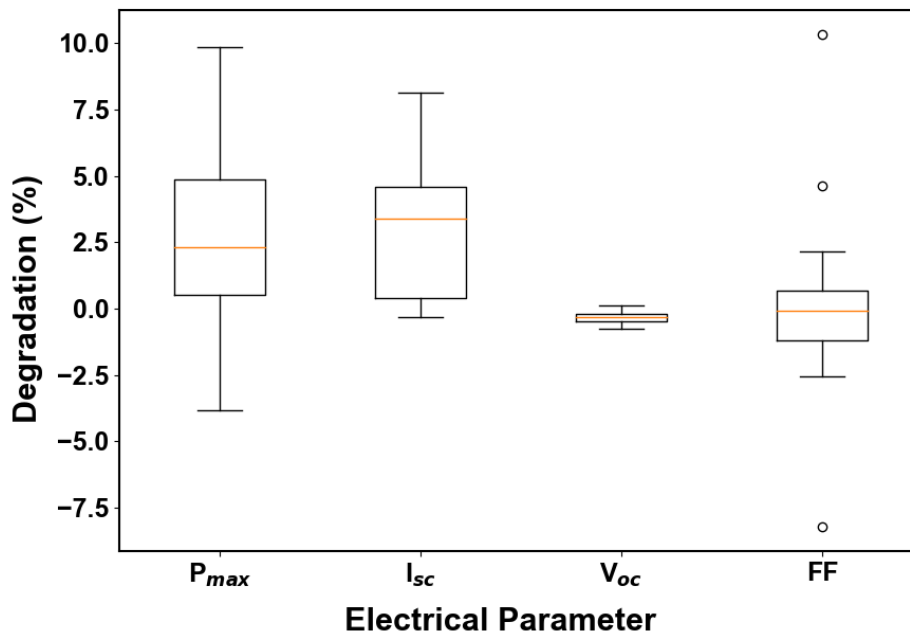
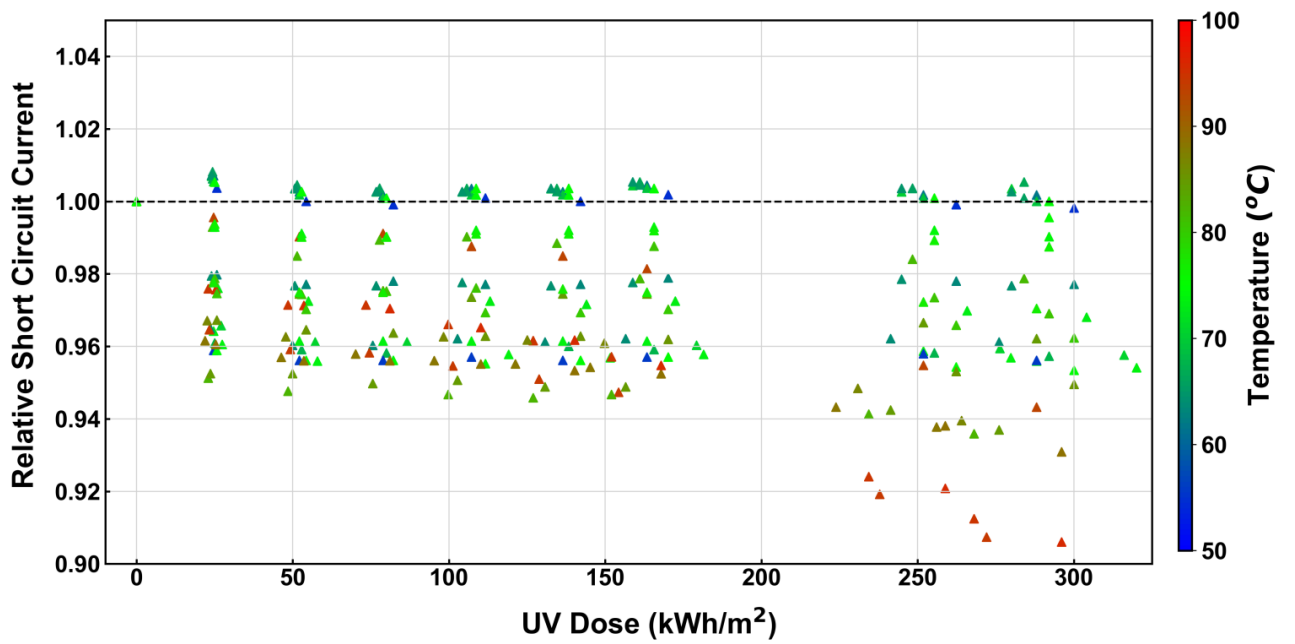
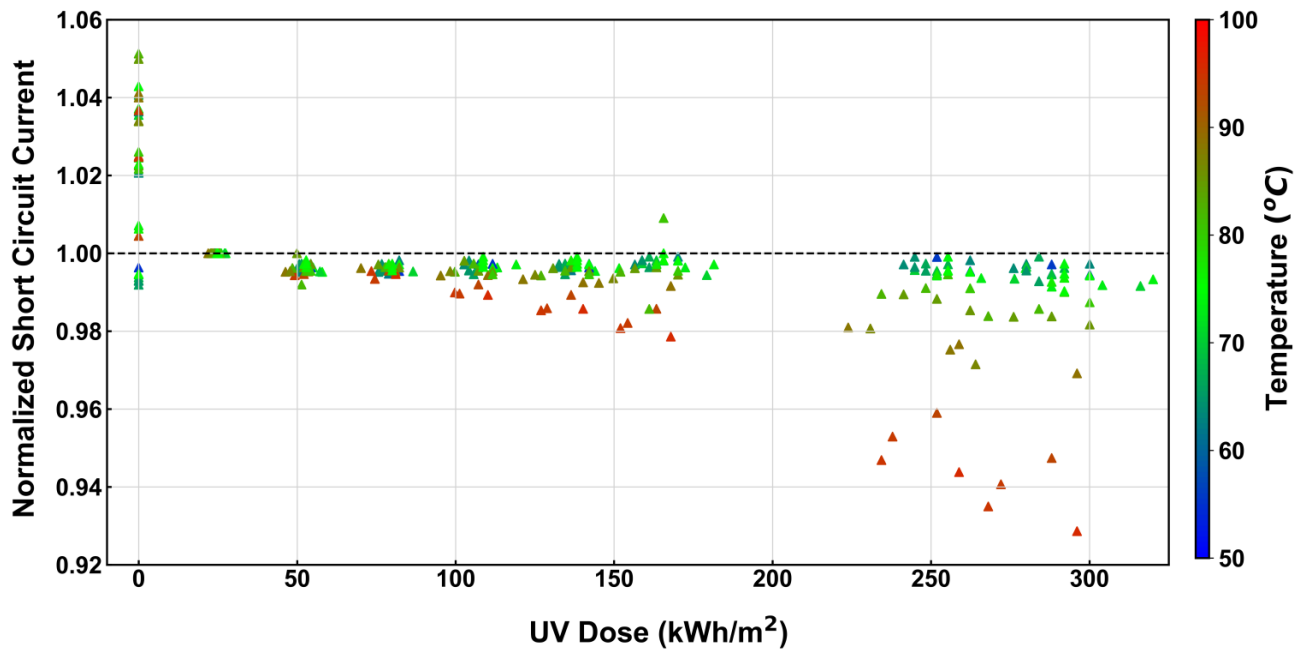


Fig. 7.22: Degradation in electrical parameters in the Xenon chamber tests. The orange horizontal line indicates the median value of the percentage degradation. The boxes indicate the spread of 50% of the data around the median value (between first and third quartiles), and the whiskers indicate the spread of the remaining data points (outside the first and third quartiles, excluding the outliers).

Figure 7.23 shows the variation of the normalized short-circuit current with UV dose. The normalization is done against the initial (pre-exposure) current output in Fig. 7.23(a), and it can be seen that there is a rapid drop in the short-circuit current (up to 5% of initial value) in the first exposure of ca. 25 kWh/m<sup>2</sup> (which may be due to Light Induced Degradation, LID). Most of the low-temperature samples seem to have stable output after this initial drop. To eliminate this initial LID effect, the short-circuit current for all doses has been normalized by dividing it by the  $I_{sc}$  value measured after the initial UV dose of 25 kWh/m<sup>2</sup>, and the result is plotted in Fig.7.23 (b). This figure confirms that most of the cells suffered less than 1% loss after the rapid initial degradation, but the high temperature samples suffered up to 7% loss in short-circuit current after the LID period (due to higher discoloration). This supports the higher discoloration observed in Hot cells in our field surveys [113].



(a)



(b)

Fig. 7.23: Short-circuit current for all the UV-cut samples – (a) normalized to initial pre-exposure value, and (b) normalized to the output current after initial UV dose of 25 kWh/m<sup>2</sup>. The data points are colour-coded based on the cell temperature during the Xenon chamber tests.

The short-circuit current loss within the first exposure of 25 kWh/m<sup>2</sup> has been plotted against the change in  $YI$  in Fig. 7.24. It can be seen that there is no correlation between the two, thereby indicating that the rapid initial loss in short-circuit current is not primarily due to the

yellowing of encapsulant but changes in cell characteristics (due to LID). The loss in short-circuit current post LID (i.e., loss between 25 kWh/m<sup>2</sup> dose to 300 kWh/m<sup>2</sup> dose) is plotted against the change in *YI* in Fig. 7.25 and strong correlation is observed between the two. It should be noted that the *YI* in this plot is from a spot measurement that does not account for variation within the cell (particularly the photo-bleached areas). The cell area affected by discoloration can be determined from the fluorescence images, as shown in Fig. 7.26. Based on this affected cell area, an “effective *YI* change” has been calculated using the following equation:

$$YI_e = YI_c \cdot A_f \quad \dots (7.2)$$

Where, *YI<sub>e</sub>* = Effective *YI* change

*YI<sub>c</sub>* = Change in *YI* at the center of the cell

*A<sub>f</sub>* = Fractional affected area of the cell (determined from fluorescence images).

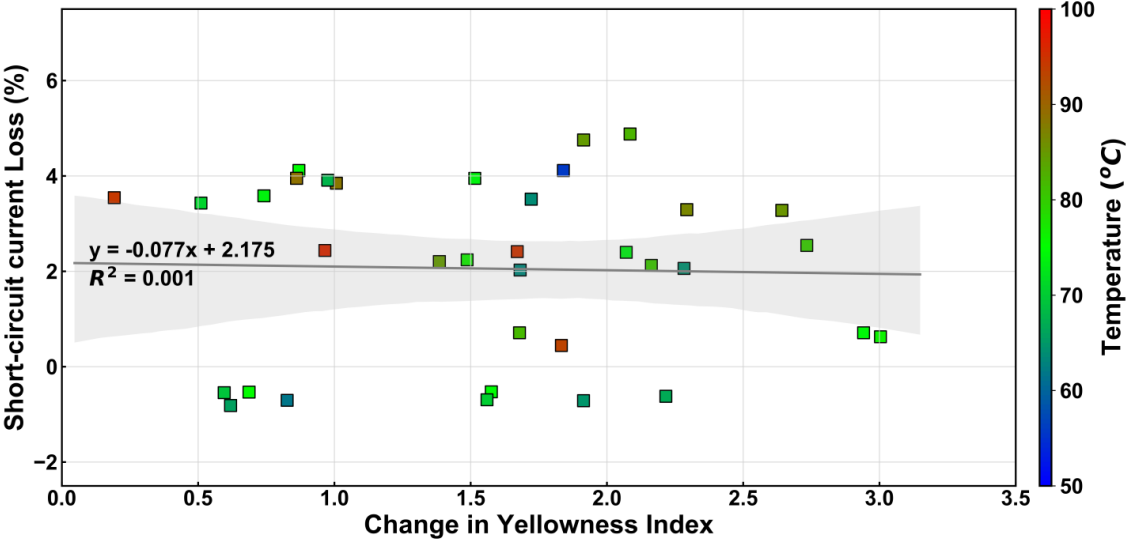


Fig. 7.24: Plot of short-circuit current loss in initial 25 kWh/m<sup>2</sup> UV exposure versus the change in *YI*. The data points are colour-coded based on the cell temperature during the Xenon chamber tests.

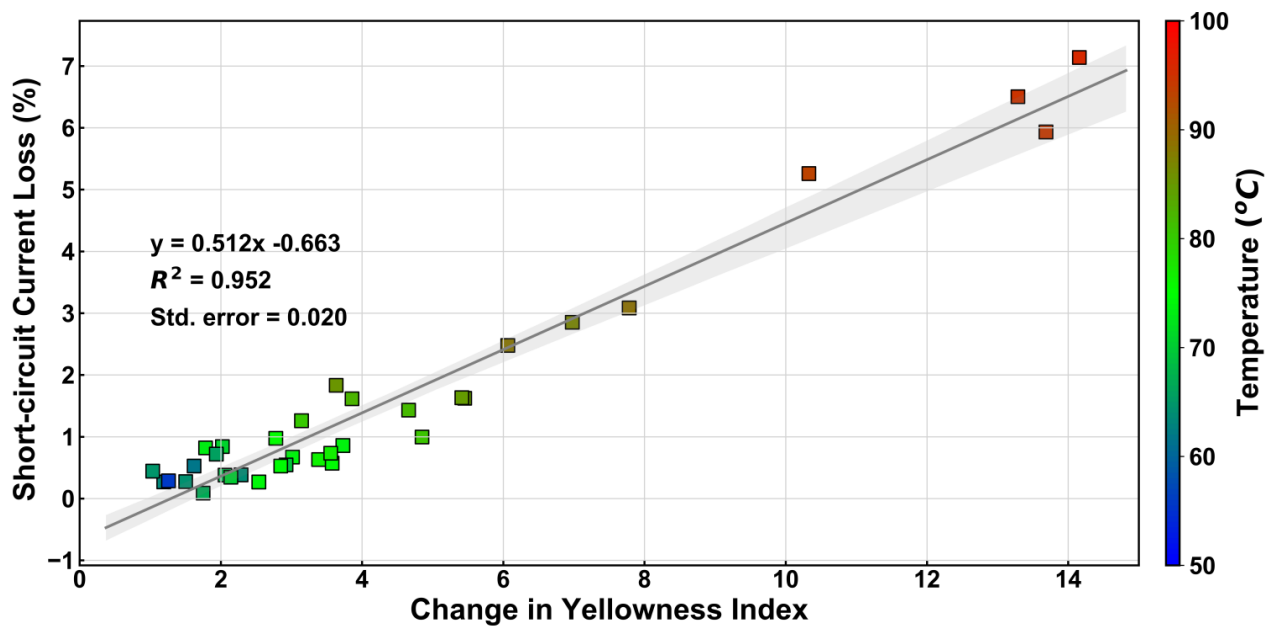


Fig. 7.25: Plot of short-circuit current loss (post LID) versus change in  $YI$ . The initial rapid loss has been discounted. The data points are colour-coded based on the cell temperature during the Xenon chamber tests.

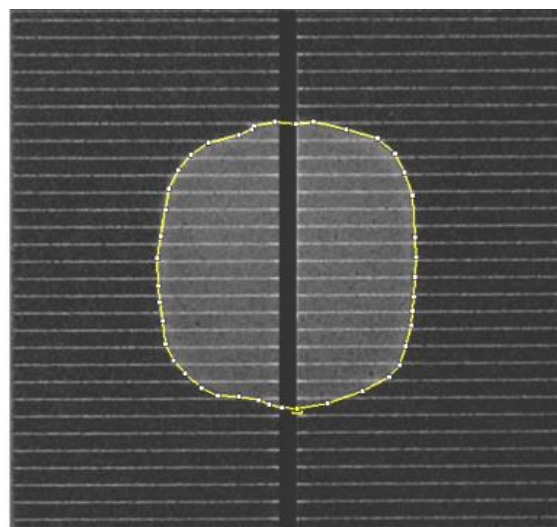


Fig.7.26: Selection of the affected area from the fluorescence image. The yellow curve is manually drawn (in Image-J software) to select the discoloured region.

Equation 7.1 assumes that the change in  $YI$  is uniform in the affected area of the cell, which is reasonable since the intensity of the fluorescence images do not show significant variation in the affected regions. Since the short-circuit current loss has been calculated after discounting for LID by considering the  $I_{sc}$  value after the first exposure dose of  $25 \text{ kWh/m}^2$  as the initial value, so the change in  $YI$  is also obtained by considering the  $YI$  after the first exposure as the initial

value. The fractional affected area for the samples ranged from 0 to 0.96. Figure 7.27 shows the plot of the short-circuit current loss versus the effective  $YI$  change, and the advantage of this plot (vis-à-vis Fig. 7.25) is that the constant term of the linear fit is reduced from -0.663 to -0.001. From this figure, it is evident that the  $I_{sc}$  decreases at the rate of ca. 0.48% for every unit increase in the effective  $YI$ .

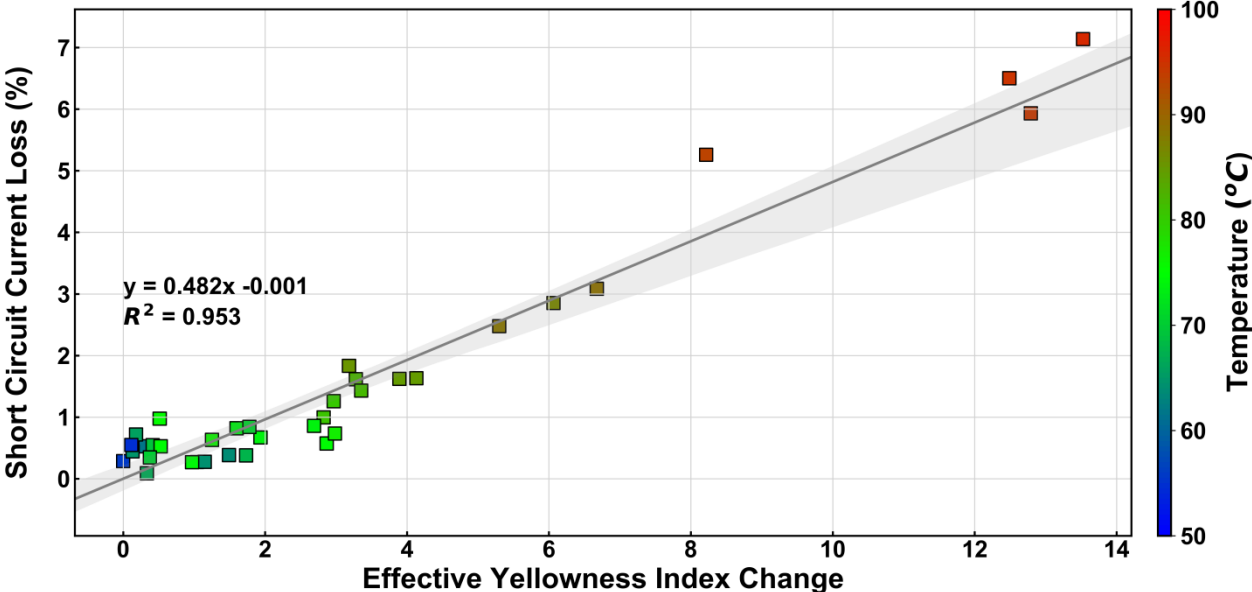


Fig. 7.27: Plot of short-circuit current loss (post LID) versus effective change in  $YI$  (averaged over cell area). The data points are colour-coded based on the cell temperature during the Xenon chamber tests.

Discoloration index (defined in Chapter 5) has also been calculated for these mini-modules, from digital (RGB) images of the mini-modules taken under natural sunlight at irradiance between  $700 \text{ W/m}^2$  to  $800 \text{ W/m}^2$  using a Nikon DSLR camera. Fig. 7.28 shows the correlation of the short-circuit current loss (post-LID) with the  $DI$  of the cells in UV-cut samples, as:

$$\% I_{sc} \text{ loss} = 27.694 \cdot DI - 1.206 \quad \dots (7.3)$$

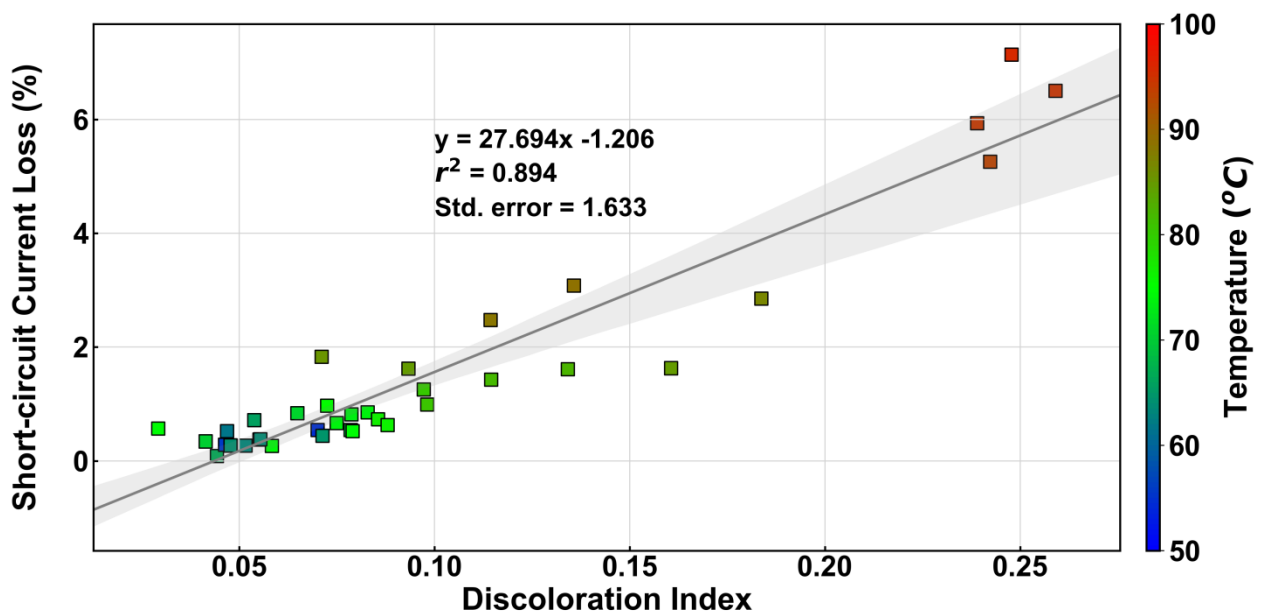


Fig. 7.28: Correlation of short-circuit current and discoloration index (calculated from visual images taken in daylight at irradiance  $>800 \text{ W/m}^2$ ) for UV-cut samples. The data points are colour-coded based on the cell temperature during the Xenon chamber tests.

Above equation indicates that the short-circuit current loss will be 28% for the maximum value of  $DI = 1$ . If %  $I_{sc}$  loss is equated to zero, then equation 7.2 yields  $DI$  value of 0.0435. So, for  $DI$  values less than 0.043, the  $I_{sc}$  loss can be considered to be practically negligible. One of the discolored modules inspected in All-India survey in 2016 (module image shown in Fig. 7.29(a)) has  $DI$  value of 0.34, from which the short-circuit current loss is estimated to be 8.21%, and this estimated loss matches closely with the actual  $I_{sc}$  loss based on  $I$ - $V$  measurement (8.3%). However, for the solar panel shown in Fig. 7.29(b), the  $I_{sc}$  loss estimated from  $DI$  value is 6.9%, while its  $I_{sc}$  loss from field  $I$ - $V$  measurement was found to be 4.6% (this variation may be partly because of inaccuracy in Nameplate values and partly due to STC translation errors).

The temperature dependence of the slope of short-circuit current loss has been shown in Fig. 7.30. The activation energy for short-circuit current loss is  $1.21 \text{ eV} \pm 0.11 \text{ eV}$  (standard error), which is almost double of the value for  $YI$ . This may be due to the fact that the short-circuit current is influenced by both the discoloration and the photo-bleached area, and the rate of oxygen ingress is also different for each cell due to differences in geometry and location within the laminate. There is a lot of scatter in the low-temperature cells (below  $74 \text{ }^\circ\text{C}$ ). In these cells, the area and also the severity of discoloration is low, as a consequence of which the short-circuit current loss is quite low (within 0.5%), and the measurement inaccuracies become

significant at such low levels of current loss. For samples above 74 °C, good correlation is evident from the figure, and most of these cells have significant discolored area.

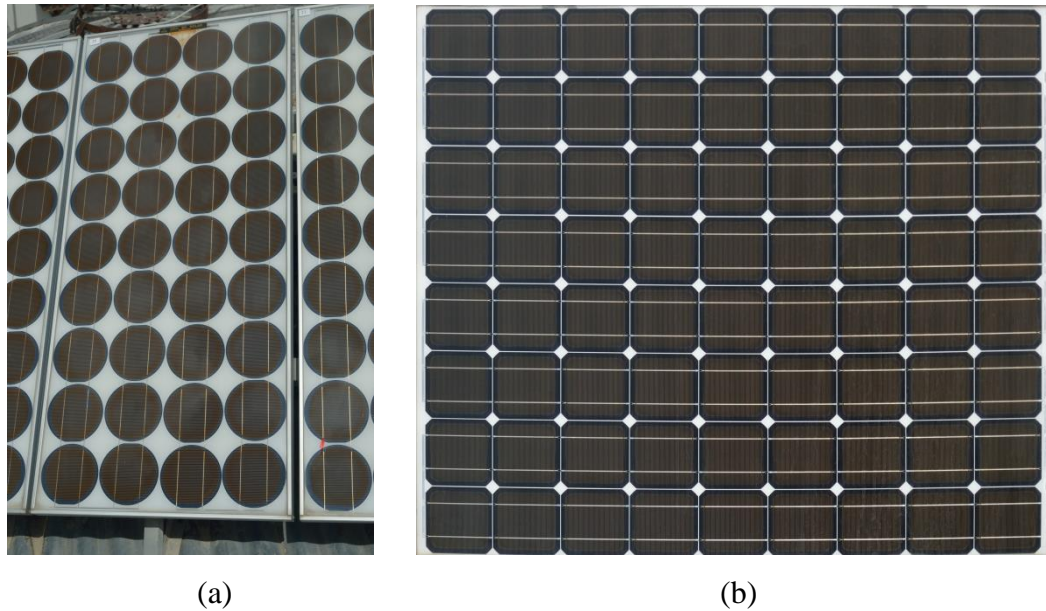


Fig. 7.29: Visual images of discolored PV modules surveyed in 2016 All-India survey – (a) a 18 years old solar panel from Cold & Sunny climate, and (b) a 6 years old solar panel from Warm & Humid climate.

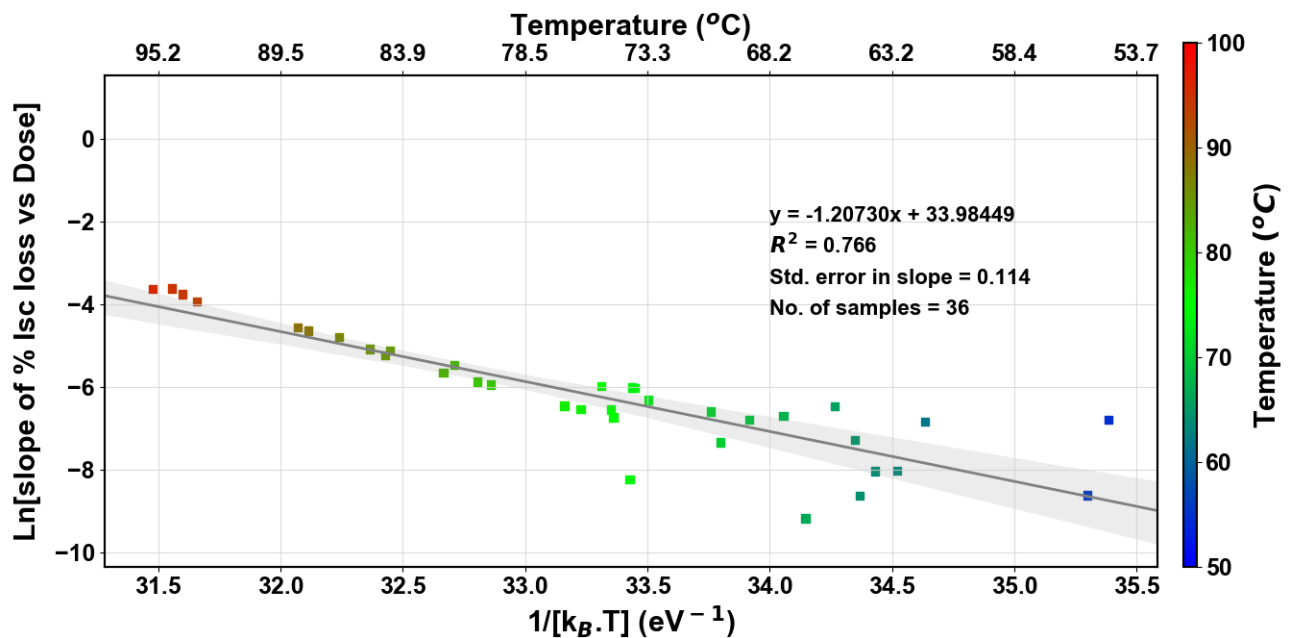


Fig. 7.30: Arrhenius analysis of the slope of  $I_{sc}$  loss versus UV dose. Slope of the linear regression line indicates the activation energy (=1.207 eV). The data points are colour-coded based on the cell temperature during the Xenon chamber tests.

### 7.3.4 Acceleration Factor for Different Locations

In our experiments, the chamber humidity has been set to dry conditions (RH = 20%), and the UV irradiance and temperature have been elevated as the stressors. The effect of temperature on the degradation rate is usually modeled by the Arrhenius model, for which the activation energy has already been calculated. Various researchers have modeled the effect of irradiance or UV dose as a linear function [84], or as power law [126]. From our discoloration data, it can be seen that the average change in  $YI$  is increasing linearly with the UV dose (as shown in Fig. 7.15), so the linear model has been adopted for estimating the acceleration factor.

Discoloration at a location can be estimated as the summation of the hourly discoloration at the site subjected to the module temperature and UV dose (neglecting any photo-bleaching effect). There will be no discoloration at night and also bleaching action of oxygen is assumed to be negligible (which is reasonable since there is no UV light and also module temperature comes down to ambient air temperature at night). The hourly module temperature can be estimated from the ambient temperature, the incident plane-of-array irradiance and wind speed. The hourly UV dose can be estimated from the POA global irradiance (assuming 5% UV content in the incident sunlight).

Based on [84], the accelerated test model for change in  $YI$  can be written as,

$$\Delta YI_{test} = A \cdot D_{test} \cdot \exp \left\{ - \left( \frac{E_a}{K_B \cdot T_{test}} \right) \right\} \quad \dots (7.4)$$

where,

$A$  = pre-factor

$D_{test}$  = UV dose in the accelerated test (=  $UVI_{test} * t_i$  i.e., UV intensity in the test chamber \* time)

$E_a$  = activation energy, eV

$K_B$  = Boltzmann constant (=0.0000861733 eV/K)

$T_{test}$  = sample temperature, K

This is a deterministic model, which does not consider any randomness or variations in the process parameters. The alternative probabilistic modeling approach was not considered due to

insufficient sample data. Similarly, for the outdoor field exposure, the following equation can be written:

$$\Delta YI_{annual} = \sum_{i=1}^{8760} A \cdot D_i \cdot \exp\left\{-\left(\frac{E_a}{K_B \cdot T_i}\right)\right\} \quad \dots (7.5)$$

where,

$\Delta YI_{annual}$  = change in  $YI$  in 1 year

$i$  = hour of the year (ranges from 1 to 8760).

$A$  = pre-factor (assumed same as in indoor test)

$D_i$  = UV dose in plane-of-array in the  $i$ -th hour (=  $UVI_i \cdot t_i$  = UV component of the POA irradiance x 1 hour)

$E_a$  = activation energy, eV

$K_B$  = Boltzmann constant (=0.000086133 eV/K)

$T_i$  = cell temperature, K, calculated based on the ambient temperature and wind speed, using Sandia model [127], as given below:

$$T_i = G_{poa} \cdot \exp(a + b \cdot WS) + T_a \quad \dots (7.6)$$

where,

$G_{poa}$  = global plane-of-array irradiance on the solar panel, W/m<sup>2</sup>

$a, b$  = constants depending on the module construction and type of mounting (-3.56, -0.075 s/m respective for glass-backsheet type modules mounted on open rack)

$WS$  = wind speed, m/s

$T_a$  = ambient temperature, K

The plane-of-array irradiance is calculated on hourly basis based on the GHI (Global Horizontal Irradiance), DHI (Diffused Horizontal Irradiance) and DNI (Direct Normal Irradiance) values, obtained from Typical Meteorological Year (TMY) files of different locations provided by the National Solar Radiation Database (NSRDB) [128]. This calculation is done using the PVLib software package [129] in Python programming language, considering albedo as 0.3 for Leh (dry soil) and 0.4 for Jodhpur (dry sand). From equations 7.4 and 7.5, the test duration needed to simulate 1 year of outdoor weathering can be calculated as follows:

$$t_{test,ann} = \sum_{i=1}^{8760} \left( \frac{UVI_i}{UVI_{test}} \right) \cdot t_i \cdot \exp \left\{ - \left( \frac{E_a}{K_B} \right) \cdot \left( \frac{1}{T_i} - \frac{1}{T_{test}} \right) \right\} \quad \dots (7.7)$$

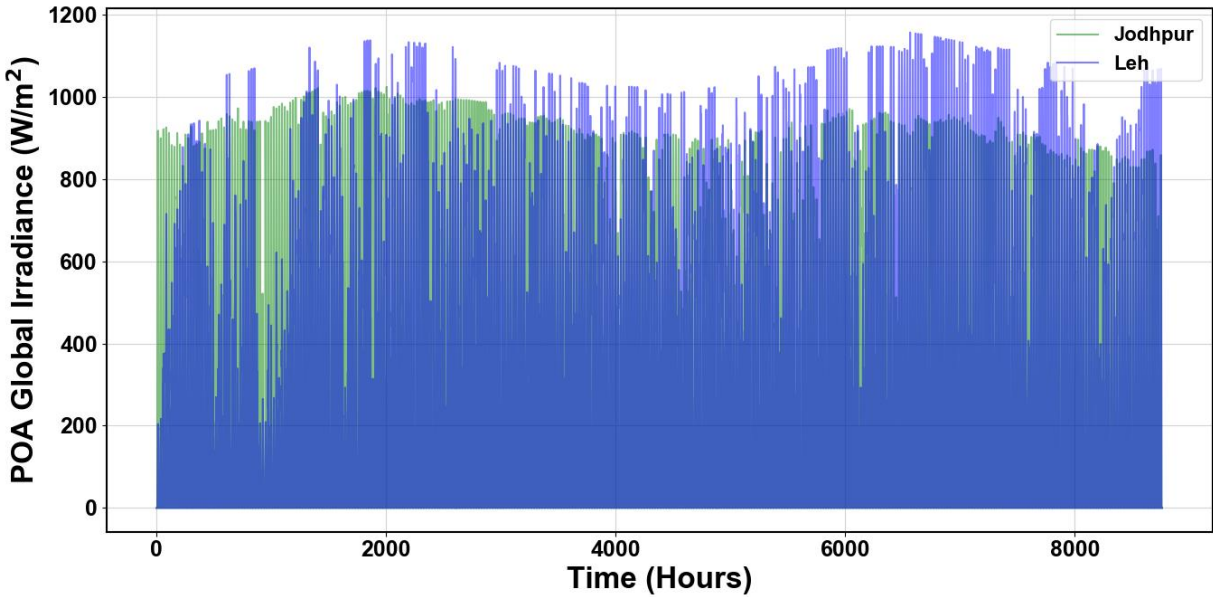
and hence, the acceleration factor can be calculated as:

$$AF = \frac{8760}{t_{test,ann}} \quad \dots (7.8)$$

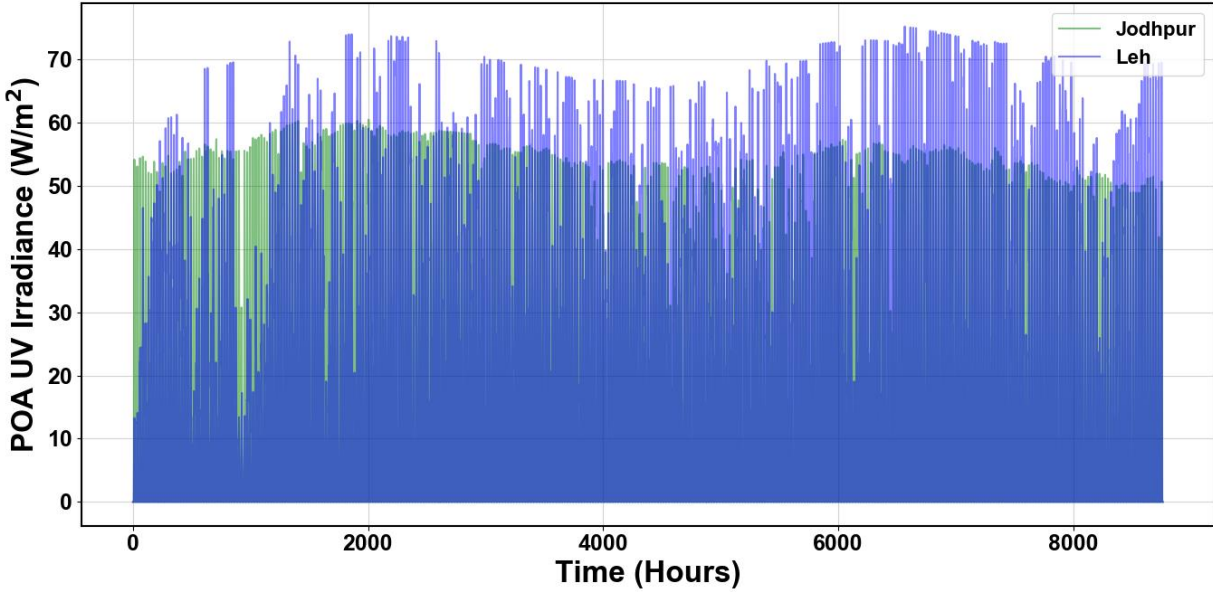
The acceleration factor thus calculated provides us an indication of how much the experiment has been accelerated in the environmental test chamber as compared to natural weathering outdoors. Based on this factor, one can calculate the accelerated test duration needed to simulate 25 years exposure outdoors in the use environment. It should be noted that every outdoor location will have differences in the solar irradiance and ambient temperatures, so it is necessary to calculate the acceleration factor separately for each of the different sites. Also, it should be noted that different encapsulants will have different degradation behavior and even a change in the additive composition can change the degradation rate.

The accelerated tests have been conducted at very low humidity levels (<20% RH), and the humidity is not considered as a factor in the acceleration model. This is a limitation of the present model and the results needs to be considered carefully. Since the accelerated tests have been conducted in dry conditions in the accelerated test, the acceleration factor has been calculated for places in dry deserts in India – (a) Jodhpur in Rajasthan, which is a Hot desert and (b) Leh in Ladakh, which is a cold desert. The TMY files for Leh and Jodhpur have been downloaded from the National Solar Radiation Database (NSRDB) website, and the relevant weather data have been analyzed. The global plane-of-array irradiance for Leh and Jodhpur have been compared in Fig. 3(a), from which it is evident that the peak irradiance is higher in Leh than in Jodhpur, but the variability is also much higher in Leh. The UV intensity for Jodhpur and Leh has been compared in Fig. 3(b), which shows that Leh has marginally higher UV content than Jodhpur (about 7% higher in terms of annual UV dose). The ambient temperatures in Jodhpur and Leh have been shown in Fig. 4(a), from which it can be clearly seen that the highest ambient temperature in Leh is around 25 °C, while it is much higher at 50 °C for Jodhpur. It should be noted that the maximum cell temperature estimated for Leh is 58 °C while for Jodhpur, it is 79 °C. The annual average day-time cell temperature for Leh is estimated to

be 15 °C, whereas it is 46 °C for Jodhpur. This difference of 31 °C is a significant factor from the point of view of material degradation.

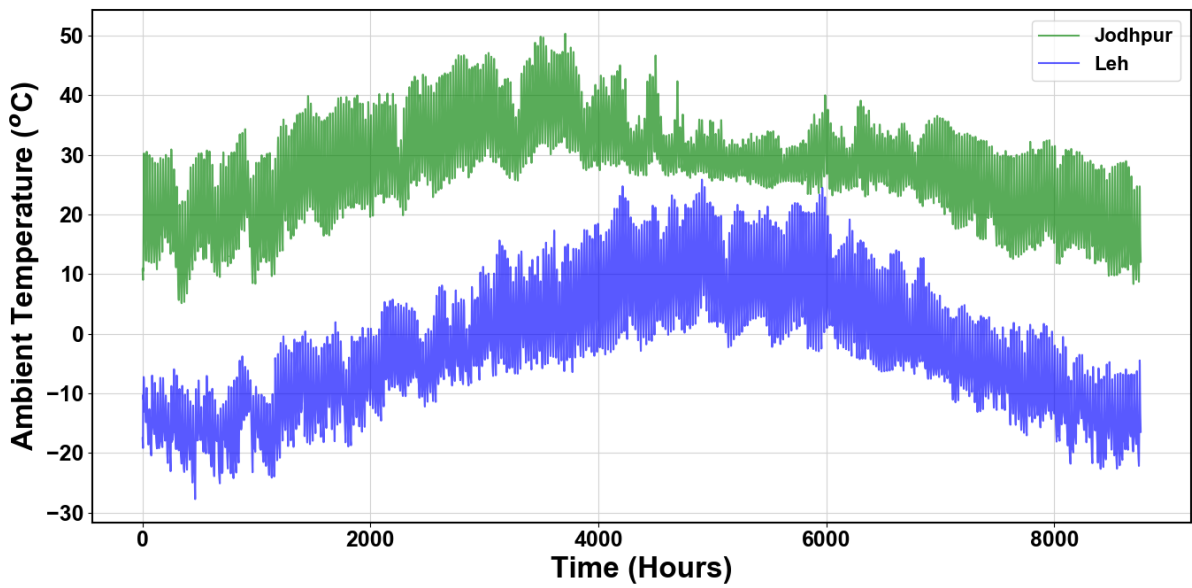


(a)

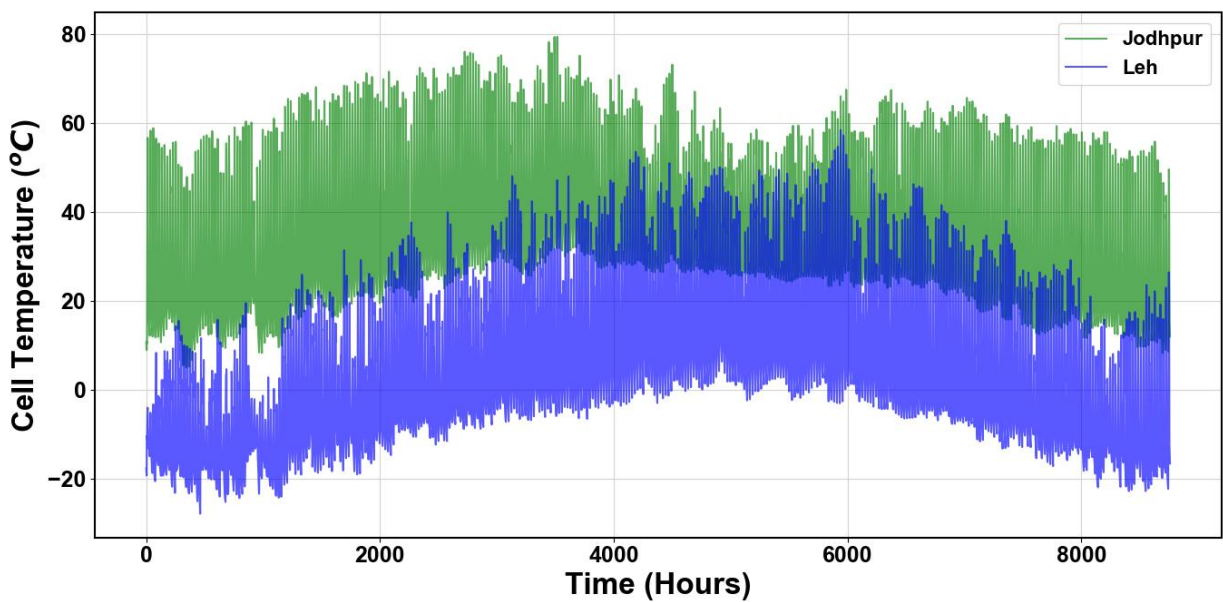


(b)

Fig. 7.31: Comparison of plane-of-array irradiance for Jodhpur (green) and Leh (blue) – (a) global total irradiance, and (b) global UV irradiance in 300 – 400 nm wavelength range.



(a)



(b)

Fig. 7.32: Comparison of temperatures for Jodhpur and Leh – (a) ambient temperature, and (b) estimated cell temperature. The average ambient temperature during daytime for Leh is  $-2\text{ }^{\circ}\text{C}$ , whereas it is  $31\text{ }^{\circ}\text{C}$  for Jodhpur.

Table 7.1 shows the acceleration factors calculated for Xenon chamber exposure at  $75\text{ W/m}^2$  total UV radiation (integrated value from 300 nm to 400 nm) and  $85\text{ }^{\circ}\text{C}$  sample temperature (henceforth referred to as “75/85” condition). This table considers the range of activation energy from  $(0.61-0.08 =) 0.53\text{ eV}$  to  $(0.61+0.08 =) 0.69\text{ eV}$ . It can be seen from the table that the acceleration factor for Jodhpur is 27 (for activation energy of 0.61 eV), while it is

165 for Leh. This means that 1-year continuous test in Xenon chamber at 75/85 conditions is equivalent to 165 years of outdoor exposure in Ladakh, whereas it is equivalent to 27 years of exposure in Jodhpur. So, the 25 years warranty period for panels installed in Leh can be covered by 55 days test in Xenon chamber (from encapsulant discoloration point of view), whereas it will need 319 days total exposure for panels installed in Jodhpur. It should be noted that the above test duration is estimated based on the assumption that the degradation behavior of the encapsulant remains same even after extended period of aging (i.e., there are no deviations from the model developed through the limited hours testing). Such a wide difference in the exposure times is seen primarily because of the colder ambient temperature in Ladakh (which keeps the module temperatures low). The maximum module temperature estimated for Leh is 55 °C while for Jodhpur it is 76 °C. Based on this data, it can be said that discoloration rate in Jodhpur will be about 6 times that in Leh. Hence, it is advisable to set up solar PV power plants in cold places like Ladakh compared to Hot sites like Jodhpur, from the perspective of EVA discoloration.

Table 7.1: Acceleration factors for Jodhpur and Leh in India.

Acceleration Factor	Activation Energy		
	0.53 eV	0.61 eV	0.69 eV
Location			
Jodhpur, Rajasthan	22	27	33
Leh, Ladakh	109	165	247

Another important result that emerges from this accelerated test is that there is 3%  $I_{sc}$  loss (after discounting LID) in the UV-cut EVA due to discoloration upon 300 kWh/m<sup>2</sup> Xenon exposure at the “75/85” condition. This corresponds to approximately 12 years in Jodhpur, and hence the average degradation rate is approx. 0.27%/year, which is well within the linear warranty condition (usually 0.7%/year).

## 7.4 Summary

The degradation of a commercially available EVA formulation (having UV cut off around 360 nm) has been studied under Xenon-based UV exposure. The mini-modules have been covered with Aluminum foil and insulating layers on back side to minimize the ingress of oxygen

and maintain the samples at elevated temperatures. Fluorescence imaging under 365 nm UV excitation has confirmed that the aluminum has minimized the oxygen ingress significantly. The yellowness index has been found to exhibit a linear rate of increase versus UV dose (after an initial jump) for temperature range up to 88 °C. This linear rate of increase exhibits Arrhenius behavior with respect to temperature and the Activation energy has been derived to be 0.61 eV based on the linear slopes of the discoloration rate.

Fluorescence spectra, measured close to the center of the cells, indicates that in the low temperature samples, there is a decrease in the peak fluorescence intensity close to 480 nm during the initial exposure. This decrease may be attributed to the extinction of the fluorophores generated during curing. There is subsequent increase in the fluorescence with peak close to 570 nm. The difference in the peak wavelengths indicate that the fluorophores generated during curing (done at 150 °C) are different from those generated during the degradation of the polymer in the Xenon chamber. The integrated fluorescence intensity (after baseline correction) increased linearly with the change in  $YI$ .

The short-circuit current of the cells has reduced in the course of the UV exposure. This decrease can be attributed to Light Induced Degradation (LID) and the discoloration of encapsulant. There was 1-5% loss in  $I_{SC}$  in the samples in the initial exposure dose of 25 kWh/m<sup>2</sup> (total UV). The LID effect has been discounted by considering the  $I_{sc}$  values after the first exposure as the initial value (post-LID). A post-LID reduction of 7% has been observed after 300 kWh/m<sup>2</sup> UV dose for the cell maintained at 95 °C, while there is a marginal reduction of 0.5% for cells operating below 74 °C. The loss in short circuit current in the accelerated test translates to a degradation rate of 0.27%/year in outdoor condition in Jodhpur (which is within the warranty limits specified by module manufacturers). The reduction in short-circuit current has been found to be proportional to the effective change in  $YI$  (based on the affected area), with a proportionality constant of 0.48%. The short-circuit current loss (post-LID) has been found to increase with temperature, with an activation energy of 1.21 eV  $\pm$  0.11 eV (standard error). The activation energy for short-circuit current loss is higher than that for change in  $YI$  (measured at center of the cells), which maybe because the short-circuit current is associated with both the discolored and photo-bleached regions. The rapid increase in discoloration of the encapsulant at temperatures above 88 °C indicates that such encapsulant should not be used for high temperature applications where the module operating temperature is expected to exceed 88 °C

regularly (for example, direct roof-mounted modules in Hot climates). The acceleration factor in Jodhpur is estimated to be 27 while it is 6 times higher for Leh. This indicates that 55 days of accelerated test is sufficient for simulating 25 years EVA performance in Ladakh, but it will take 319 days total exposure to simulate the same period in Jodhpur. Considering the lower discoloration rate in the cold climate of Leh, it is recommended to set up solar PV power plants in cold places like Ladakh compared to Hot sites like Jodhpur, from the perspective of EVA discoloration. Also, the quality of the encapsulant (and other materials) becomes of paramount importance for solar panels intended for applications in the Hot climates, given the high sensitivity to module temperature.

## **Chapter 8**

# **Comparative Study of UV-cut and UV-pass EVA Encapsulants**

### **8.1 Introduction**

The conventional UV-absorbing EVA has been the primary choice of most PV module manufacturers for decades, but the push towards higher efficiency modules with better UV and blue light response has led to the demand for UV-transparent encapsulant material. Some manufacturers have introduced UV-transparent EVA, which allows more UV light to pass to the solar cells, leading to an increase of ca. 1% (percentage points) in the power output of the cells [130]. Also, it is claimed by the manufacturers that this UV-transparent EVA is more stable to UV rays than the conventional EVA material. The performance of the conventional UV-absorbing EVA (UV-cut) and the UV-transparent EVA (UV-pass) has been compared in

accelerated tests for determining which material is better suited for the Hot climate of India. Two types of encapsulants used in these studies are:

- (a) UV blocking EVA (UV-cut) – blocks UV light below 360 nm (refer Fig. 8.1)
- (b) UV transparent EVA (UV-pass) – transparent to all wavelengths above 250 nm

The Vinyl Acetate (VA) content for both the EVA (UV-cut and UV-pass) obtained from an Indian manufacturer has been found to be 29% (from TGA analysis) and the Gel content is 88% for UV-cut and 87% for UV-pass (determined by Soxhlet extraction method). A major difference between the two encapsulant types is the use of a UV absorber in UV-cut EVA. The EVA film manufacturers do not openly disclose the composition of their EVA formulation as it is their trade secret. However, various analytical techniques can help in identifying the additives. The transmission data of UV-cut and UV-pass EVA laminated between quartz glass coupons is shown in Fig. 8.1. The absorption by the UV absorber in the UV region is clearly visible for UV-cut coupon.

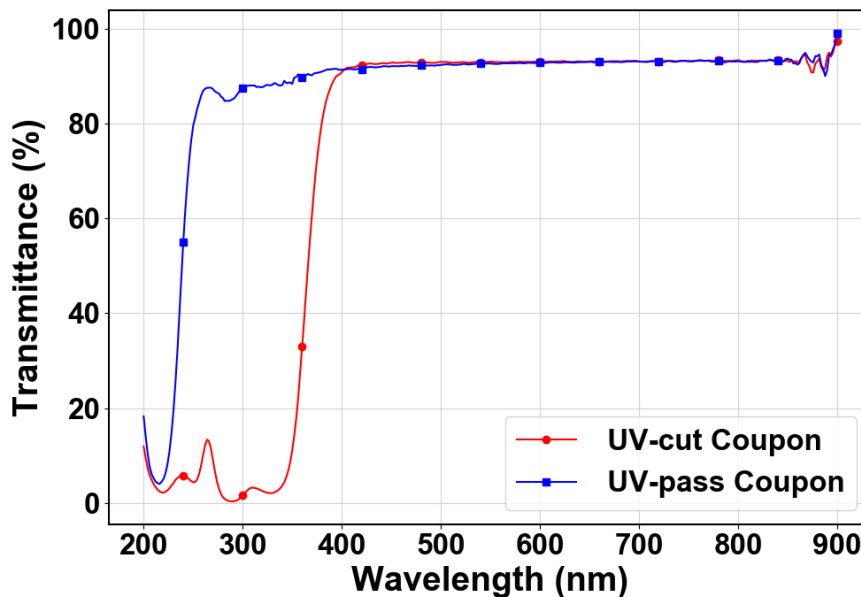


Fig 8.1: Transmittance spectra of UV-cut and UV-pass EVA coupons (laminated between quartz glass sheets). The UV-cut EVA absorbs most of the UV below 350 nm, whereas the UV-pass transmits it.

The absorbance of the UV-cut coupon has been calculated from the transmittance data (%*T*) using the relation:

$$Absorbance = 2 - \log(\%T) \quad \dots (8.1)$$

In Fig. 8.2, the absorbance curve of the UV-cut coupon based on measured transmittance spectra has been compared to the absorbance of the UV absorber Cyasorb UV-531, also known as Chimassorb 81, given in the datasheet [131]. The two curves almost overlap (after suitable scaling of the spectra of Cyasorb UV-531 to nullify the concentration differences), indicating that this UV absorber has been used in the UV-cut EVA.

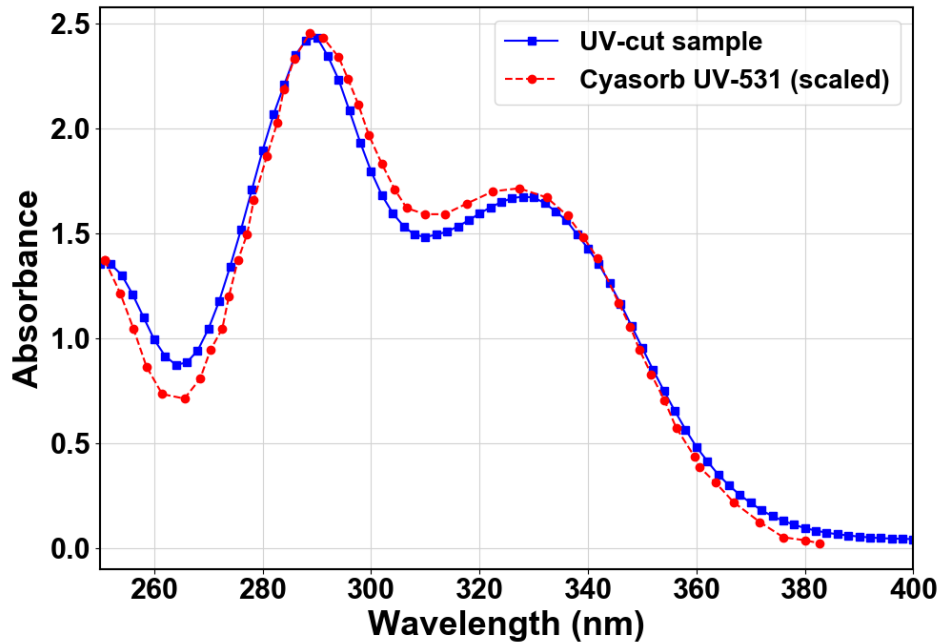


Fig. 8.2: UV absorbance spectra of UV-cut sample (measured) and Cyasorb UV-531 (from datasheet [131]). The close match between the peaks indicates that the additive in the UV-cut sample is Cyasorb UV-531.

Different types of accelerated test chambers are available for degradation studies of materials. The Xenon chamber uses Xenon arc lamps which emit radiation very similar to the outdoor solar radiation. The use of additional glass filters in the chamber improves the match to the solar spectrum [132]. However, Xenon chambers usually do not offer high irradiance intensity, and hence take months to produce degradation in the materials. Also, standard chambers do not have the facility to test the samples in different atmosphere (like oxygen-rich and oxygen-deficient), which can be useful in understanding the degradation processes. To achieve such capabilities, a UV test chamber has been developed using a 365 nm LED-based UV source, which produces ca. 900 W/m<sup>2</sup> UV intensity at the center of the beam, and the test chamber is equipped with a heating plate which can go up to 120 °C. We shall discuss the results of accelerated tests of UV-cut and UV-pass samples in these two chambers (UV-365 and Xenon) in this chapter.

The test samples were prepared to suit the chamber capabilities, as indicated in Table 8.1. Small encapsulant coupons (of size 2 cm x 2 cm) were laminated at IIT Bombay and exposed to UV radiation in the UV-365 test chamber. Also, 9-cell mini-modules were prepared using different types of EVA from two different manufacturers at Arizona State University (ASU). Mini-modules prepared with EVA from manufacturer A were shipped to IIT Bombay for accelerated testing in Xenon chamber, while Kshitiz *et al.* [79] conducted accelerated tests at ASU on EVA from manufacturer B. A 9-cell laminate of UV transparent EVA was prepared at IIT Bombay for the Xenon chamber tests.

Table 8.1: Accelerated tests for EVA discoloration.

	<b>UV-365 Chamber</b>	<b>Xenon Chamber</b>
<b>Type of UV source</b>	UV-365 nm LED	Xenon Arc lamp
<b>Type of samples</b>	Glass-EVA-Backsheet laminates (2 cm x 2 cm size)	Glass-EVA-Cell-Backsheet laminates (20 cm x 20 cm size)
<b>Atmosphere</b>	(1) Dry Air (2) Nitrogen	Dry Air (20% RH)

UV absorbing EVA has been commonly used by PV module manufacturers, so we have studied the impact of Xenon aging on the UV-cut sample over a broad temperature range (55 °C to 95 °C), as reported in Chapter 7. In this chapter, the comparative tests performed on UV-cut and UV-pass EVA in the UV-365 chamber (at elevated temperature of 90 °C) and also in Xenon chamber (at temperature range of 55 °C – 70 °C) has been reported.

## 8.2 Accelerated test in Xenon chamber

### 8.2.1 Methodology

As discussed in Chapter 7, mini-modules comprising of 9 cells have been used in the Xenon chamber tests. In the case of the UV-pass sample, the UV transparent EVA film has

been used on both the glass side and the back-sheet side of the cells for lamination (performed at 145 °C for 14 minutes). In the UV-pass sample, the insulation layers of polyurethane (PU) foam have been attached in staggered fashion (as shown in Fig. 8.3) to ensure that the different temperatures are achieved in the different cells. The temperature range finally achieved in this UV-pass sample is 56 °C to 74 °C which is comparable to the temperature range achieved in UV-cut sample UVC-2, so the degradation in these two samples shall be compared. The temperatures were measured using IR thermography as shown in Fig. 8.4 (procedure discussed in detail in Chapter 7). Thermocouples were also connected to the back side of the samples which helped to confirm the temperatures detected through IR thermography.

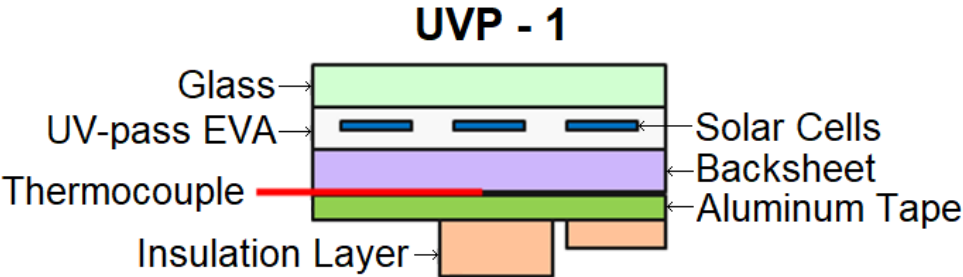


Fig 8.3: Schematic diagram of UV-pass samples (UVP-1) used in the Xenon chamber tests.

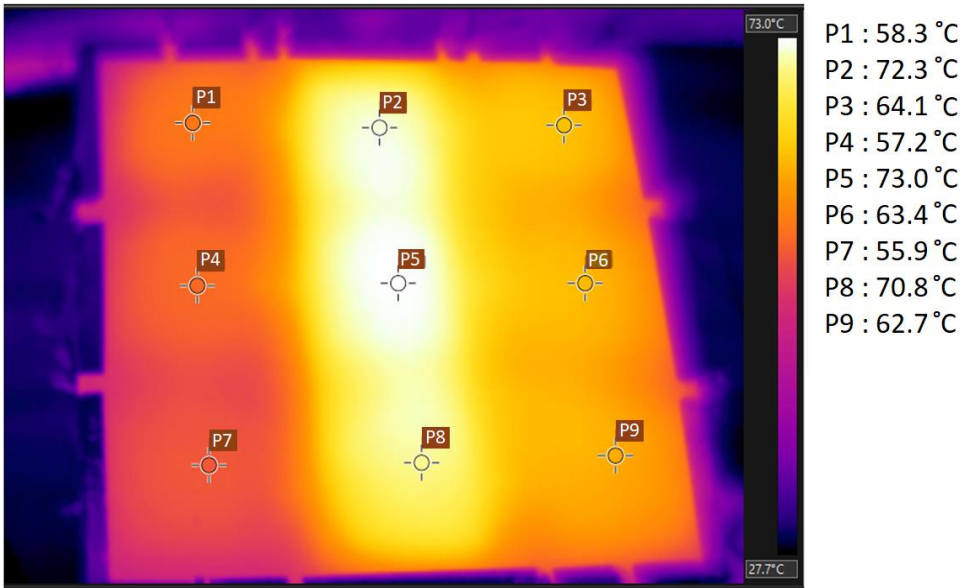


Fig 8.4: IR image of UV-pass sample (UVP-1) showing that the temperature of the cells was highest in the middle section (which had highest insulation thickness). The highest temperature in the IR image is 73 °C.

## 8.2.2 Results and Discussion

### a) Effect on Yellowness Index

In the mini-modules, the yellowness index was measured close to the center of each solar cell (using a mask to ensure that the same spot is measured repeatedly after each exposure cycle). The change in *YI* (increase from the pre-exposure value) of the UV-cut and UV-pass samples in the Xenon chamber tests has been plotted in Fig. 8.5. It can be seen that the UV-cut EVA has suffered higher increase in the *YI* value as compared to the UV-pass EVA. The variation in the *YI* values across the different cells in the two samples is partly due to the different temperatures of the samples and the measurement uncertainty (of  $\pm 0.5$  units, which is significant at such low levels of discoloration observed in these samples). Also, some part of the variability may come from other factors that are not measured (like lamination temperature variations, etc.). Fig. 8.6 shows the comparison of UV-cut and UV-pass cells at temperatures of around 64 °C and 74 °C. It can be seen that the slope of the linear fit is 3.5 times higher for UV-cut sample as compared to UV-pass sample at 64 °C.

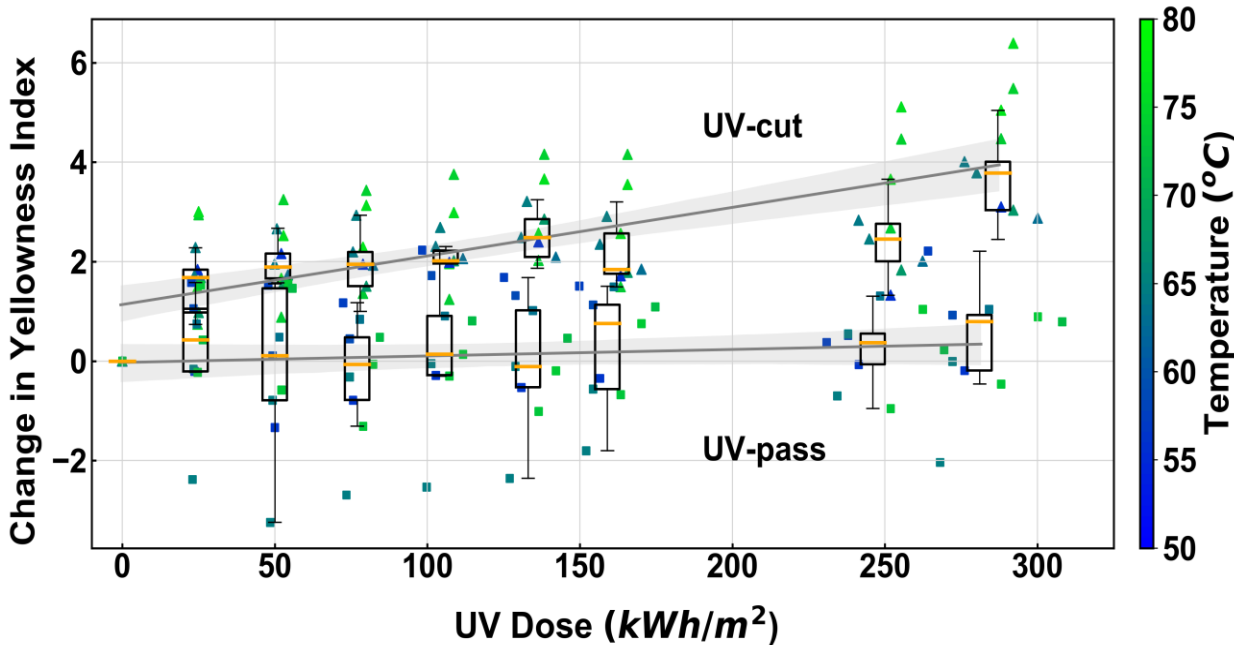


Fig 8.5: Box plot showing comparison of the change in *YI* of UV-cut and UV-pass samples. Each data point (marked with *triangle* for UV-cut and *square* for UV-pass) represents the change in *YI* at the center of the cell (sample), at corresponding dose. The orange lines inside the box indicate the median value of the data points. UV-cut samples discolor at faster rate than UV-pass samples.

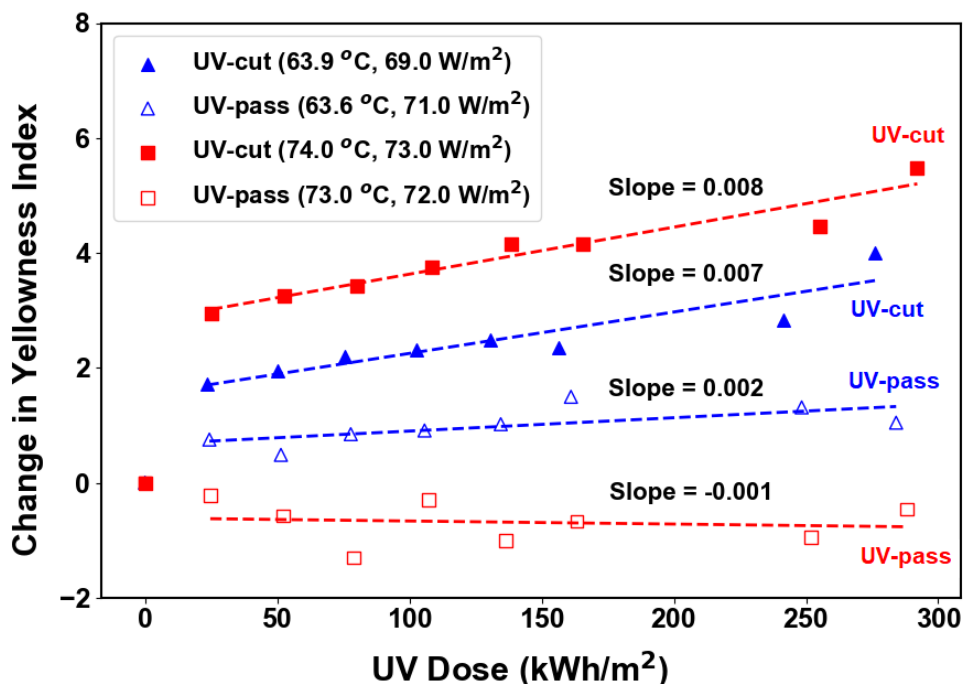
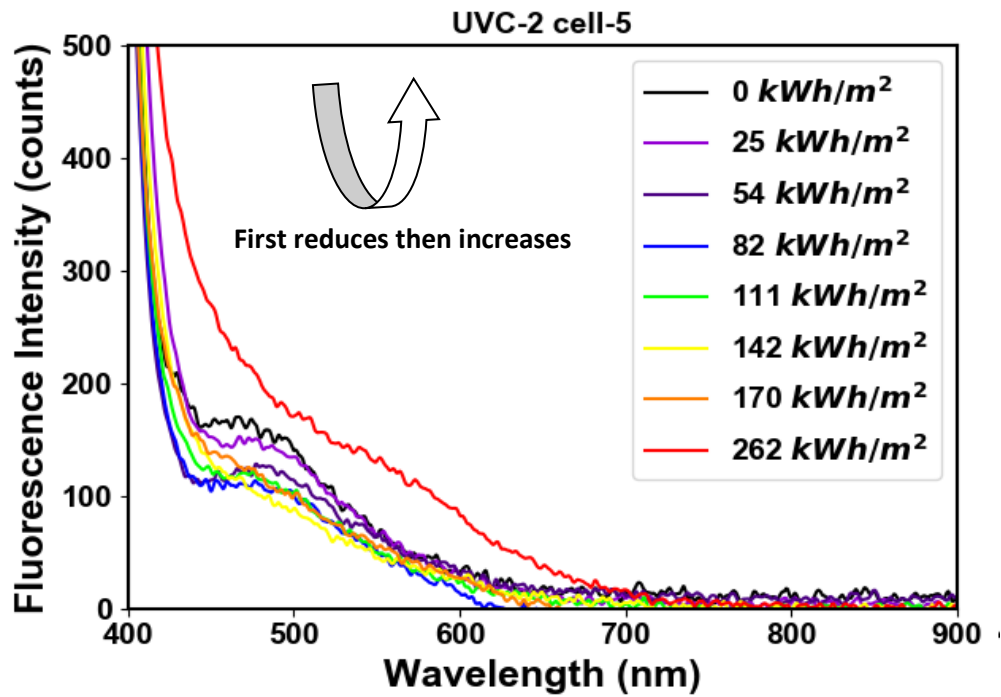


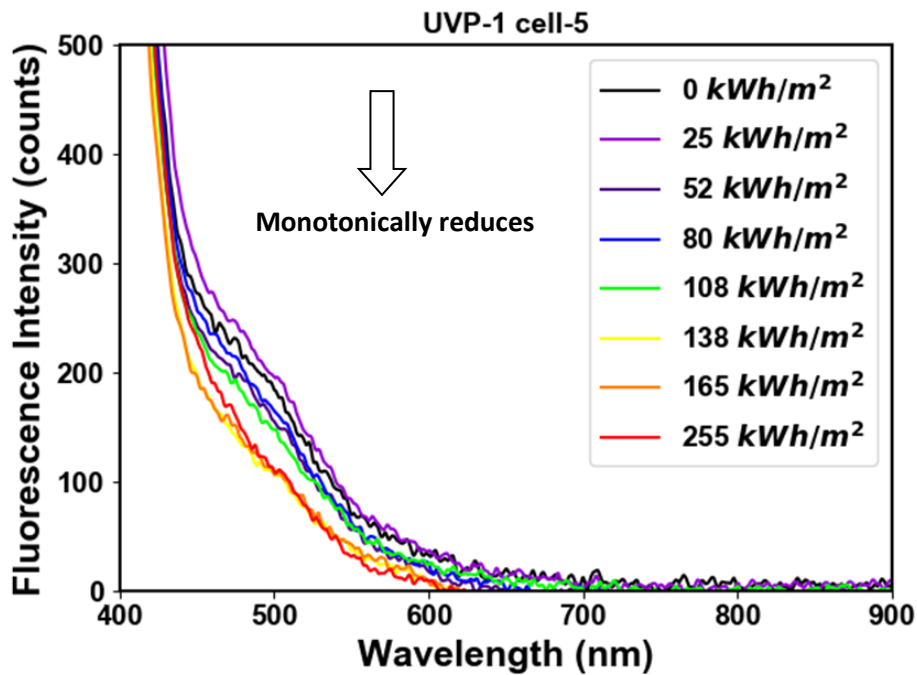
Fig 8.6: Comparison of the change in *YI* of UV-cut and UV-pass samples at selected temperatures (ca. 64 °C and 74 °C). *YI* change rate is about 3.5 times higher for UV-cut sample.

### b) Effect on Fluorescence Emission

The fluorescence spectra (at the center of the middle solar cell) in the UV-cut and UV-pass samples are plotted for the Xenon chamber test in Fig. 8.7. The 365 nm UV source has been used as the excitation source for this measurement. The UV-cut and UV-pass cells have comparable temperature ( $74 \pm 1$  °C) and irradiance ( $75 \pm 1$  W/m<sup>2</sup>). The UV-cut samples initially show a decrease in the fluorescence intensity at around 480 nm, followed by an increase in the fluorescence intensity (indicating the generation of new fluorophores). However, the UV-pass sample shows a gradual decrease in the fluorescence intensity with UV exposure (indicating that no new fluorophores are generated but instead, existing fluorophores are disintegrated in the course of this experiment).



(a)



(b)

Fig 8.7: Fluorescence spectra of UV-cut and UV-pass samples with increase in UV dose, under Xenon exposure - (a) UV-cut (UVC-2), (b) UV-pass (UVP-1).

Figure 8.8 shows the fluorescence images of the samples. The photo-oxidative bleaching effect along the edges of some of the solar cells is clearly visible in the UV-cut sample. However,



**c) Effect on Short-circuit Current**

The short-circuit current ( $I_{sc}$ ) of the samples was measured both before the exposure, and after the exposure at regular intervals. The normalized short circuit current of the UV-cut and UV-pass samples (UVC-2 and UVP-1) are shown in Fig. 8.10 (normalized with respect to the initial pre-exposure value). In this figure, each box plot corresponds to the 9 cells in each sample, measured at regular interval of UV dose. Each cell is at a different temperature and has different severity of discoloration, so there is the spread in the data points. A maximum loss of 4% in  $I_{sc}$  has been observed for the UV-cut sample, while ca. 7% has been observed for the UV-pass sample. In order to discount for the initial Light Induced Degradation (LID), we can neglect the  $I_{sc}$  degradation till the first measurement upon UV exposure (approx. 25 kWh/m<sup>2</sup> UV dose). For the UV-cut samples, there is no significant  $I_{sc}$  loss after the initial LID period, but there is some additional loss in the UV-pass sample (of around 1%). This loss may be due to the delamination observed in this module. Also, it can be seen from Fig. 8.10 that the lower temperature cells have a higher reduction in current as compared to the high-temperature cells. This decrease in  $I_{sc}$  can be primarily due to Light Induced Degradation (LID). It has been assumed that the LID would stabilize after the initial UV dose of 25 kWh/m<sup>2</sup>, considering that IEC 61215 standard has recommended a minimum irradiation dose of 15 kWh/m<sup>2</sup> for initial stabilization of crystalline silicon modules [17].

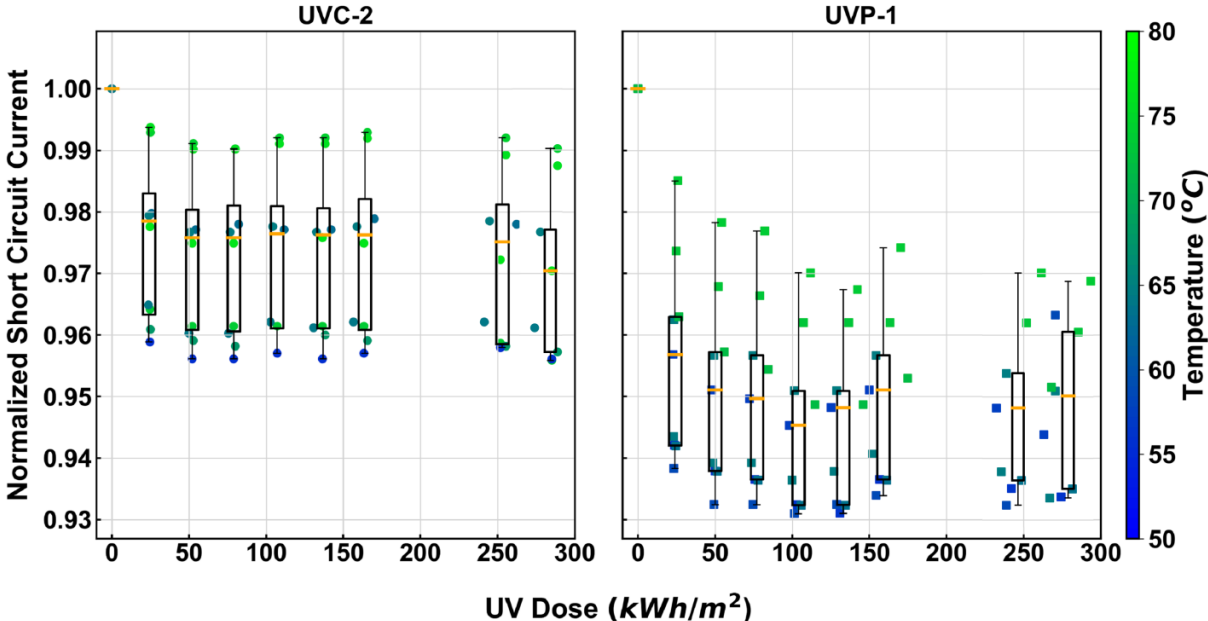


Fig. 8.10: Normalized short-circuit current of UV-cut sample (left) and UV-pass sample (right) versus UV dose in Xenon chamber.

During the Xenon exposure, the cell at the center of the laminate was kept under short-circuit (shown with triangular marker in blue color in Fig. 8.11), while the other cells (along the periphery of the laminates) were kept at open-circuit condition (shown with square marker in red color). The open-circuited cells have shown higher loss in  $I_{sc}$  as compared to the short-circuited cells (at same temperature of exposure). This may be attributed to LID caused by the generation of Boron-Oxygen complex which is assisted by minority carrier recombination in the bulk of the semiconductor [134].

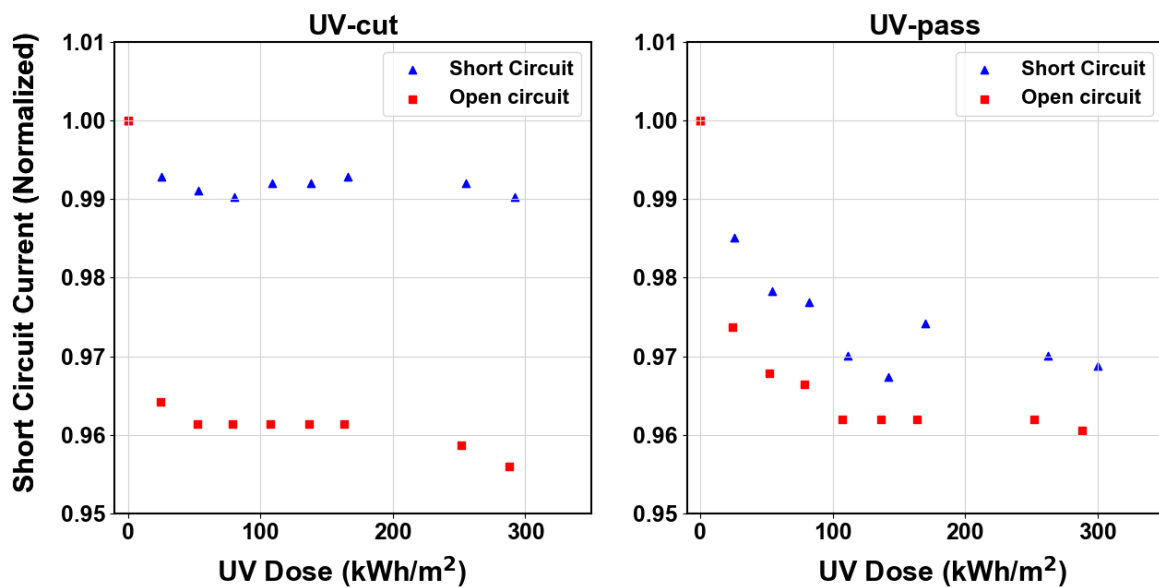
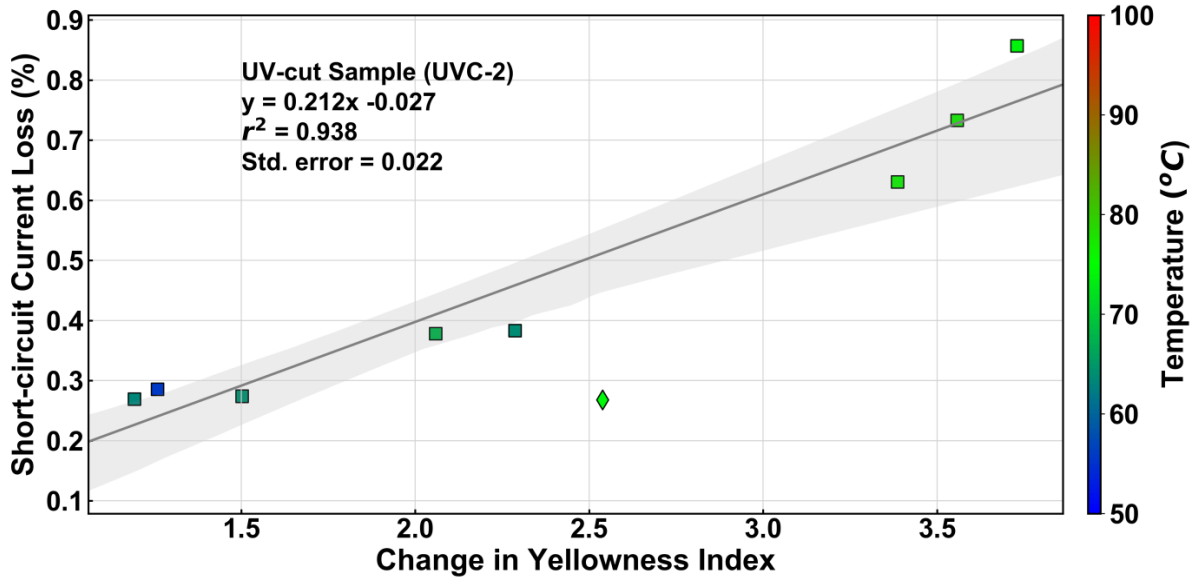


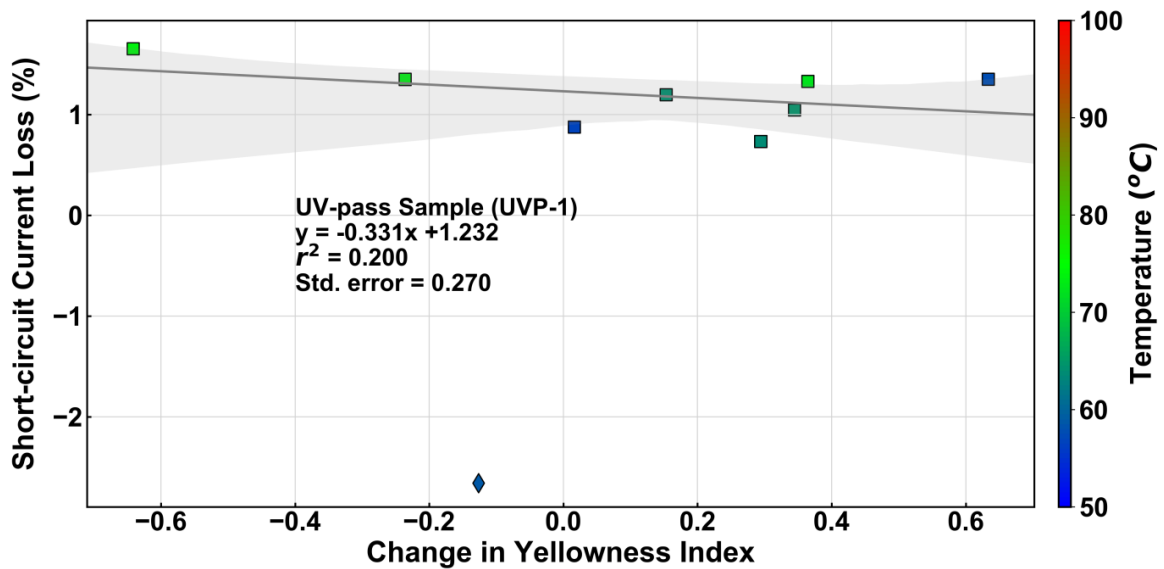
Fig 8.11: Normalized short-circuit current of UV-cut sample (*left*) and UV-pass sample (*right*) versus UV dose under Xenon exposure – Comparison of short-circuit and open-circuit cells at 74 °C sample temperature.

In order to correlate the  $I_{sc}$  loss with the discoloration of EVA, we have plotted the loss of  $I_{sc}$  versus the increase in  $YI$  after discounting for initial LID (by considering the values after the first exposure as initial value), as shown in Fig. 8.12. A correlation between the  $I_{sc}$  degradation and the  $YI$  change is evident for UV-cut EVA, but no such correlation is found for the UV-pass EVA. This indicates that  $I_{sc}$  loss in the UV-pass EVA sample is not due to discoloration (but due to other issues like LID and/or delamination as discussed earlier). Difference in the extent of LID in the UV-cut and UV-pass EVA samples may be due to the differences in initial cell/wafer quality. Also, there is a possibility of higher degradation of the surface passivation layer of the silicon solar cells in the UV-pass sample due to higher UV incident on the cells

[133]. Hence, it is advisable to use UV-resistant cells and backsheet in PV modules that use UV-transparent EVA.



(a)



(b)

Fig. 8.12: Correlation of short-circuit current loss with the change in  $YI$  - (a) UV-cut sample (UVC-2), and (b) UV-pass sample (UVP-1). The data point shown with diamond marker is an outlier and has not been considered for fitting the trend line. Correlation is present for the UV-cut sample but not for the UV-pass sample.

The comparative test of the UV-cut and UV-pass EVA coupons in the Xenon chamber establishes the higher stability of the UV-pass EVA under moderate sample temperature up to 74 °C (which is in the range of the highest temperatures expected in rack-mounted PV modules in India). However, Xenon chambers are costly to maintain, and the tests take long duration to create noticeable degradation (due to low irradiance intensity). It was hence decided to experiment with the possibility to perform accelerated tests at higher irradiance and temperature using a high-intensity UV source. So, a UV-365 based source was used to develop a UV test setup, and high-temperature accelerated tests have been carried out in this chamber, the results of which are presented in the next section.

## **8.3 Accelerated Tests in UV-365 Chamber**

### **8.3.1 Test Chamber Design**

The UV-365 test chamber comprises of a UV light source (make: Thorlabs, model: SOLIS-365C), with an optical output of 3 Watts (nominal). The UV source is located outside the chamber, and the light from the UV source enters the sealed chamber through a Quartz glass window, as shown in Fig. 8.13. The samples are held against a copper heating plate, whose temperature is controlled using a PID controller (make: Taiwan Instrument & Control Co. Pvt. Ltd., model: FU400). The chamber is provided with gas filling lines and a vent valve. A humidity sensor is placed inside the chamber which communicates with a computer through an Arduino board for logging the humidity data. The possibility to change the atmosphere in the chamber is an added advantage which is not available in standard off-the-shelf UV chambers and has enabled us to test the effect of dry air and nitrogen (oxygen-deficient) atmosphere on the degradation rate of the encapsulant.

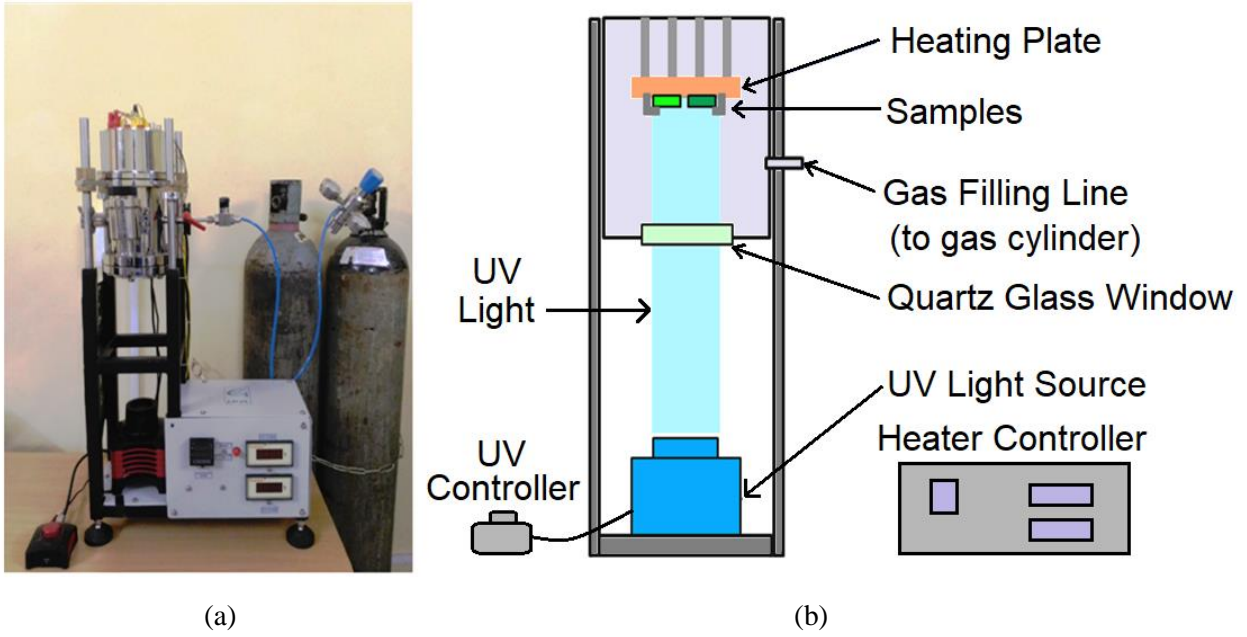


Fig. 8.13: UV-365 test setup – (a) visual image of full setup (b) schematic diagram of the setup.

### 8.3.2 Effective Intensity of UV-365 source

The maximum intensity of the UV source is close to  $900 \text{ W/m}^2$ , which is approximately 20 times higher than the total UV intensity in the AM1.5G spectrum ( $46 \text{ W/m}^2$ ), shown in Fig. 8.14. It has been suggested in literature [135] that UV intensity greater than 5 times the UV content in sunlight is not advisable for accelerated tests since it may induce degradation modes not seen outdoors in natural environment.

However, Xiahong *et al.* [73] have indicated that all wavelengths are not equally efficient in causing degradation of the EVA polymer, and the shorter wavelengths have greater efficiency than the longer wavelengths, as shown in Fig. 8.15. The effective UV intensity of the AM1.5G solar spectrum corresponding to 365 nm wavelength is:

$$UVI = \sum_{w=280 \text{ nm}}^{400 \text{ nm}} G(w) \cdot \phi(w) = 517.67 \text{ W/m}^2 \quad \dots (8.2)$$

where,

$G(w)$  = UV Irradiance at wavelength 'w' (obtained from [136])

$\phi(w)$  = Relative efficiency of wavelength 'w' (obtained from [73])

Hence, the 365 nm UV intensity of 900 W/m<sup>2</sup> is approximately **1.8 times** of the effective AM1.5G UV intensity and can be theoretically considered for accelerated testing of encapsulants used in PV modules.

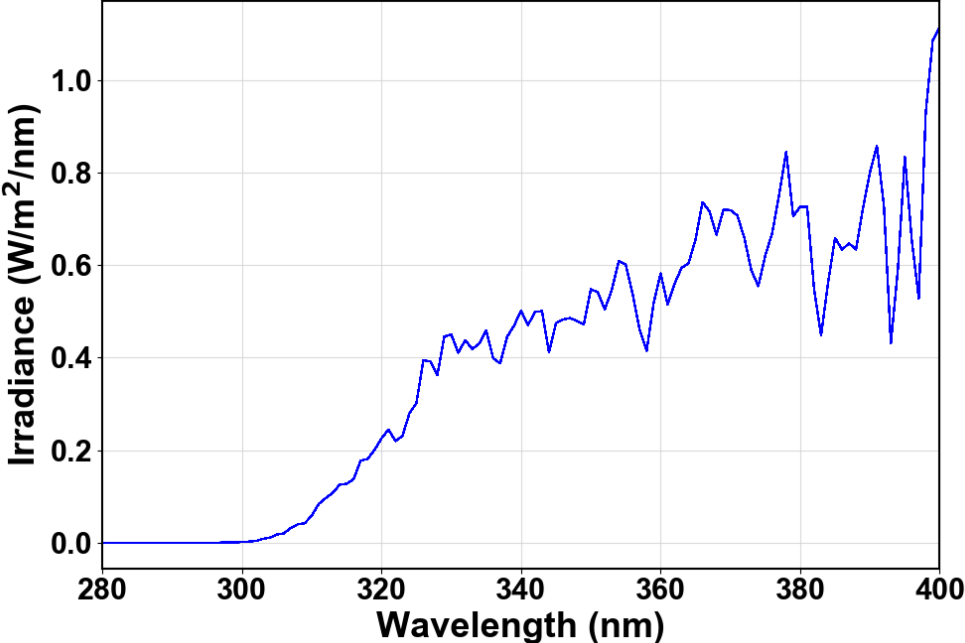


Fig. 8.14: UV Irradiance in the AM1.5G spectrum (after Emery [136]).

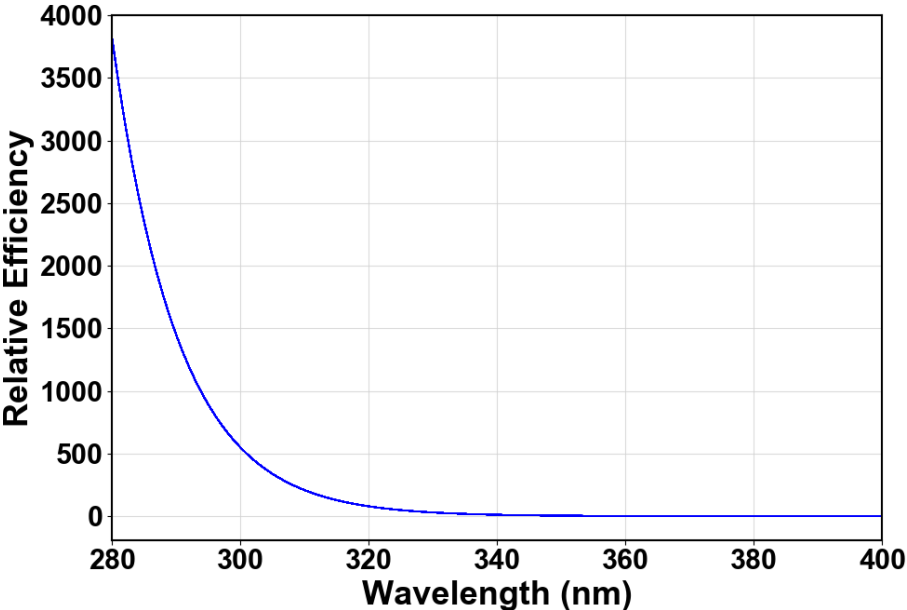


Fig. 8.15: Relative efficiency of different UV wavelengths in causing yellowing of EVA, relative to 365 nm (based on Xiahong *et al.* [73]). Shorter wavelengths close to 300 nm are much more detrimental than longer UV wavelengths close to 400 nm.

### 8.3.3 Methodology

Coupons comprising of 2 cm x 2 cm quartz glass (of thickness 2 mm) and fluoropolymer based backsheet are laminated using UV-cut and UV-pass EVA (schematically shown in Fig. 8.16). The lamination of these coupons is done in a laboratory-scale semi-automatic laminator supplied by AW Solutions (India), at a curing temperature of 145 °C (+/- 5 °C) with total cycle time of 14 minutes (which includes 7 minutes curing time).

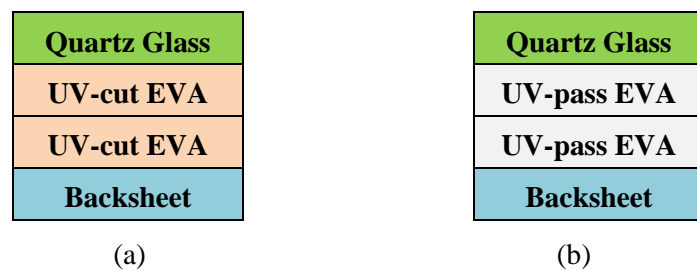


Fig. 8.16: Construction of the EVA test coupons for the UV-365 chamber – (a) UV-cut coupon, and (b) UV-pass coupon.

After the lamination, the samples were subjected to various characterization tests as given below:

- a) *YI* was measured at selected spots (sample center and two edges) using Colorimeter
- b) Fluorescence spectrum was measured at selected spots using Fiber Optics Spectrometer
- c) Transmittance and reflectance were measured in UV-Vis Spectrometer

After the pre-exposure characterization of the samples, the samples are mounted on the heating plate inside the chamber, with the glass side facing downwards (towards the UV light source). The chamber is purged with dry air so that the relative humidity inside the chamber is below 20%. The UV light source is set at its maximum intensity (3 Watt optical output), and the sample heater is set to 90 °C. The humidity inside the chamber is monitored using a DHT22 sensor (accuracy: ±3% RH) connected to an Arduino-Uno based data logger. In both coupons, one part is exposed to high-intensity UV rays while the other part is exposed to lower intensity as shown in Table 8.2. The samples are removed from the chamber from time to time for measurements. The UV intensity has been calculated from the short circuit current of a silicon photo-diode (FIL-20C) as per the equation given below:

$$\text{UV Intensity (W/m}^2\text{)} = \frac{\text{Sensor current}}{\text{Sensor responsivity} \times \text{Sensor area}} \quad \dots(8.3)$$

where,

Sensor current = short circuit current of the sensor when exposed to the light source (measured using Keysight 34465A digital multimeter).

Sensor sensitivity = spectral responsivity of the sensor at 365 nm (= 0.05 A/W [137])

Sensor area = active area of the photo-diode (= 0.0000164 m<sup>2</sup> [137])

Table 8.2: UV Intensity at different points, measured using photodiode.

		Position	UV Intensity (W/m <sup>2</sup> )
		1	382
		2	762
		3	884
		4	878
		5	812
		6	456

### 8.3.4. Spatial non-uniformity of UV intensity

The SOLIS 365C source from Thorlabs has a rated optical output of 3 Watts. It generates a square beam of approximate size 4 cm x 4 cm, but the intensity is not uniform over the exposure area. Figure 8.17 shows the fluorescence of a sheet of paper upon exposure to the UV-365 light source, in which the spatial non-uniformity towards the edges is clearly visible. The intensity of the incident UV light was measured at various positions of the two samples using a silicon photodiode (UDT FIL-20C, having 16.4 mm<sup>2</sup> active area), and the values are given in Table 8.2. The UV intensity at one edge of each sample is almost 2 times of that at the other edge. The positions marked as 1 to 6 on the two samples are also the position at which the *YI* was measured, in order to determine the correlation between the UV intensity and the extent of discoloration.

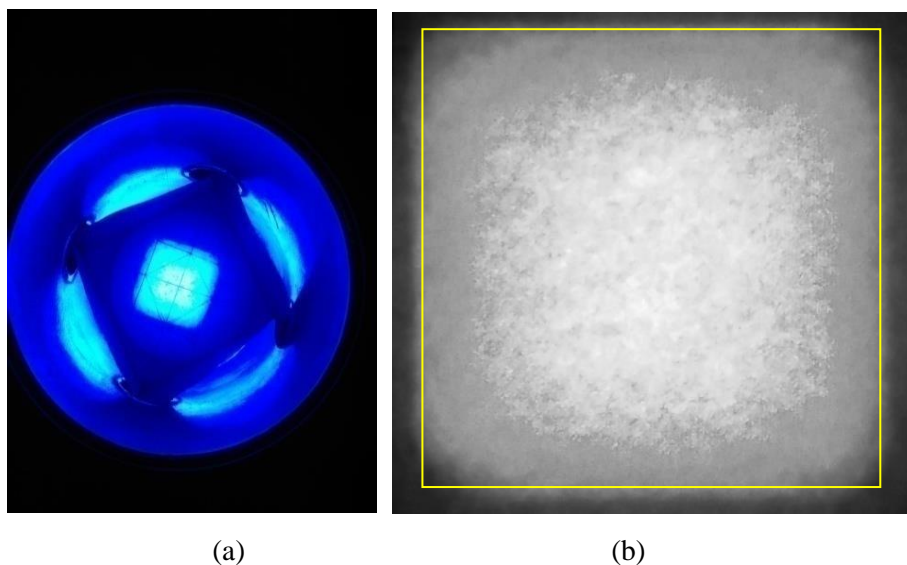


Fig. 8.17: Fluorescence images of paper placed inside the UV-365 chamber – (a) digital image taken from top, (b) grayscale image clearly shows the variation in the UV intensity in the region of interest (4 cm x 4 cm exposure area is marked with yellow box). The intensity (brightness) is lower at the edges as compared to the center of the exposure area.

### 8.3.5 Results & Discussion

#### a) Yellowness Index

The highly accelerated tests on the 2 cm x 2 cm coupons in the UV-365 chamber has led to significant discoloration in the UV-cut coupon, as shown in Fig. 8.18. There is non-uniformity in the UV intensity inside the chamber (refer to intensity distribution shown in Fig. 8.18), which led to higher discoloration at one edge than the other edge of the coupons. Figure 8.19 shows the change in *YI* with UV dose for the UV-cut and UV-pass samples (at the discolored edge of the samples). It is evident that the UV-cut EVA degrades about 5 times faster than the UV-pass EVA in the highly accelerated test. The UV intensity incident is about 880 W/m<sup>2</sup> at 365 nm, while the sample back-plate (hot plate) temperature is 90 °C. This shows that the UV-pass EVA is a better formulation which discolors lower than UV-cut EVA even in harsh conditions.

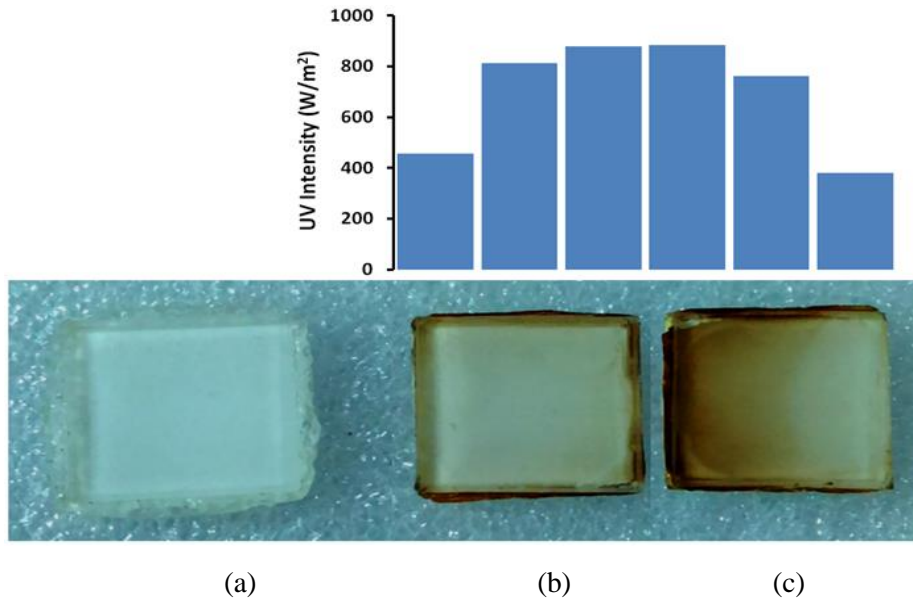


Fig.8.18: Effect of UV-365 exposure on the coupons – (a) unexposed coupon, (b) exposed UV-pass coupon and (c) exposed UV-cut coupon (UV intensity is shown on top of the exposed coupons). Higher discoloration is observed in UV-cut coupon than in UV-pass coupon.

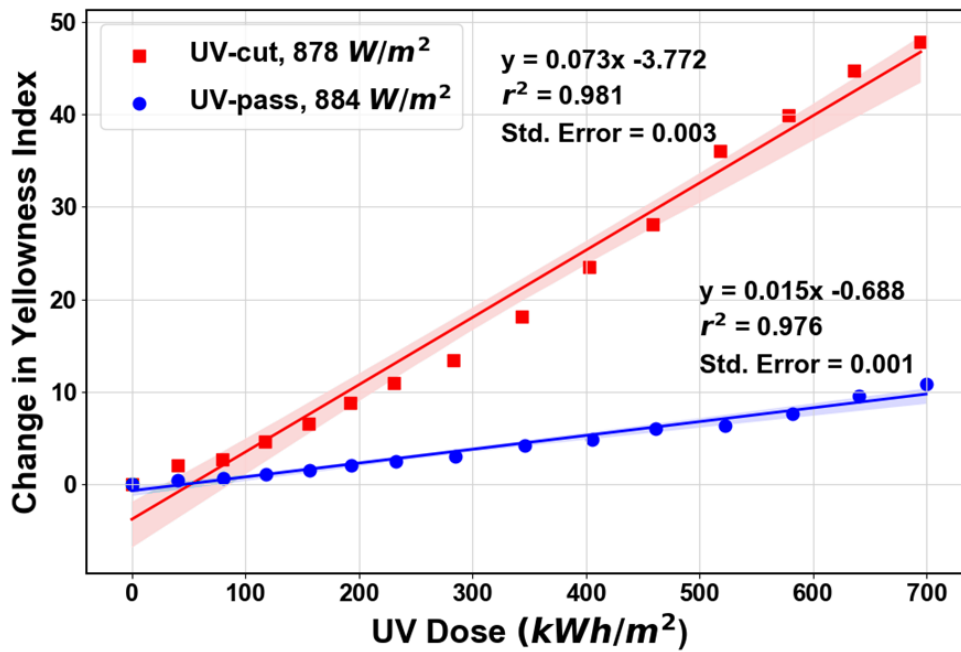


Fig.8.19: Change in *YI* of UV-cut and UV-pass samples, in UV-365 chamber tests (measured at discolored edge, positions 3 & 4 in Table 8.2). Discoloration rate is almost 5 times higher in UV-cut coupon.

## b) Fluorescence Spectroscopy

The yellow color in the degraded EVA encapsulant is caused by fluorescent long-chain polyenes formed during the degradation process [2]. Hence, fluorescence spectroscopy can be used as a technique for early detection of polymer degradation (much before there is any visible change in the visible color of the encapsulant). A fiber optics spectrometer coupled with the UV-365 light source has been used to track the increase in the fluorescence of the samples. Fig. 8.20 shows the fluorescence spectra for the different spots on the UV-cut sample after approximately 700 kWh/m<sup>2</sup> UV exposure. The UV-pass sample's fluorescence is much lower than that from the UV-cut sample (about 4.4 times lower at 629 nm peak wavelength at UV dose of ca. 700 kWh/m<sup>2</sup>).

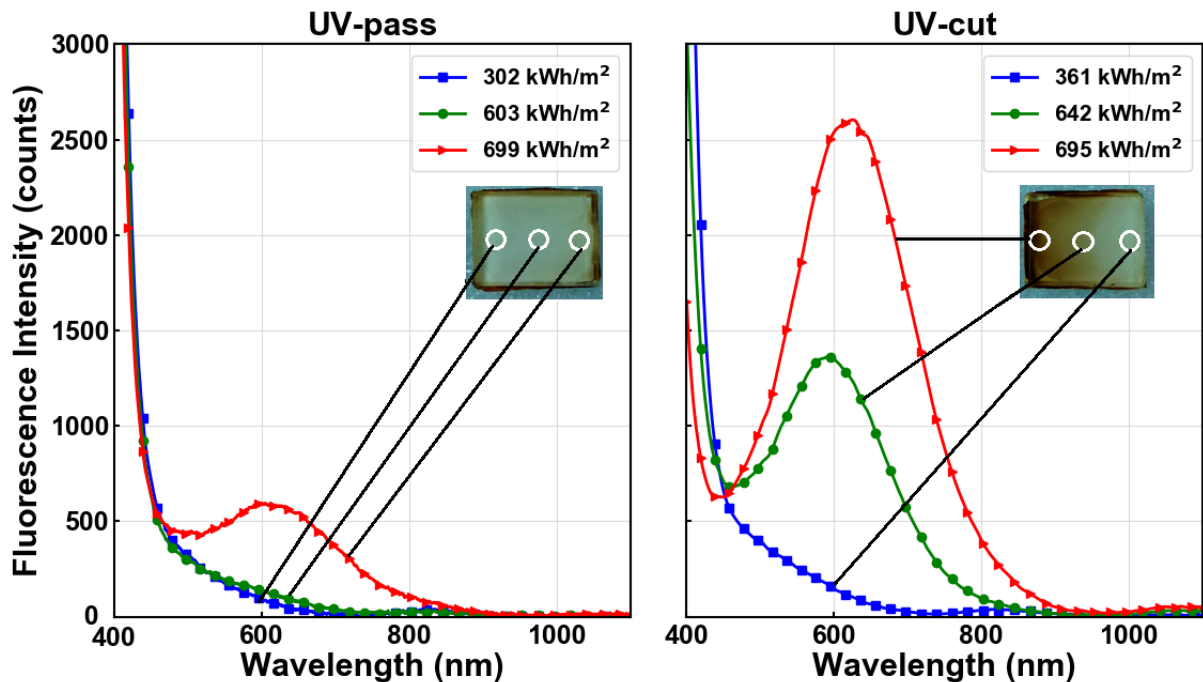
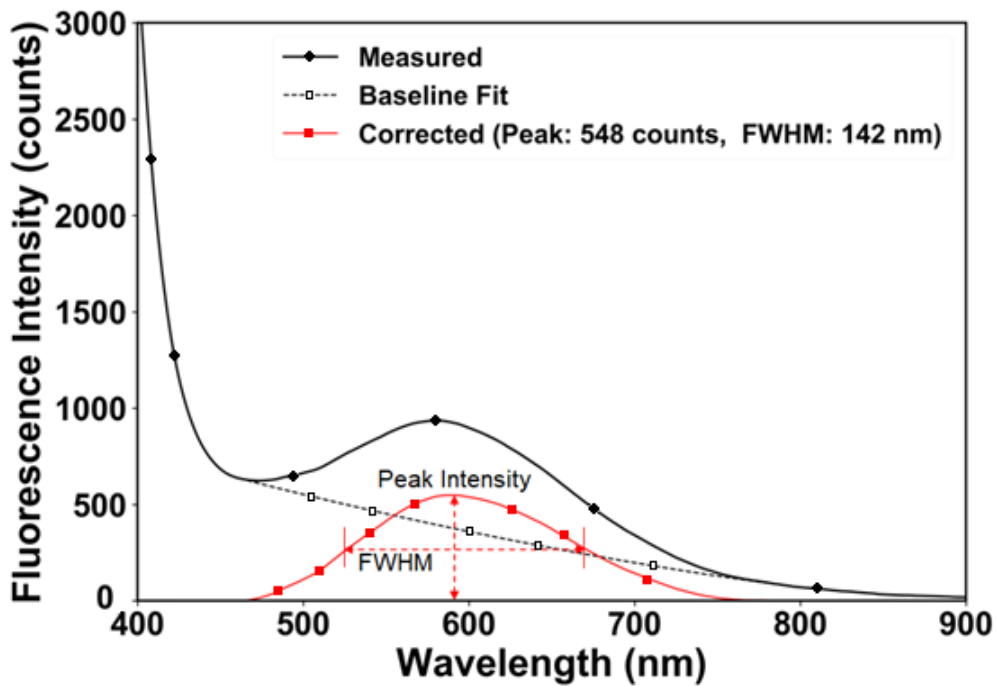


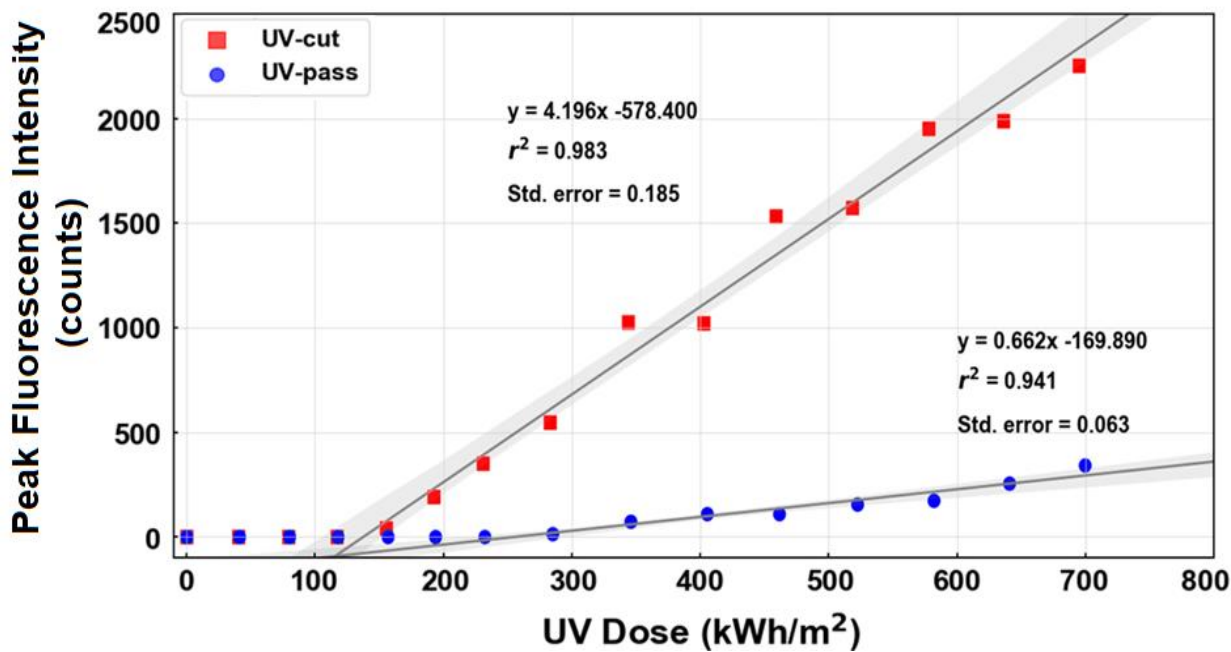
Fig. 8.20: Fluorescence spectra of UV-cut and UV-pass coupons after 700 kWh/m<sup>2</sup> exposure in UV-365 chamber. The peak intensity is almost 5 times higher in UV-cut coupon.

Baseline correction has been applied to extract the fluorescence peak from the spectrum (which includes the long tail of the excitation waveform), as shown in Fig. 8.21(a). The peak intensity and the Full Width at Half Maximum (FWHM) are shown in this plot. The peak fluorescence intensity (after baseline correction) is plotted against the UV dose for the discolored edge of the UV-cut and UV-pass coupons in Fig. 8.21(b). This plot shows that the fluorescence intensity of both coupons was below detection limit of the instrument till about

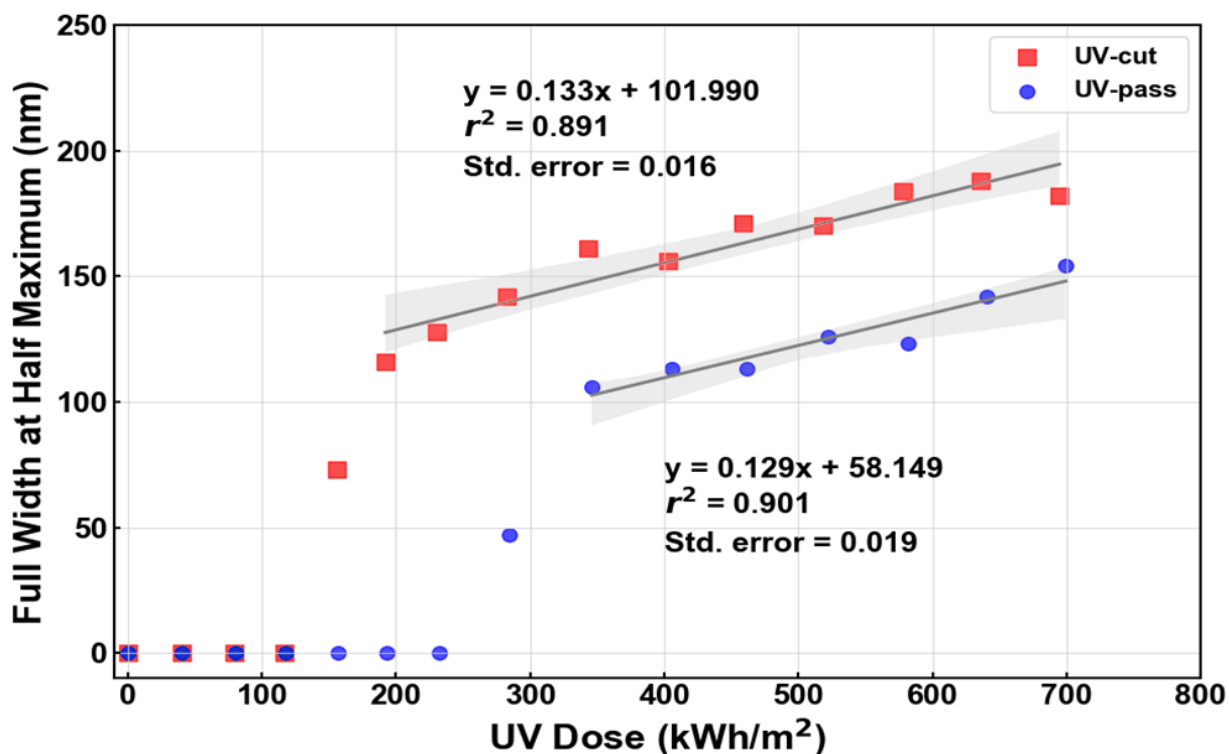
150 kWh/m<sup>2</sup> UV dose. Beyond this dose, the UV-cut coupon shows faster increase in the fluorescence intensity (about 6 times faster than UV-pass coupon). It may be noted that considering the standard errors in the two slopes (0.185 and 0.063), the lowest ratio of the slopes (considering 95% confidence interval) is around 4.8, which is comparable to the ratio of the discoloration rates shown in Fig. 8.19. The FWHM values of the fluorescence spectra, plotted in Fig. 8.21(c), indicate that the FWHM for the UV-pass coupon is lower than that of the UV-cut coupon (though the rate of increase is similar).



(a)



(b)

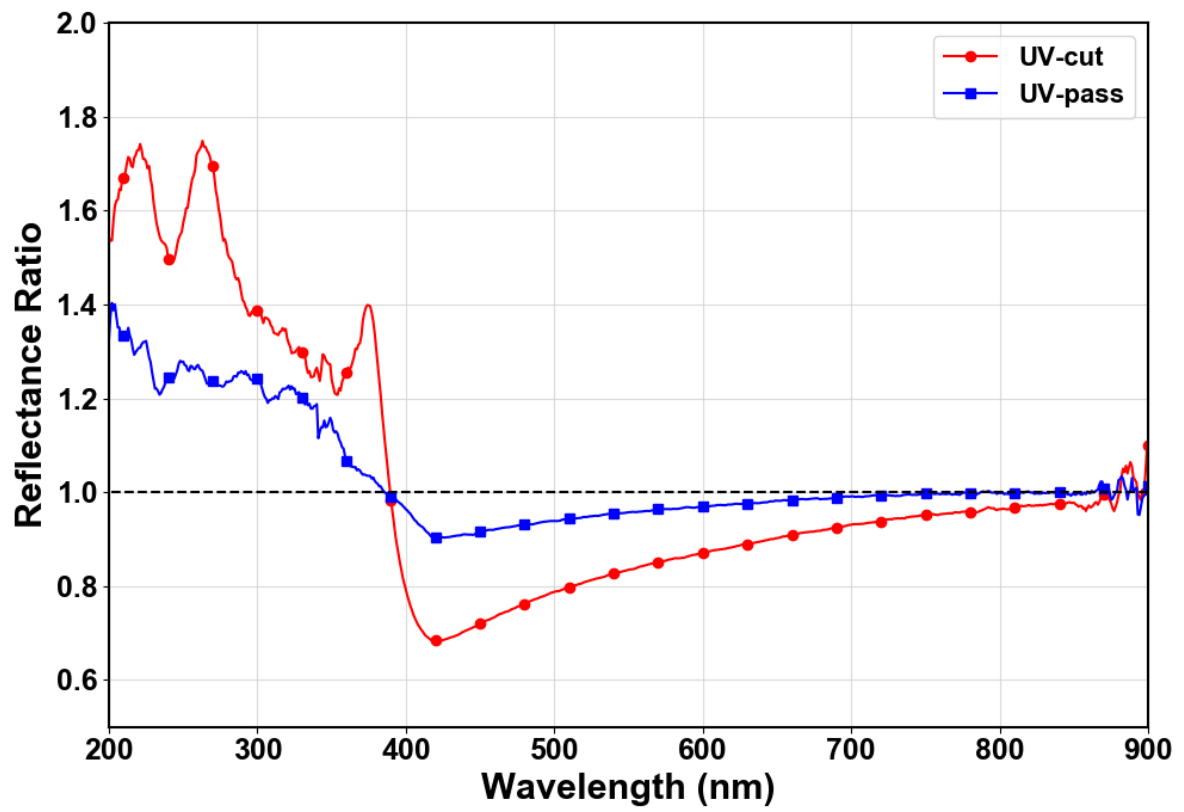


(c)

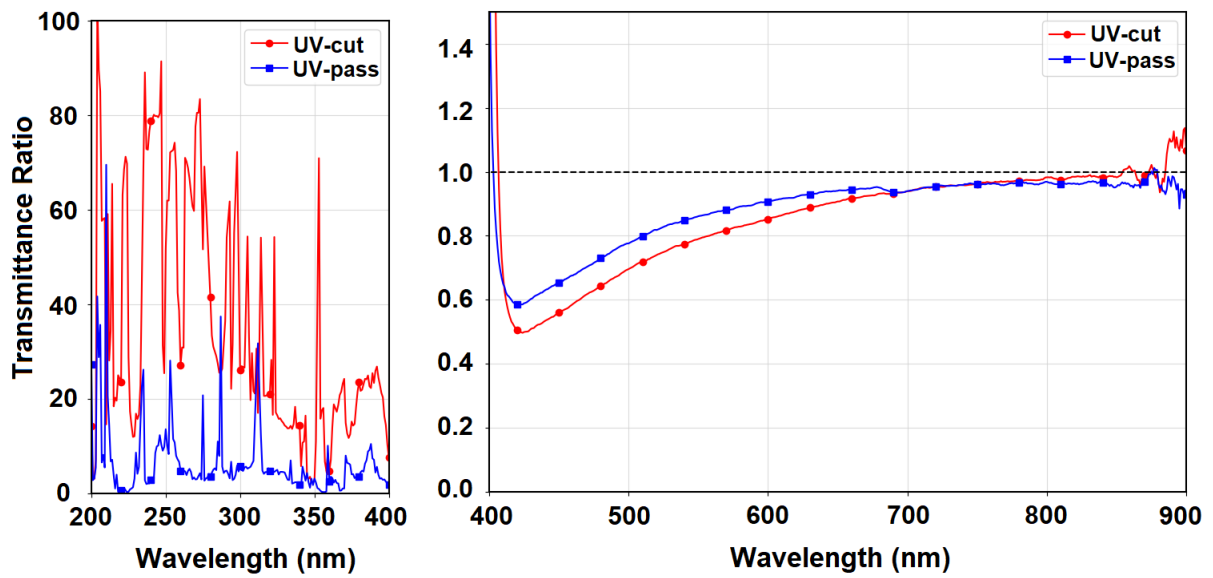
Fig. 8.21: (a) Baseline correction of Fluorescence Spectra, indicating the peak intensity and the full width at half maximum (FWHM), (b) evolution of the fluorescence peak intensity in UV-cut and UV-pass coupons with UV exposure, and (c) evolution of the FWHM in UV-cut and UV-pass coupons with UV exposure. Fluorescence peak intensity increased 6.3 times faster in the UV-cut coupon.

### c) UV-Vis Spectroscopy

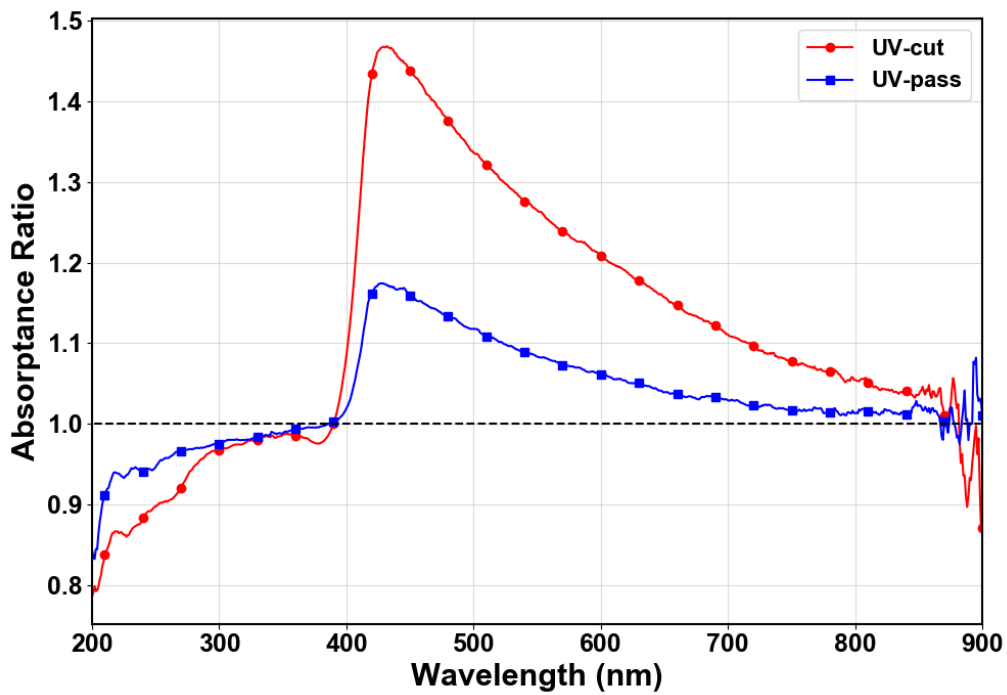
The reflectance and transmittance of the coupons exposed to 365 nm UV light have been measured using a UV-Vis spectrometer equipped with an integrating sphere (make: Jasco, model: V-750). It should be noted that the reflectance from the Glass-EVA-backsheet sample includes the reflected light from the air-glass, glass-EVA, and EVA-backsheet interfaces and is influenced by the transmittance (absorption) of light by the EVA. Based on the reflectance and transmittance measurements, the absorptance of the sample has been calculated ( $= 1 - \text{Transmittance} - \text{Reflectance}$ ). The percentage change in reflectance, transmittance, and absorptance from the initial (pre-exposure) value is shown in Fig. 8.22, for both the UV-cut and UV-pass coupons. The absorptance of the UV-cut coupon increased by ca. 60% at 450 nm while that of the UV-pass coupon increased by 19%. Also, the UV absorption (in the 200 – 300 nm range) decreased more in the UV-cut coupon than the UV-pass coupon, indicating the depletion of the UV absorbers. It may be noted that these values are for the full coupon cross-section (comprising of glass, EVA, and backsheet) but nonetheless indicate the effect of the higher degradation suffered by the UV-cut coupon as compared to the UV-pass coupon. The increase in absorptance ratio is found to be highest around 430 nm, so the variation in the absorptance ratio at 430 nm is plotted against the UV dose in Fig 8.23. The 430 nm Absorptance ratio for UV-cut coupon increased almost 2.8 times faster than the UV-pass coupon.



(a)



(b)



(c)

Fig. 8.22: Ratio of optical properties for UV-cut and UV-pass coupons after ca. 700 kWh/m<sup>2</sup> UV dose with respect to initial values – (a) reflectance (b) transmittance and (c) absorbance. The properties are measured at the center of the UV-cut and UV-pass coupons. Higher Absorbance of UV-cut coupon is due to its higher discoloration.

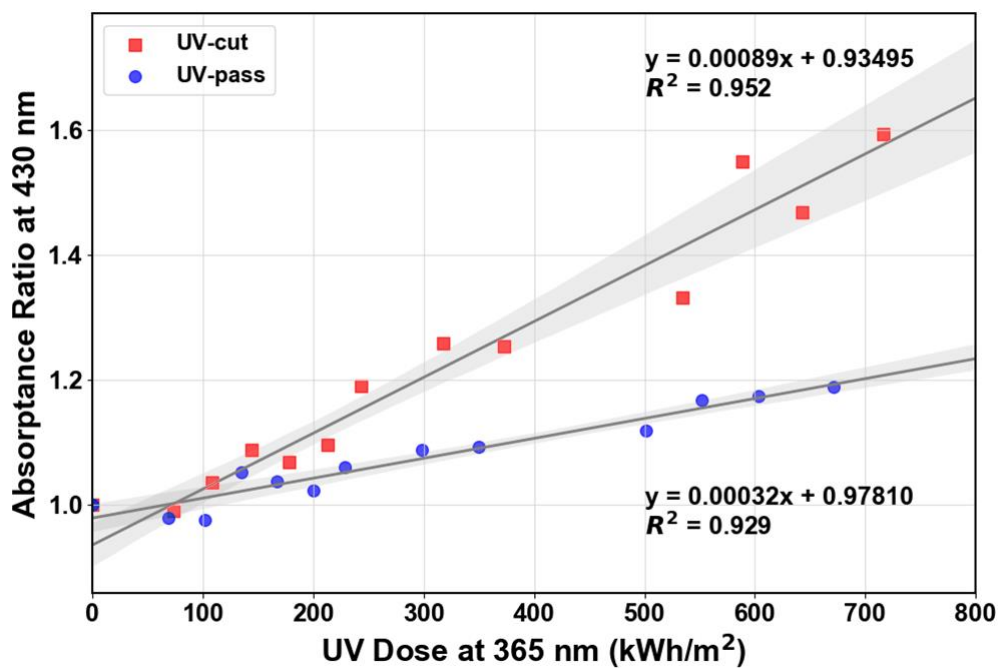


Fig. 8.23: Absorbance ratio (at 430 nm wavelength) versus UV dose for UV-cut and UV-pass coupons. The rate of increase is 2.8 times higher in UV-cut as compared to UV-pass coupon.

#### d) Effect of Oxygen on Yellowing Rate of the UV-cut Sample

Oxygen is an important stressor present in our atmosphere, which affects the degradation rates of different components of the PV modules. In the EVA encapsulant discoloration process, oxygen is known to act as a bleaching agent in the presence of light, removing the brown color of the discolored encapsulant and turning it to transparent material (by breaking up the long-chain conjugated polyenes) [48]. Accelerated tests have been performed on UV-cut EVA coupons in both dry air atmosphere and nitrogen (oxygen deficient) atmosphere, at backplate temperature of 90 °C. The discoloration of the coupons is compared in Fig. 8.24, where it can be seen that the discoloration (change in  $YI$ ) is lower in the nitrogen atmosphere than the dry air. This indicates that oxygen can act as a degradation initiator, at high operating temperature. The log-linear plot of the change in  $YI$  versus the UV dose (shown in Fig. 8.25) clearly differentiates between the discoloration rates in dry air and nitrogen atmosphere. The change in  $YI$  is exponential function of the UV dose in dry air atmosphere and nitrogen atmosphere, as indicated below.

$$\ln(\Delta YI) = 0.00583 \cdot (UV \text{ Dose}) + 0.05906 \quad (\text{in dry air atmosphere}) \quad \dots(8.4)$$

$$\ln(\Delta YI) = 0.01442 \cdot (UV \text{ Dose}) - 3.64915 \quad (\text{in nitrogen atmosphere}) \quad \dots(8.5)$$

By subtracting the change in  $YI$  obtained from these two equations (i.e.  $\Delta YI_{DA} - \Delta YI_{N_2}$ ), we can see the effect of oxygen on the discoloration rate, as shown in Fig. 8.26. Oxygen is aiding in the discoloration process initially, at low UV dose. However, after sufficient UV exposure, the photo-bleaching action of oxygen comes into play, reducing the difference in  $YI$  between the dry air and the nitrogen experiments. Experiments at NIST [57] have shown that oxygen atmosphere leads to higher chain scission in EVA film, which can explain the initial behaviour. After sufficient UV dose, as the concentration of the chromophoric degradation products increases and becomes available for reaction with oxygen, the photo-bleaching action of oxygen disintegrates these degradation products, removing their colour-producing ability. Thus there is a competition between the oxygen-assisted degradation reaction (increasing the yellowing) and the photobleaching reaction (reducing the yellowing). This experiment hints at the dual role of oxygen as a degradation initiator and a bleaching agent. The role of oxygen in the thermal degradation of various other polymers has been investigated previously by many

researchers. Gupta *et al.* [74] have studied the effect of oxygen on the degradation of Poly-Vinyl Chloride (PVC) and proposed a degradation mechanism based on the formation of unstable peroxy radicals through the reaction of oxygen with the radicals generated in PVC. A similar degradation pathway based on polymer peroxide formation is also reported by Peterson *et al.* [75]. Xiahong *et al.* [57] have also reported that photodegradation of EVA in oxygen atmosphere caused higher discoloration as compared to argon atmosphere, which supports the role of oxygen in photo-degradation of EVA encapsulant.

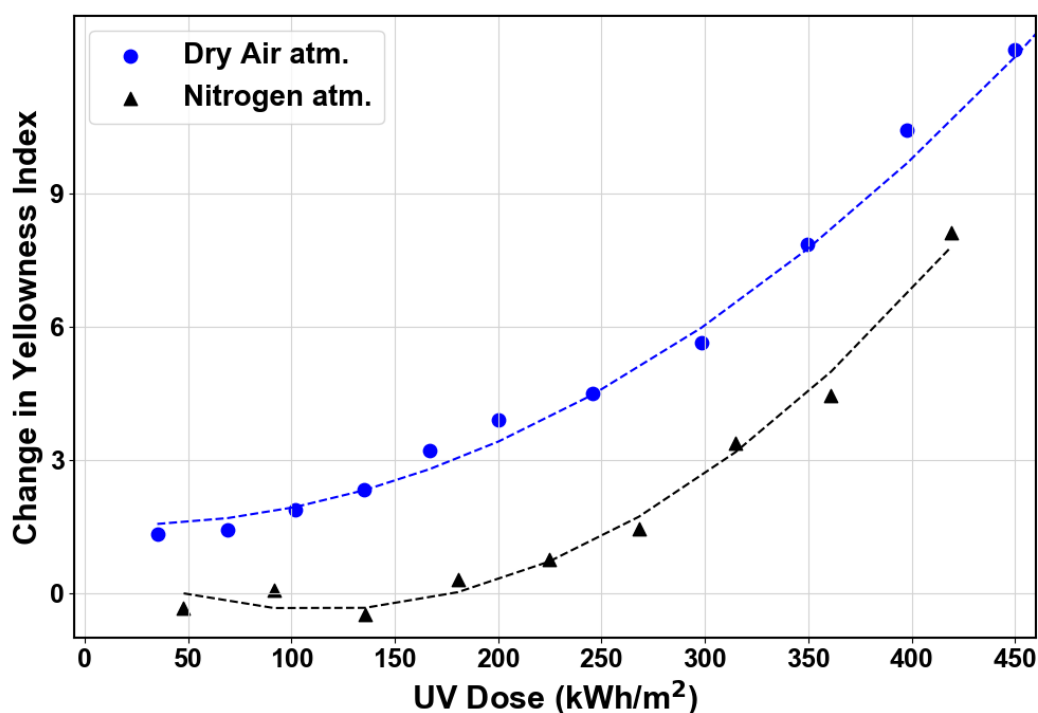


Fig. 8.24: Comparison of discoloration in dry air and nitrogen atmosphere in UV-365 chamber at 90 °C back-plate temperature. The yellowing is higher in presence of oxygen.

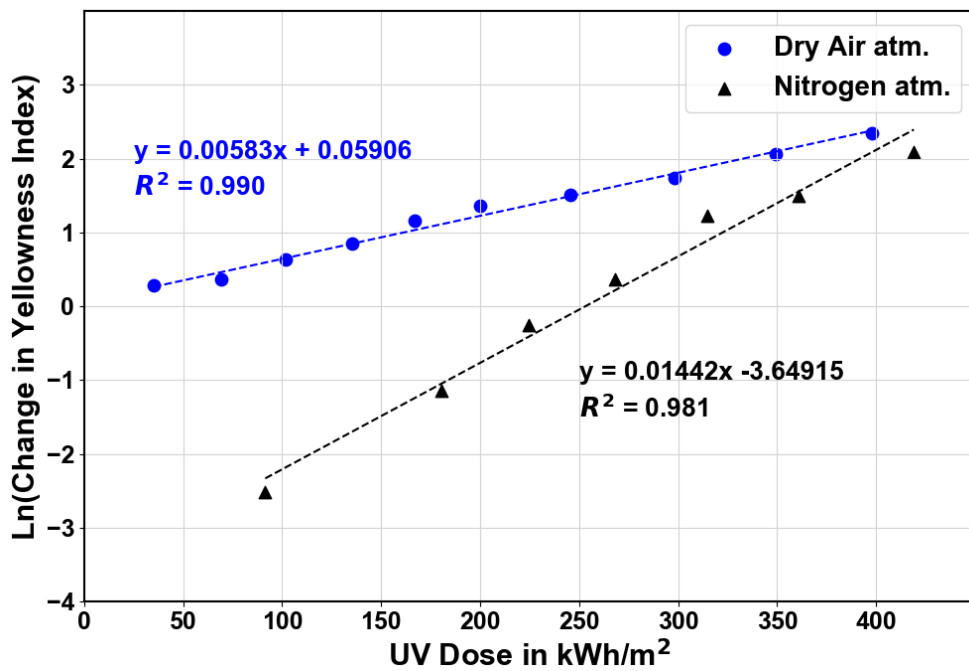


Fig. 8.25: Comparison of discoloration in dry air and nitrogen atmosphere in UV-365 chamber at 90 °C back-plate temperature, based on logarithm of the change in *YI*.

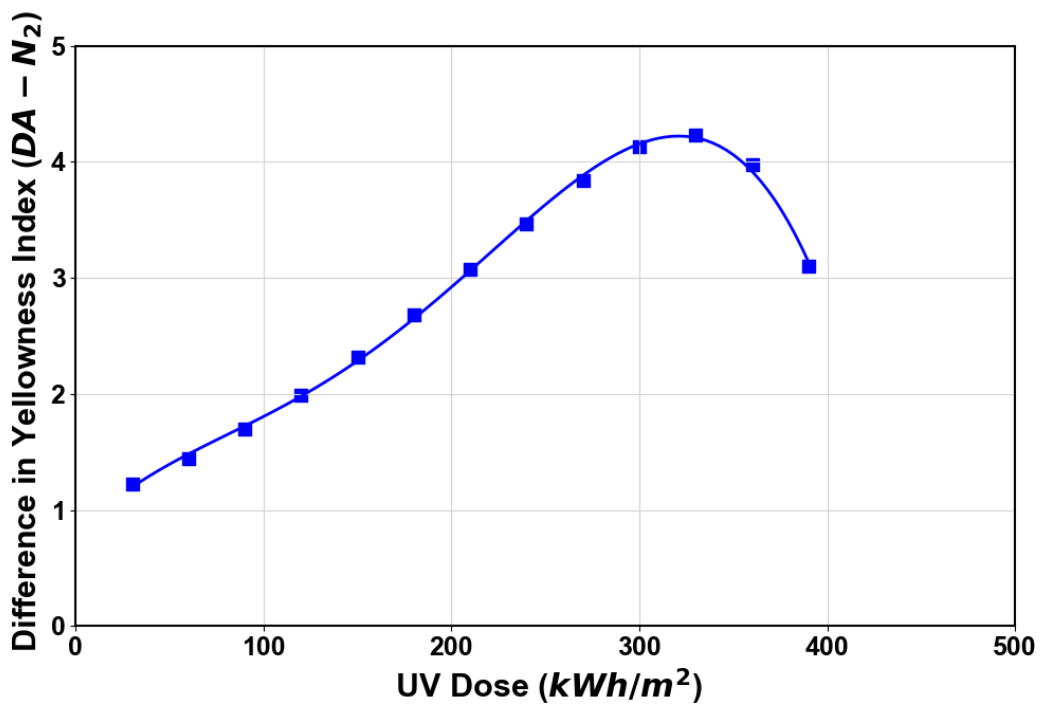


Fig. 8.26: Difference in *YI* of UV-cut coupon between dry air and nitrogen atmosphere, plotted against UV dose. This plot shows the effect of oxygen on discoloration of EVA encapsulant (relative to nitrogen atmosphere).

The accelerated tests on UV-cut EVA in the UV-365 chamber in dry air and nitrogen atmosphere have been conducted at a high sample plate temperature of 90 °C, with UV intensity of ca. 800 W/m<sup>2</sup> (at 365 nm). The difference in the yellowing rate between the oxygen and nitrogen environment indicates the role of oxygen as a degradation supporter in the initial stage in such elevated conditions (high UV radiation intensity and elevated temperatures).

## 8.4 Summary

UV-cut and UV-pass EVA based laminates have been studied under Xenon exposure for 4000 hrs, with a total UV intensity (between 300 – 400 nm wavelength) set point of 75 W/m<sup>2</sup>, black panel temperature of 60 °C and chamber relative humidity of 20%. The sample temperatures varied in the range of 58 – 76 °C. The UV-cut EVA samples showed significantly higher increase in *YI* as compared to the UV-pass samples. Fluorescence measurements also showed increase in the UV-cut EVA but there was a continuous decrease in case of the UV-pass sample. The short-circuit current of the samples decreased initially (which may be attributed to Light Induced Degradation) before stabilizing. A correlation could be obtained between the  $I_{sc}$  loss and the increase in *YI* for the UV-cut EVA, but not for the UV-pass EVA. Though there was no visible discoloration in the UV-pass sample, delamination has been observed between the solar cells, which may be due to the higher UV penetration in the laminate.

Activation energy for discoloration of the UV-cut sample was calculated to be 0.61 eV, but no such activation energy could be obtained for the UV-pass EVA. However, significant increase in *YI* could be observed for both the UV-cut and UV-pass EVA coupons exposed to accelerated stress test in the UV-365 chamber (ca. 880 W/m<sup>2</sup> UV intensity at 365 nm with sample temperature of 90 °C). The rate of increase of the yellowness index in the UV-cut EVA coupon was found to be 4 times of that in the UV-pass coupon in this highly accelerated test. This conclusively confirms that the UV-pass encapsulant discolors at a slower rate than the UV-cut EVA, and can be a better alternative for deployment of PV modules in Hot climatic conditions (from discoloration point of view), provided the problem of delamination of the encapsulant can be solved. Since the UV-pass EVA allows UV light to pass through, there is a possibility of degradation of the underlying materials (solar cell passivation layer and backsheets) due to UV

exposure. Hence it is necessary to consider the compatibility of the materials when adopting the UV transparent EVA encapsulant in module production.

The experiments in the UV-365 chamber have been performed on glass-EVA-backsheet laminates and bring us to the following conclusions:

1. The UV-pass EVA samples degrade almost 5 times slower than the UV-cut EVA samples, at  $880 \text{ W/m}^2$  UV-365 intensity and  $90 \text{ }^\circ\text{C}$  sample plate temperature, under a dry atmosphere ( $\text{RH} < 20\%$ ).
2. The absorptance of both the UV-cut and UV-pass coupons decreased in the UV range (200 – 400 nm), but increased in the 400 – 800 nm range, indicating degradation of the encapsulant. The rate of increase in Absorptance (at 450 nm) versus UV dose was 2.6 times higher in the UV-cut EVA as compared to the UV-pass EVA.
3. Discoloration starts later but increases at a faster rate in nitrogen atmosphere as compared to Dry Air (at elevated sample plate temperature of  $90 \text{ }^\circ\text{C}$  and UV intensity close to  $800 \text{ W/m}^2$  at 365 nm). This indicates that oxygen plays dual role, both as degradation initiator and as a bleaching agent (in such elevated experimental conditions). In the initial phase of UV exposure, the degradation initiator role is dominant, but at later stages, the bleaching role becomes dominant.

The experiments in the Xenon chamber have been performed on glass-EVA-cell-backsheet laminates, which are shielded with an aluminum layer in the backside to minimize the oxygen ingress. The Xenon lamp spectrum is closely matched to the noontime solar spectrum, so the results of this test are of greater significance. The conclusions from the Xenon chamber tests are as follows:

1. UV-cut EVA discolors much faster than UV-pass EVA. At  $64 \text{ }^\circ\text{C}$  sample temperature, the discoloration rate of UV-pass EVA is 3.5 times slower than the UV-cut EVA.
2. In the UV-cut sample, the discoloration rate increased with increase in temperature, but in the UV-pass sample the discoloration rate decreased with increase in temperature.

Arrhenius type relation between the discoloration and the sample temperature is observed in the UV-cut sample but not in the UV-pass sample.

3. The short-circuit current of the mini-modules have been found to reduce significantly (up to 5%) within the first 25 kWh/m<sup>2</sup> Xenon exposure, which is probably due to Light Induced Degradation (LID). The short-circuit current loss (post-LID) has been found to be proportional to the change in *YI* in the case of UV-cut samples, but no correlation is found for the UV-pass sample.
4. Fluorescence peaks in the UV-pass sample decreased monotonously upon UV exposure, whereas it increased in UV-cut sample after an initial period of decrease. This indicates that discoloring fluorophores are generated in the UV-cut sample but not in the UV-pass sample.
5. Delamination has been observed between cells in the UV-pass sample but not in the UV-cut sample. This hints that the higher UV penetration is degrading the adhesion of the backsheet, which is a matter of concern. Manufacturers have advised the use of UV-cut EVA at the back side in combination with UV-pass EVA in front so that the backsheet can be protected from the adverse effects of higher UV penetration into the laminate. Also, higher UV penetration can be detrimental to the surface passivation of the solar cell as per [133]. Hence it is important to use UV resistant materials in the PV module when using the UV-pass EVA.

This page is intentionally left blank.

## **Chapter 9**

### **Conclusions & Future Work**

#### **9.1 Conclusions**

We have surveyed PV modules in different parts of the country to identify the major degradation modes in different climatic zones. Encapsulant discoloration has been found to be a common degradation mode, affecting 35% of all inspected modules. In the young modules, installed less than 5 years ago, discoloration has been observed to be localized to a few cells, while for the older modules, mostly all the cells in the module are affected. The effect of discoloration on the electrical degradation of the surveyed modules has been investigated. Hot spots identified through infrared thermography have been found to be the root-cause for localized discoloration of encapsulant. Further, we have performed accelerated tests in the laboratory using 365 nm high power LED source and Xenon based sources to understand the problem of encapsulant discoloration and compared between the conventional UV-blocking

EVA formulation and a recently developed UV-transparent EVA formulation. The major conclusions from our study are given below:

### **1. Prevalence of various degradation modes in Indian climatic conditions**

- The Hot climatic zone (comprising of Hot & Dry, Warm & Humid and Composite) is found to be more severe than the Non-Hot climates for both the encapsulant and backsheet, based on the percentage of defective panels. Percentage of discolored modules in young sites (aged less than 5 years) is significantly higher in the Hot zone than Non-Hot zone. Among the old sites, the percentage of modules with delamination and backsheet defects are higher in Hot zone than Non-Hot zone. Though the average degradation in the Non-Hot zone is lower than Hot zone, there are also reports of very high degradation in some modules installed in Non-Hot climate. Hence, it is important for the PV system installers to ensure the quality of manufacturing, transportation and installation, irrespective of climatic zone.
- Encapsulant discoloration and backsheet degradation has been observed in more than 10% of the young modules (aged less than 5 years) while Snail tracks have been observed in about 26% of the young modules. Snail tracks are found in significantly higher number of modules (almost 3 times higher) in the sites having high power degradation rates (Group Y sites) as compared to better performing sites (Group X sites). This raises concerns about the product quality and the 25-year power warranty claimed by these module manufacturers.
- The small/medium sites (installation size < 100 kW) have been found to suffer from higher percentage of modules with discoloration, metallization discoloration and backsheet problems, as compared to the large sites (installation size > 100 kW), which indicates that the quality of modules used for small installations is not as good as for the large installations. This is a matter of concern since 40% of the National Solar Mission's target is allocated to small rooftop installations.

## 2. Quantification of severity of encapsulant discoloration in field surveys

- The severity of encapsulant discoloration in PV modules has been quantified in terms of a discoloration index, which is computed from the RGB values of each pixel of the digital image of PV module. The digital image is captured (in RAW format) in natural sunlight at irradiance greater than  $700 \text{ W/m}^2$ , and a pseudo yellowness index is calculated for every pixel on the silicon cell area, excluding the metallization and backsheet areas):

$$PYI = 0.25 \cdot \left( \frac{1.3013 \cdot X - 1.1498 \cdot Z}{Y} \right) \cdot 100 - 9.3793$$

where, X,Y,Z are tristimulus values calculated from the RGB color values of the digital image.

The *DI* is then calculated based on the difference of the average *PYI* value of the whole cell from the average *PYI* of the un-discolored portion of the cell (5% area along the edge of the cell is considered for this calculation):

$$DI = \frac{PYI_{avg} - PYI_{blue}}{30 - PYI_{blue}}$$

- Modules coming out of manufacturing plants have *DI* values within 0.05, while modules with minor discoloration have *DI* within 0.25. The worst discolored modules observed in our surveys have *DI* value close to 0.5. The average degradation of the modules (in short-circuit current and power output) has been found to increase linearly with the *DI* category.

## 3. Localized discoloration due to Hot Cells and their impact on module performance

- Localized discoloration of the EVA encapsulant is caused by hot spots in the solar cells, usually seen in cracked cells. The thermal mismatch between the cells in PV modules has been quantified in terms of the “Thermal Mismatch Index” (*TMI*), which normalizes the maximum temperature difference in the PV module (*Module*  $\Delta T$ , linearly translated to  $1000 \text{ W/m}^2$  irradiance) by the number of cells (*N*) and the initial efficiency of the module ( $\eta$ ), as per the following relation:

$$TMI = \frac{\text{Module } \Delta T}{\eta \cdot N}$$

- *TMI* value greater than 0.5 has been considered as the criteria for identifying “Hot Cells” (this corresponds to temperature difference of 5 °C within the module, for standard 60-cell 15% efficiency modules). Analysis of the Infrared thermography data from the All-India surveys shows that average power degradation (%) is higher for modules with Hot Cells, and the effect is accelerated in the Hot climate. The major contributing factor to the higher power degradation of modules with Hot Cells is fill factor degradation.
- The electrical degradation due to localized Hot spot discoloration (having major contribution from FF degradation) is different from the case of uniform discoloration in modules (where the electrical degradation is primarily due to short circuit current reduction). In the modules with hot spots, the localized discoloration is generated due to high temperatures owing to an underlying defect in the solar cell (usually cell cracks) and tends to further increase the mismatch between the cells, as the discoloration reduces the light incident on the cell, leading to further decrease in module’s fill factor.

#### **4. Effect of UV and temperature on discoloration rate of conventional EVA encapsulant**

- Xenon chamber tests show that the discoloration of the conventional fast-cure UV absorbing EVA encapsulant (containing Cyasorb UV-531 UV absorber) is dependent on the temperature, with activation energy of 0.61 eV (standard error:  $\pm 0.08$  eV). This value is within the range reported in recent literature for similar encapsulant [125]. The discoloration rate at 80 °C is approximately 3 times higher than the rate at 60 °C.
- The degradation mechanism seems to change for module temperature exceeding 88 °C, wherein the linear relation with UV dose changes to an exponential relation. Miller *et al.* [125] have also reported change in degradation mechanism at temperature around 80 °C. For modules installed directly on the roof (direct roof mounted), or rack mounted modules having severe cell cracks leading to Hot cells, the cell temperatures

would exceed 90 °C on sunny days, under which condition this encapsulant (containing Cyasorb UV-531) will discolor rapidly, leading to significant loss in power generation.

- The primary cause for the degradation in power output due to discoloration is the reduction in short-circuit current. The short-circuit current loss has been correlated to the discoloration index of the UV-cut mini-modules after 4000 hours of Xenon-based UV exposure. The relation between the current loss and discoloration index has been found to be:

$$\% I_{sc} \text{ loss} = 27.694 \cdot DI - 1.206$$

This equation indicates that the  $I_{sc}$  loss will be negligible for  $DI$  values close to 0.05. Also, this relation indicates that the  $I_{sc}$  loss will be about 13% for a PV module with  $DI$  value of 0.5 (worst case discoloration observed in our surveys). This value of 13% is close to the actually observed worst case  $I_{sc}$  loss in Group X modules of about 15% (with an accuracy of 2% in irradiance measurement).

- Acceleration factor for the Hot & Dry desert location of Jodhpur is estimated to be 27 while it is 6 times higher for the Cold & Arid desert in Leh, Ladakh. This means that 55 days of test at 75 W/m<sup>2</sup> total UV irradiance and 85 °C sample temperature is sufficient for simulating 25 years field exposure in the Cold climate of Ladakh (from encapsulant discoloration point of view) but it will take 319 days cumulative exposure to simulate the 25 years warranty period in the Hot climate of Jodhpur.

## 5. Comparison of UV-absorbing and UV-transparent EVA encapsulants

- The UV-absorbing (UV-cut) samples discolored at a faster rate than the UV-transparent (UV-pass) samples in both Xenon chamber tests and UV-365 chamber tests. In the Xenon chamber, the UV-pass sample discolored at 3.5 times slower rate as compared to the UV-cut sample (sample temperature of 64 °C and UV intensity of 74 W/m<sup>2</sup>). Similarly, in the UV-365 chamber with sample plate temperature of 90 °C and irradiance of ca. 880 W/m<sup>2</sup>, the UV-pass coupon discolored at 5 times slower rate than the UV-cut coupon. Both the chambers operated under dry condition (relative

humidity around 20%). This confirms the claim of the UV-pass EVA manufacturers with regard to lower discoloration under UV exposure.

- Fluorescence images under 365 nm UV excitation show discolored and photo-bleached areas distinctly on UV-cut mini-modules but not in UV-pass modules. Fluorescence spectra also indicated absence of fluorophores in the UV-pass EVA. However, possible signs of delamination were observed in the UV-pass mini-modules between the solar cells, but not in the UV-cut modules. Thus, the UV-pass EVA is a better encapsulant from discoloration point of view but is not a good choice from delamination perspective. A possible solution indicated by some module manufacturers is to use UV-cut EVA on back side of solar cells in combination with UV-pass EVA in front so that the excess UV light is prevented from reaching the backsheet.
- In the Xenon chamber tests, the short-circuit current of the samples decreased initially (which may be attributed to Light Induced Degradation) before stabilizing. Correlation could be obtained between the  $I_{sc}$  loss and the increase in yellowness index for the UV-cut EVA, but not for the UV-pass EVA samples. Activation energy could not be determined for the UV-pass samples (since the discoloration is too low), which is also the case reported by Miller *et al.* [125].

Based on above results, it is recommended that PV module manufacturers as well as installers give more emphasis on the quality of the materials that are being used in the solar panels, particularly for panels intended for use in Hot climates. The UV-absorber based EVA encapsulant widely used in PV modules is expected to discolor rapidly in direct roof-mounted applications in Hot climates, so alternative encapsulants need to be used for such applications. The UV-absorber free encapsulant (referred to as “UV-pass”) is a good alternative from discoloration perspective but the problem of delamination in such modules needs to be investigated further.

## 9.2 Scope of Future Work

We have performed All-India surveys to understand the degradation of PV modules in the field in different climatic zones of India. In many cases, we have found initial signs of degradation (discoloration, snail tracks and delamination) and many of these systems show higher than usual degradation rates. It is advisable to regularly monitor the degradation of such modules, which will provide important feedback for future installations. The year-on-year data shall provide accurate degradation rates, which can be used to fine-tune the financial models of the power plant owners, and enhance the confidence of the business community on the performance of PV modules.

Based on our field survey data, we have tried to develop correlations for the loss in electrical parameters with the physical degradation. We have developed a technique to quantify the encapsulant discoloration from digital images (in the form of discoloration index) and correlate it with the short-circuit current loss. Similarly, we have shown that modules with higher hot cell temperatures tend to have higher power degradation, which is mostly due to fill factor degradation (originating from cell cracks). However, further work is needed to establish an accurate correlation between the module temperature and the power output, which will enable estimation of the power degradation of modules based on IR images alone (without the need for intrusive contact-based *I-V* measurements). Unmanned aerial vehicles (drones) are now-a-days being used for IR thermography of large power plants spread across acres of land, and the determination of the module power loss through aerial IR thermography is the logical next step for the PV industry.

The accelerated testing of UV-cut and UV-pass EVA encapsulant laminates have been performed for close to 4000 hours in the Xenon chamber. It has been found that the degradation mechanism changes at sample temperature exceeding 88 °C so higher temperatures cannot be used for accelerating the reaction rate. The total UV exposure of 300 kWh/m<sup>2</sup> corresponds to about 3 years of outdoor exposure in tropical climate (assuming average 5 peak sun hours per day and 5% UV component in the solar radiation). Considering the activation energy of 0.6 eV and sample temperature of 85 °C, the 4000-hour test would correspond to approx. 14 years in tropical climate. It would be beneficial to continue such accelerated tests for at least 8000 hours duration to simulate the 25-year warranted life of PV modules. Also, we have found

delamination in the UV-pass sample and one possible solution to prevent delamination (as per module manufacturers) is to use UV-cut EVA on the backside of the cells. This claim needs to be verified through independent testing. Further, we have performed accelerated tests only under dry state (relative humidity < 20%), and further tests are necessary at higher humidity levels to understand the impact of humidity on the discoloration and degradation of EVA encapsulants. Some of these tests have already been started at our laboratory by other students as part of their PhD work.

## **Appendix I**

### **Visual Inspection Checklist**

The visual inspection checklist developed by Packard *et al.* [47] has been modified into a two-page checklist for quick evaluation of the condition of a solar panel through visual inspection at site. The checklist is provided in the following pages.

Site No.: .....		Date: .....	
Location: .....		Lat/Long: .....	
Altitude: .....			
<b>Module Details:</b> Manufacturer: ..... <input type="text" value="Photo No."/> Type of Module: <i>Mono-cSi / Multi-cSi / Thin Film</i> (.....) No. of Cells: ..... Dimension of Cells (cm): ..... x ..... Dimension of Module (cm): ..... x .....		<b>Module Name Plate Available:</b> Y/N <input type="text"/> Model No. & Sl. No. : ..... Name Plate Condition: <i>Like New / Discolored / Torn</i> Certification: <i>IEC61215 / IEC61646 / IEC61730 / UL1703</i> Estimated deployment date: .....	
<b>Crystalline Silicon Module :</b> Y/N <input type="text"/> Cells in each string x strings in series/parallel: ..... x ..... <b>Spacing:</b> Cell to cell = ..... mm Frame to cell (mm) = ..... (top), ..... (bottom), ..... (left), ..... (right) Module Discoloration: <i>None / Light / Dark</i> , (.....% area) No. of cells discoloured: ..... Discoloration Location : <i>Overall / Module centre / Module edges / Cell Center / Cell edges / over fingers / over busbars / over tabbing / between cells / individual cells darker than others / partial cell discoloration / others</i> (.....) Effect in JB area: <i>Same as elsewhere / more / less</i> Effect in Name Plate area: <i>Same as elsewhere / more / less</i> Damage : <i>Burn marks / Cracks / Moisture / Snail tracks / foreign particles embedded</i> Burn marks (nos.): ..... Cells cracked (nos.): ..... Cells with Snail Tracks (nos.): ..... Cells with Framing (nos.): ..... Area Delaminated: <i>Nil / Over cells (...%), Between cells (...%), uniform / from edges / at corners / near JB / near Interconnects (cell or string)</i>		<b>Backsheet Applicable:</b> Y/N <input type="text"/> Texture: <i>Like New / Wavy (Delam / No Delam.) / Dented</i> Damage: <i>None / Small Localized / Extensive</i> Discoloration: <i>Like New / Major / Minor</i> Chalking: <i>None / Slight / Significant</i> Delaminated area (%) : <i>&lt;5 / 5-25 / 25-50 / 50-75 / &gt;75%</i> Bubbles (nos., dimension): ... , <i>&lt;5mm / 5-30mm / &gt;30mm</i> Fraction of area with bubbles > 5mm: <i>&lt;5% / 5-25% / 25-50% / 50-75% / &gt;75%</i> Cracks/scratches (nos. & location): ..... , <i>random / over cells / between cells</i> Cracks location: <i>Only Near JB / Only near Nameplate / Other</i> (.....) Fraction of cracks/scratches that exposes the circuit: <i>&lt;5% / 5-25% / 25-50% / 50-75% / &gt;75%</i> Burn Marks (nos. & area): ..... , <i>&lt;5% / 5-25% / 25-50% / 50-75% / &gt;75%</i>	
<b>Front Cover :</b> Glass / Polymer / Others <input type="text"/> Features: <i>Smooth / slightly textured / pyramid texture / ARC</i> Damage: <i>None / Small Localized / Extensive</i> Shattered (tempered/non-tempered): Y/ N (.....) Cracks: nos. : <i>1 / 2 / 3 / 4-10 / &gt;10</i> Cracks start from: <i>mod. corner / mod. edge / cell / JB</i> Chips: nos. : <i>1 / 2 / 3 / 4-10 / &gt;10</i> Chipping location: <i>module corner / module edge</i> Damaged Area : <i>&lt;5% / 5-25% / 25-50% / 50-75% / &gt;75%</i> Fraction of area affected by Haziness / milky discoloration: <i>NA / &lt;5% / 5-25% / 25-50% / 50-75% / &gt;75%</i>		<b>Metallization :</b> <input type="text"/> A1: <i>&lt; 5%</i> , A2: <i>5-25%</i> , A3: <i>25-50%</i> , A4: <i>50-75%</i> , A5: <i>&gt;75%</i> <b>Fingers:</b> <i>NA / Like New / Discolored (Light / Dark, .....%)</i> <b>Busbars:</b> <i>NA / Like New / Discolored (Light / Dark, .....%) / Obvious Corrosion / Diffuse Burn Marks / Misalignment</i> <b>Cell Interconnect Ribbon:</b> <i>NA / Like New / Discolored (Light / Dark, .....%) / Obvious Corrosion / Burn Marks / Breakage</i> <b>String Interconnect:</b> <i>NA / Like New / Discolored (Light / Dark, .....%) / Obvious Corrosion / Burn Marks / Breakage / Arc tracks (thin burns)</i>	

<b>Frame Applicable: Y/N</b> <input type="checkbox"/> Appearance: <i>Like New / Damaged / Missing</i> Damage: <i>Corrosion (major or minor) / Bent/ Joints separated/ Cracking</i> Frame Adhesive : <i>Not visible / Like New / Degraded / oozed out / missing in some areas</i>	<b>Frame Grounding Present: Y/N</b> <input type="checkbox"/> Original State : <i>No ground / Wired / Resistive/ Unknown</i> Corrosion : <i>Nil / Minor / Major</i> Functionality: <i>Well Grounded / No Connection</i>
<b>Wires:</b> <input type="checkbox"/> <i>NA / Like New / pliable but degraded / embrittled / Cracked or disintegrated insulation / burnt / corroded / animal bites /soiled</i>	<b>Connectors: Y/N</b> <input type="checkbox"/> Type: <i>MC3 or MC4 / Tyco / Others</i> Condition: <i>Like New / pliable but degraded / embrittled / Cracked or disintegrated insulation / burnt / corroded / animal bites / soiled</i>
<b>Junction Box (JB) Applicable: Y/N</b> <input type="checkbox"/> Physical state : <i>Intact / unsound / weathered / cracked / burnt/ warped/ output terminals corroded</i> Lid : <i>Intact(potted) / loose / fell off / cracked</i> Attachment : <i>Well attached / loose / fallen off</i> Wire attached in JB : <i>Well attached / Loose / Fell off/ arced / caused fire</i> Seal : <i>Good sealing / will Leak</i>	<b>Mounting Structure Details:</b> <input type="checkbox"/> Material: ..... Condition of structure: <i>Good / rusted / bent / broken</i> Installation Site : <i>Roof top / Ground</i> Type of Floor: <i>Soil / Cement / Other (.....)</i> Tilt Angle: ..... Direction of PV Panels: ..... Height of lowest part of module from floor: .....
<b>Rear-Side Glass Applicable: Y/N</b> <input type="checkbox"/> Damage: <i>None/ Small Localized / Extensive</i> Craze (or other non-crack damage): ..... Shattered (tempered/non-tempered): ..... Cracks: nos. : <i>1 / 2 / 3 / 4-10 / &gt;10</i> Cracks start from: <i>mod. corner / mod. edge / cell / JB / foreign object impact spot</i> Chips: nos. : <i>1 / 2 / 3 / 4-10 / &gt;10</i> Chipping location: <i>module corner / module edge</i>	<b>Thin Film Module : Y/N</b> <input type="checkbox"/> Cells in each string (nos.): ..... Strings in parallel (nos.): ..... Distance between frame and cell : ..... mm Module Discoloration: <i>None / Light / Dark, (..... % area)</i> Discoloration Type : <i>White Spots/ Haze/ Other</i> Discoloration Location : <i>Overall / Module centre / Module edges / Cell Center / Cell edges / near cracks</i> Damage : <i>No / Small Localized / Extensive</i> Damage Type : <i>Burn Marks / Cracking / Moisture / Foreign particles embedded</i> Delamination : <i>None / Small Localized / Extensive</i> Delamination Location: <i>From edges / uniform / corners/ near junction box / near busbar / along scribe lines</i> Delamination Type : <i>Absorber delamination/ AR Coating delamination/ Other</i>
<b>Frameless Edge Seal Applicable: Y/N</b> <input type="checkbox"/> Appearance: <i>Like New / discolored / Visibly degraded</i> Discoloration area : <i>&lt;5% / 5-25% / 25-50% / 50-75% / &gt;75%</i> Material Problems : <i>Squeezed Out / signs of moisture penetration</i> Delamination : <i>Localized / widespread</i> Delaminated area (%) : <i>&lt;5 / 5-25 / 25-50 / 50-75 / &gt;75%</i>	<b>Remarks :</b>

This page is intentionally left blank.

## References

- [1] L. Capuano, “International Energy Outlook 2018”, US Energy Information Administration, [online] Available: [https://www.eia.gov/pressroom/presentations/capuano\\_07242018.pdf](https://www.eia.gov/pressroom/presentations/capuano_07242018.pdf) [Accessed: Feb. 5, 2019].
- [2] Paul Przyborski, “World of Change – Global Temperatures”, NASA Earth Observatory [Online] Available: <https://earthobservatory.nasa.gov/world-of-change/global-temperatures>. [Accessed: Feb. 5, 2019].
- [3] H. Shaftel. “Effects | Facts – Climate Change: Vital Signs of the Planet,” NASA Global Climate Change [Online]. Available: <https://climate.nasa.gov/effects/> [accessed: Nov. 11, 2021]
- [4] “The Paris Agreement”, United Nations Framework Convention on Climate Change (UNFCCC), [Online] Available: <https://unfccc.int/process-and-meetings/the-paris-agreement/the-paris-agreement> [Accessed: Feb. 5, 2019].
- [5] V. Masson-Delmotte, P. Zhai, H.-O. Pörtner, D. Roberts, J. Skea, P.R. Shukla, A. Pirani, W. Moufouma-Okia, C. Péan, R. Pidcock, S. Connors, J.B.R. Matthews, Y. Chen, X. Zhou, M.I. Gomis, E. Lonnoy, T. Maycock, M. Tignor, and T. Waterfield (eds.), “IPCC, 2018: Summary for Policymakers. In: Global Warming of 1.5°C,” Intergovernmental Panel on Climate Change, 2018. [Online] Available: [https://www.ipcc.ch/site/assets/uploads/sites/2/2019/05/SR15\\_SPM\\_version\\_report\\_LR.pdf](https://www.ipcc.ch/site/assets/uploads/sites/2/2019/05/SR15_SPM_version_report_LR.pdf) [Accessed: Feb. 10, 2019].
- [6] Government of India, “Revision of cumulative targets under National Solar Mission from 20,000 MW by 2021-22 to 1,00,000 MW,” Press Information Bureau (PIB), June 17, 2015. [Online]. Available: <http://pib.nic.in/newsite/PrintRelease.aspx?relid=122566> [Accessed: Feb. 10, 2019].

- [7] “PM promises 500 GW renewable energy to meet India’s 50% energy requirements by 2030,” *Economic Times*, 2 November 2021 [Online]. Available: <https://economictimes.indiatimes.com/industry/renewables/pm-promises-500-gw-renewable-energy-to-meet-indias-50-energy-requirements-by-2030/articleshow/87480837.cms?from=mdr> [Accessed: Nov 18, 2021].
- [8] J. S. Hill, “Global Solar Market Installed 98.9 Gigawatts In 2017”, *Cleantechnica*, March 19, 2018. [Online]. Available: <https://cleantechnica.com/2018/03/19/global-solar-market-installed-98-9-gigawatts-in-2017/> [Accessed: Feb 11, 2019].
- [9] Z. Shahan, “13 Charts On Solar Panel Cost & Growth Trends”, *Cleantechnica*, September 4, 2014. [Online]. Available: <https://cleantechnica.com/2014/09/04/solar-panel-cost-trends-10-charts/> [Accessed: Feb 11, 2019].
- [10] J. Trube, “International Technology Roadmap for Photovoltaic – 2018 Results”, *Verband Deutscher Maschinen- und Anlagenbau*, Frankfurt, Germany. [Online] Available: <https://pv-manufacturing.org/wp-content/uploads/2019/03/ITRPV-2019.pdf> [Accessed: Feb. 11, 2019].
- [11] US Energy Information Administration, “Coal Explained,” *US Energy Information Administration*. [Online]. Available: [https://www.eia.gov/energyexplained/index.php?page=coal\\_home](https://www.eia.gov/energyexplained/index.php?page=coal_home) [Accessed: Feb. 12, 2019].
- [12] World Energy Council, “World Energy Resources – Solar”, *World Energy Council*, 2013 [Online]. Available: [https://www.worldenergy.org/wp-content/uploads/2013/10/WER\\_2013\\_8\\_Solar\\_revised.pdf](https://www.worldenergy.org/wp-content/uploads/2013/10/WER_2013_8_Solar_revised.pdf) [Accessed: Feb. 12, 2019].
- [13] International Energy Agency, “Statistics - Total Final Consumption (TFC) by source”, January, 2019. [Online]. Available: <https://www.iea.org/statistics/?country=WORLD&year=2016&category=Energy%20consumption&indicator=TFCbySource&mode=chart&dataTable=BALANCES> [Accessed: Feb. 6, 2019].

- [14] C. S. Solanki, *Solar Photovoltaics: Fundamentals, Technologies And Applications*, PHI Learning Pvt. Ltd., Delhi, 2015.
- [15] M. Green, “Silicon Photovoltaic Modules: A Brief History of the First 50 Years,” *Progress in Photovoltaics: Research & Applications*, vol. 13, pp. 447 – 455, 2005, doi: 10.1002/pip.612.
- [16] TSEC Corporation, “Solar Overview” [Online]. Available: [http://www.tsecpv.com/en-global/solar\\_knowledge/index/zero\\_house\\_02](http://www.tsecpv.com/en-global/solar_knowledge/index/zero_house_02) [Accessed: Feb. 7, 2019].
- [17] *Crystalline Silicon Terrestrial Photovoltaic (PV) Modules – Design qualification and type approval*, IEC 61215-2005, 2005.
- [18] J. Wohlgemuth, “IEC 61215: What it is and isn’t,” NREL PV Module Reliability Workshop, Golden, Colorado, 2012. [Online] Available: <https://www.nrel.gov/docs/fy12osti/54714.pdf> [Accessed: Feb. 15, 2019].
- [19] R. Dubey, S. Chattopadhyay, V. Kuthanazhi, J. John, C. S. Solanki, A. Kottantharayil, B. M. Arora, K.L.Narsimhan, J. Vasi, B. Bora, Y. Singh and O.S. Sastry, “All India Survey of Photovoltaic Module Degradation: 2013”, National Center for Photovoltaic Research and Education (NCPRE) and National Institute of Solar Energy (NISE), Technical Report [Online] Available: <http://www.ncpre.iitb.ac.in/research/reports.html>.
- [20] R. Dubey, S. Chattopadhyay, V. Kuthanazhi, J. John, F. Ansari, S. Rambabu, B. M. Arora, A. Kottantharayil, K. L. Narasimhan, J. Vasi, B. Bora, Y. K. Singh, K. Yadav, M. Banger, R. Singh and O.S. Sastry, “All India Survey of Photovoltaic Module Reliability: 2014”, National Center for Photovoltaic Research and Education (NCPRE) and National Institute of Solar Energy (NISE), Technical Report [Online] Available: <http://www.ncpre.iitb.ac.in/research/reports.html>.
- [21] S. Chattopadhyay, R. Dubey, V. Kuthanazhi, S. Zachariah, S. Bhaduri, C. Mahapatra, S. Rambabu, F. Ansari, A. Chindarkar, A. Sinha, H. K. Singh, N. Shiradkar, B. M. Arora, A. Kottantharayil, K. L. Narasimhan, S. Sabnis, B. Bora, G. Kumar, Y. K. Singh, M. Bangar, M. Kumar, A. K. Haldkar, R. Singh, S. Raghava, M. Morampudi, G.

- Ganesh, R. Kumar and O. S. Sastry and J. Vasi, “All India Survey of Photovoltaic Module Reliability: 2016”, National Center for Photovoltaic Research and Education (NCPRE) and National Institute of Solar Energy (NISE), Technical Report [Online] Available: <http://www.ncpre.iitb.ac.in/research/reports.html>.
- [22] D. Jordan and S. R. Kurtz, "Photovoltaic Degradation Rates - An Analytical Review," *Progress in Photovoltaics: Research and Applications*, vol. 21, no. 1, Dec. 2012, doi: 10.1002/pip.1182.
- [23] M. Kontges, G. Oreski, U. Jahn, M. Herz, P. Hacke, K. A. Weiss, “Assessment of Photovoltaic Module Failures in the Field”, International Energy Agency, Technical Report no. IEA-PVPS T13-09:2017. [Online] Available: [www.iea-pvps.org/index.php?id=92&eID=dam\\_frontend\\_push&docID=4059](http://www.iea-pvps.org/index.php?id=92&eID=dam_frontend_push&docID=4059) [Accessed: Feb. 12, 2019].
- [24] S. Tatapudi, C. Libby, C. Raupp, D. Srinivasan, J. Kuitche, B. Bicer and G. TamizhMani, "Defect and Safety Inspection of 6 PV Technologies from 56 ,000 Modules Representing 257,000 Modules in 4 Climatic Regions of the United States”, in *Proceedings of the 43<sup>rd</sup> IEEE Photovoltaic Specialists Conference*, Portland, 2016, pp. 1747-1751, doi: 10.1109/PVSC.2016.7749923.
- [25] D. C. Jordan, S. R. Kurtz, K. VanSant, and J. Newmiller, “Compendium of photovoltaic degradation rates,” *Progress in Photovoltaics: Research & Applications*, vol. 24, pp. 978– 989, 2016, doi: 10.1002/pip.2744.
- [26] N. K. Bansal and G. Minke, *Climatic Zones and Rural Housing in India*. Julich: Forschungszentrum Julich GmbH, 1995.
- [27] J. Campbell, Y. Zemen, B. Richardson, and B. Striner, “Photovoltaic Module Performance and Degradation as Compared in Distinct Climatic Regions”, in *Proceedings of the 38<sup>th</sup> IEEE Photovoltaic Specialists Conference*, Austin, 2011, pp. 1250-1255. doi: 10.1109/PVSC.2012.6317829.

- [28] N. Bogdanski, W. Herrmann, F. Reil, M. Köhl, and K.A. Weiss, and M. Heck, “Results of a German Four-Year Joint Project Results of Three Years Module Weathering In Four Different Climates”, in *Proceedings of the 25<sup>th</sup> European Photovoltaic Solar Energy Conference and Exhibition*, Valencia, 2010, pp. 4339-4343. doi: 10.4229/25thEUPVSEC2010-4AV.3.110.
- [29] M. Va´zquez, & I. Rey-Stolle, “Photovoltaic Module Reliability Model Based on Field Degradation Studies”, *Progress in Photovoltaics: Research and Applications*, vol. 16, 2008, pp. 419-433, doi: 10.1002/pip.825.
- [30] B. Raghuraman, V. Lakshman, J. Kuitche, W. Shisler, G. TamizhMani, H. Kapoor, “An overview of SMUDs outdoor photovoltaic test program at Arizona State University”, in *Proceedings of the IEEE Photovoltaic Specialist Conference*, Waikoloa, 2006, doi: 10.1109/WCPEC.2006.279948.
- [31] J. Singh, J. Belmont and G. TamizhMani, “Degradation Analysis of 1900 PV modules in a Hot Dry Climate: Results after 12 to 18 years of field exposure,” in *Proceedings of the 39<sup>th</sup> IEEE Photovoltaic Specialist Conference*, Tampa, 2013, doi: 10.1109/PVSC.2013.6745149.
- [32] C. Raupp, C. Libby, S. Tatapudi, D. Srinivasan, J. Kuitche, B. Bicer, G. TamizhMani, “Degradation Rate Evaluation of Multiple PV Technologies from 59,000 Modules Representing 252,000 Modules in Four Climatic Regions of the United States,” in *Proceedings of the IEEE 43<sup>rd</sup> Photovoltaic Specialists Conference (PVSC)*, Portland, June 2016, doi: 10.1109/PVSC.2016.7749590.
- [33] M. Kumar, S.S. Chandel, A. Kumar, “Performance analysis of a 10 MWp utility scale grid-connected canal-top photovoltaic power plant under Indian climatic conditions,” *Energy*, vol. 204, 2020, pp. 117903, doi: 10.1016/j.energy.2020.117903.
- [34] V. Sharma, O.S. Sastry, A. Kumar, B. Bora, S.S. Chandel, “Degradation analysis of a-Si, (HIT) hetero-junction intrinsic thin layer silicon and m-c-Si solar photovoltaic technologies under outdoor conditions,” *Energy*, vol. 72, 2014, pp. 536-546, doi: 10.1016/j.energy.2014.05.078.

- [35] O.S. Sastry, S. Saurabh, S. K. Shil, P.C..Pant, R. Kumar, A. Kumar, B. Bandopadhyay, “Performance analysis of field exposed single crystalline silicon modules,” *Solar Energy Materials & Solar Cells*, vol. 94, 2010, pp. 1463–1468, doi: 10.1016/j.solmat.2010.03.035.
- [36] A. Sinha, O.S. Sastry, Y.K. Singh, M. Kumar, R. Gupta, “Performance of Champion Modules of PV Modules of PV Lighting Systems in India”, in *Proceedings of the 27<sup>th</sup> European Photovoltaic Solar Energy Conference (EUPVSEC)*, 2012, doi: 10.4229/27thEUPVSEC2012-4BV.3.36.
- [37] P. Rajput, G.N. Tiwari, O.S. Sastry, B. Bora, V. Sharma, “Degradation of mono-crystalline photovoltaic modules after 22 years of outdoor exposure in the composite climate of India,” *Solar Energy*, vol. 135, 2016, pp. 786–795. doi: 10.1016/j.solener.2016.06.047.
- [38] Vikrant Sharma, S.S. Chandel, “A novel study for determining early life degradation of multi-crystalline-silicon photovoltaic modules observed in western Himalayan Indian climatic conditions,” *Solar Energy* 134 (2016) 32–44. doi: 10.1016/j.solener.2016.04.023.
- [39] Tony Sample, “Failure modes and degradation rates from field-aged crystalline silicon modules”, in *Proceedings of the Photovoltaic Module Reliability Workshop*, Golden, Colorado, USA, 2011. Available: [http://www1.eere.energy.gov/solar/pdfs/pvmrw2011\\_28\\_csi\\_sample.pdf](http://www1.eere.energy.gov/solar/pdfs/pvmrw2011_28_csi_sample.pdf). [Accessed March 14, 2014].
- [40] S.S. Chandel, M. Nagaraju Naik, Vikrant Sharma, Rahul Chandel, “Degradation analysis of 28-year field exposed mono-c-Si photovoltaic modules of a direct coupled solar water pumping system in western Himalayan region of India”, *Renewable Energy*, vol. 78, 2015, pp. 193-202, doi: 10.1016/j.renene.2015.01.015.
- [41] M. Köntges, I. Kunze, V. Naumann, S. Richter, C. Hagendorf, J. Berghold, M. Roericht, “Snail Tracks (Schnecken Spuren), Worm marks & Cell Cracks”, *International Energy Agency* [Online]. Available: <http://iea->

pvps.org/index.php?id=223&eID=dam\_frontend\_push&docID=1272  
[Accessed: March 12, 2019].

- [42] S. Meyer, S. Timmel, S. Richter, M. Werner, M. Gläser, S. Swatek, U. Braun, and C. Hagendorf, "Silver nano particles cause snail tracks in photovoltaic modules," *Solar Energy Materials and Solar Cells*, vol. 121, pp. 171-175, 2014, doi: 10.1016/j.solmat.2013.11.013.
- [43] M. Kontges, S. Kurtz, C. Packard, U. Jahn, K. A. Berger, K. Kato, T. Friesen, H. Liu, M. V. Iseghem, J. Wohlgemuth, D. C. Miller, M. Kempe, P. Hacke, F. Reil, N. Bogdanski, W. Herrmann, C. Buerhop, G. Razongles, G. Friesen, "Review of Failures of Photovoltaic Modules," *International Energy Agency*, Technical Report no. IEA-PVPS T13-01:2014. [Online] Available: [http://www.iea-pvps.org/fileadmin/dam/intranet/ExCo/IEA-PVPS\\_T13-01\\_2014\\_Review\\_of\\_Failures\\_of\\_Photovoltaic\\_Modules\\_Final.pdf](http://www.iea-pvps.org/fileadmin/dam/intranet/ExCo/IEA-PVPS_T13-01_2014_Review_of_Failures_of_Photovoltaic_Modules_Final.pdf) [Accessed: March 6, 2019].
- [44] S. Meyer, S. Timmel, M. Glasser, U. Braun, V. Wachtendorf and C. Hagendorf, "Polymer foil additives trigger the formation of snail trails in PV modules," *Solar Energy Materials and Solar Cells*, vol. 130, pp. 64-70, 2014, doi: 10.1016/j.solmat.2014.06.028.
- [45] M. Vannini, "Educating Customers and Learning from them," *PV Magazine*, no. 9-2011, 2011 [Online]. Available: [https://www.pv-magazine.com/magazine-archive/educating-customers-and-learning-from-them\\_10004114/](https://www.pv-magazine.com/magazine-archive/educating-customers-and-learning-from-them_10004114/) [Accessed: June 18, 2019].
- [46] "Dupont Global PV Reliability – 2019 Field Analysis", Dupont Report, 2019 [Online] Available: [https://www.dupont.com/content/dam/dupont/products-and-services/solar-photovoltaic-materials/solar-photovoltaic-materials-new/documents/DPVS\\_Field\\_Study\\_Analysis-1.pdf](https://www.dupont.com/content/dam/dupont/products-and-services/solar-photovoltaic-materials/solar-photovoltaic-materials-new/documents/DPVS_Field_Study_Analysis-1.pdf) [Accessed: June 10, 2019].
- [47] C. Packard, J. Wohlgemuth and S. Kurtz., "Development of a visual inspection data collection tool for evaluation of fielded PV Module condition," National Renewable

- Energy Laboratory, Technical Report no. NREL/TP-5200-56154, Golden, Colorado, USA, 2012, doi: 10.2172/1050110.
- [48] A. W. Czanderna and F. J. Pern, "Encapsulation of PV Modules using ethylene vinyl acetate Co-polymer as a pottant: A Critical review," *Solar Energy Materials & Solar Cells*, vol. 43, pp. 101-181, 1996, doi: 10.1016/0927-0248(95)00150-6.
- [49] M. Kempe, "Overview of scientific issues involved in selection of polymers for PV applications," in *Proceedings of the 37<sup>th</sup> IEEE Photovoltaic Specialist Conference*, Seattle, 2011, pp. 000085-000090, doi: 10.1109/PVSC.2011.6185851.
- [50] C. Caulbert, A. Gupta, R. Liang and E. Cuddihy, "Flat Plate Solar Array Project Final Report - Volume VII Module Encapsulation ," Jet Propulsion Laboratory, Pasadena, California, USA, Technical Report No. DOE/JPL 1012-125, 1986.
- [51] C. Peike, I. Hadrich, K.-A. Weiss, and I. Durr, "Overview of PV Module Encapsulation Materials," *Photovoltaics International*, vol. 19, pp. 85-92, 2013.[online] Available: <https://www.pv-tech.org/technical-papers/overview-of-pv-module-encapsulation-materials/> [Accessed: April 10, 2019].
- [52] LG Chemicals, "EVA Catalogue". [Online]. Available: [http://www.ecpl.ru/articles/eva\\_catalog.pdf](http://www.ecpl.ru/articles/eva_catalog.pdf) [Accessed: Feb. 9, 2019].
- [53] A.W. Czanderna and F.J. Pern, "Encapsulation of PV modules using ethylene vinyl acetate copolymer as a pottant: A critical review ," *Solar Energy Materials and Solar Cells*, vol. 43, pp. 101-181, 1996, doi: 10.1016/0927-0248(95)00150-6.
- [54] A.W.Czanderna, K.A.Emery, R.G. Dhere and F.J.Pern, "Weathering degradation of EVA encapsulant and the effect of its yellowing on solar cell efficiency," in *Proceedings of the 22<sup>nd</sup> IEEE Photovoltaics Specialists Conference*, Las Vegas, 1991, pp. 557-561, doi: 10.1109/PVSC.1991.169275.

- [55] P. Klemchuk, "Investigation of the degradation and stabilization of EVA-based encapsulant in field-aged solar energy modules," *Polymer Degradation and Stability*, vol. 55, no. 3, pp. 347 - 365, 1997, doi: 10.1016/S0141-3910(96)00162-0.
- [56] H. Gong, G. Wang, L. Zhen, and M. Gao, "Reliability and Durability of High UV transmission EVA for PV modules," in *Proceedings of the 31st European Specialists Conference*, Hamburg, 2015, pp. 2061 – 2065, doi: 10.4229/EUPVSEC20152015-5AV.6.45.
- [57] X. Gu, C. Lin, S. Ogier, Y. Pang, K. Tan, K. Connolly, P. Krommenhoek, and J. Chin, "Accelerated Laboratory Testing of PV Polymers using Simultaneous UV Radiation, Temperature and Moisture," in *2nd Annual Atlas/NIST workshop*, 2013, [Online] Available: <https://www.nist.gov/materials-and-structural-systems-division/2nd-atlasnist-workshop-photovoltaic-materials-durability> [Accessed: March 12, 2019].
- [58] C. Pieke, P. Hülsmann, M. Blüml, P. Schmid, K. Weiß, and M. Köhl "Impact of Permeation Properties and Backsheet-Encapsulant interactions on reliability of PV modules," *ISRN Renewable Energy*, 2012, doi: 10.5402/2012/459731.
- [59] M. D. Kempe, M. Kilkenny, T. J. Moricone and J. Z. Zhang, "Accelerated Stress testing of hydro-carbon based encapsulants for medium CPV applications," in *Proceedings of the 34th IEEE Photovoltaic Specialists Conference*, Philadelphia, 2009, doi: 10.1109/PVSC.2009.5411508.
- [60] D. H. Brainard and A. Stockman. (2009, August) [Online]. Available: [www.color.psych.upenn.edu/brainard/papers/Brainard\\_Stockman\\_Colorimetry.pdf](http://www.color.psych.upenn.edu/brainard/papers/Brainard_Stockman_Colorimetry.pdf) [Accessed: March 4, 2019].
- [61] W.S. Stiles and J. M. Burch, "NPL colourmatching investigation: Final report," *Optica Acta: International Journal of Optics*, vol. 6, pp. 1-26, 1959, doi: 10.1080/713826267.
- [62] "A Guide to Understanding Color," Xrite Corporation Web site. [Online]. Available: [https://www.xrite.com/-/media/xrite/files/whitepaper\\_pdfs/110-](https://www.xrite.com/-/media/xrite/files/whitepaper_pdfs/110-)

- 001\_a\_guide\_to\_understanding\_color\_communication/110-001\_understand\_color\_en.pdf [Accessed: Feb. 25, 2019].
- [63] *Standard Practice for Calculating Yellowness and Whiteness Indices from Instrumentally Measured Color Coordinates*," ASTM Standard No. ASTM E313-15e1, 2015.
- [64] *CIE Standard Illuminants for Colorimetry*, ISO 10526:1999/CIE S005/ E-1998.
- [65] M. P. Lamb, W. Yoon, C.G. Bailey, D. Scheiman, J.G. Tischler and R.J. Walters, "Modelling and Analysis of High performance, multi-colored, anti-reflective coatings for solar cells," *Optics Express*, vol. 21, pp. A585-594, 2013, doi: 10.1364/OE.21.00A585.
- [66] Sushanth Gudla, "Quantification of Solar Photovoltaic Encapsulant Browning Level Using Image Processing Tool," MS Thesis, *Arizona State University*, Tempe, USA, 2016.
- [67] R. Bunsen and H. E. Roscoe, "Photochemische Untersuchungen," *Poggendorff's Annalen*, vol. 108, pp. 193 - 273, 1989, doi: 10.1002/andp.18631931202.
- [68] K. Schwarzschild, "On the Deviations from the Law of Reciprocity for Bromide of Silver Gelatine," *Astrophysical Journal*, vol. 11, p. 89, 1900, doi: 10.1086/140669.
- [69] J. W. Martin, J. W. Chin and T. Nguyen, "Reciprocity Law Experiments in Polymeric Photodegradation: A Critical Review," *Progress in Organic Coatings*, vol. 47, pp. 292-311, 2003, doi: 10.1016/j.porgcoat.2003.08.002.
- [70] S R Logan, "The origin and status of Arrhenius equation," *Journal of Chemical Education*, vol. 59, no. 4, pp. 279 - 281, 1982, doi: 10.1021/ed059p279.
- [71] J. Clark, "The Arrhenius Equation," [Online]. Available: [https://chem.libretexts.org/Bookshelves/Physical\\_and\\_Theoretical\\_Chemistry\\_Textbook\\_Maps/Supplemental\\_Modules\\_\(Physical\\_and\\_Theoretical\\_Chemistry\)/Kinetics](https://chem.libretexts.org/Bookshelves/Physical_and_Theoretical_Chemistry_Textbook_Maps/Supplemental_Modules_(Physical_and_Theoretical_Chemistry)/Kinetics)

/Modeling\_Reaction\_Kinetics/Temperature\_Dependence\_of\_Reaction\_Rates/  
The\_Arrhenius\_Law/The\_Arrhenius\_Equation [Accessed: Feb 17, 2019].

- [72] L. A. Escobar and W. Q. Meeker, "A Review of Accelerated Test Models," in *Statistical Science* 2006, vol. 21, no. 4, pp. 552–577, doi: 10.1214/088342306000000321.
- [73] X. Gu, "Reciprocity Study and Spectral UV Wavelength Effect on PV Components Degradation," presented at the *3rd Atlas-NIST Workshop on PV Materials Durability*, Gaithersburg, Maryland, USA, 2015.
- [74] V. P. Gupta and L. E. St. Pierre, "Thermal degradation of poly(vinyl chloride): effect of oxygen on the thermal degradation of poly(vinyl chloride)," *Journal of Polymer Science: Polymer Chemistry Edition*, vol. 17, no. 3, pp. 797-806, 1979, doi: 10.1002/pol.1979.170170318.
- [75] J. D. Peterson, S. Vyazovkin, C. A. Wight, "Kinetics of the Thermal and Thermo-Oxidative Degradation of Polystyrene, Polyethylene and Polypropylene," *Journal of Molecular Chemistry and Physics*, vol. 202, pp. 775-784, 2001, doi: 10.1002/1521-3935(20010301)202.
- [76] A. Beinert, C. Peike, I. Durr, M. D. Kempe, G. Reiter, K. Weiss, "The influence of the additive composition on degradation induced changes in EVA during photochemical aging," in *Proceedings of the 29th European Photovoltaic Solar Energy Conference*, Amsterdam, Netherlands, 2014, pp. 3126 – 3132, doi: 10.4229/EUPVSEC20142014-5BV.4.6.
- [77] R. L. Gray, R. E. Lee, and B. M. Sanders, "Aging Conditions Effect on UV Durability," in *Weathering of Plastics - Testing to Mirror Real Life Performance*, George Wypych, Ed.: William Andrew, 1999, pp. 70 – 75, doi: 10.1016/B978-188420775-4.50007-6.
- [78] D. Miller, E. Annigoni, A. Ballion, J G. Bokria, L. S. Brukman, D. M. Burns, X. Chen, L. Elliot, J. Feng, R. H. French, S. Fowler, X. Gu, P. L. Hacke, C. C. Honeker, M. D. Kempe, H. Khonker, M. Koehl, L. Perret-Aebi, Nancy H. Philips, K. P. Scott, F. Schulati-Meillaud, T. Shioda, S. Suga, S. Watanabe, J. H. Wohlgemuth, "Degradation

- in PV Encapsulation Transmittance: An Interlaboratory Study Towards a Climate-Specific Test," in *Proceedings of the 2015 IEEE 42nd Photovoltaic Specialists Conference (PVSC)*, New Orleans, 2015, doi: 10.1109/PVSC.2015.7355607.
- [79] K. Dolia, A. Sinha, S. Tatapudi, J. Oh, G. Tamizhmani, "Early Detection of Encapsulant Discoloration by UV Fluorescence Imaging and Yellowness Index Measurements," in *Proceedings of the 2018 IEEE 7<sup>th</sup> World Conference on Photovoltaic Energy Conversion (A Joint Conference of 45th IEEE PVSC, 28th PVSEC & 34th EU PVSEC)*, Waikoloa Village, HI, USA, 2018, doi: 10.1109/PVSC.2018.8547939.
- [80] *First EVA Product Sheet*, Astenik Solar. [Online]. Available: [http://www.asteniksolar.com/products/materials/First\\_eva/Product\\_sheet\\_eva.pdf](http://www.asteniksolar.com/products/materials/First_eva/Product_sheet_eva.pdf) [Accessed: Feb. 16, 2019].
- [81] F. J. Pern, "Factors that affect the EVA encapsulant discoloration rate upon accelerated exposure," *Solar Energy Materials and Solar Cells*, vol. 41, pp. 587 - 615, 1996, doi: 10.1016/0927-0248(95)00128-X.
- [82] B. Nehme, N. Sirdi, T. Akiki, and A. Naamane, "Contribution to the modeling of ageing effects in PV cells and modules," in *Energy Procedia*, vol. 62, 2014, doi: 10.1016/j.egypro.2014.12.418.
- [83] M. Mikofski, F.J. Kavulak, David Okawa, Y. Shen, A. Terao, M. Anderson, S. Caldwell, D. Kim, N. Boitnott, J. Castro, L. A. L. Smith, R. Lacerda, D. Benjamin, and E. F. Hasselbrink, "PVLife: An Integrated Model for Predicting PV Performance Degradation over 25+ Years," in *Proceedings of the 2012 IEEE 38th Photovoltaic Specialists Conference (PVSC)*, Austin, TX, 2012, pp. 001744-001749, doi: 10.1109/PVSC.2012.6317932.
- [84] M. Koehl, "Accelerated Service-Life Testing of Photovoltaic Modules," in *Service Life Prediction of Exterior Plastics - Global Perspectives*, C. C. White, J. Martin, and J.T. Chapin (Eds.), Springer, 2015.

- [85] C.B.Honsberg and S.G.Bowden, "Photovoltaics Education Website," [Online] Available: [www.pveducation.org](http://www.pveducation.org), 2019. [Accessed: March 8, 2019].
- [86] *Photovoltaic (PV) systems – Requirements for testing, documentation and maintenance – Part 3: Photovoltaic modules and plants – Outdoor infrared thermography*, IEC TS 62446-3, 2017.
- [87] R. Moretón, E. Lorenzo, J. Leloux, J. M. Carrillo, "Dealing in Practice with Hot Spots," in *proceedings of the 29th European Photovoltaic Solar Energy Conference and Exhibition*, Amsterdam, 2014, doi: 10.13140/2.1.3066.7528.
- [88] C. Vodermayr, M. Mayer, T. Müller, M. Niess, G. Wotruba, G. Becker, M. Zehner, J. Schumacher, "First Results – Correlations between IR images and Electrical Behaviour and Energy Yield of PV Modules", in *Proceedings of the 23rd European Photovoltaic Specialists Conference*, 2008, Spain, pp. 3134 – 3137.
- [89] C. Buerhop, D. Schlegel, M. Niess, C. Vodermayr, R. Weissman, C. J. Brabec, "Reliability of IR-imaging of PV-plants under operating conditions", *Solar Energy Materials and Solar Cells*, vol. 107, pp. 154-164, 2012, doi: 10.1016/j.solmat.2012.07.011.
- [90] I. A. Tsanakas, E. Pilat, L. D. Ha, F. A. Shakarchi, "Early Reliability Issues and Symptoms Evaluated in Four Large PV Plants in Southern France", presented at the *NREL Photovoltaic Module Reliability Workshop*, Denver, CO, USA, 2017.
- [91] D. L. Ha and I. A. Tsanakas, "Method and System for Estimating a Loss of Energy Production of a Photovoltaic Module", French Patent No. FR3036900B1, May 26, 2015.
- [92] C. Camus, C. Buerhop, S. Wrana, J. Adams, T. Pickel, H. Scheuerpflug, C. Zetsmann, E. Malguth, J. Hauch, C. J. Brabec "Direct Evidence for Hot Cell induced modifications in PV Module Encapsulants," in *Proceedings of the 31st European Photovoltaic Specialists Conference*, Germany, 2016, doi: 10.4229/EUPVSEC20162016-5BO.10.6.

- [93] *PVA-1000S PV Analyzer Datasheet*, Solmetric Corporation [Online] Available: [http://www.solmetric.net/get/Solmetric\\_PVA\\_Brochure\\_single-page\\_081314.pdf](http://www.solmetric.net/get/Solmetric_PVA_Brochure_single-page_081314.pdf) [Accessed: March 11, 2019].
- [94] Spire Corporation, "Spire Solar 5600SLP Blue 230ms," [Online] Available: <https://www.spireolar.com/products/solar-simulators/spi-sun-simulator-5600slp-blue/> [Accessed: March 11, 2019].
- [95] *Photovoltaic devices - Part 9: Solar simulator performance requirements*, IEC Standard 60904-9, 2007.
- [96] B. Knisely, "Angle of Incidence and Non-Intrusive Cell Quantum Efficiency Measurements of Commercial Photovoltaic Modules," MS Thesis, Arizona State University, Tempe, USA, 2013. [Online] Available: [https://repository.asu.edu/attachments/125762/content/Knisely\\_asu\\_0010N\\_13297.pdf](https://repository.asu.edu/attachments/125762/content/Knisely_asu_0010N_13297.pdf) [Accessed: March 12, 2019].
- [97] *Jasco V-650 Spectrometer datasheet*, Jasco Incorporated, 2017 [Online] Available: [https://jascoinc.com/wp-content/uploads/2017/08/V650\\_Leaflet.pdf](https://jascoinc.com/wp-content/uploads/2017/08/V650_Leaflet.pdf) [Accessed: March 12, 2019].
- [98] *Thorlabs SOLIS-365C datasheet*, Thorlabs Corporation, 2018. [Online] Available: <https://www.thorlabs.com/drawings/99d51f044ff816c6-A029E778-A85D-1C7F-D7B03CBEF1844D25/SOLIS-365C-SpecSheet.pdf> [Accessed: March 6, 2019].
- [99] *Fiber Optics Spectrometer Datasheet*, Research-India, 2010. [Online] Available: <https://www.research-india.co.in/RI%20SERIES.pdf> [Accessed: March 10, 2019].
- [100] *Nikon D3200 datasheet*, Nikon Corporation, 2010. [Online] Available: <https://www.nikonusa.com/en/nikon-products/product-archive/dslr-cameras/d3200.html#tab-ProductDetail-ProductTabs-TechSpecs> [Accessed: March 12, 2019].

- [101] "Precision Color Devices," Testronix Instruments [Online] Available: <http://www.testronixinstruments.com/precision-color-device/> [Accessed: March 12, 2019].
- [102] *E-60 Datasheet*, FLIR Corporation. [Online] Available: <https://www.flir-direct.com/pdfs/cache/www.flir-direct.com/e60/datasheet/e60-datasheet.pdf> [Accessed: March 14, 2019].
- [103] C. Mahapatra, R. Dubey, S. Chattopadhyay, S. Zachariah, S. Sabnis, "Statistical Analysis of Degradation Data for c-Si modules observed in India in 2016," in *Proceedings of the 2017 IEEE 44<sup>th</sup> Photovoltaic Specialists Conference (PVSC)*, Washington, DC, USA, 2017, doi: 10.1109/PVSC.2017.8366657.
- [104] W.W. Holley and S.C. Argo, "Advanced EVA Based Encapsulants: Final Report," National Renewable Energy Laboratory, Golden, CO, USA, Technical Report No. NREL/SR-520-25296, September 1998 [Online] Available: <https://www.nrel.gov/docs/legosti/fy97/25296.pdf> [Accessed: April 6, 2019].
- [105] L. Spinella and N. Bosco, "FTIR Investigation of EVA Chemical Bonding Environment and Its Impact on Debond Energy," *IEEE Journal of Photovoltaics*, vol. 9, no. 3, pp. 790-795, May 2019, doi: 10.1109/JPHOTOV.2019.2904219.
- [106] R. Dubey, "Electrical Degradation of Crystalline Silicon PV modules in Indian Climates and its correlation with Cell Cracks: Field and Laboratory Studies", PhD Dissertation, Dept. of Electrical Engineering, Indian Institute of Technology Bombay, Mumbai, 2021.
- [107] "Digital Camera Sensors," Cambridge in Color [Online]. Available: [www.cambridgeincolor.com/tutorials/camera-sensors.htm](http://www.cambridgeincolor.com/tutorials/camera-sensors.htm) [Accessed: March 12, 2019].
- [108] "Application Note - Yellowness Index", Hunterlab [Online] Available: <https://www.hunterlab.se/wp-content/uploads/2012/11/Yellowness-Indices.pdf> [Accessed: March 12, 2019].

- [109] B. J. Lindbloom, “RGB to XYZ”, [Online] Available: [http://www.brucelindbloom.com/index.html?Eqn\\_RGB\\_to\\_XYZ.html](http://www.brucelindbloom.com/index.html?Eqn_RGB_to_XYZ.html) [Accessed: March 12, 2019].
- [110] N. Schaller, “Color Conversion Algorithms,” Rochester Institute of Technology [Online]. Available: [https://www.cs.rit.edu/~ncs/color/t\\_convert.html](https://www.cs.rit.edu/~ncs/color/t_convert.html) [Accessed: March 10, 2019].
- [111] A. Rockikz, “How to Use K-Means Clustering for Image Segmentation using OpenCV in Python”, Pythoncode website [Online] Available: <https://www.thepythoncode.com/article/kmeans-for-image-segmentation-opencv-python>.
- [112] *Photovoltaic Devices – Procedure for temperature and irradiance corrections to measured I-V characteristics*, IEC 60891, 2009.
- [113] S. Chattopadhyay, R. Dubey, S. Bhaduri, S. Zachariah, H. K. Singh, C.S. Solanki, A. Kottantharayil, N. Shiradkar, B.M.Arora, K.L.Narasimhan, J. Vasi, “Correlating Infrared Thermography With Electrical Degradation of PV Modules Inspected in All-India Survey of Photovoltaic Module Reliability 2016,” *IEEE Journal of Photovoltaics*, vol. 8, no. 6, pp. 1800-1808, 2018, doi: 10.1109/JPHOTOV.2018.2859780.
- [114] I. Haedrich, H.Wirth, M. Storz, and G. Klingebiel, “PV module efficiency analysis and optimization,” Fraunhofer ISE, Freiburg, Germany, Webinar, Sep. 2012.[Online] Available: <https://www.slideshare.net/Web2present/for-the-presentation-of-fraunhofer-institute-clicke-here> [Accessed on 12 July 2019].
- [115] M. R. Vogt, H. Holst, M.Winter, R. Brendel, and P. P. Altermatt, “Numerical modeling of c-Si PV modules by coupling the semiconductor with the thermal conduction, convection and radiation equations,” *Energy Procedia*, vol. 77, pp. 215–224, 2015, doi: 10.1016/j.egypro.2015.07.030.
- [116] R. Dubey, S. Chattopadhyay, S. Zachariah, S. Rambabu, H. K. Singh, A. Kottantharayil, B. M. Arora, K. L. Narsimhan, N. Shiradkar, J. Vasi, “On-site electroluminescence

- study of field-aged PV modules,” in *Proceedings of the 2018 IEEE 7<sup>th</sup> World Conference on Photovoltaic Energy Conversion (A Joint Conference of 45th IEEE PVSC, 28th PVSEC & 34th EU PVSEC)*, Waikoloa Village, HI, USA, 2018, pp. 0098-0102, doi: 10.1109/PVSC.2018.8548080.
- [117] S. Bhaduri, S. Chattopadhyay, R. Dubey, S. Zachariah, V. Kuthanazhi, C. S. Solanki, B. M. Arora, K. L. Narsimhan, A. Kottantharayil and J. Vasi., “Correlating Infra-red thermography with electrical degradation of modules inspected in All India Survey of Photovoltaic Module Reliability 2016,” presented at the *NREL Photovoltaic Module Reliability Workshop*, Lakewood, WA, USA, 2017, pp. 199. [Online]. Available: <https://www.nrel.gov/docs/fy17osti/68942.pdf>
- [118] J. Oh and G. TamizhMani, “Temperature testing and analysis of PV modules per ANSI/UL 1703 and IEC 61730 standards,” in *Proceedings of the 2010 IEEE 35th Photovoltaic Specialists Conference (PVSC)*, Honolulu, HI, USA, 2010, pp. 984–988, doi: 10.1109/PVSC.2010.5614569.
- [119] S. Chattopadhyay, R. Dubey, Vivek K., J. John, C. S. Solanki, A. Kottantharayil, B. M. Arora, K.L. Narasimhan, J. Vasi, B. Bora, Y. K. Singh, and O.S. Sastry, “Effect of hot cells on power degradation rate of PV modules,” presented at the *NREL Photovoltaic Module Reliability Workshop*, Lakewood, WA, USA, 2016, pp. 244. [Online]. Available: <https://www.nrel.gov/docs/fy17osti/68116.pdf>.
- [120] A. Morlier, A. Hasse, and M. Kontges, “Impact of cracks in multicrystalline silicon solar cells on PV module power – a simulation study based on field data,” *IEEE Journal of Photovoltaics*, vol. 5, no. 6, pp. 1735–1741, Nov. 2015, doi: 10.1109/JPHOTOV.2015.2471076.
- [121] R. Dubey, S. Chattopadhyay, V. Kuthanazhi, Anil K., C. S. Solanki, B. M. Arora, K. L. Narasimhan, J. Vasi, B. Bora, Y. K. Singh, O. S. Sastry, “Comprehensive study of performance degradation of field-mounted photovoltaic modules in India,” *Energy Science & Engineering*, vol. 5, pp. 51-64, 2016, doi: 10.1002/ESE3.150.

- [122] *Spectral Power Distribution for Q-Sun, QUV and Noon Summer Sunlight*, Q Lab [Online]. Available: <http://www.q-lab.com/documents/private/e60de24c-d6c3-497b-9ee4-e4aad832c76b.pdf> [Accessed: March 21, 2019].
- [123] M. Siebert, I. Kunze, G. Mathiak, M. Kontges and A. Morlier, "Detecting Photovoltaic Module Failures in the Field during Daytime with Ultraviolet Fluorescence Imaging Inspection," *IEEE Journal of Photovoltaics*, vol. 7, no. 6, pp. 1710 – 1716, 2017, doi: 10.1109/JPHOTOV.2015.2471076.
- [124] M. E. Davis and R. J. Davis, *Fundamentals of Chemical Reaction Engineering*, 1st ed. New York, USA: McGraw-Hill Higher Education, 2003.
- [125] D. C. Miller, J. G. Bokria, D M. Burns, S. Fowler, X. Gu, P. L. Hacke, C. C. Honekar, M. D. Kempe, M. Kohl, N. H. Philips, K. P. Scott, A. Singh, S. Suga, S. Watanabe, and A. F. Zielnik, "Degradation in Photovoltaic Encapsulant Transmittance: Results of the first PVQAT TG5 Artificial Weathering Study," *Progress in Photovoltaics: Research & Applications*, pp. 1-19, 2019, doi: 10.1002/pip.3103.
- [126] Y. Hong, W. Q. Meeker, D. L. Stanley, Y. Duan, and X. Gu, "Photodegradation modeling based on laboratory accelerated test data and predictions under outdoor weathering for polymeric materials," *The Annals of Applied Statistics*, vol. 11, no. 4, pp. 2052-2079, 2017, doi: 10.1214/17-AOAS1060.
- [127] "Sandia Module Temperature Model," Sandia National Laboratory website [Online]. Available: <https://pvpmc.sandia.gov/modeling-steps/2-dc-module-iv/module-temperature/sandia-module-temperature-model/> [Accessed: May 21, 2019].
- [128] *National Solar Radiation Database*, U.S. Department of Energy, National Renewable Energy Laboratory, Golden, CO, USA. [Online] Available: <https://maps.nrel.gov/nsrdb-viewer/> [Accessed: June 10, 2019].
- [129] W. F. Holmgren, C. W. Hansen, and M. A. Mikofski, "PVlib python: a python package for modeling solar energy systems," *Journal of Open Source Software*, vol. 3, no. 29, p. 884, 2018, doi: 10.21105/joss.00884.

- [130] C. Schmid, J. Chapon, G. Kinsey, J. Bokria, and J. Woods, "Impact of High Light Transmission EVA based encapsulant on the performance of PV Modules," in *Proceedings of the 27<sup>th</sup> European Photovoltaic Specialists Conference and Exhibition*, Frankfurt, Germany, 2012, pp. 3494 – 3498, doi: 10.4229/27thEUPVSEC2012-4BV.3.28.
- [131] *UV 531 – Technical Datasheet*, Hunan Chemical [Online]. Available: <https://hunan-chem.com/wp-content/uploads/2016/06/UV-Absorber-531.pdf> [Accessed: March 10, 2019].
- [132] *Q-Sun Xenon Test Chamber Brochure*, Q Lab [Online]. Available: <https://www.q-lab.com/documents/public/41b5935b-d41d-4368-a53e-98a3d528baf1.pdf> [Accessed: March 21, 2019].
- [133] Boris Vieth-Wolf, "Effect of UV Illumination on the Passivation Quality of AlO<sub>x</sub>-cSi Interfaces," in *Proceedings of the 2016 IEEE 43<sup>rd</sup> Photovoltaic Specialist Conference*, Portland, OR, USA, 2016, pp. 1173 – 1178, doi: 10.1109/PVSC.2016.7749799.
- [134] B. Sopori, P. Basnyat, S. Shet, V. Mehta, J. Bins, J. Appel, "Understanding Light-Induced Degradation in c-Si Solar Cells," in *Proceedings of the 2012 IEEE 38<sup>th</sup> Photovoltaic Specialist Conference (PVSC)*, Austin, TX, USA, 2012, pp. 1115 – 1120, doi: 10.1109/PVSC.2012.6317798.
- [135] J. Wohlgemuth, M. Kempe and D. Miller, "Discoloration of PV Encapsulants," in *Proceedings of the 2013 IEEE 39<sup>th</sup> Photovoltaic Specialist Conference (PVSC)*, Tampa, FL, USA, 2013, pp. 3260-3265, doi: 10.1109/PVSC.2013.6745147.
- [136] Keith Emery, "Reference Solar Spectral Irradiance: AM 1.5 Global" [Online]. Available: <https://rredc.nrel.gov/solar//spectra/am1.5/> [Accessed: June 10, 2019].
- [137] UDT Sensors Inc., "Planar Diffused Silicon Photodiodes", Datasheet [Online]. Available: [https://peshkin.mech.northwestern.edu/datasheets/Optoelectronics/Photodiode\\_UDT\\_catalog.pdf](https://peshkin.mech.northwestern.edu/datasheets/Optoelectronics/Photodiode_UDT_catalog.pdf) [Accessed: June 10, 2019].

This page is intentionally left blank.

# List of Publications

## International Journals

1. **S. Chattopadhyay**, R. Dubey, S. Bhaduri, S. Zachariah, H. K. Singh, C. S. Solanki, Anil K., N. Shiradkar, B. M. Arora, K. L. Narsimhan, J. Vasi, “Correlating Infrared Thermography with Electrical Degradation of PV Modules Inspected in All-India Survey of Photovoltaic Module Reliability 2016”, *IEEE Journal of Photovoltaics*. Vol. 8 Issue 6, pp. 1800-1808, 2018, doi: 10.1109/JPHOTOV.2018.2859780 (cited 12 times).
2. **S. Chattopadhyay**, R. Dubey, Vivek K., J. John, C. S. Solanki, A. Kottantharayil, B.M. Arora, K.L. Narasimhan, V. Kuber, J. Vasi, A. Kumar, O.S. Sastry, “Visual Degradation in Field-aged Crystalline Silicon PV Module in India and Correlation with electrical degradation”, *IEEE Journal of Photovoltaics*, Vol. 4 Issue 6, pp. 1470 - 1476. 2014. DOI: 10.1109/JPHOTOV.2014.2356717 (**Oral presentation** at 41<sup>st</sup> *IEEE Photovoltaic Specialists Conference*, Denver, 2014, cited 56 times).
3. R. Dubey, **S. Chattopadhyay**, V. Kuthanazhi, Anil K., C. S. Solanki, B. M. Arora, K. L. Narasimhan, J. Vasi, B. Bora, Y. K. Singh, O. S. Sastry, “Comprehensive study of performance degradation of field-mounted photovoltaic modules in India”, *Energy Science & Engineering*, Vol. 5, 51-64. 2016, doi: 10.1002/ESE3.150 (cited 43 times).
4. B. Adothu, **S. Chattopadhyay**, P. Bhatt, P. Hui, F. R. Costa, S. Mallick, “Early-stage identification of encapsulants photobleaching and discoloration in crystalline silicon photovoltaic module laminates”, *Progress in Photovoltaics*, vol. 28, no. 8, pp. 767-778, 2020. doi: 10.1002/pip.3269 (cited 2 times).
5. B. Adothu, P. Bhatt, **S. Chattopadhyay**, S. Zele, J. Oderkerk, H.P. Sagar, F. R. Costa, S. Mallick, “Newly developed thermoplastic polyolefin encapsulant—A potential candidate for crystalline silicon photovoltaic modules encapsulation,” *Solar Energy*, vol. 194, pp. 581-588, 2019. doi: 10.1016/j.solener.2019.11.018 (cited 9 times).

## International Conferences

1. **S. Chattopadhyay**, C. S. Solanki, Anil K., K. L. Narasimhan, J. Vasi, S. Tatapudi, G. Tamizhmani, “Quantification of PV Module Discoloration using Visual Image Analysis”, in *Proceedings of the 2017 IEEE 44<sup>th</sup> Photovoltaic Specialists Conference (PVSC)*, Washington, DC, USA, 2017, doi: 10.1109/PVSC.2017.8366593 (cited 1 time).
2. **S. Chattopadhyay**, R. Dubey, Vivek K., J. John, C. S. Solanki, A. Kottantharayil, B. M. Arora, K.L. Narasimhan, J. Vasi, B. Bora, Y. K. Singh, O.S. Sastry, “Effect of Hot Cells on Power Degradation of PV Modules,” presented at the *2016 NREL Photovoltaic Module Reliability Workshop*, Golden, CO, USA, 2016, pp. 244 [Online] Available: <https://www.nrel.gov/docs/fy17osti/68116.pdf> (**Best Poster Award** in “Module Reliability in Extreme Climates” category).
3. **S. Chattopadhyay**, R. Dubey, Vivek K., J. John, C. S. Solanki, A. Kottantharayil, B. M. Arora, K.L. Narasimhan, J. Vasi, B. Bora, Y. K. Singh, O.S. Sastry, “All India Survey of Photovoltaic Module Degradation 2014: Survey Methodology and Statistics,” in *Proceedings of the 2015 IEEE 42<sup>nd</sup> Photovoltaic Specialists Conference (PVSC)*, New Orleans, LA, USA, 2015, pp. 1-6, doi: 10.1109/PVSC.2015.7355712 (cited 13 times).
4. R. Dubey, **S. Chattopadhyay**, S. Zachariah, V. Kuthanazhi, S. Rambabu, S. Bhaduri, H. K. Singh, C. S. Solanki, Anil K., B. M. Arora, K. L. Narasimhan, N. Shiradkar, B. Bora, O. S. Sastry, J. Vasi, “Investigation of Poor Performing PV Modules observed in All-India Survey of Photovoltaic Module Reliability 2016,” in *Proceedings of the 2018 IEEE 7<sup>th</sup> World Conference on Photovoltaic Energy Conversion (A Joint Conference of 45<sup>th</sup> IEEE PVSC, 28<sup>th</sup> PVSEC & 34<sup>th</sup> EU PVSEC)*, Waikoloa, HI, USA, 2018, pp. 690-694, doi: 10.1109/pvsc.2018.8548000 (cited 1 time).
5. P. Mundle, **S. Chattopadhyay**, C. S. Solanki, N. Shiradkar, K. L. Narasimhan, Anil K., J. Vasi, B. K. Chakraborty, “Effect of Aluminum Back plate on PV Module Temperature and Performance”, in *Proceedings of the 2018 IEEE 7<sup>th</sup> World Conference on Photovoltaic Energy Conversion (A Joint Conference of 45<sup>th</sup> IEEE PVSC, 28<sup>th</sup>*

*PVSEC & 34th EU PVSEC*), Waikoloa, HI, USA, June 2018, pp. 745-748, doi: 10.1109/PVSC.2018.8547921 (cited 1 time).

6. S. Bhaduri, **S. Chattopadhyay**, R. Dubey, S. Zachariah, V. Kuthanazhi, C. S. Solanki, B. M. Arora, K. L. Narsimhan, A. Kottantharayil, J. Vasi, “Correlating Infrared Thermography with Electrical Degradation of Modules inspected in All India Survey of Photovoltaic Module Reliability 2016”, presented at the *2017 NREL Photovoltaic Reliability Workshop*, Golden, CO, USA, 2017, pp. 199 [Online] Available: <https://www.nrel.gov/docs/fy17osti/68942.pdf> (**Best Poster Award**).
7. R. Dubey, **S. Chattopadhyay**, Vivek K., J. John, C. S. Solanki, A. Kottantharayil, B. M. Arora, K. L. Narasimhan, J. Vasi, B. Bora, Y. K. Singh, O.S. Sastry, “Correlation of Electrical and Visual Degradation Seen in Field Survey in India”, in *Proceedings of the 2016 IEEE 43rd Photovoltaic Specialist Conference (PVSC)*, Portland, OR, USA, 2016, pp. 1692-1696, doi: 10.1109/PVSC.2016.7749912 (**Best Poster Award**, cited 3 times).
8. R. Dubey, **S. Chattopadhyay**, Vivek K., Jim John, C.S.Solanki, Anil K., B.M. Arora, K.L. Narasimhan, J. Vasi, A. Kumar, O.S. Sastry, “Performance Degradation of Field-aged crystalline silicon PV Modules in different Indian climatic conditions,” in *Proceedings of the 2014 IEEE 40<sup>th</sup> Photovoltaic Specialists Conference (PVSC)*, Denver, CO, USA, 2014, pp. 3182 - 3187, doi: 10.1109/PVSC.2014.6925612 (cited 27 times).
9. R. Dubey, **S. Chattopadhyay**, Vivek K., Jim John, C.S.Solanki, Anil K., B.M. Arora, K.L. Narasimhan, J. Vasi, “Daylight Electroluminescence Imaging of Photovoltaic Modules by Image Difference Technique,” presented at the *6<sup>th</sup> World Conference on Photovoltaic Energy Conversion*, Kyoto, Japan, 2014.
10. R. Dubey, S. Zachariah, **S. Chattopadhyay**, V. Kuthanazhi, S. Rambabu, S. Bhaduri, H. K. Singh, A. Sinha, C. S. Solanki, Anil K., B. M. Arora, K. L. Narasimhan, J.Vasi, B. Bora, R. Kumar, O. S. Sastry, “Performance of Field-Aged PV Modules in India: Results from 2016 All India Survey of PV Module Reliability”, in *Proceedings of the 2017 IEEE 44<sup>th</sup> Photovoltaic Specialists Conference (PVSC)*, Washington, DC, USA, 2017, doi: 10.1109/PVSC.2017.8366143 (**Oral presentation**, cited 8 times).

11. Vivek K., R. Dubey, **S. Chattopadhyay**, J. John, C.S.Solanki, Anil K., B.M. Arora, K.L. Narasimhan, J. Vasi, A. Kumar, O.S. Sastry, “Linking Performance of PV Systems in India with Socio-economic Aspects of Installation,” in *Proceedings of the 2014 IEEE 40<sup>th</sup> Photovoltaic Specialists Conference (PVSC)*, Denver, CO, USA, 2014, pp. 1448 - 1451, doi: 10.1109/PVSC.2014.6925188 (cited 4 times).
12. S. Bhaduri, S. Zachariah, Y. R. Golive, **S. Chattopadhyay**, R. Dubey, R. Ingle, A. Kottantharayil, A. A. Khattab, H. K. Singh, S. Mallick, J. Vasi and N. Shiradkar, “Correlating the Hot Spots and Power Degradation seen in crystalline silicon modules in All India Survey of PV Module Reliability 2018”, in *Proceedings of the 2019 IEEE 46<sup>th</sup> Photovoltaic Specialists Conference (PVSC)*, Chicago, IL, USA, 2019, pp. 861-865, doi: 10.1109/PVSC40753.2019.8980514.
13. S. Zachariah, R. Dubey, G. Y. Rao, S. Bhaduri, **S. Chattopadhyay**, C. S. Solanki, A. Kottantharayil, B. M. Arora, K.L. Narasimhan, H. K. Singh, J. Vasi and N. Shiradkar, “Electroluminescence Study of over 700 Fielded PV Modules in All India Survey 2018,” in *Proceedings of the 2019 IEEE 46<sup>th</sup> Photovoltaic Specialists Conference (PVSC)*, Chicago, IL, USA, 2019, doi: 10.1109/PVSC40753.2019.8981208.

## Reports

1. **S. Chattopadhyay**, R. Dubey, Vivek K., S. Zachariah, S. Bhaduri, C. Mahapatra, S. Rambabu, F. Ansari, A. Chindarkar, A. Sinha, H. K. Singh, N. Shiradkar, B. M. Arora, A. Kottantharayil, K. L. Narasimhan, S. Sabnis, B. Bora, G. Kumar, Y. K. Singh, M. Bangar, M. Kumar, A. Kumar Haldkar, R. Singh, S. Raghava, M. Morampudi, G. Ganesh, R. Kumar, O. S. Sastry and J. Vasi, “All-India Survey of PV Module Reliability: 2016,” National Centre for Photovoltaic Research and Education, Mumbai, India, 2015. [Internet] Available: [http://www.ncpre.iitb.ac.in/research/pdf/All\\_India\\_Survey\\_of\\_Photovoltaic\\_Module\\_Reliability\\_2016.pdf](http://www.ncpre.iitb.ac.in/research/pdf/All_India_Survey_of_Photovoltaic_Module_Reliability_2016.pdf)
2. R. Dubey, **S. Chattopadhyay**, Vivek K., J. John, C.S. Solanki, Anil K., B.M. Arora, K.L. Narasimhan, V. Kuber, J. Vasi, B. Bora, Y. K. Singh, O.S. Sastry, “All-India Survey of PV Module Reliability: 2014,” National Centre for Photovoltaic Research and Education, Mumbai, India, 2015 [Internet] Available: [www.ncpre.iitb.ac.in/uploads/All\\_India\\_Survey\\_of\\_Photovoltaic\\_Module\\_Reliability\\_2014.pdf](http://www.ncpre.iitb.ac.in/uploads/All_India_Survey_of_Photovoltaic_Module_Reliability_2014.pdf)

3. R. Dubey, **S. Chattopadhyay**, Vivek K., J. John, C.S. Solanki, Anil K., B.M. Arora, K.L. Narasimhan, V. Kuber, J. Vasi, A. Kumar, O.S. Sastry, "All-India Survey of PV Module Degradation: 2013," National Centre for Photovoltaic Research and Education, Mumbai, India, Mar. 2014 [Internet] Available: [www.ncpre.iitb.ac.in/uploads/All\\_India\\_Survey\\_of\\_Photovoltaic\\_Module\\_Degradation\\_2013.pdf](http://www.ncpre.iitb.ac.in/uploads/All_India_Survey_of_Photovoltaic_Module_Degradation_2013.pdf)

This page is intentionally left blank.

# Resume

## **Shashwata Chattopadhyay**

Ph. D. Student

Energy Science & Engineering Department

Indian Institute of Technology, Bombay

sunny.shashwat@gmail.com

+91 9833514618

### **Education**

#### **Ph. D. Energy Science & Engineering** (pursuing)

Indian Institute of Technology, Bombay

- Guides: Prof. Chetan Singh Solanki, Prof. Anil Kottantharayil
- CPI: 7.9/10

#### **Bachelor of Technology - Power Engineering** (6/2006)

National Power Training Institute (ER), West Bengal University of Technology, Kolkata

- CGPA: 8.6

#### **Intermediate/+2** (7/2002)

D.A.V. Model School, C.B. S. E

- Percentage: 81.2%

#### **Matriculation** (7/2000)

Pranavananda Vidyamandir, I. C. S. E

- Percentage: 87.3%

**Note:** Joined IIT Bombay as a M. Tech. student in 2011, and converted to joint M. Tech. – Ph. D. program in 2014.

### **Area of Interest**

- Photovoltaic Module Performance Characterization
- Accelerated testing and Reliability analysis of Photovoltaic Modules

### **Research Highlights**

- Identification of **PV module degradation modes** in field-aged PV modules through All-India surveys of PV module reliability conducted in 2013, 2014 and 2016
- Quantification of **PV module discoloration** using visual (RGB) image analysis (using OPENCV computer vision library in Python programming language)
- Correlation of **Hot Cells with electrical degradation** in PV modules inspected in All-India Survey of Photovoltaic Module Reliability.’
- Determination of **activation energy for encapsulant discoloration** and comparison of different EVA-based encapsulants in UV accelerated tests

### **Professional Experience**

- **SolarMarQ Engineering LLP (Co-founder)**  
[May 2019 to present]
  - Solar Panel Testing Products include Portable EL Tester, Mini Module EL Tester and DML Tester
  - On-site EL Inspection & Reporting Services for MW scale solar power plants

- **Project Research Assistant in National Center for Photovoltaic Research and Education (NCPRE), IIT Bombay**  
[August 2011 to June 2019]
  - Participated in All India Survey of Photovoltaic Module Reliability in 2013, 2014 and 2016.
  - Initiated accelerated testing of encapsulant polymers at NCPRE
  - Involved in development of UV-365 accelerated test chamber at NCPRE
  - Involved in development of portable EL Tester at NCPRE
- **Design Engineer in Development Consultants Pvt. Ltd. Kolkata**  
[August 2006 to March 2010]
  - Involved in preparation of tender specifications for coal-fired thermal power plants.

### **Internships**

#### **Research Intern at Arizona State University – Photovoltaic Reliability Laboratory (ASU-PRL) under Dr. G. TamizhMani, funded through the SERIUS-MAGEEP fellowship**

[Nov. 2016 to Feb. 2017]

- Worked on quantification of discoloration of solar panels, and also involved in preparatory work for accelerated testing of different EVA encapsulants (leading to accelerated testing of encapsulants in Xenon chamber at IIT Bombay).
- Involved in analysis of electroluminescence (EL) images and *I-V* data of cracked solar panel to determine correlation between the dark area in EL image and power loss of affected cell.
- Involved in preparatory work for accelerated testing of module level inverters.

### **Conferences Attended**

- 40<sup>th</sup> IEEE Photovoltaic Specialist Conference held in June, 2014 at Denver, Colorado.
- 42<sup>nd</sup> IEEE Photovoltaic Specialist Conference held in June, 2015 at New Orleans, Louisiana, USA.
- NREL PV Module Reliability Workshop held in February 2016 at Golden, Colorado, USA in February, 2016.
- 44<sup>th</sup> IEEE Photovoltaic Specialist Conference held in June, 2017 at Washington D.C. Washington, USA.
- Workshop on “Standards for Solar PV Modules” organized by NISE (India) and PTB (Germany), at Gurgaon, Haryana in September 2016.

### **Awards/Fellowships**

- Best poster award at the NREL PV Module Reliability Workshop 2017 for the poster: “Correlating Infrared Thermography with Electrical Degradation of Modules inspected in All India Survey of Photovoltaic Module Reliability 2016”, by S. Bhaduri, S. Chattopadhyay, R. Dubey, S. Zachariah, V. Kuthanazhi, C. S. Solanki, B. M. Arora, K. L. Narsimhan, A. Kottantharayil, J. Vasi
- Best poster award at the NREL PV Module Reliability Workshop 2016 for the poster: “Effect of Hot Cells on Electrical Degradation of PV Modules”, by S. Chattopadhyay, R. Dubey, V. Kuthanazhi, J. J. John, J. Vasi, A. Kottantharayil, B. M. Arora, K. L. Narsimhan, C. S. Solanki, B. Bora, Y. K. Singh and O.S. Sastry.
- Best poster award at the 43<sup>rd</sup> IEEE Photovoltaic Specialist Conference for the poster: “Correlation of Electrical and Visual Degradation Seen in Field Survey in India”, by R. Dubey,

S. Chattopadhyay, V. Kuthanazhi, J. J. John, C. S. Solanki, B. M. Arora, K. L. Narasimhan, A. Kottantharayil, J. Vasi, B. Bora, Y. K. Singh, O. S. Sastry.

- Received SERIUS MAGEEP fellowship in year 2016 for perusing three months internship at Arizona State University.

### **Technical Skills**

**Characterization & Testing Equipment** : Solar Simulator (Spire SPI-Sun 5600 SPL Blue),  
Portable *I-V* tracer (Solmetric PVA-1000S),  
Thermal Imager (FLIR E60),  
Electroluminescence camera (Sensovation HR-830),  
Multicurve *I-V* tracer (Daystar MT-5),  
Xenon chamber (QLab QSun Xe3),  
Fiber Optics Spectrometer (Research-India RISC),  
Colorimeter (Textronix TP-110).

**Programming Languages** : Octave, Python, C, C++

This page is intentionally left blank.

## **Acknowledgements**

I am thankful to my guide, Prof. Chetan Singh Solanki, and co-guide, Prof. Anil Kottantharayil, for their guidance and support. I am grateful to Prof. Juzer Vasi, Prof. K. L. Narasimhan, and Prof. B.M.Arora for their expert guidance and active involvement in the research work. I am thankful to my colleagues Mr. Rajiv Dubey, Mr. Vivek Kuthanazhi, Mr. Birinchi Bora, Mr. Yogesh Kumar Singh and other team members from IIT Bombay and National Institute of Solar Energy (NISE) for their suggestions, and active help and support during the All-India Surveys. I am also thankful to Mr. Sugunna Rambabu and Mr. Ajeesh Alath, who have been very helpful both in the NCPRE laboratory and in the All-India surveys. Also, I would like to give thanks to Mr. Balaji Adothu, Ms. Sonali Bhaduri, Mr. Yogeshwar Golive and Mr. Sachin Zachariah for their help and suggestions in various measurements and data analysis. Also, I would like to mention that Ms. Ishita Kumar and Mr. Zaksh Manekshana did internship on the accelerated testing of encapsulants and their help and support is much appreciated.

I am grateful to Prof. G. TamizhMani for accepting my proposal for internship at Arizona State University (ASU), during which time I learnt a lot through direct interactions with him and his group. I would like to acknowledge the help obtained from Mr. Sai Tatapudi and other students at Arizona State University, not only inside the laboratory but also in various other matters related to daily life at ASU campus. I have worked jointly with Kshitiz Dolia at ASU during my internship on the EVA accelerated testing project and I am thankful to him for preparing the mini-modules (of UV-cut EVA) which I have used for accelerated tests at IIT Bombay.

I am thankful to the National Centre for Photovoltaic Research & Education (NCPRE) for financially supporting my work in Photovoltaics. I am also grateful to the Indian Institute of Technology (IIT) Bombay for granting me access to the various laboratory facilities and online journals. I would also like to acknowledge the support provide by Solar Energy Research Institute for India and the United States (SERIUS) in attending various international conferences and also thank SERIUS for funding my three-month internship at Arizona State University, through the MAGEEP fellowship.